Three-axis Hybridized Quantum Accelerometer for Inertial Navigation

Simon Templier

▶ **To cite this version:**

Simon Templier. Three-axis Hybridized Quantum Accelerometer for Inertial Navigation. Atomic Physics [physics.atom-ph]. Université de Bordeaux, 2021. English. NNT : . tel-03296219v1

HAL Id: tel-03296219

https://hal.science/tel-03296219v1

Submitted on 22 Jul 2021 (v1), last revised 19 Aug 2021 (v2)

HAL is a multi-disciplinary open access archive for the deposit and dissemination of scientific research documents, whether they are published or not. The documents may come from teaching and research institutions in France or abroad, or from public or private research centers.

L'archive ouverte pluridisciplinaire **HAL**, est destinée au dépôt et à la diffusion de documents scientifiques de niveau recherche, publiés ou non, émanant des établissements d'enseignement et de recherche français ou étrangers, des laboratoires publics ou privés.

université de BORDEAUX

université de BORDEAUX

THÈSE PRÉSENTÉE

POUR OBTENIR LE GRADE DE

DOCTEUR

DE L'UNIVERSITÉ DE BORDEAUX

ECOLE DOCTORALE SCIENCES PHYSIQUES ET DE L'INGENIEUR

LASERS, MATIERE ET NANOSCIENCES

Par **Simon TEMPLIER**

Three-axis Hybridized Quantum Accelerometer for Inertial Navigation

---

Sous la direction de : **Baptiste BATTELIER**

Soutenue le 21 Avril 2021

Membres du jury :

M. Daniel COMPARAT	Directeur de Recherche	Président du jury
M. Arnaud LANDRAGIN	Directeur de Recherche	Rapporteur
M. Malo CADORET	Maître de conférences	Rapporteur
M. Philippe BOUYER	Directeur de Recherche	Examinateur
M. Marco PREVEDELLI	Professeur associé	Examinateur
M. Henri PORTE	Directeur de Recherche	Examinateur
M. Brynle BARRETT	Chargé de Recherche	Invité

Accéléromètre Quantique 3-axes Hybridé pour la Navigation Inertielle

Résumé : L'objectif du laboratoire commun iXatom, issu de la collaboration entre le laboratoire photonique numérique et nanoscience (LP2N) et l'entreprise iXblue, est de développer des solutions pour améliorer la navigation inertielle avec des capteurs quantiques. En effet les capteurs inertiels classiques délivrent un biais non constant sur la mesure qui fausse la trajectoire calculée par une centrale inertielle. Les interféromètres atomiques à ondes de matière offrent une mesure absolue avec une précision et une stabilité sans précédent. Ces capteurs présentent un intérêt important pour la navigation inertielle.

Ces capteurs inertiels quantiques atteignent une maturité dans le monde académique qui justifie un transfert vers l'industrie. Ces instruments, comprenant une enceinte à ultra-vide, une architecture de contrôle poussée, un système laser agile, multi-fréquence et cohérent en phase, demeurent complexes et imposants. Ils nécessitent un effort d'intégration pour les applications industrielles et embarquées.

Ce travail de thèse s'intéresse à l'amélioration des accéléromètres pour la navigation inertielle. L'hybridation entre des accéléromètres atomiques et classiques apporte une complémentarité des performances requises dans ce contexte. En effet les mesures de l'interféromètre atomique ont une dynamique restreinte et subissent des temps morts nécessaires à la préparation des atomes froids pour l'interrogation, ce qui réduit la bande-passante. Les accéléromètres classiques apportent une mesure continue avec une grande plage dynamique, nécessaire pour la navigation. L'accéléromètre hybride fournit une mesure avec une large bande-passante, une grande dynamique et pour laquelle le biais est amorti. Certains défis, dont la mesure multi-axe et selon une orientation quelconque du capteur atomique, sont adressés. Egalement une méthode pour la calibration de l'interféromètre atomique trois-axes est proposée et mise en œuvre, comprenant l'étude des effets systématiques et la correction des désalignements entre les axes de mesure.

Mots-clés : Interférométrie atomique, Accéléromètre, Navigation Inertielle, Source Laser

---

Laboratoire Photonique, Numérique et Nanosciences
UMR 5298 LP2N, 33000 Bordeaux, France.

Three-axis Hybridized Quantum Accelerometer for Inertial Navigation

Abstract: The spirit of the shared laboratory iXatom, involving the collaboration between the laboratoire photonique numérique et nanoscience (LP2N) and the company iXblue, is to develop solutions and improvements for inertial navigation with quantum sensors. Indeed classical inertial sensors suffer from a time-varying bias which mislead the computed trajectory by inertial navigation systems. Atom interferometers based on matter-waves offer an absolute measurement with a dramatic precision and stability. Such sensors are considered as a serious candidate to help inertial navigation systems.

Cold-atom inertial sensors are reaching a certain level of maturity in the academic community which justify a technological transfer toward the industry. However such instruments, including an ultra-high vacuum chamber, a complex control system, an agile multi-frequency laser architecture with phase coherence and control, remain complex and massive. Efforts are necessary for their integration into industrial and on-board applications.

This thesis work addresses the improvement of accelerometers dedicated to inertial navigation. The hybridization between classical and quantum accelerometers afford complementary performances. Actually the measurements of the atomic interferometer experience a reduced dynamic and dead-times during the preparation of the atomic cloud, leading to a limited bandwidth. Classical accelerometers present continuous measurements with a large dynamic range necessary for navigation. The hybrid accelerometer provides high-bandwidth measurements with a wide dynamic range and without biases. Other challenges, such as multi-axis measurements with a random orientation of the atomic sensor, are investigated. Furthermore a method to calibrate the 3-axis atom interferometer is proposed and realised, which involves a full study of the systematic effects and the correction of misalignments between measurement axes.

Keywords: Atom Interferometry, Accelerometer, Inertial Navigation, Laser Source

---

Laboratoire Photonique, Numérique et Nanosciences
UMR 5298 LP2N, 33000 Bordeaux, France.

Remerciements

Ces travaux de thèse s'inscrivent dans le cadre du laboratoire commun iXatom, issu d'une collaboration entre le Laboratoire Photonique Numérique et Nanosciences (LP2N) et l'entreprise iXblue. Ce doctorat a été effectué avec l'appui de l'Association Nationale de la Recherche et de la Technologie (ANRT) via l'attribution d'une bourse CIFRE.

Je remercie chaleureusement mon directeur de thèse Baptiste Battelier, ainsi que mon référent iXblue Henri Porte. La confiance que vous m'avait confiée dès le départ m'a permis de démarrer avec assurance et de m'épanouir scientifiquement. Je remercie également Philippe Bouyer et Fabien Napolitano, avec qui les échanges, certes bref, sont très utiles et précieux, et sans qui l'aventure iXatom n'aurait jamais vu le jour.

Je tiens à remercier les membres de mon jury, mes rapporteurs Arnaud Landragin et Malo Cadoret, ainsi que mes examinateurs Daniel Comparat et Marco Prevedelli, qui ont accepté d'évaluer mes travaux, pour lesquels un intérêt fort a été suscité. Les conditions très particulières liées à la situation sanitaire nous ont amené à échanger uniquement via visioconférence, y compris pour la soutenance... Malgré tout, des discussions intéressantes ont émergées. En espérant vous rencontrer prochainement en vrai !

Je remercie chaleureusement Brynle, qui m'a accompagné au quotidien, et qui, de part sa pédagogie, son perfectionnisme et son enthousiasme permanent, m'a permis de mener ma thèse dans d'excellentes conditions. Brynle est plus qu'un collègue, un ami, avec qui jouer du AC/DC, du Muse ou du Lynyrd Skynyrd au sein des Deamb's boys, et écouter du Tool était plaisant. Bon vent au Canada et bon courage pour ta nouvelle aventure ! Je remercie également Pierrick qui, malgré les aller-retours hebdomadaires entre Paris et Bordeaux pendant près de 3 ans (!), a gardé et su transmettre la motivation et ses grandes compétences au sein de l'équipe pour avancer sur le projet. Je tiens à saluer Baptiste Gouraud, qui a rejoint l'équipe au milieu de ma thèse, et à qui je souhaite plein de bonheur avec la petite qui vient d'agrandir la famille. Je voudrais souhaiter bonne chance à Quentin, qui nous a rejoint sur le projet iXatom en tant que doctorant pour continuer le projet. Ton début de thèse a été compliqué à cause du contexte épidémique, mais tu as su t'adapter et avancer malgré tout. Je n'ai pas de doute : la manip est entre de bonnes mains !

Je voudrais remercier Lauriane, qui m'a encadré lors de mon stage durant mes études et m'a ainsi introduit dans le monde fascinant des atomes froids. Je remercie

les collègues de l'équipe ICE, notamment Laure, qui m'a ouvert la voie en début de thèse, mais également Gabriel, Laura, Martin, Romain, Vincent et Célia, avec qui beaucoup d'échanges ont été fructueux. Aussi je remercie l'équipe MIGA avec Dylan, Joseph et Grégoire, et l'ensemble de l'équipe du CAB, le Cold Atoms in Bordeaux, avec Devang, Hodei, Max, Grigor, Adèle, Maxime, Romain, Jean-Baptiste, Vincent, Guillaume, Chen-Hao, Xinhao, Simon, Benjamin et Andrea. Egalement je remercie le support technique du laboratoire, dont notre mécano Philippe, toujours présent pour nous fabriquer des pièces et nous faire des retouches, nos électroniciens Jean-Hugues et Arnaud et aussi le support administratif Stéphanie et Fabien.

Je voudrais remercier l'ensemble de l'équipe iXblue de Besançon, avec qui j'ai pris beaucoup de plaisir pendant près d'un an à confectionner la ModBox iXatom : Jérôme, Jonathan, Alexandre, Steve, Laurent, Sandrine, Hervé et tous les autres. Les équipes m'ont accueilli à bras ouverts. Ce fut une période très enrichissante pour ma part.

Pour finir, je voudrais remercier ma famille, mes proches et surtout Axelle, qui m'a soutenu, supporté et encouragé tout le long sans faille, surtout dans les moments difficiles. Je salue mes amis de Pau, Hugo, Huy et Florian avec qui les années passantes, le contact se fait difficilement mais est toujours aussi important. Un merci spécial à mes chevaliers, Martin, Mariette, David, Mélanie, Spinnato, Cauchy, Crevette, Botch, Cyril, Doat, Maël, Pinoges, et à tous mes amis de Toulouse Paul, Yoann, Etxe, Seb, Mike, Pauline, Aurélie, Laureen, Marine, Maeva, Soizick, Gaudefroi, John et tous les autres avec qui j'ai passé de bons moments depuis le début de mes études !

Contents

Introduction **11**

1 Improving inertial navigation using cold atoms: motivation and prospects **15**

1.1 Inertial navigation with classical sensors 17
1.1.1 Inertial measurement unit 17
1.1.2 Data fusion and inertial navigation algorithms 19
1.1.3 Limitations of inertial navigation 25
1.2 Benefits of atomic sensors 30
1.2.1 Absolute sensor 30
1.2.2 State-of-the-art of the atom accelerometers 31
1.2.3 Challenges for inertial navigation compatibility of atomic accelerometers 32
1.3 Target performances 33
1.3.1 Applications 33
1.3.2 Selected technology baseline 34
1.3.3 Specification of the 3-axis hybrid accelerometer 37

2 Matter-wave interferometry for acceleration sensing **39**

2.1 Atom interferometry 41
2.1.1 Rubidium 87 for atom interferometry 41
2.1.2 Atom trapping and cooling 41
2.1.3 Two-photon Raman transitions 42
2.1.4 Wave-packet diffraction by atom optics 46
2.1.5 Matter-wave propagation 48
2.1.6 Mach-Zehnder interferometer 49
2.1.7 Sensitivity and transfer function of the atom interferometer . . . 52
2.1.8 Scale factor of the atom accelerometer 55
2.2 Atom accelerometer with a reference mirror 61
2.3 Hybridization with classical accelerometers 63
2.3.1 Hybridization schemes 63
2.3.2 Real-time correlations 65
2.4 Tracking algorithms 66

2.4.1 Kalman filter . . . 66
2.4.2 Mid-fringe lock algorithm . . . 68
2.4.3 Sequential 3-axis hybrid accelerometer . . . 73

3 3-axis accelerometer apparatus 77
3.1 Design architecture . . . 80
3.2 Sensor head . . . 82
3.2.1 Vacuum chamber . . . 83
3.2.2 Magnetic fields . . . 83
3.2.3 Free-space optics . . . 85
3.2.4 Liquid-crystal retardance waveplates . . . 87
3.2.5 Fluorescence detection system . . . 89
3.3 Classical accelerometers . . . 90
3.3.1 Characteristics of the classical accelerometers . . . 90
3.3.2 Temperature calibration . . . 92
3.3.3 Triad calibration . . . 94
3.4 Control system . . . 97
3.4.1 Hardware elements . . . 97
3.4.2 Software elements . . . 99
3.4.3 Real-time system . . . 100
3.4.4 Experimental sequence . . . 101
3.4.5 Detection and signal extraction . . . 103
3.5 Mobile and calibration apparatuses . . . 105
3.5.1 Marble table . . . 105
3.5.2 Rotational platform . . . 105
3.5.3 Mobile platform . . . 107

4 Agile integrated laser using advanced electro-optic modulation 111
4.1 Agile laser system using advanced electro-optic modulation . . . 114
4.1.1 Electro-optic modulation . . . 114
4.1.2 CS-DSSB modulation with an IQ modulator . . . 115
4.1.3 Laser architecture . . . 119
4.1.4 Optical spectrum measurements of the modulated laser source . . . 122
4.1.5 Resonant transitions produced by residual parasitic lines . . . 125
4.1.6 Phase shift induced by parasitic lines . . . 126
4.1.7 Splitting, recombining and switching fiber optical bench . . . 130
4.1.8 Rack integration . . . 132
4.2 RF Source . . . 133

4.2.1 Architecture and spectrum . . . 133
4.2.2 Phase noise . . . 134
4.2.3 Frequency stability . . . 135
4.2.4 Phase non-linearity of RF-filters . . . 137
4.2.5 Hybrid coupler . . . 138
4.3 Laser architecture improvements . . . 140
4.3.1 IQ modulator operating at 780 nm . . . 140
4.3.2 Single diode architecture based on a discrete lock . . . 141

5 Characterization of the atom accelerometer along the vertical axis 147
5.1 Operation of the atom accelerometer along the vertical axis . . . 149
5.1.1 Raman transitions . . . 149
5.1.2 Atom interferometer . . . 150
5.2 Preparation of the atomic source . . . 151
5.2.1 Temperature of the atomic source . . . 151
5.2.2 Preparation into non-magnetic states . . . 151
5.3 Performances of the atom interferometer . . . 153
5.3.1 Acceleration sensitivity . . . 153
5.3.2 Long-term stability with the tracking algorithm . . . 154
5.3.3 Magnetic field . . . 155
5.3.4 Light shifts . . . 157
5.3.5 Cloud position dependence of Rabi frequencies . . . 160
5.3.6 Scale factor error . . . 162
5.3.7 Other systematic effects . . . 164
5.3.8 Summary of systematic effects . . . 168
5.3.9 Relative accuracy . . . 168

6 3-axis atomic accelerometer 173
6.1 Operation of the 3-axis atomic sensor . . . 175
6.2 Tilt of the sensor head . . . 177
6.2.1 Axes quantization and states preparation . . . 177
6.2.2 Temperature along the direction of each axis . . . 177
6.3 Performances of the 3-axis atom interferometer . . . 178
6.3.1 Acceleration sensitivity on each axis . . . 178
6.3.2 Long-term stability of the 3-axis atomic accelerometer . . . 180
6.4 Calibration of the 3-axis atom accelerometer . . . 181
6.4.1 Protocol for the calibration of the 3-axis atomic accelerometer . . . 181
6.4.2 Rabi oscillations along the 3 laser beams profile . . . 182

6.4.3 3D mapping of the magnetic field . . . 182
6.4.4 Systematic effects . . . 183
6.4.5 Correction of the 3-axis frame misalignments . . . 187

7 3-axis real-time hybrid accelerometer 193
7.1 Operation of the 3-axis real-time hybrid accelerometer . . . 195
7.2 Real-time hybridization . . . 197
7.2.1 Correlations with the classical accelerometer . . . 197
7.2.2 Doppler frequency shift compensation . . . 197
7.2.3 Bias tracking of the classical accelerometer . . . 199
7.3 Performances of the real-time hybridization . . . 200
7.3.1 Long-term stability of the 3-axis hybrid accelerometer . . . 200
7.3.2 Limits of the real-time correlations to the sensitivity . . . 201
7.3.3 Residual discontinuous phase from the frequency jumps . . . 204
7.3.4 Systematic effects and calibration of the 3-axis hybrid accelerometer 208
7.3.5 3-axis hybrid accelerometer outside of the laboratory . . . 212

Conclusion and outlook 217

Introduction

Positioning and navigation systems are fundamentals today to walk as a pedestrian or to drive vehicles, such as cars, aircrafts, ships, submarines, rockets or satellites. Dead-reckoning instruments and inertial navigation systems afford solutions to navigate. However classical inertial sensors are usually not absolute and suffers from drifts. The advent of the global navigation satellite system (GNSS) changed radically the approach of navigation. It offers an estimation of the position within a few meters confidence. However the GNSS relies on the availability of the signal broadcasted by the satellites. Some regions are not covered by this signal, as Space, underwater or underground operations. For such situations, inertial navigation systems are required.

Quantum sensors, providing absolute measurements with atoms, are promising to be integrated into inertial navigation systems. Indeed the theoretical performances and the demonstrated ones would afford an advanced tool and could lead to a technological breakthrough for navigation. However such instruments are complex and large. Advanced efforts and solutions are needed to develop instruments with dedicated architectures compatible for inertial navigation, with reduced size, power and complexity.

The joint laboratory iXatom brings together the knowledge of the French company iXblue, expert in optical gyroscopes, photonics and inertial navigation, and from the Laboratoire Photonique Numérique et Nanosciences (LP2N). The purpose of this collaboration is to make technological advances using cold atoms to develop the next generation of inertial sensors for industrial, military and Space applications, with anticipated improvements in their performance. In particular, different technological building blocks are addressed, as for instance, the laser source based on a novel electro-optic modulation.

In this thesis work, we propose a 3-axis hybrid accelerometer composed of 3 atom accelerometers hybridized with 3 classical accelerometer. By hybridization, we mean the data fusion between two sensors technologically different but complementary. Whereas the classical sensor suffers from biases and drifts, the atomic accelerometer offers unprecedented sensitivity, stability and accuracy. On the other hand, the atomic accelerometer encounters dead-times and a reduced dynamic, where the classical accelerometer provides continuous high-bandwidth measurements with a high dynamic. In other words, we couple the best of the two worlds to afford accurate continuous measurements with high dynamics along three axes, in the scope of inertial navigation

operations compatibility.

Organization of the thesis

On Chapter 1, we introduce general aspects of inertial navigation. In particular we present classical inertial sensors employed for inertial navigation operations. The use of Kalman filter helps to exploit and combine coherently different sources of aiding navigation systems. We expose the limitations of inertial navigation to accurately determine the position and motivate the benefits to explore atomic sensors as a aiding inertial sensor.

On Chapter 2, we describe some basics and theoretical tools for atom interferometry dedicated to acceleration sensing. Different operation schemes and tracking algorithms of the hybridization between the atom interferometer and the classical accelerometer are depicted. Specifically, we propose a method to operate a sequential 3-axis hybrid accelerometer delivering multi-axis high-bandwidth and bias-free acceleration measurements.

On Chapter 3, we depict the apparatus of the 3-axis hybrid accelerometer. It includes the description of the sensor head design, the classical accelerometers, the control system and the platforms dedicated to calibrations and mobile operations.

On Chapter 4, we present the fiber laser system integrated into a compact rack and dedicated to our 3-axis atom interferometer. The architecture is based on a novel electro-optic modulation with an IQ modulator at 1560 nm and a second harmonic generation stage to reach 780 nm. This chapter describes as well the RF source adapted to this specific modulation scheme and the fiber bench operating at 780 nm to split, switch and recombine the laser beams for the 3-axis atomic sensor head.

On Chapter 5, we report the performances and systematic effects of our atom interferometer prototype along the vertical axis, as a gravimeter. This preliminary study is necessary before exploring the 3-axis accelerometer. Specifically, we characterize the atom cooling and the preparation of the atomic states for interferometry. Furthermore we analyse the sensitivity, the stability and the systematic shifts of the atomic accelerometer operating vertically.

On Chapter 6, we detail the study of the 3-axis atomic accelerometer including the optimization of cooling operation and state preparation. We also characterize the acceleration sensitivity, stability and the systematic effects depending on the tilt of the sensor head along each axis. Furthermore, we conduct the calibration of the misalignments from the 3-axis triad and analyse the norm of the total acceleration vector.

On Chapter 7, we report the study and the performances of the 3-axis hybrid

accelerometer, which affords continuous accelerations provided by the classical accelerometers, whose biases are tracked and removed by the atom interferometers. In particular, real-time feedback correlations of the reference mirrors and Doppler frequency shift compensation during interferometry are demonstrated. We also discuss the calibration of the full apparatus to optimize the accuracy. Finally, the 3-axis hybrid accelerometer is demonstrated to operate outside of the laboratory for static operations.

We mention that in metrology, the unit used to characterize the acceleration is the $m.s^{-2}$, or the gal, where 1 Gal = 0.01 $m.s^{-2}$. In practice, the unit g is commonly used in the navigation community, where 1 g = 9.80665 $m.s^{-2}$, and is rather employed in this manuscript.

Chapter 1

Improving inertial navigation using cold atoms: motivation and prospects

This chapter introduces general aspects of inertial navigation. In particular we present classical inertial sensors employed for inertial navigation operations and integrated into architectures. The use of Kalman filter helps to exploit and combine coherently different sources of aiding navigation systems. We show the limitations of inertial navigation to accurately determine the position and motivate the benefits to integrate atomic sensors.

Contents

1.1 Inertial navigation with classical sensors 17

1.1.1 Inertial measurement unit 17

1.1.2 Data fusion and inertial navigation algorithms 19

1.1.3 Limitations of inertial navigation 25

1.2 Benefits of atomic sensors 30

1.2.1 Absolute sensor 30

1.2.2 State-of-the-art of the atom accelerometers 31

1.2.3 Challenges for inertial navigation compatibility of atomic accelerometers 32

1.3 Target performances 33

1.3.1 Applications 33

1.3.2 Selected technology baseline 34

1.3.3 Specification of the 3-axis hybrid accelerometer 37

Introduction

Inertial navigation is a necessary technology to locate and navigate on Earth. Historical dead-reckoning tools such as magnetic compass, stellar navigation instruments or more recently terrestrial radio have been used to navigate with ships, aircrafts and submarines. However, inertial sensors and navigation technics suffer from instability over time. It can lead to huge uncertainties on the position of the mobile vehicle.

The advent of the global navigation satellite system (GNSS) transformed our vision of localization and navigation. Institutions have developed different GNNS as the global positioning system (GPS) operated by the U.S. government, GLONASS in Russia or Galileo in Europe. The GNSS offers a full position, navigation and time (PNT) system, which allows to navigate or to recalibrate an inertial navigation system.

Nonetheless the GNSS is efficient for navigation as long as the communication with broadcasted signal from satellites is available. Aside from non-cover areas and environmental barriers (building, underwater, underground), GNSS availability and reliability can be disturbed by jamming and spoofing. GNSS jamming consists of overpowering the weak GNSS electromagnetic signal intentionally. The GNSS spoofing is the transmission of fake GNSS signal, which is hard to detect. In any cases when the GNSS signal is not available or wrong, inertial navigation tools help to navigate or detect anomalies in case of spoofing.

Cold atoms are considered as a serious candidate to help inertial navigation systems by increasing the stability and providing absolute measurements. However, integrating such complex and novel instrument into a system with decades of maturity represents a big challenge. In this chapter, we motivate the technological choices of the instrument studied in this thesis.

1.1 Inertial navigation with classical sensors

1.1.1 Inertial measurement unit

An inertial measurement unit (IMU) is a set of sensors including a triad of three accelerometers and gyroscopes with basic electronic to deliver the measurements into a bus. An IMU measures the acceleration and the angular velocity along three axes and represents the fundamental part of inertial navigation.

Accelerometer

The physical principle of an accelerometer relies on the displacement measurement of a proof mass, mechanically isolated, relative to the sensor chassis. The force measured to evaluate the displacement varies according to different technology. In a magnetic balanced force accelerometer, the proof mass is magnetic and is held by magnets or magnetic coils. A displacement of the magnetic proof mass induces a variation of the magnetic field which can be measured and feedbacks to the magnetic coils to compensate the displacement. In electrostatic balanced force accelerometers, the proof mass is placed between capacitor plates and the displacement is characterized by a capacitance fluctuation. Another type of accelerometer is the vibrating beam accelerometer. It relies on a cantilever vibrating at a controlled frequency and where a proof mass is attached. When the proof mass moves due to acceleration, the resonance frequency of the cantilever varies and is related to the acceleration.

Gyroscope

Three technologies gyroscopes comply with inertial navigation requirements. The two optical gyroscopes, the ring laser gyroscope (RLG) and the fiber-optic gyroscope (FOG), estimate the rotation velocity with a Sagnac interferometer in respectively free-space and guided optics. On the other hand, the vibratory gyroscope measures the Coriolis acceleration of a vibrating element and is usually integrated into MEMS technology, such as the hemispherical resonator gyroscopes (HGR). Here we present the basic approach to measure angular velocities with a FOG.

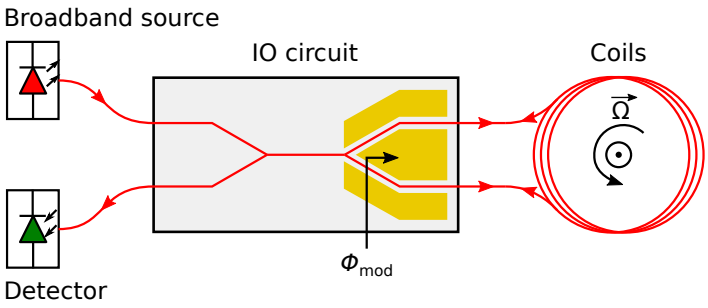

Figure 1.1: Scheme of a fiber-optic gyroscope where a double integrated Y-junction distributes the light to the fiber coils. "IO circuit" stands for integrated optics circuit.

Figure 1.1 presents the physical scheme of the FOG [1]. Optical light is sent in the two direction inside the fiber-optics coils to create interferences at the output between the two paths. The light provided by an optical source is split by a Y-junction inside an integrated optics circuit (IOC). An additional Y-junction is used to guide the feedback light onto a detector. The resulted phase shift is defined as the Sagnac phase $\Delta\Phi_S$ and is related to the angular velocity $\vec{\Omega}$ and the surface area $\vec{A}$ enclosed by the light path and perpendicularly oriented as:

$$\Delta\Phi_S = \frac{4\omega}{c^2}\vec{A}\cdot\vec{\Omega} \tag{1.1}$$

where ω is the frequency of the light and c is the celerity in vacuum. The sensitivity of the FOG relies on the size of the coils and number of turns. The response signal of the FOG is sinusoidal according to $\Delta\Phi_S$. The sensitivity is optimized by controlling a modulation phase ϕ_{mod} inside the Y-junction with an integrated phase modulator. The modulation phase controls the measurement phase and tracking algorithms can be applied.

Broadband light sources are employed instead of monochromatic lasers. No coherence from broadband light helps to avoid interferences with coherent backscattering from guided light inside very long fibers. Instead a path difference is added to the interferometer from spurious coherent backscatterings. Whereas coherent backscattering induces a phase shift, incoherent backscattering adds rather noise.

Calibration of the inertial measurement unit

Classical sensors from an IMU do not deliver absolute measurements. Their scale factors and biases, depending on numerous parameters, require an empirical calibration with a reference. In addition, the triad formed by the sensor should be ideally orthogonal. However misalignments occurs between the three axes and need to be measured and corrected. Furthermore lever arms from the center of the triad mislead the measurement

of the sensors. The calibration is necessary to operate correctly the IMU. Inside a moving mobile in the context of inertial navigation, the IMU is placed according to the center of mass. Such placement is critical to avoid additional lever arms.

Attitude and heading reference system

An attitude and heading reference system (AHRS) is a dead-reckoning instrument composed of a low-cost IMU, a central processing unit (CPU) and a magnetic compass. It provides the 3 attitude components of the mobile , the roll, the pitch and the yaw, by integrating the gyroscopes measurements. The roll and pitch can be calculated with the accelerometers used as tiltmeters, which has the advantage to make measurements in static without gyroscopes. The magnetic compass measures the magnetic north which indicates the heading. However a AHRS is not a navigation system by itself. Indeed it does not calculate the position nor inertial parameters like the velocity, critical for navigation. The AHRS addresses low-grade mobile systems such as light aircraft and unmanned autonomous vehicles (UAV).

1.1.2 Data fusion and inertial navigation algorithms

Initialization

Inertial navigation assumes to know the initial position, velocity and attitude of the mobile with a certain precision. Measuring the initial position requires dead-reckoning instruments, such as altimeters, odometers, radars, sonars or lidars. Another method is to operate a comparison to a calibrated reference such as global navigation satellite system (GNSS), terrestrial radio beacons, local measurements matching with known maps such as magnetic or gravity field anomalies. To measure the initial orientation of the static mobile reference frame, in addition to dead-reckoning instruments, a compass can determine the cardinal directions. A magnetic compass determines the magnetic north of the Earth's geomagnetic field, but the measurement is generally perturbed by ambient ferromagnetic materials of the mobile. A gyrocompass is a gyroscope measuring the gyroscopic precession of the Earth induced by its rotation. It measures the true cardinal north compared to a magnetic compass. Strapdown compasses, as fiber optic or HRG gyrocompasses, are the most commonly used in high-end navigation systems and avoid complex system, such as gimbals which maintain the gyroscope aligned with the center of the Earth.

Inertial navigation system

An inertial navigation system (INS) is composed of an IMU and a CPU to calculate the trajectory for autonomous operations. It relies on the calculation of the position and the attitude of the mobile starting from a known initial position. In addition to the acceleration of the mobile, the accelerometers measures the gravitational acceleration, which needs to be removed with the model.

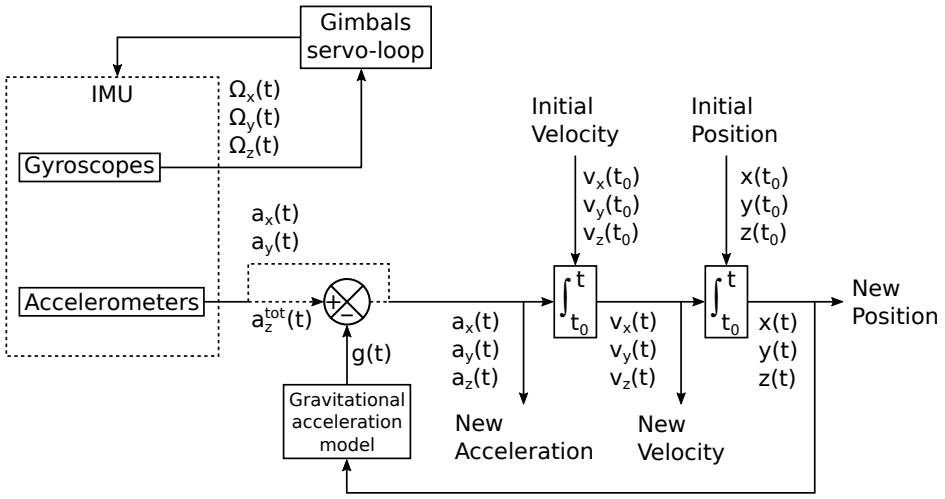

Figure 1.2: Operation of a gimbaled INS. The axis $\vec{z}$ is settled with respect to the gravity vector.

Historically the first INS, called gimbaled INS, relied on an IMU mounted on gimbals composed of 3 or 4 rotational frames. Indeed at that time, the CPUs were not fast enough to compute the full equations of motion including rotations and translations. Figure 1.2 describes the operation of a gimbaled INS [2]. The mounting base benefits from the 3-axis gyroscope, delivering the angular velocities Ω_x, Ω_y and Ω_z, to correct the orientation with a feedback loop onto the gimbals. The accelerometers, measuring accelerations along each axis a_x, a_y and a_z^{tot}, are isolated from rotations of the mobile. Assuming that the gravity vector is along the axis $\vec{z}$, the compensation of the gravitational acceleration g is performed on a_z^{tot} to produce the acceleration of the mobile a_z. The time-integration of the accelerations from the initial velocities generates the current velocity of the mobile v_x, v_y and v_z. Another time-integration delivers the components of the position x, y and z. The new position is used to relocate the gravitational acceleration model correctly. Such architecture is suited for low performances CPU, since it requires a few calculations. However the gimbals structure is a complex mechanism and the performances are non-optimal due to perfectible mechanical compensation of the rotation.

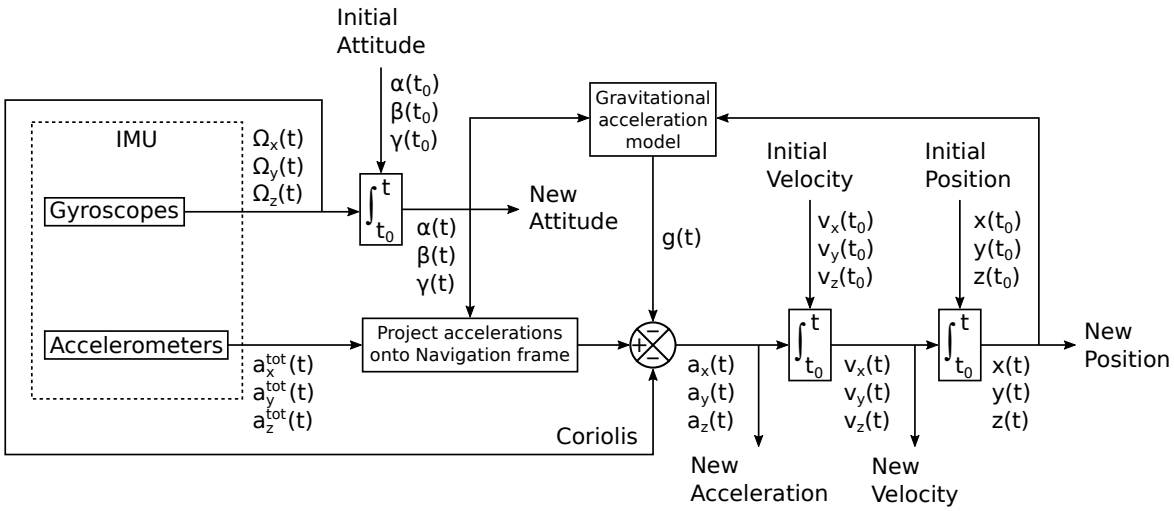

Figure 1.3: Operation of a strap-down INS.

With the advent of higher performances of calculations inside the CPUs, the INS can operate in strap-down configuration. It relies on a mechanical fixation of the INS to the moving mobile. Figure 1.3 presents the operational scheme of a strap-down INS. The angular velocities delivered from the gyroscopes are time-integrated with initial attitude to determine the current attitude with Euler angles α, β and γ. In contrary to the gimbaled INS, the accelerometers from the strap-down INS measure the 3-axis acceleration where the gravitational is projected into each component a_x^{tot}, a_y^{tot} and a_z^{tot} and the Coriolis accelerations perturb the measurement. Firstly the accelerations are projected onto the frame determined with the current Euler angles of the mobile, called the navigation frame. Then the accelerations are corrected with the Coriolis acceleration calculated with the gyroscopes and the gravitational acceleration g(t). The time-integration generates the velocities and an additional one provides the position of the mobile.

Kalman filter

The state-space representation is powerful and versatile to manipulate complex systems with numerous variables [3]. The Kalman filter, based on the state-space approach, defines the state vector with all the parameters which needs to be estimated and tracked. The state vector is updated each time the sensors provide a measurement. In addition, the Kalman filter provides the uncertainty on each parameter. It is crucial in the context of navigation to determine the precision of the position estimation. Another strength of the Kalman filter is the adaptive Kalman gain which is readjusted at each iteration depending on different inputs, such as the estimates of the parameters or noise characteristics. The description of the model output of the sensor is not critical to operate the Kalman filter. However a good knowledge of the sensors response, including

noise characterization, helps for a better estimate and to reduce the uncertainty.

To introduce the operation of the Kalman filter, we take a simple 1D linear model. We consider an accelerometer generating noisy acceleration measurements y where we want to track the velocity $\dot{x}$ and the position x in addition to the acceleration $\ddot{x}$. The state vector is defined as:

$$X = \begin{bmatrix} x \\ \dot{x} \\ \ddot{x} \end{bmatrix} \tag{1.2}$$

Supposing a linear dynamic system, the measurement of the sensor can be predicted with the state vector as:

$$y(X) = HX + \delta u \tag{1.3}$$

where $H = \nabla_X y$ is the measurement matrix corresponding to the Jacobian of the output model according to the state vector and $\delta u \sim \mathcal{N}(O, \sigma_y)$ is the noise distribution of the output measurement of the sensor. In our case, the measurement matrix is $H = \begin{bmatrix} 0 & 0 & 1 \end{bmatrix}$. The time evolution of the state vector relies on the transition (or evolution) matrix F. The matrix P, including the uncertainty of the parameters, depends on the covariance matrix Q and its time evolution relies on the transition matrix F. We obtain the following dynamical evolution:

$$X(t + \delta t) = FX(t) + w \tag{1.4}$$

$$P(t + \delta t) = FP(t)F^{\mathrm{T}} + Q \tag{1.5}$$

where w is a vector including the standard deviations σ_x, $\sigma_{\dot{x}}$ and $\sigma_{\ddot{x}}$ of each parameter. In our case, the transition matrix F and the covariance matrix Q are defined as:

$$F = \begin{bmatrix} 1 & \delta t & \frac{\delta t^2}{2} \\ 0 & 1 & \delta t \\ 0 & 0 & 1 \end{bmatrix} \tag{1.6}$$

$$Q = \begin{bmatrix} \sigma_x^2 & \sigma_x\sigma_{\dot{x}} & \sigma_x\sigma_{\ddot{x}} \\ \sigma_{\dot{x}}\sigma_x & \sigma_{\dot{x}}^2 & \sigma_{\dot{x}}\sigma_{\ddot{x}} \\ \sigma_{\ddot{x}}\sigma_x & \sigma_{\ddot{x}}\sigma_{\dot{x}} & \sigma_{\ddot{x}}^2 \end{bmatrix} \tag{1.7}$$

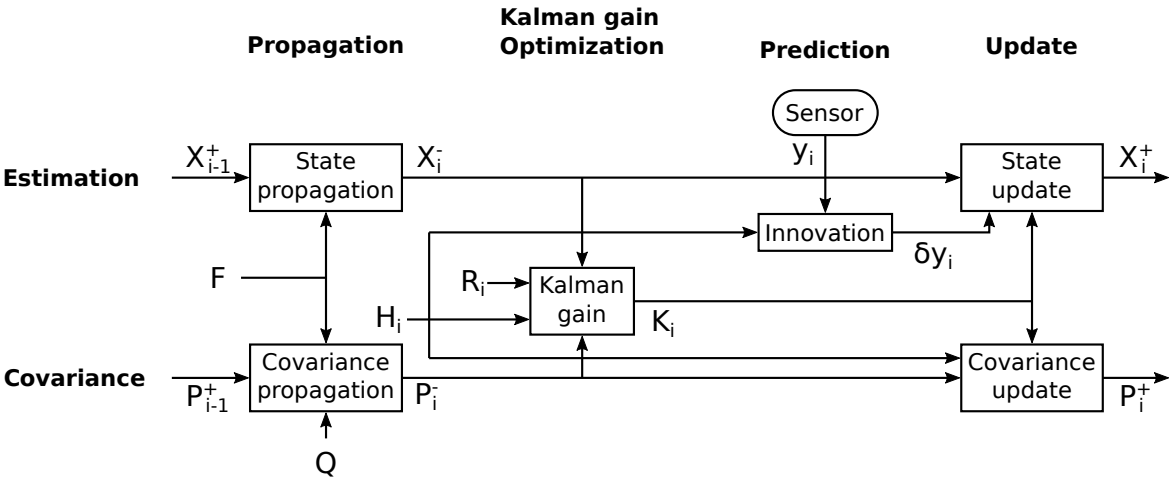

Figure 1.4: Operation of the Kalman filter.

Figure 1.4 describes the operation of the Kalman filter [4]. The estimation and the covariance of the parameters are tracked within four processes during each step: the propagation of the estimates and the covariances, the optimization of the Kalman gain, the prediction of the measurement to extract the innovation and the update of the estimates and the covariances. The propagation of the state vector X and the covariance P from the $(i-1)^{\text{th}}$ step to the i^{th} is:

$$X_i^- = FX_{i-1}^+ \tag{1.8}$$

$$P_i^- = FP_{i-1}^+F^{\mathrm{T}} + Q \tag{1.9}$$

The innovation δy defines the difference between the measurement of the sensor and the expected output as:

$$\delta y_i = y_i - y(X_i^-) \tag{1.10}$$

$$= y_i - (H_iX_i^- + \delta u) \tag{1.11}$$

From the propagation step, we also adapt the optimal Kalman gain as [4]:

$$K_i = P_iH_i^{\mathrm{T}}(H_iP_iH_i^{\mathrm{T}} + R_i)^{-1} \tag{1.12}$$

where $R_i = E[(y_i - H_iX_i)(y_i - H_iX_i)^{\mathrm{T}}]$ is the measurement noise covariance matrix and is defined by the expectation $E[\ldots]$ of the innovation. In our case, it corresponds to the variance of the measurement noise $R = \sigma_{\delta u}^2$.

Finally, the estimate and the covariance are improved with the innovation and the Kalman gain at the update step as:

$$X_i^+ = X_i^- + K_i \delta y_i \tag{1.13}$$

$$P_i^+ = (I - K_i H_i) P_i^- \tag{1.14}$$

Feature matching technics

Feature matching technics rely on comparing features of the environment with a pre-existing map or database. Those maps are based on physics models and surveys of local anomalies. For instance, in addition to latitude dependency due to non-perfect spherical Earth, the local gravity is influenced by density and large movements of matter inside the Earth. Gravity field matching navigation is largely used today thanks to advanced gravity maps. Airborne and space surveys can probe the gravity field efficiently over large areas. The current standard global gravity error map is the EGM2008 that combines satellite-based at long wavelength and terrestrial observation at shorter scale. Aside from gravity map matching navigation, gravity gradiometry is a more advanced technic, delivering the full gravity gradient tensor $\partial\vec{g}/\partial\vec{r}$. It contains the 9 components of the gravitational acceleration gradient projected along each direction, helping to reject noises and bias drifts.

The Earth's geomagnetic field is regular at a certain height, where for instance orbital spacecrafts can compare local measurement with a global magnetic model. Anomalies of the Earth's geomagnetic field are present at lower altitude and can be measured to produce a database. However those anomalies may be time varying, which limits the efficiency of the Earth's geomagnetic field matching navigation. The stellar navigation exploits the position of celestial bodies by using a star tracker based on a telescope with a light detector on gimbals. Hypsometry and bathymetry surveys measure respectively the land elevation and the depth of oceans. The resulting maps contribute to generate a global relief model of Earth used for matching navigation by comparing the model with local measured profile with sonars, lidars or radars.

Multi-sensor integrated navigation

The Kalman filter is particularly adapted in the context of multi-variable control. The flexibility of the Kalman filter offers data fusion with aiding sensors or navigation tools. A large number of aiding systems can contribute to inertial navigation. The INS is generally the heart of the navigation, but one can imagine complementary IMU with different characteristics to help. The most obvious aid system to assist navigation is the GNSS. Indeed the GNSS recalibrates the position with a small uncertainty, when it is accessible. A wide range of dead-reckoning technics provides

useful data for navigation. For example, AHRS and magnetic sensors can contribute to the attitude evaluation, barometer, depth gauge and altimeter to measure depth and height, odometer to calculate the velocity of the wheels of the mobile. Feature matching technics, where physical properties of local environment are compared with known maps, establish advanced and effective tools for navigation. Sonars, lidars or radars, in addition to constitute feature matching technics, afford useful informations about the local displacement of the mobile. Wireless broadcast networks, such as global system for mobile communication (GSM), telecommunication networks or terrestrial radio, offer a localization of the mobile relative to transmitters. The mobile receiver needs a dedicated antenna and signal treatment to navigate with networks.

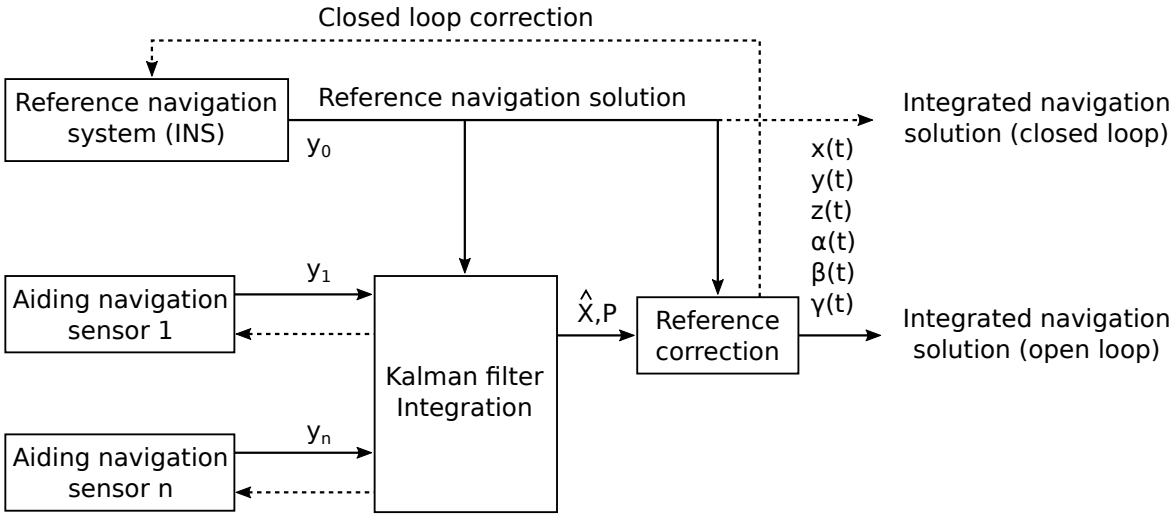

Figure 1.5: Centralized integration architecture with Kalman filter.

Figure 1.5 presents an architecture where the Kalman filter integrates aiding sensors or tools to a reference navigation system, which is generally an INS [4]. In such scheme, the measurements y_0 of the reference system and of the aiding systems $y_1 \dots y_n$ are communicated to the Kalman filter. The state vector X is adapted according to the measurements of the sensors and the parameters which need to be tracked. It contains necessarily the position parameters x, y and z and the attitude parameters α, β and γ of the mobile. In addition to the estimates $\hat{X}$, the covariance P evaluates the error on each parameter. An elegant method is to feedback the correction from the centralized integration onto the INS, where the navigation solution is directly delivered by the INS.

1.1.3 Limitations of inertial navigation

Inertial navigation systems suffer from positioning errors deriving from various origins. In particular, inertial navigation relies on the time-integration of the accelerations

and the rotation rates. Any error cumulates over time. An important aspect provided by Kalman filters is the uncertainty on the estimation of the position. To reduce such inaccuracies, characterizing the sensors is essential.

Sensor performances

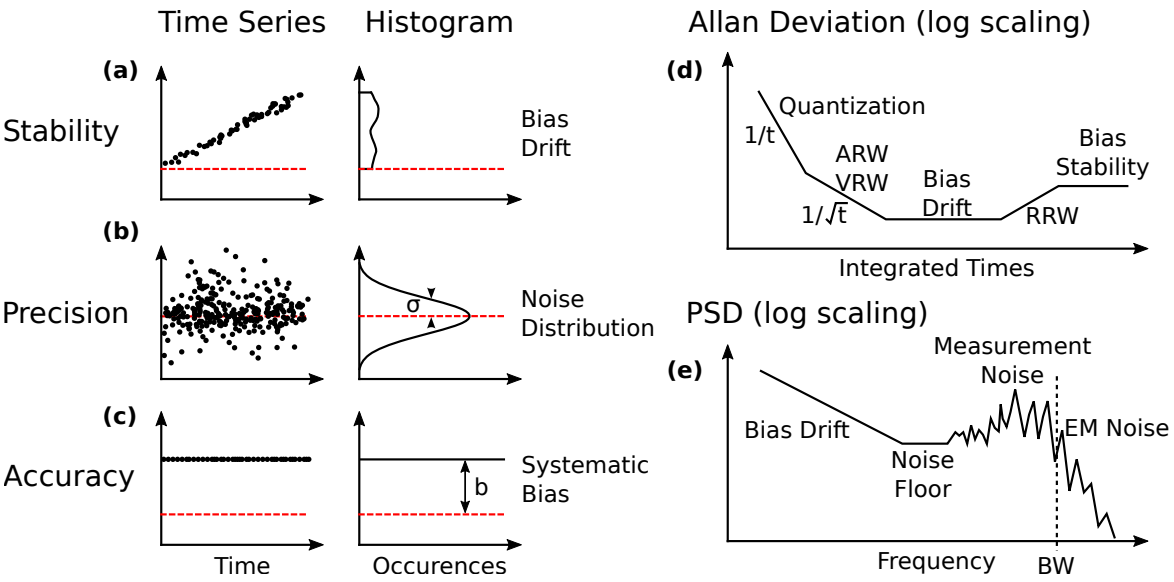

Figure 1.6: Analysis of the signal from a sensor with time series and associated histograms, the Allan deviation (d) and the power spectral density (PSD) (e). The Allan deviation and PSD plots are presented on a logarithmic scale. The time series and histograms describe data stability with a bias drift on (a), data precision with a Gaussian distribution of the noise on (b), data accuracy with a constant systematic bias on (c). ARW: Angle random walk ; VRW: Velocity random walk ; RRW: Rate random walk ; EM noise: Electro-magnetic noise ; BW: Bandwidth.

Figure 1.6 presents some tool analysis to characterize data measurements of a sensor. Three main criteria define the performances of a sensor: the stability, the precision and the accuracy. The stability characterizes the ability of the sensor and the acquisition to measure a constant value and is usually reduced by bias drifts. The precision relies on the sensitivity of the sensor and noises from the acquisition. A common type of noise is the white noise defined by a normal (or Gaussian) distribution defined by a variance σ^2 quantifying the spreading of the data nearby the true value. The accuracy represents the absolute trueness of the measurement where constant bias shifts are detrimental.

The Allan deviation, presented in Figure 1.6 (d), gives the sensitivity and the stability of the measurements over integrated times. The Allan deviation relies on the square-root of the quadratic sum of differential measurements, between time overlapped intervals and weighted by the number of samples. In practice, it quantifies the relative precision of the measurements over time. The Allan deviation is composed of typical

trends. At short integrated time intervals, the precision increases as $1/t$ by averaging quantization noises. The quantization noise derives from the discretization of the measurements by the analog-to-digital converter (ADC). Then the Allan deviation decreases as $1/\sqrt{t}$ until reaching the ultimate precision of the sensor, where biases start to drift on those time scales. This decrease is explained by the random walk of the time-integrated measurements, usually distributed with a white noise (Gaussian distribution). For accelerometers and gyroscopes, it corresponds respectively to the velocity and angle random walk. This trend characterizes the sensitivity of the sensor, usually recorded at 1 s and expressed in unit/$\sqrt{\text{Hz}}$. Later the Allan deviation drifts due to unstable biases, meaning that the sensor looses precision. This part is usually called rate random walk. Finally the Allan deviation stabilizes at the bias amplitude variation.

The power spectral density (PSD) is the square modulus of the Fourier transform of the time series signal, and is presented in Figure 1.6 (e). It characterizes the frequency response of the sensor including the acquisition. It depicts the frequency bandwidth (BW) of the sensor for which measurements at higher frequency loose fidelity. Usually nearby that frequency, electro-magnetic (EM) noises appear on the PSD and express the limitations of the sensor where the acquisition pains to treat the signal. Below that frequency, the measurements are reproduced with noise, characterized by the sensitivity of the sensor. The highest sensitivity of the sensor is in the frequency region where the noise is minimal (noise floor), usually around 1 Hz. At low frequency, the drift of the biases deteriorates the PSD, describing instabilities of the measurements.

Figure 1.7 presents common irregularities of the response of sensors. An ideal response to a physical quantity would depict a linear response. The scale factor is interpreted by the rate of the linear curve. Figure 1.7 (a) illustrates the case of a pure bias shift. A first order misestimation of the scale factor, as illustrated on Figure 1.7 (b), can easily be calibrated. However the real response of a sensor is not quite linear and is also sensitive to environment. The non-linearities of a sensor can be measured and corrected with higher order scale factor model. But such non-linearities are generally dependent on physical properties of the environment and difficult to calibrate, which burdens the model. The quantization relies on the resolution of the ADC and degrades the sensitivity when the resolution is low. Hysteresis effects emanate typically from the physical principle of the sensor and are complex to correct since they are not often reproducible.

In addition to the response characterization presented here, the response depends on the frequency oscillation of the physical quantity to measure and is valid within a certain bandwidth, as shown on the PSD from Figure 1.6 (e). Furthermore the

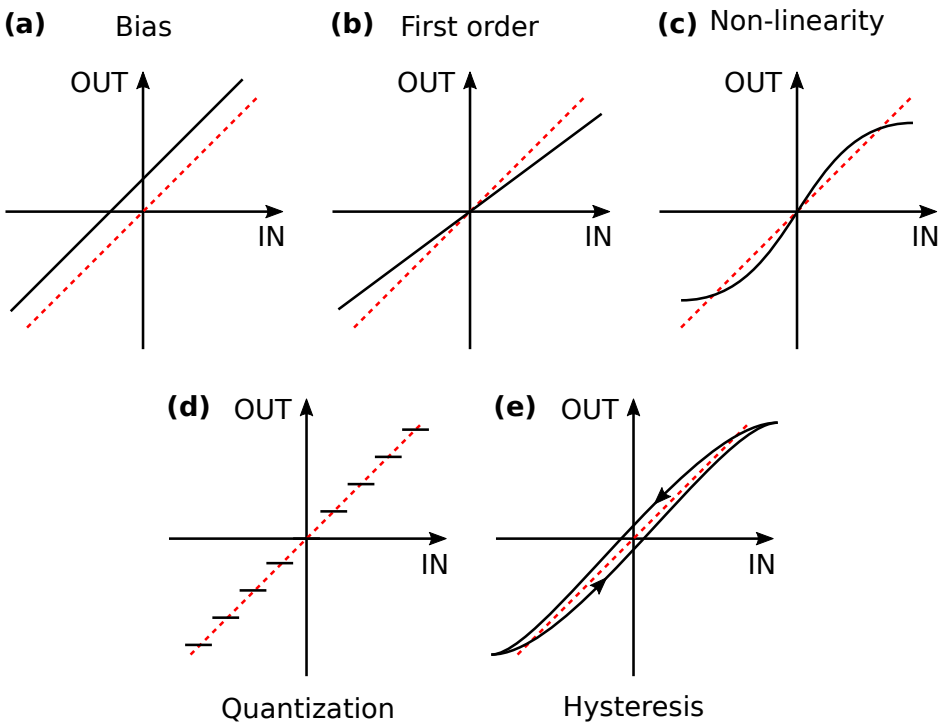

Figure 1.7: Usual irregularities of the transfer function from a perfect linear scale factor. (a) Pure bias shift. (b) First order error on the scale factor. (c) Non-linearity on the scale factor. (d) Quantization of the measurements. (e) Hysteresis on the scale factor.

response in phase is not flat. For instance, due to low-pass filtering effect, the response in phase exhibits phase shift at high frequency, starting nearby the upper frequency bandwidth and reaching -90° or -180° depending the order of the filter. Furthermore, the acquisition takes a large part in the fidelity of the measurements and can degrade the signal, as the quantization of an ADC does for instance. When the sensitivity is critical the electronic noise requires high attention. Offsets on the signal can be added by voltage reference, aging over time, or ground loop and generate biases.

The response of the classical sensors is sensitive to physical properties of the environment, such as temperature, pressure, humidity, electro-magnetic fields. Any error on the measurement propagates into the navigation algorithm and increase the uncertainty on the estimation of the position.

Navigation error propagation

Error source	Position error
Initial velocity error δv	$\frac{\sin(\omega_S t)}{\omega_S}\delta v$
Initial attitude error $\delta\psi$	$(1-\cos(\omega_S t))\delta\psi$
Accelerometer bias b_a	$R_E\frac{1-\cos(\omega_S t)}{\omega_S^2}b_a$
Gyroscope bias b_Ω	$R_E\left(t-\frac{\sin(\omega_S t)}{\omega_S}\right)b_\Omega$

Table 1.1: Position error on the horizontal plane at medium-term timing (several hours), depending on the source of the error.

Aside from biases emanating from the classical sensors, errors on the initial position, velocity or attitude of the mobile propagate onto the navigation algorithm. Table 1.1 reports simple common propagation errors [4]. Due to the projection of the gravity model g on the round surface of the Earth with a geocentric radius R_E, the resulted position errors oscillate according to Schuler tuning defined by a frequency of:

$$\omega_S = \sqrt{\frac{g}{R_E}} \tag{1.15}$$

It can be seen as a pendulum acting on the mobile with its pivot on the center of the Earth. We observe that an initial velocity error is not critical since the resulted error on the position is oscillating. Additionally an error on the initial attitude or a bias from the accelerometers induces constant biases. However a bias from a gyroscope is serious because it produces a linear drift on the position error.

In addition to those error sources, the precision of the gravity model and gravitational anomalies map are critical to not increase the navigation error. Aiding sensors and navigation tools, as feature matching technics or dead-reckoning instruments, are valuable to reduce the error on the position.

Performances grade for inertial navigation

IMU grade	Accelerometer bias stability (g)	Position accuracy (km)	Gyroscope bias stability (rad/s)	Position accuracy (km)
Consumer	$> 5 \times 10^{-2}$	> 320	$> 5 \times 10^{-4}$	$> 10^4$
Industrial	10^{-2}	64	5×10^{-5} - 5×10^{-4}	10^3 - 10^4
Tactical	10^{-3}	6.4	5×10^{-6} - 5×10^{-5}	10^2 - 10^3
Intermediate	10^{-4}	0.64	5×10^{-8} - 5×10^{-6}	1 - 100
Navigation	5×10^{-5}	0.32	$> 5 \times 10^{-8}$	< 1
Strategic	5×10^{-6}	0.032	$> 5 \times 10^{-9}$	< 0.1

Table 1.2: Classification of accelerometer and gyroscope performances. The position accuracy is estimated after 1 hour of integration assuming no error on the initial position, velocity or attitude.

The limited performances of the classical sensors lead to errors on the position using inertial navigation approach. The classification of the performances according to different grade is helpful to adapt the appropriate IMU to the inertial navigation system depending on the application. Table 1.2 presents the performances grade of the IMUs [5]. The data reported are characterized over one hour of integration. The position accuracy is calculated with the corresponding sensor bias and the Schuler oscillation.

We observe that the main limitation of the IMU for navigation is the gyroscopes. Indeed in addition to a strong impact from the bias of the gyroscopes directly on the position error, the attitude depends on the stability of the gyroscopes and impacts the position error.

1.2 Benefits of atomic sensors

1.2.1 Absolute sensor

Atomic based instruments represent new classes of inertial sensors with unprecedented sensitivity, stability and accuracy including gravimeters [6, 7], gravity gradiometers [8, 9], and gyroscopes [10, 11]. For instance, these high-performance inertial sensors will lead to a breakthrough in technology for many fields, including geophysics [12], metrology [13], and particularly inertial navigation [14]. In atom interferometry, cold atoms inside vacuum apparatus serve as a perfect proof mass in free fall, delivering absolute measurements.

1.2.2 State-of-the-art of the atom accelerometers

Tremendous improvements have been achieved and commercial gravimeters based on the same technology reach a stability of <1 ng and an absolute accuracy of $\simeq 1$ ng with a noise on the order of 10 ng/$\sqrt{\text{Hz}}$. However, these instruments are typically large, complex laboratory experiments that require quiet, stable conditions in order to operate. In-field and onboard applications demand a drastic reduction in the size, weight and power consumption of these devices [15, 16, 17], while also requiring a high level of robustness and resistance to environmental disturbances. Over the past few years significant progress has been made in the commercialization of cold-atom-based sensors [18].

A number of research teams and companies have developed transportable cold-atom gravimeters. By transportable, we mean that the setup can be transported from one test site to another and installed within a few hours. However, these systems cannot be operated in movement and usually require a stable and quiet environment to operate at their nominal performances. Two companies provide commercial products: AOSense [19] and μQuans [20] in relatively compact packages weighting respectively 20 kg and 100 kg. Several universities and research centers have also developed transportable experiments in less integrated packages [21, 22, 23, 24].

Laboratory/Company	**Noise (ng/$\sqrt{\text{Hz}}$)**	**Stability (ng)**	**Accuracy (ng)**
SYRTE [23]	5.7	< 0.1	2
Humboldt University [21]	10	0.05	3.2
μQuans [18]	46	1	TBD

Table 1.3: Performances of the best current cold-atom gravimeters.

Table 1.3 presents the noise and accuracy of some of the most performant existing gravimeters. Due to the large interrogation times used in these setups, the intrinsic bandwidth is typically less than 10 Hz and the dynamic is reduced. Furthermore, the need for a laser-cooling stage prior to the interferometer sequence produces dead times and limits the data rate to the Hz range. These setups participate regularly to comparison campaign between different absolute and relative gravimeters such as falling corner cube absolute gravimeters, relative spring and superconducting gravimeters.

In contrast to a transportable experiment, a mobile system can operate while in movement and in a relevant navigation environment. To this day, very few experiments are truly mobile. In reference [25] a gravity gradiometer is operated in a truck but only at very low speed (1 cm/s). The most mature mobile setups are the ICE double species experiment at LP2N and the ONERA mobile gravimeter. The ICE experiment aims at

testing the weak equivalence principle by using a double-species interferometer in the microgravity environment available in the Zero-G plane operated by Novespace [16, 26]. Furthermore the ICE experiment also demonstrated the first mobile horizontal atom accelerometer [27]. The ONERA gyro-stabilized gravimeter participates to sea-borne [17] and recently air-borne gravity mapping campaigns [28]. During the marine gravimetry survey in the North Atlantic Ocean, they have demonstrated a gravity mapping reproducibility below 1 μg, slightly higher errors have been obtained in the flight campaign over Greenland.

1.2.3 Challenges for inertial navigation compatibility of atomic accelerometers

Atomic accelerometers suffer from dead times which reduces the bandwidth of the measurements. Additionally in dynamic environment, the atoms can leave the optical beams if the acceleration is too high. The dynamic of the measurements is limited by the size of the instrument. Furthermore the atom interferometer is sensitive to the Doppler shift, deriving from the relative velocity between the free-falling atoms and the mobile, meaning that the velocity must be known during interferometry. The hybridization with a classical sensor, offering continuous measurements with high bandwidth and a large dynamic, is a key solution to improve the atomic accelerometer on those aspects [29, 14, 30].

The precision obtained with mobile apparatuses is still several orders of magnitude larger compared to static operations. Several problems encountered in mobile operation explain this discrepancy. Vibration noise leads to an ambiguity on the measurement on the fringe of the atom interferometer. This ambiguity can be resolved by combining the atom interferometer with a classical accelerometer. The classical accelerometer provides a rough estimation of the acceleration which permits to solve the fringe ambiguity and the atom interferometer provides the precise measurement similar to the use of a Vernier scale [31].

Rotations encountered in mobile operations constitute another difficult issue. If the apparatus is in rotation during the interferometer, the 3 light pulses of the Mach-Zehnder interferometer are not applied in the same direction. In this case, the wavepackets are not overlapped at the last pulse and the interferometer is not closed. This leads to a strong loss of contrast. The ONERA experiment avoids this issue by setting-up the gravimeter on a gyro-stabilized platform with the drawback of a non strap-down setup with a heavier and more complex system. Another solution is to set the reference mirror of the atom interferometer on a tip-tilt stage which counter-acts inverse rotations [32].

Measuring the acceleration along three-axis is fundamental to operate inertial

navigation. For now, a very few atom interferometers operates multi-axis measurements [33, 34]. Atomic accelerometers are bulky and complex instruments. The compactness of the apparatuses is crucial for on-board applications. Furthermore reducing the complexity is an important aspect to address for future industrialization and eventually adapting the atom accelerometer into a turn-key solution.

1.3 Target performances

To benefit plainly from atomic accelerometer for inertial navigation, we need to measure the acceleration along 3 axes. In this thesis work, we develop a 3-axis atom accelerometer to fulfill this task. Furthermore each atomic accelerometer needs to be hybridized with a classical accelerometer to run efficiently. Consequently we are going further by conceiving a 3-axis hybrid accelerometer. In this section, we discuss about the applications and the technological guidelines for the realization of our 3-axis hybrid accelerometer and the possible applications for such instrument.

1.3.1 Applications

Improve inertial navigation systems

The natural application of atomic accelerometers is to improve the stability of the acceleration measured by the navigation system. Indeed atomic accelerometers rely on an absolute measurement of the acceleration. A 3-axis atom accelerometer can be integrated into an architecture with a Kalman filter as illustrated in Figure 1.5. The first objective here is to improve the strategic IMU grade with an acceleration stability of 500 ng which is 1 order of magnitude gain on the state-of-the-art.

Mobile gravimetry

The 3-axis hybrid accelerometer represents an alternative to mobile gyro-stabilized gravimeter. The gravitational acceleration is provided by the total acceleration vector from the 3-axis hybrid accelerometer. It could represent an aiding sensor for gravity matching technics. Aside from inertial navigation applications, the 3-axis hybrid accelerometer can be used for gravity mapping airborne or space survey where high-end mobile absolute sensors are required.

Space missions

The development of such compact multi-axis cold atom interferometer can be applied for fundamental physics. Space technologies require high expectations in terms

of size, weight and power (SWaP). All the architecture developed besides this project can be applicable for fundamental science in Space. Studying the atom in micro-gravity represents a high interest in the field of theoretical physics such as relativistic effects (equivalence principle, redshift clocks), gravitational-wave detection, search for dark matter, transition matter under specific environment. The main idea is to increase interrogation time thanks to microgravity which improves the sensitivity in interferometry.

Navigation in Space is uncommon since a lot of usual navigation tools or dead-reckoning instruments are not useable and GNSS is not accessible. In general, satellites and spacecrafts navigate with stellar navigation. The quantum sensors are applicable in Space and one can imagine using 3-axis atomic accelerometers as navigation system. Such navigation systems propose an alternative to correct long term biases and facilitate space-navigation.

High-end multi-tool sensor

Apart from the sensitivity to accelerations and rotations, the atoms can be extended as a multi-tool sensor. The cold atoms gradiometer proposed in reference [35] presents a single initial atomic cloud split in two to conduct two parallel interferometers where both gravity gradient and rotation rate are measured. The magnetic field can be probed accurately by measuring the frequency shift of magnetic energy state levels sensitive to magnetic field. Hyperfine spectroscopy with a Ramsey interferometer offers a measurement of the perennial clock transition of the atom and delivers a time-base clock very stable over time [36].

One can imagine a multi-tool atomic sensor with alternative sequences for different physical measurement including accelerometer, gyroscope, magnetometer, frequency oscillator. For instance, the sensor would calibrate the INS or on-board classical clocks and measure precisely magnetic fields on purpose.

1.3.2 Selected technology baseline

In this work, we focus on the development of a sequential 3-axis hybrid accelerometer. For this laboratory prototype, mature and trust technological building blocks are adopted in the scope of future industrial transfer. Furthermore exploring new fields as on-board applications outside the laboratory, requires improved and controlled experiments. Some technological choices rely on a trade-off between compactness or reduced complexity for mobility and performances.

Atom species

Alkali atoms are the most suitable species to make interferometry and are easy to manipulate since they have one valence electron. The cycling transition for Rubidium and Potassium are adapted for easy cooling and trapping. The energy levels of the hyperfine structure are closer for Potassium compared to Rubidium, which allows farther cooling detuning for Rubidium and colder cloud. In addition, the optical transitions of the Rubidium are accessible by doubling the telecom wavelengths from 1560 nm to 780 nm, whereas the optical transitions for the Cesium are trickier to achieve [37]. For those reasons, we choose to operate our instrument with Rubidium 87 (^{87}Rb).

Cold atoms vs ultra-cold atoms

Non dissipative very narrow and deep traps allow to produce ultra-cold atoms. For instance dipole traps, using high intensity lasers to confine the atoms, increase the phase-space density necessary to reach Bose-Einstein condensate (BEC). Evaporation cooling is adapted to reach sufficient temperatures to generate a BEC, at the expense of reducing drastically the number of atoms.

BEC are suitable in interferometry for very specific cases requiring very high sensitivity, such as metrology or fundamental physics [38]. The performances delivered by BEC interferometry are not required for inertial navigation. For instance, cold atoms are used for state-of-the-art atomic gravimeters [18]. The complexity (additional strong magnetic fields or intensity lasers) and the timing (evaporation cooling) required to produce a BEC are incompatible for mobile and high data rate applications for now, but guided atoms on chip are promising for the future.

Raman vs Bragg transitions

Two types of transitions are used for optically induced atom interferometry: stimulated Raman and Bragg transitions [39]. The main difference is the coupling between two different ground states in Raman interferometry, whereas only one energy state is used in Bragg interferometry. The advantage of Bragg interferometry is the large momentum transfer technic (LMT) which allows to open the atom interferometer with a large area and permits to reach high sensitivity [40]. LMT interferometry with Raman transitions is achievable but is mainly limited by large spontaneous emission cumulated at each pulse [41, 42].

The drawback of using the same energy state for interferometry is the requirement of spatial resolution for detection with a camera. On the other hand for Raman

interferometry, the coupling between the two ground states allows to detect the population between the two interferometric atomic clouds by fluorescence, which require only a photodiode. It simplifies the setup and the data analysis compared to camera imaging. In addition Raman transitions allows to measure the hyperfine splitting frequency of the atoms, which can recalibrate an oscillator accurately.

Free-falling atoms vs atomic fountain and trapped atoms

The usual scheme for atom interferometry is to let fall the atoms under the gravitational acceleration. An atomic fountain is produced by launching the atoms with a momentum induced by the lasers. Atomic fountains for atom interferometry reduce the free-fall atomic distance induced by gravity and increase the interrogation time (and the sensitivity) for a given apparatus dimension [43]. Atomic fountains are particularly adapted for atomic gyroscopes or accelerometers by expanding the opened area of the interferometer. However atomic fountains are hard to implement and complicate the apparatus. Moreover the high sensitivity obtained with atomic fountains is not necessary for inertial navigation. To extend the concept of gravity compensation to maximize the sensitivity, the atoms can be trapped into an optical lattice [44] or a magnetic trap [45]. The complexity of trapped atoms is also higher but such technic paves the way of very compact apparatuses, such as atom chips.

The advent of atom interferometry on atom chip opens the field of miniaturized apparatuses [46]. For now atom chips have been used for gravimetry and are interesting for future integration for inertial navigation. However inertial navigation requires multi-axis accelerometers and atom chips are not mature concerning multiple optical access. Indeed collimators are bulky and are necessary to conduct interferometry along different axes. In the meantime, an atom accelerometer relies on the acceleration of the atoms relative to a reference mirror. A partial solution could be to transport the atoms far from the atom chip to have access.

Sequential vs simultaneous multi-axis

A recent proposal presents a simultaneous multi-axis interferometric scheme where Raman transitions operate in different directions [47]. This architecture allows to obtain the acceleration along arbitrary axis and obtain the full acceleration vector within one shot. Additionally the coriolis acceleration can be extracted on multiple axes from the interferometric signal of one shot. Such implementation into current apparatuses is not mature and some aspects, such as 3-dimensional detection or control of multi-axis Raman transitions, have not been yet experimented.

Strap-down vs gyro-stabilization

A gyro-stabilized gravimeter offers an advanced system for mobile gravimetry [17, 28]. One main function is the mapping of the gravitational acceleration anomalies during surveys. Another purpose is the gravity matching navigation where the local gravitational acceleration, measured with a gyro-stabilized gravimeter, is compared to known maps.

One can think of a gyro-stabilized 3-axis atomic accelerometer adapted for the historical gyro-stabilized INS, where the IMU is stabilized by gimbals. Indeed a gyro-stabilized apparatus is beneficial to correct parasitic rotations for the recombination of the atomic cloud during interferometry. However the gyro-stabilization is achieved with an hexapod which represents a heavy and complex system. Such apparatus is not flexible and depends on the performances of the hexapod defining the stability of the verticality. Conversely the strap-down 3-axis accelerometer is fully compatible with actual inertial navigation system.

1.3.3 Specification of the 3-axis hybrid accelerometer

The sequential 3-axis hybrid accelerometer combines three atom accelerometers with three classical accelerometers fixed to the reference mirror of each atom interferometer. The resulted dynamic range expected is the one from classical accelerometers ± 20 g. Furthermore the resulted bandwidth is the one from the classical accelerometer, delivering measurements at 1 kHz. The short-term sensitivity will be restricted by the classical accelerometers and we target a sensitivity $< 2\ \mu g/\sqrt{Hz}$ for each hybridized accelerometer. The mid-term stability should be improved by the atom accelerometers, aiming for < 100 ng of bias stability on each axis. The accuracy intended on each axis should reach $\simeq 100$ ng with a good characterization of the systematic shifts of the atom interferometers. Long-term stability requires higher level of qualification for atomic sensors where all the components need to sustain continuous operation. The objective can be fixed to a stability $< \mu g$ over 100 days.

Conclusion

We have presented some classical inertial sensors and their applications to inertial navigation. The strength of the Kalman filter relies on its flexibility to integrate and fuse measurements from multiple sources likes sensors or navigation tools. Those additional measurements contribute to the accuracy of the navigation positioning and improve bias instabilities from inertial sensors.

The quantum sensor benefits from the absolute measurement of cold atoms inside vacuum apparatuses. In particular, atom accelerometers raise high interests for inertial navigation. One can consider a 3-axis atomic accelerometer as an aiding sensor integrated into a centralized Kalman filter architecture. However, the complexity and large size of atomic apparatuses complicate mobile operations. Significant efforts are necessary to optimize and adapt such instruments for on-board applications outside the laboratory.

Chapter 2

Matter-wave interferometry for acceleration sensing

This chapter reports some basics and theoretical tools for atom interferometry dedicated to acceleration sensing. Different operation schemes and tracking algorithms of the hybridization between the atom interferometer and the classical accelerometer are depicted. Specifically, we propose a method to operate a 3-axis hybrid accelerometer corresponding to a multi-axis high-bandwidth and bias-free accelerometer.

Contents

2.1 Atom interferometry 41

2.1.1 Rubidium 87 for atom interferometry 41

2.1.2 Atom trapping and cooling 41

2.1.3 Two-photon Raman transitions 42

2.1.4 Wave-packet diffraction by atom optics 46

2.1.5 Matter-wave propagation 48

2.1.6 Mach-Zehnder interferometer 49

2.1.7 Sensitivity and transfer function of the atom interferometer 52

2.1.8 Scale factor of the atom accelerometer 55

2.2 Atom accelerometer with a reference mirror 61

2.3 Hybridization with classical accelerometers 63

2.3.1 Hybridization schemes 63

2.3.2 Real-time correlations 65

2.4 Tracking algorithms 66

2.4.1 Kalman filter 66

2.4.2 Mid-fringe lock algorithm 68

2.4.3 Sequential 3-axis hybrid accelerometer 73

Introduction

The stability and the exactitude of the atomic energy states provide absolute measurements with quantum instruments. Inertial sensing, magnetometer or frequency clock metrology are examples of physical measurements achieved with atoms. The advent of the monochromatic laser permitted to interact with atoms by accessing to single energy states transitions. The proposition of the magneto-optical trap (MOT) of atoms by Jean Dalibard was first demonstrated by the team of Steven Chu and reported in reference [48]. The trapping and cooling of atoms paved the way of atom optics and atomic wavepackets manipulation as a result of accessible and coherent de Broglie wavelengths. A few years later, Mark Kasevich and Steven Chu demonstrated the first gravimeter based on atom interferometry in 1991 [6]. Since then, the interest for quantum sensor dedicated to inertial sensing is expanding. Over the past few years significant progress has been made in the commercialization of cold-atom-based sensors [18], and it is widely believed that these high-performance inertial sensors will lead to a technological breakthrough in many fields, including geophysics [12], metrology [13], and inertial navigation [14].

The main characteristics of a sensor are the sensitivity, the stability of the bias drifts and the accuracy or systematic shifts. Classical sensors, such as classical accelerometers, are very sensitive to the environment including temperature, pressure, humidity. Their characterization is mostly empirical and requires a periodic calibration to provide confident measurements over long time periods. The quantum sensors present apparatuses where the atoms are isolated from external environment into vacuum chambers or cells. Consequently the atomic accelerometer measurements are exact with predictable transfer and sensitivity functions, scale factor and systematic shifts.

However, beside a valuable accuracy and stability, the atomic accelerometer suffers from a low dynamic range and a low bandwidth due to dead-times between measurements. The spirit of hybridization between sensors is to combine the strengths of multiple sensors. Whereas the classical accelerometers provide a high-bandwidth measurement but suffer from large biases drifting in time, the quantum accelerometers offer absolute measurements which could correct the classical one. Conversely the dead-times of the quantum sensor can be filled with continuous classical measurements. One can see analogy with the hybridization of a classical oscillator inside an atomic clocks.

2.1 Atom interferometry

2.1.1 Rubidium 87 for atom interferometry

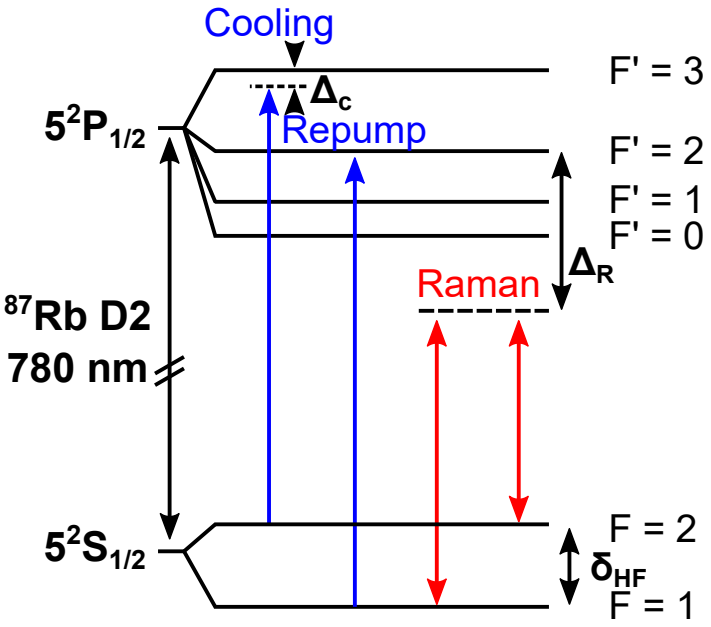

Figure 2.1: D2 transition of ^{87}Rb.

Alkali atomic species, composed of one valence electron, are good candidates to be operated and controlled straightforwardly. Figure 2.1 presents the D2 transition of the isotope 87 of the Rubidium [49]. The clock transition (or hyperfine transition) of ^{87}Rb is $\delta_{\mathrm{HF}}/2\pi \approx 6.834$ GHz. The cooling and repumper light is used for trapping, cooling and detection, whereas Raman transitions drives coherent transition for atom interferometry. The detuning $\Delta_{\mathrm{R}} \approx 1$ GHz avoids spontaneous emission during two-photon transitions.

2.1.2 Atom trapping and cooling

A cooling beam addresses the cycling transition $|F = 2\rangle \rightarrow |F' = 3\rangle$ as depicted in Fig. 2.1. The detuning Δ_c authorizes to address different velocity classes of atoms during cooling by compensation of the Doppler frequency shift. A repumper beam $|F = 1\rangle \rightarrow |F' = 2\rangle$ is set simultaneously and repump the atoms into the energy state $|F = 2\rangle$ for cooling.

Two opposed current loops in anti-Helmholtz coils configuration deliver a gradient magnetic field. This configuration generates a position-dependent Zeeman shift gradient of the magnetic sub-states whish vanishes at the center of the coils configuration. Combined with 6 circularly polarized counter-propagating cooling and repumping lasers, the arrangement produces a three dimensional magneto-optical trap (3D-MOT).

Any atom escaping from the center of the trap sees its degenerated excited levels shifted by Doppler effect relative to the laser beams. The laser beams push it toward the trap center. An easy way to produce a 3D-MOT is to generate the light field of 3 retro-reflected laser beams with mirrors.

Doppler cooling is not sufficient to reach decent temperature < 10 μK for atomic coherence. Red detuned optical molasses employing Sisyphus scheme [50] or grey molasses [51] guarantees to reach sub-Doppler temperatures $\simeq 1$ μK. Raman sideband cooling allows even lower temperature down to $\simeq 1$ nK [52, 53]. Evaporation cooling is adapted to reach temperatures $\simeq 100$ nK at the expense of reducing drastically the number of atoms.

2.1.3 Two-photon Raman transitions

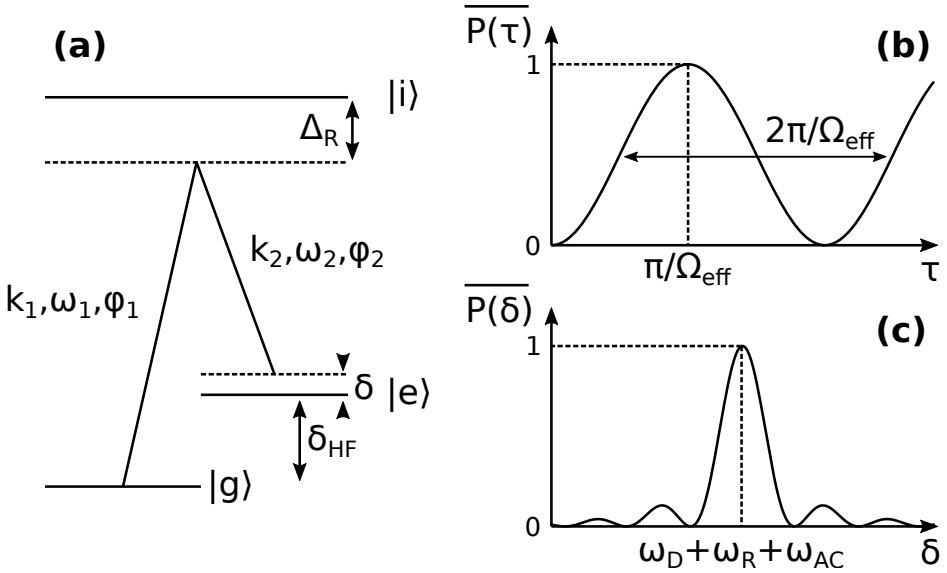

Figure 2.2: (a) Illustration of the Raman transitions. The resulted probability transition between the ground $|g\rangle$ and excited $|e\rangle$ energy levels are plotted in function of the pulse length when the lasers are in resonance on (b) and in function of the resonance detuning when the pulse length is optimized on (c).

The two energy levels $|F = 1\rangle$ and $|F = 2\rangle$ on the D2 transition of ^{87}Rb, defined respectively as ground state $|\mathrm{g}\rangle$ and excited state $|\mathrm{e}\rangle$, are not connected by a transition at optical frequency. To drive coherent transitions at optical frequencies, we consider a three level atom system where the energy state $|F'\rangle$ corresponds to an intermediate energy state $|\mathrm{i}\rangle$ such that optical transitions $|\mathrm{g}\rangle \leftrightarrow |\mathrm{i}\rangle$ and $|\mathrm{e}\rangle \leftrightarrow |\mathrm{i}\rangle$ are authorized.

Figure 2.2(a) illustrates the principle of the Raman transitions with a frequency Raman detuning Δ_R and a resonance detuning δ. The probability transition of the atoms subjected to Raman transitions derives from the Fourier transform of the pulse shape and, by assuming a square shaped Rabi pulse, is equal to [54, 55]:

$$P(\tau, \delta, r, v) = \frac{\Omega_{\text{eff}}^2(r)}{\omega^2(\delta, v, r)} \sin^2\left(\frac{\omega(\delta, v, r)\tau}{2}\right) \tag{2.1}$$

where τ is the length of the Rabi pulse, $\omega(\delta, v, r) = \sqrt{\Omega_{\text{eff}}^2(r) + (\delta - \omega_{\text{D}}(v) - \omega_{\text{R}} - \omega_{\text{AC}})^2}$ is the exact Rabi frequency depending on the controlled resonance detuning δ between the lasers, the Doppler frequency $\omega_{\text{D}}(v) = k_{\text{eff}} v$ with the velocity v relative to the beams, the recoil frequency $\omega_{\text{R}} = \hbar k_{\text{eff}}^2 / 2M$ and the light shift ω_{AC}. $\vec{k_{\text{eff}}} = \vec{k_1} - \vec{k_2}$ is the effective wavevector corresponding to the momentum exchange of the Raman transition and $k_{\text{eff}} = |\vec{k_1}| + |\vec{k_2}|$. The effective Rabi frequency $\Omega_{\text{eff}}(r)$ is defined for large Raman detuning Δ_{R} as [55]:

$$\Omega_{\text{eff}}(r) = \frac{\Omega_1^*(r)\Omega_2(r)}{2\Delta_{\text{R}}} \tag{2.2}$$

where Rabi frequencies $\Omega_1(r)$ and $\Omega_2(r)$ are associated to each single-photon transition. We define the effective frequency of the pair of lasers as $\omega_{\text{eff}} = \omega_1 - \omega_2 = \delta_{\text{HF}} + \delta$. When the frequency of the two lasers are in resonance between the ground and excited states, meaning that $\delta = \omega_{\text{D}}(v) + \omega_{\text{R}} + \omega_{\text{AC}}$, the probability transition depends only on the effective Rabi frequency $\Omega_{\text{eff}}(r)$ and is controlled by the pulse length τ. The effective probability transition corresponds to the integration of $P(\tau, \delta, r, v)$ over $N(r)$ and $G(v)$ representing respectively the spatial and velocity distribution of the atomic cloud:

$$\overline{P(\tau, \delta)} = \iint N(r)G(v)P(\tau, \delta, r, v)drdv \tag{2.3}$$

For most of the cases, the spatial distribution of the cloud is negligible and $N(r) = 1$. The velocity distribution relies typically on a Gaussian distribution and is expressed as:

$$G(v) = \frac{1}{\sigma_v\sqrt{2\pi}} e^{-\frac{(v-v_0)^2}{2\sigma_v^2}} \tag{2.4}$$

with σ_v the width of the velocity classes of the atoms equivalent to the temperature of the cloud and v_0 the central velocity of the distribution. Figure 2.2(b) and (c) shows the probability transition when respectively the pulse length and the resonance detuning are varying. The spontaneous emission and the velocity distribution $G(v) = 1$ are ignored on the probability transitions $\overline{P(\tau)}$ and $\overline{P(\delta)}$ depicted.

Quantization axis and polarization of the light

To control the Raman transitions between magnetic sub-levels, the axis along the laser beam needs to be quantized by generating a magnetic field along the beam path. The degeneracy between magnetic states is raised where the Zeeman frequency shift

separates them.

The standard architecture to drive two-photon Raman transitions uses the same light beam retro-reflected by a reference mirror and containing the two Raman frequency lines. In this configuration, the Raman lasers can drive the transitions with two co-propagating Raman beams or two counter-propagating Raman beams. The interaction between the electro-magnetic field of the light beam with the atomic dipole depends on the polarization of the light and is governed by transitions selection rules.

In Chapter 3, we explain our choice to use the same retro-reflected beams for the MOT and the Raman transitions, mostly for compactness purpose in our apparatus. In such configuration, the beams are inevitably retro-reflected and blocking the return path of the beam would cut off the MOT. Co-propagating lasers interact with the atoms when they are circularly polarized $\sigma+/\sigma+$ or $\sigma-/\sigma-$ and drive co-propagating Raman transitions. To rotate conveniently the polarization between the straight and retro-reflected beam, a quarter waveplate is placed between the atoms and the mirror. Conversely, when the Raman lasers are linearly polarized as $\pi^{\odot}/\pi^{\rightarrow}$ or $\pi^{\rightarrow}/\pi^{\odot}$ (also noted lin⊥lin), the counter-propagating beams drive counter-propagating Raman transitions.

Co-propagating Raman transitions

Since the absorption and the stimulated emission of the photons are opposite for co-propagating Raman transitions, they are not sensitive to Doppler frequency shift. The exact Rabi frequency becomes $\omega_{\text{co}}(\delta, r) = \sqrt{\Omega_{\text{eff}}^2(r) + (\delta - \omega_{\text{AC}})^2}$. The co-propagating Raman transitions are driven when the frequency difference $\omega_{\text{eff}} = \omega_2 - \omega_1$ is equal to the clock transition δ_{HF} assuming no light shifts $\omega_{\text{AC}} = 0$.

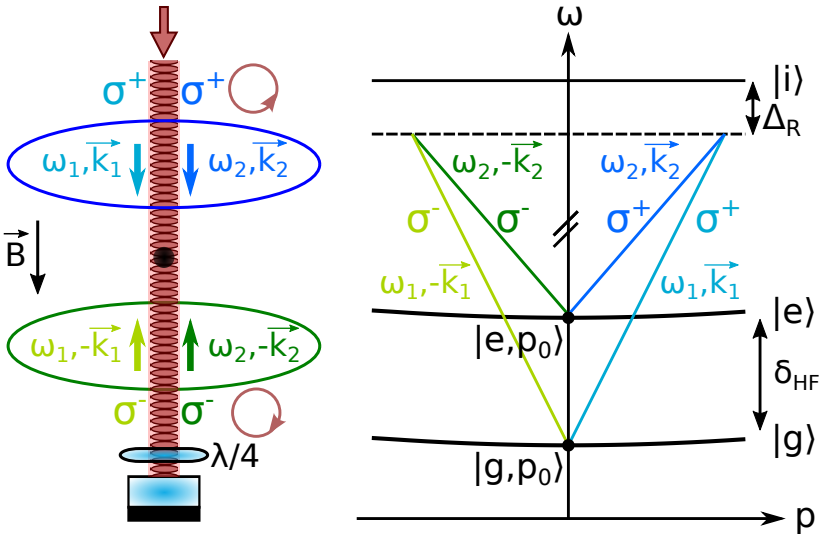

Figure 2.3: Illustration of the co-propagating Raman transitions.

Figure 2.3 illustrates the co-propagating Raman transitions in a retro-reflected configuration with a quarter waveplate between the atoms and the reference mirror. Here the momentum of the atoms is considered null $p_0 = 0$. Two pairs of transitions are allowed with polarizations $\sigma+/\sigma+$ and $\sigma-/\sigma-$.

The co-propagating Raman transitions are adapted to transfer atoms into different energy states without inducing a spatial displacement, or to measure magnetic fields and clock frequency. For instance, to prepare the atoms into the non-magnetic energy $|F = 1, m_f = 0\rangle$, the transitions are addressed with the resonance detuning δ. The magnetic field is probed by measuring the frequency Zeeman shift between magnetic-states with a frequency spectroscopy of the resonance detuning δ. In addition Ramsey spectroscopy, composed of two successive co-propagating Raman pulses, enables to probe the hyperfine transition δ_{HF}. With that scheme, we obtain an interferometric pattern frequency dependent, which is scanned with the resonance detuning δ. For example, we use this scheme in Chapter 4 to measure the stability of the timebase system of our apparatus.

Velocity-sensitive counter-propagating Raman transitions

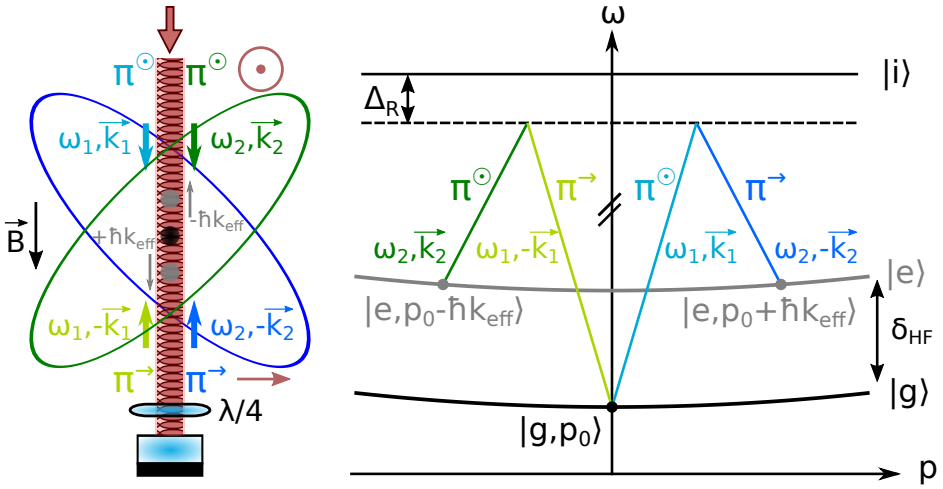

Figure 2.4: Illustration of the counter-propagating Raman transitions

Figure 2.4 illustrates the counter-propagating Raman transitions with atoms of momentum $p_0 = 0$. The counter-propagating Raman transitions are sensitive to the velocity v of the atoms relative to the frequency lasers since the absorption and the stimulated emission of the photons are in the same direction. The effective wavevector $\vec{k_{\mathrm{eff}}} = \vec{k_1} - \vec{k_2}$ defines the direction of the recoil momentum of the atoms transferred by the Raman pulse. Depending on the pair of Raman beams used to transfer the atoms, the direction of the recoil can be $+\vec{k_{\mathrm{eff}}} \equiv k_\uparrow$ or $-\vec{k_{\mathrm{eff}}} \equiv k_\downarrow$.

When the momentum of the atoms relative to the lasers is zero $p_0 = 0$, double diffraction occurs meaning that the two pairs of counter-propagating Raman transitions are driven [39]. To lift the degeneracy of double diffraction process, the optical frequencies of the two pairs need to be different with a non zero Doppler frequency shift $\omega_D(v) \neq 0$ meaning that the velocity of the atoms relative to the laser should be sufficient. The vertical drop of the atoms due to gravitational force fulfills this condition after a few ms. However for horizontal laser beams or in micro-gravity situation, other technics are required. A controlled moving molasses can provide a certain velocity to the atoms along the laser beam. To select which pair of counter-propagating beams will drive single Raman diffraction, the resonance detuning δ is adapted according to the Doppler frequency $\omega_D(v) = \pm k_{\text{eff}} v$. A recent method employs a fast frequency chirp on the laser to simulate a Doppler shift to the atomic transitions [56].

2.1.4 Wave-packet diffraction by atom optics

The deflection of the trajectory, when atoms are transferred by counter-propagating Raman beams, controls spatially the atomic cloud. It relies on a coherent superposition of energy states of the atoms spatially split.

Evolution of the atomic wavefunction

We consider the space-time trajectories of the atomic cloud paths presented in Fig. 2.5. They represent the possible cases when the atomic cloud is illuminated by counter-propagating Raman beams of wavevectors k_1 and $-k_2$, frequencies ω_1 and ω_2 and phases ϕ_1 and ϕ_2.

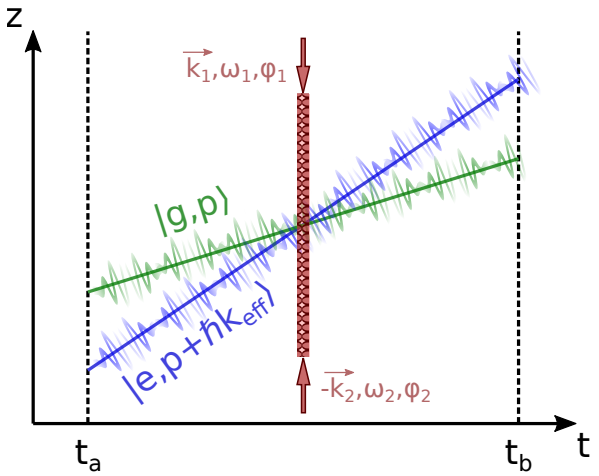

Figure 2.5: Diffracted paths when the atomic cloud is exposed to a pair of counter-propagating Raman lasers.

The evolution operator U describes the time evolution of a quantum system between

an initial time t_a and a final time t_b as:

$$|\psi(t_b)\rangle = U(t_b, t_a)\,|\psi(t_a)\rangle \tag{2.5}$$

We define the phase shift Φ^{laser} as the total phase imprinted by the Raman lasers onto the atomic wavefunction as:

$$U(t_b, t_a) = P e^{i\Phi^{\text{laser}}} \tag{2.6}$$

where P represents the transition probability between the two energy states $|g\rangle$ and $|e\rangle$. The interaction of the Raman lasers with the atomic cloud affects the wavefunction with the following evolution operators according to four different cases:

$$\begin{aligned} U_{eg} &= P_{eg} e^{i(k_{\text{eff}} z - \omega_{\text{eff}} t + \phi)} && \text{for } |g\rangle \rightarrow |e\rangle \\ U_{ge} &= P_{ge} e^{-i(k_{\text{eff}} z - \omega_{\text{eff}} t + \phi)} && \text{for } |e\rangle \rightarrow |g\rangle \\ U_{gg} &= P_{gg} && \text{for } |g\rangle \rightarrow |g\rangle \\ U_{ee} &= P_{ee} && \text{for } |e\rangle \rightarrow |e\rangle \end{aligned} \tag{2.7}$$

where $k_{\text{eff}} = k_1 + k_2$ is the effective wavevector, $\omega_{\text{eff}} = \omega_1 - \omega_2$ is the frequency difference, $\phi = \varphi_1 - \varphi_2$ is the phase difference, P_{eg}, P_{ge}, P_{gg} or P_{ee} represent the transition probabilities between the ground state $|g\rangle$ and the excited state $|e\rangle$.

Atomic cloud mirror and splitter

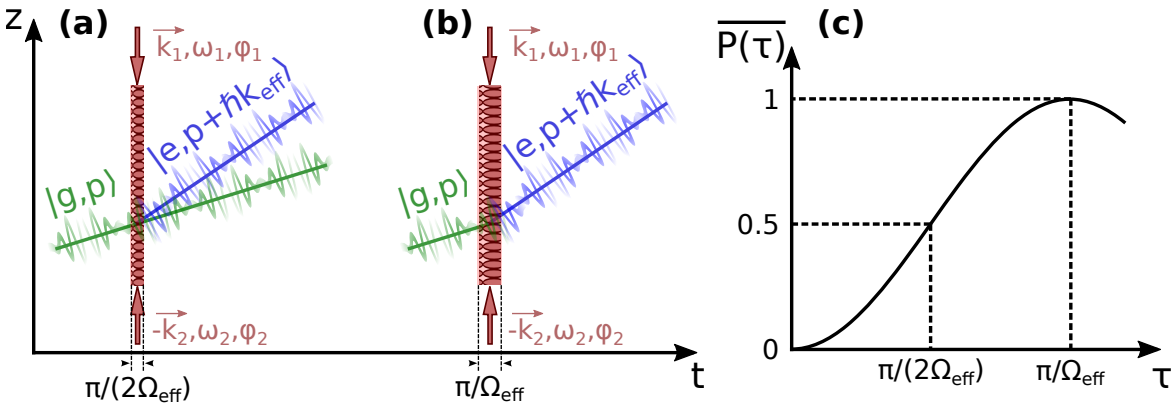

Figure 2.6: Diffraction of the atomic wave-packet with counter-propagating Raman transitions.(a) Beam splitter pulse ($\pi/2$-pulse) where the wave-packet is separated in space with the same quantity of atoms in each energy state $|g\rangle$ and $|e\rangle$. (b) Mirror pulse (π-pulse) where all the atoms are transferred from $|g\rangle \rightarrow |e\rangle$ and deflected spatially. (c) Rabi oscillations quantifying the number of atoms transferred into the other energy state, depending on the pulse length τ.

The deflection of the atomic cloud by the counter-propagating Raman transitions is exploited to spatially split, reflect or recombine the atoms. By controlling the amount

of atoms transferred between the diffracted and undiffracted paths, we are able to construct an atomic cloud splitter with a $\pi/2$-pulse or an atomic cloud mirror with a π-pulse as shown respectively on Figure 2.6 (a) and (b). The Rabi oscillations, relying on the transition probability function $\overline{P(\tau, \delta)}$ depending on the effective Rabi frequency Ω_{eff}, describes the quantity of atoms transferred between the energy states $|g\rangle$ and $|e\rangle$ and is displayed on Figure 2.6 (c).

When an atom is transferred from one energy state to another with Raman transition, the phase difference of the Raman lasers $\phi = \varphi_2 - \varphi_1$ is imprinted onto its wavefunction. The phase coherence of the Raman lasers is critical to control the phase of the atomic wave-packets. A reference mirror serves to retro-reflect the counter-propagating Raman beams and allows to generate the two phase coherent frequency lines within the same beam.

2.1.5 Matter-wave propagation

The matter-wave propagation can be treated with the Feynman path integral approach [57], relying on the Lagrangian mechanics which describes the dynamic of a classical particle. The Lagrangian $\mathcal{L}$ is defined by the difference between the kinetic energy $T(\dot{z})$, depending on the velocity $\dot{z}$, and the potential energy $V(z)$, depending on the position z, as:

$$\mathcal{L}(z, \dot{z}) = T(\dot{z}) - V(z) \tag{2.8}$$

$$= \frac{1}{2} M \dot{z}^2 - V(z) \tag{2.9}$$

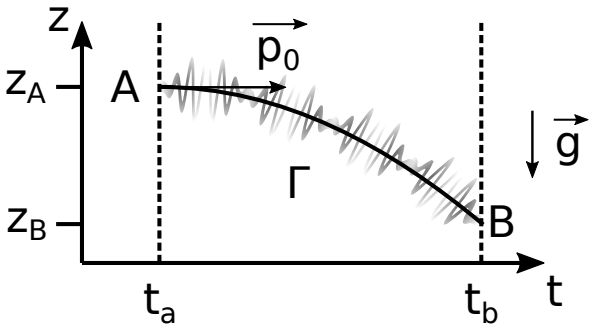

Figure 2.7: Classical path Γ of a particle for a Lagrangian $\mathcal{L}_g$ with initial momentum $\vec{p_0}$.

The principle of least action states that the space-time path taken by a particle is classic. The classical path Γ is the one for which the action is extremal and derived from a classical action S_{cl}. Figure 2.7 shows an example of such path. The classical action is defined as the temporal integral of the Lagrangian over a given space-time classical path Γ from $z_A = z(t_a)$ to $z_B = z(t_b)$:

$$S_{\mathrm{cl}} = S_{\Gamma} = \int_{t_a}^{t_b} \mathcal{L}(z(t), \dot{z}(t))dt \tag{2.10}$$

The differential of the classical action, deriving from the Lagrangian partial derivatives, of a particle can be expressed with the momentum p and the total energy Hamiltonian H:

$$dS_{\mathrm{cl}} = \frac{\partial S_{\mathrm{cl}}}{\partial z}dz + \frac{\partial S_{\mathrm{cl}}}{\partial t}dt = pdz - Hdt \tag{2.11}$$

The dynamic of a classical particle along the classical path Γ^0_{cl} is described by the final wavefunction $\psi(B)$ as:

$$\psi(B) = \psi(A)e^{i\frac{S_{\mathrm{cl}}}{\hbar}} \tag{2.12}$$

We define the propagation phase Φ^{prop} along the unperturbed classical path as:

$$\Phi^{\mathrm{prop}} = \frac{S_{\mathrm{cl}}}{\hbar} \tag{2.13}$$

In our case, we consider the Lagrangian $\mathcal{L}_g$ describing a particle in a gravitational field as:

$$\mathcal{L}_g = \frac{1}{2}M\dot{z}^2 - Mgz \tag{2.14}$$

When the particle is subjected to a gravitational field $\vec{g} = g\vec{z}$, the classical action between two points z_A and z_B is easily calculated as [57]:

$$\begin{aligned} S_{\mathrm{cl}} &= \int_{t_a}^{t_b} \mathcal{L}_g(t)dt && (2.15)\\ &= \int_{t_a}^{t_b} \frac{1}{2}Mv(t)^2 - Mgz(t)dt && (2.16)\\ &= \frac{M}{2T}\left[(z_b - z_a)^2 - g(z_b + z_a)T^2 - \frac{1}{12}g^2T^4\right] && (2.17) \end{aligned}$$

where $T = t_b - t_a$.

2.1.6 Mach-Zehnder interferometer

With the velocity-sensitive counter-propagating Raman transitions, we are able to design a series of pulses to control the atomic cloud. The Mach-Zehnder atomic interferometer, as the optical one, is composed of a $\pi/2$-pulse, a π-pulse and a $\pi/2$-pulse to respectively split equally, reflect and recombine the atomic wavepackets coherently.

Figure 2.8 shows the path of the atomic cloud with a Mach-Zehnder interferometer exposed to different Lagrangian. In that section, we consider infinitely short-time pulses compared to the interrogation time $\tau \ll T$.

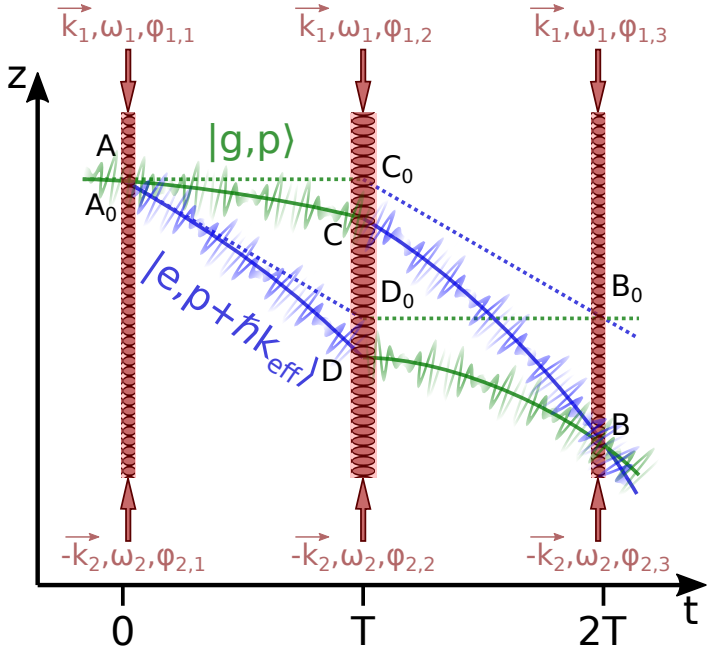

Figure 2.8: Matter-wave Mach-Zehnder interferometer with the quantum system treated as a free particle in dotted lines and in a gravitational field in solid lines.

The paths $(A_0C_0B_0)$ and $(A_0D_0B_0)$ are defined by the dynamical evolution of the quantum system as a free particle. We obtain a closed area formed by a parallelogram resulting in:

$$z_{c_0} + z_{d_0} - z_{a_0} - z_{b_0} = 0 \tag{2.18}$$

The paths (ACB) and (ADB) are defined by the dynamical evolution of the quantum system subjected to a gravitational field $\vec{g}$ described by the Lagrangian $\mathcal{L}_g$. The closed area formed by the two paths is defined by the points:

$$z_a = z_{a_0} \tag{2.19}$$
$$z_b = z_{b_0} - 2gT^2 \tag{2.20}$$
$$z_c = z_{c_0} - \frac{1}{2}gT^2 \tag{2.21}$$
$$z_d = z_{d_0} - \frac{1}{2}gT^2 \tag{2.22}$$

We consider the quantum system subjected to a gravitational field and want to extract the phase shift from the wavefunction of the atoms between the two arms. The propagation phase is calculated using the classical path expression from Eq. 2.17:

$$\begin{aligned}
\Phi^{\text{prop}} &= S_{\text{cl}}(AC) + S_{\text{cl}}(CB) - S_{\text{cl}}(AD) - S_{\text{cl}}(DB) && (2.23)\\
&= \frac{M}{T}(z_c - z_d)(z_c + z_d - z_a - z_b - gT^2) && (2.24)\\
&= \frac{M}{T}(z_c - z_d)(z_{c_0} + z_{d_0} - z_{a_0} - z_{b_0}) && (2.25)\\
&= 0 && (2.26)
\end{aligned}$$

The phase shift Φ^{laser} imprinted onto the atomic wavefunction by the Raman lasers is calculated with Eqs. 2.7 as:

$$\begin{aligned}
\Phi^{\text{laser}} &= \Phi^{\text{laser}}_{ACB} - \Phi^{\text{laser}}_{ADB} && (2.27)\\
&= [k_{\text{eff}} z_c - \omega_{\text{eff}} T - \phi_2] && (2.28)\\
&\quad - [(k_{\text{eff}} z_b - 2\omega_{\text{eff}} T - \phi_3) - (k_{\text{eff}} z_d - \omega_{\text{eff}} T - \phi_2) + (k_{\text{eff}} z_a - \phi_1)] && (2.29)\\
&= -k_{\text{eff}} g T^2 + \phi_1 - 2\phi_2 + \phi_3 && (2.30)
\end{aligned}$$

The total phase shift of the atomic wavefunction at the output of the interferometer is:

$$\begin{aligned}
\Phi &= \Phi^{\text{prop}} + \Phi^{\text{laser}} && (2.31)\\
&= -k_{\text{eff}} g T^2 + \phi_1 - 2\phi_2 + \phi_3 && (2.32)\\
&= \phi_{\text{kin}} + \phi_{\text{laser}} && (2.33)
\end{aligned}$$

where we define the inertial phase ϕ_{kin} measuring the acceleration experienced by the atoms and the imprinted laser phase ϕ_{laser} controlled by the Raman lasers during the interferometer as:

$$\begin{aligned}
\phi_{\text{kin}} &= -k_{\text{eff}} g T^2 && (2.34)\\
\phi_{\text{laser}} &= \phi_1 - 2\phi_2 + \phi_3 && (2.35)
\end{aligned}$$

2.1.7 Sensitivity and transfer function of the atom interferometer

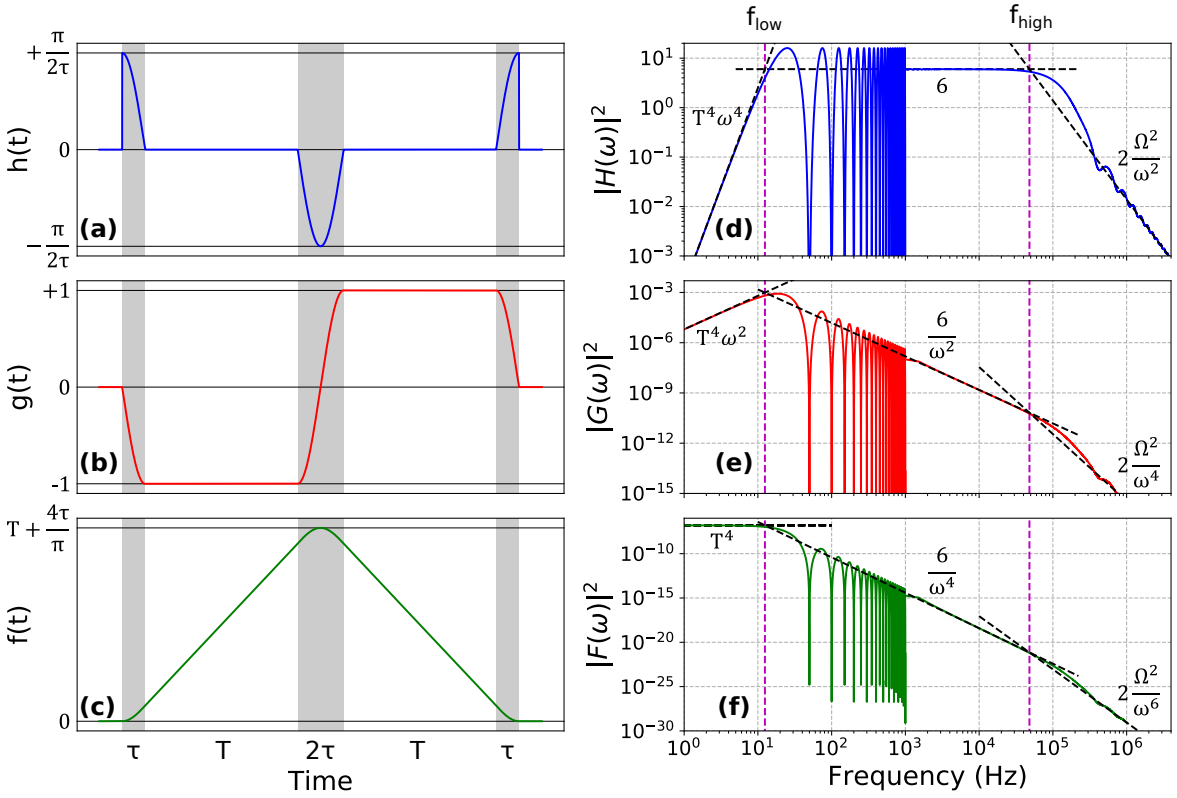

Figure 2.9: Sensitivity functions h(t), g(t) and f(t) describing the response of the atom interferometer to respectively time-varying phases, frequencies and chirps on (a), (b) and (c). Corresponding squared modulus of the transfer functions $H(\omega)$, $G(\omega)$ and $F(\omega)$ characterizing respectively periodic variation of the phase, frequency and chirp on (d), (e) and (f). The transfer functions are averaged above 1 kHz to not overburden the graphs and are calculated for an interrogation time $T = 20$ ms, a pulse length of $\tau = 3$ μs and an effective Rabi frequency $\Omega = \pi/(2\tau)$. $f_{low} = 12$ Hz and $f_{high} = 48$ kHz correspond to the cutoff frequencies of the transfer functions.

The sensitivity function of the atom interferometer is defined by [58]:

$$g(t) = 2 \lim_{\delta\phi \to 0} \frac{\delta P(\delta\phi, t)}{\delta\phi} \tag{2.36}$$

where $\delta P(\delta\phi, t)$ represents a change in the transition probability during Raman transition while a phase jump $\delta\phi$ occurs on the Raman phase difference ϕ at time t. Assuming perfect Raman squared pulses of length τ and effective Rabi frequency Ω and a Raman interrogation time T, the frequency sensitivity function is [59]:

$$g(t) = \begin{cases} 0, & t \leq 0 \text{ and } t > 2T + 4\tau \\ -\frac{\sin(\Omega t)}{\sin(\Omega \tau)}, & 0 < t \leq \tau \\ -1, & \tau < t \leq T + \tau \\ -\frac{\sin(\Omega(t-T-2\tau))}{\sin(\Omega \tau)}, & T + \tau < t \leq T + 3\tau \\ +1, & T + 3\tau < t \leq 2T + 3\tau \\ -\frac{\sin(\Omega(t-2T-4\tau))}{\sin(\Omega \tau)}, & 2T + 3\tau < t \leq 2T + 4\tau \end{cases} \tag{2.37}$$

We define the phase sensitivity function $h(t)$ and the response function $f(t)$ as [58]:

$$h(t) = -\frac{dg(t)}{dt} \tag{2.38}$$

$$f(t) = -\int_0^t g(t')dt' \tag{2.39}$$

Figure 2.9 shows the plot of each sensitivity function. The phase shift of the atom interferometer ϕ_{laser} induced by a variation of the phase difference of the Raman lasers $\phi(t)$ is defined as:

$$\phi_{\text{laser}} = \int_{-\infty}^{+\infty} g(t)\frac{d\phi(t)}{dt}dt \tag{2.40}$$

Furthermore, the response of the atom interferometer can be identified according to the evolution of the time-varying phase difference $\phi(t)$, the time-varying frequency difference $\omega(t)$ or the time-varying chirp $\alpha(t)$ as:

$$\phi_{\text{laser}} = \int_{-\infty}^{+\infty} h(t)\phi(t)dt \tag{2.41}$$

$$= \int_{-\infty}^{+\infty} g(t)\omega(t)dt \tag{2.42}$$

$$= \int_{-\infty}^{+\infty} f(t)\alpha(t)dt \tag{2.43}$$

The phase sensitivity function $h(t)$ is convenient for computing the effect from phase discontinuity of the laser (phase noise or phase non-linearity) and relies on the position of the atoms relative to the reference mirror. The sensitivity function $g(t)$ is adapted for phase-continuous frequency changes of the laser or frequency shift of the atomic resonances (light shifts, Zeeman shifts) and is related to velocities of the atoms relative to the retro-reflected laser beams linked to the reference mirror (Doppler shifts). The response function $f(t)$ provides response from phase-continuous chirp of the laser and correlates accelerations of the atoms relative to the reference mirror.

The transfer function of the atom interferometer is determined by its harmonic

response to a perturbation at frequency ω and is defined by the Fourier transform of the sensitivity function $g(t)$ as:

$$G(\omega) = \int_{-\infty}^{+\infty} e^{-i\omega t} g(t) dt \tag{2.44}$$

We obtain the following transfer function:

$$G(\omega) = \frac{2i\Omega}{\omega^2 - \Omega^2} \left[\sin(\omega(T + 2\tau)) + 2\frac{\Omega}{\omega} \sin\left(\frac{\omega T}{2}\right) \sin\left(\frac{\omega(T + 2\tau)}{2}\right) \right] \tag{2.45}$$

In the same way as $G(\omega)$ defining the transfer function of the interferometer to a periodic variation of the frequency difference $\omega(t)$, we determine the transfer function of the atom interferometer to a periodic variation of the phase $\phi(t)$ or chirp $\alpha(t)$ of the laser with respectively the phase transfer function $H(\omega)$ and response transfer function $F(\omega)$ as:

$$H(\omega) = -\omega G(\omega) \tag{2.46}$$

$$F(\omega) = -\frac{G(\omega)}{\omega} \tag{2.47}$$

The three transfer functions are presented in Figure 2.9. We observe oscillations at periodicity $1/(T + 2\tau)$. The two frequency cuts f_{low} and f_{high} characterize the sensitivity of the atom interferometer as:

$$f_{\text{low}} = \frac{1}{2\pi} \frac{\sqrt[4]{6}}{T} \tag{2.48}$$

$$f_{\text{high}} = \frac{1}{2\pi} \frac{\Omega}{\sqrt{3}} \tag{2.49}$$

The phase transfer function $H(\omega)$ is a band-pass, meaning that phase noise mostly affects the sensitivity of the atom interferometer in the band between f_{low} and f_{high}. The transfer function $G(\omega)$ presents a maximum nearby frequency $f_{\text{low}} \simeq 10$ Hz, which indicates that variations of the energy state levels at that frequency impacts mostly the atom interferometer. For instance, laser power (implying light shifts) or magnetic field (implying Zeeman shifts) fluctuating at those frequencies are inconvenient. The response transfer function $F(\omega)$ is a low-pass filter meaning that the atom interferometer acts as a low-pass filter to accelerations of the reference mirror and is sensitive mainly to DC accelerations.

Imbalanced Mach-Zehnder interferometer

In the case where the Rabi frequencies are different during each pulse and the timings of the interferometer are not symmetric, the sensitivity function si modified as:

$$g(t) = \begin{cases} -\frac{\sin(\Omega_1 t)}{\sin(\Omega_1 \tau_1)}, & 0 < t \leq \tau_1 \\ -1, & \tau_1 < t \leq T_1 + \tau_1 \\ -\frac{\sin(\Omega_2 (t - T_1 - \tau_1 - \tau_2/2))}{\sin(\Omega_2 \tau_2/2)}, & T_1 + \tau_1 < t \leq T_1 + \tau_1 + \tau_2 \\ +1, & T_1 + \tau_1 + \tau_2 < t \leq T_1 + T_2 + \tau_1 + \tau_2 \\ -\frac{\sin(\Omega_3 (t - T_1 - T_2 - \tau_1 - \tau_2 - \tau_3))}{\sin(\Omega_3 \tau_3)}, & T_1 + T_2 + \tau_1 + \tau_2 < t \leq T_1 + T_2 + \tau_1 + \tau_2 + \tau_3 \end{cases} \tag{2.50}$$

where Ω_1, Ω_2, Ω_3 and τ_1, τ_2, τ_3 correspond respectively to the effective Rabi frequencies and light pulse lengths at first, second and last pulse; T_1 and T_2 are the interrogation times during respectively the first and second free-fall time part of the atom interferometer. For instance, the response of the interferometer is altered in case of laser power fluctuation or jitter in the synchronization of the sequence. Consequently, the phase sensitivity and response functions $h(t)$ and $f(t)$ are affected as well. Here the shape of the light pulses are considered perfectly squared, but are actually subject to slight latencies and noises [60]. All those effects modify the scale factor of the atom interferometer and such error on the scale factor derived as a systematic error on the measurement.

2.1.8 Scale factor of the atom accelerometer

The phase response of the atom interferometer $\Phi = \phi_{\text{kin}} + \phi_{\text{laser}}(\phi)$, where $\phi_{\text{kin}} = -gk_{\text{eff}}T^2$ and $\phi_{\text{laser}}(\phi)$ is the imprinted laser phase onto the atoms depending on the Raman laser phase ϕ, is valid assuming infinitely short Raman pulses $\tau \ll T$. Actually, the Raman pulses are defined by a finite length time $\tau \simeq 1\ \mu$s, leading to an interferometer with timings τ-2τ-τ. In that case, the effective interrogation time T_{eff} is different from T and the inertial phase is calculated with the response function $f(t)$ as:

$$\begin{aligned} \phi_{\text{kin}} &= k_{\text{eff}} \int_{-\infty}^{+\infty} g(t)(v_1 - gt)dt & (2.51) \\ &= -gk_{\text{eff}} T_{\text{eff}}^2 & (2.52) \\ &= -gk_{\text{eff}} \left(T + 2\tau\right) \left[T + \frac{2}{\Omega} \tan\left(\frac{\Omega\tau}{2}\right)\right] & (2.53) \end{aligned}$$

where Ω is the effective Rabi frequency and v_1 is the velocity of the atomic cloud at the start of the interferometer. We define the inertial scale factor as $S_{\text{kin}} = k_{\text{eff}} T_{\text{eff}}^2$.

We note that, in the case of an imbalanced interferometer where the effective Rabi frequencies are fluctuating, we deduce from Eq. 2.50:

$$\begin{aligned}\phi_{\text{kin}} \;=\; & -k_{\text{eff}} v_1 \left[\tfrac{1}{\Omega_3}\tan\left(\tfrac{\Omega_3\tau}{2}\right) - \tfrac{1}{\Omega_1}\tan\left(\tfrac{\Omega_1\tau}{2}\right)\right] \\ & -gk_{\text{eff}}\left(T+2\tau\right)\left[T + \tfrac{1}{\Omega_1}\tan\left(\tfrac{\Omega_1\tau}{2}\right) + \tfrac{1}{\Omega_3}\tan\left(\tfrac{\Omega_3\tau}{2}\right)\right. \\ & +\tau\left(\tfrac{\cot(\Omega_1\tau)}{\Omega_1} - \tfrac{2\cot(\Omega_2\tau)}{\Omega_2} + \tfrac{\cot(\Omega_3\tau)}{\Omega_3}\right) \\ & \left. -\left(\tfrac{1}{\Omega_1^2} - \tfrac{2}{\Omega_2^2} + \tfrac{1}{\Omega_3^2}\right)\right]\end{aligned} \tag{2.54}$$

where Ω_1, Ω_2 and Ω_3 are the effective Rabi frequencies of respectively the first, second and third pulses of the atom interferometer. At first order, the expression of the scale factor $S_{\text{kin}} = k_{\text{eff}} T_{\text{eff}}^2$ is valid.

During the interferometer, the Doppler frequency shift is compensated by adjusting the frequency $\omega(t)$ of the Raman lasers. A basic frequency ramp $\omega(t) = \alpha t$ implies a quadratic laser phase $\phi = \alpha t^2/2$ which naturally corresponds to the position of the atoms relative to the reference mirror. However in the context of an accelerometer, the acceleration measured a is varying in time. The Doppler frequency shift is trickier to compensate with the laser frequency $\omega(t)$ and at the same time, measuring the inertial phase $\phi_{\text{kin}} = -ak_{\text{eff}} T_{\text{eff}}^2$ with the imprinted laser phase $\phi_{\text{laser}}(\phi)$. For that reason, we choose to apply a series of phase-continuous frequency jumps ω_1, ω_2 and ω_3 to control the compensation of the Doppler shift at each pulse. For instance, the first atomic gravimeter operates with a series of phase-continuous frequency jumps [6].

Furthermore, we want to separate the Doppler shift compensation with $\omega(t)$ from the Raman laser phase ϕ to better control the imprinted laser phase $\phi_{\text{laser}}(\phi)$. For that we apply a series of phase-discontinuous frequency jumps ω_1, ω_2 and ω_3. Figure 2.10 presents the three different frequency-phase schemes which are applied to a Mach-Zehnder atom interferometer. We also mention that generating a pure frequency ramp is not physically possible and is discretised by a series of very tiny steps defined by the maximal resolution of the digital to analog converter (DAC) [61].

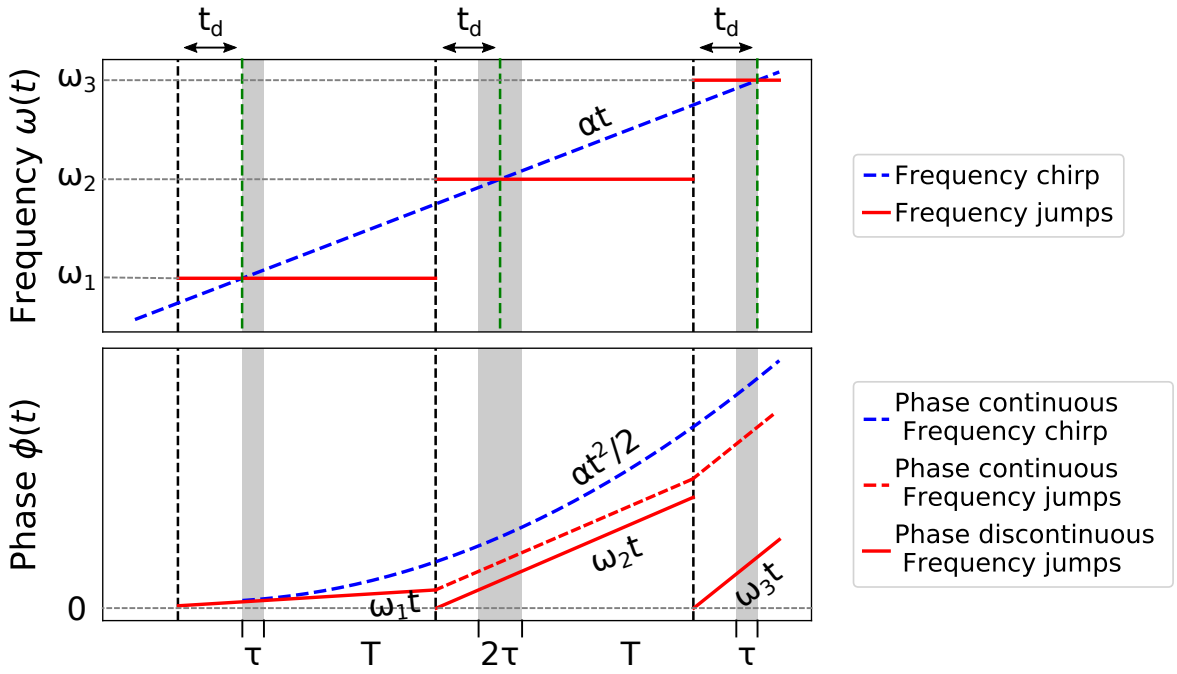

Figure 2.10: Frequency schemes of the Mach-Zehnder atom interferometer and their impact on the imprinted laser phase ϕ_{laser}.

Phase-continuous chirp

In the case of a gravimeter, the acceleration of the atoms relative to the reference mirror is $a = g$. With a chirp $\alpha = gk_{\text{eff}}$ applied as $\omega(t) = \alpha t$, the Raman laser phase ϕ generated is:

$$\phi = \frac{1}{2}\alpha t^2 = \frac{1}{2} g k_{\text{eff}} t^2 \tag{2.55}$$

The imprinted phase onto the atom interferometer from the chirp α is determined with the response function $f(t)$ from Eq. 2.39 and its integral response function from Eq. 2.43. After some algebra we find:

$$\begin{aligned} \phi_{\text{chirp}} &= \int_{-\infty}^{+\infty} f(t)\alpha dt & (2.56)\\ &= \alpha\,(T + 2\tau)\left[T + \frac{2}{\Omega}\tan\left(\frac{\Omega\tau}{2}\right)\right] & (2.57) \end{aligned}$$

From this expression, we identify the scale factor of the atom interferometer S_{chirp} determined by the effective interrogation time T_{eff} as:

$$\frac{S_{\text{chirp}}}{k_{\text{eff}}} = T_{\text{eff}}^2 = (T + 2\tau)\left[T + \frac{2}{\Omega}\tan\left(\frac{\Omega\tau}{2}\right)\right] \tag{2.58}$$

For an optimal effective Rabi frequency $\Omega\tau = \pi/2$, we can simplify the expression

as:

$$\frac{S_{\text{chirp}}}{k_{\text{eff}}} = (T+2\tau)\left[T+\frac{4\tau}{\pi}\right] \tag{2.59}$$

In the case of an imbalanced interferometer where the effective Rabi frequencies are fluctuating and assuming perfect timings of the pulses, we deduce from Eq. 2.50:

$$\begin{aligned}\phi_{\text{chirp}} \;=\; & \omega_1\left[\tfrac{1}{\Omega_3}\tan\left(\tfrac{\Omega_3\tau}{2}\right)-\tfrac{1}{\Omega_1}\tan\left(\tfrac{\Omega_1\tau}{2}\right)\right]\\ & +\alpha\,(T+2\tau)\left[T+\tfrac{1}{\Omega_1}\tan\left(\tfrac{\Omega_1\tau}{2}\right)+\tfrac{1}{\Omega_3}\tan\left(\tfrac{\Omega_3\tau}{2}\right)\right.\\ & +\tau\left(\tfrac{\cot(\Omega_1\tau)}{\Omega_1}-\tfrac{2\cot(\Omega_2\tau)}{\Omega_2}+\tfrac{\cot(\Omega_3\tau)}{\Omega_3}\right)\\ & \left.-\left(\tfrac{1}{\Omega_1^2}-\tfrac{2}{\Omega_2^2}+\tfrac{1}{\Omega_3^2}\right)\right]\end{aligned} \tag{2.60}$$

where Ω_1, Ω_2 and Ω_3 are the effective Rabi frequencies of respectively the first, second and third pulses of the atom interferometer and ω_1 is the frequency at the front of the first pulse. Assuming the Doppler frequency shift is compensated, the inertial phase and the laser phase are the same $\phi_{\text{chirp}} + \phi_{\text{kin}} = 0$. As the inertial phase, at first order we extract the scale factor as:

$$\frac{S_{\text{chirp}}}{k_{\text{eff}}} = \frac{S_{\text{kin}}}{k_{\text{eff}}} = (T+2\tau)\left[T+\frac{1}{\Omega_1}\tan\left(\frac{\Omega_1\tau}{2}\right)+\frac{1}{\Omega_3}\tan\left(\frac{\Omega_3\tau}{2}\right)\right] \tag{2.61}$$

Phase-continuous frequency jumps

Contrarily to a static gravimeter, where the inertial phase $\phi_{\text{kin}} = gk_{\text{eff}}T_{\text{eff}}^2$ is nearly constant and applying a frequency chirp to the laser phase is convenient, we apply a series of phase-continuous frequency jumps ω_1, ω_2 and ω_3 for our accelerometer. Indeed the atomic accelerometer is subjected to an arbitrary acceleration $a = g_{\text{proj}} + a_{\text{proj}}$ related to the projection of the gravitational acceleration g_{proj} and the projection of the acceleration of the mobile frame a_{proj}. By setting the frequency jumps with a pretrigger delay t_d relative to the front, the middle and the end of respectively the first, the second and the last pulse of the interferometer, we obtain the following laser phase:

$$\phi_{\text{continuous}} = \int_{-\infty}^{+\infty} g(t)\omega(t)dt \tag{2.62}$$

$$= T(\omega_2-\omega_1)+(t_d-\tau)(\omega_1-2\omega_2+\omega_3)+\frac{\omega_3-\omega_1}{\Omega}\tan\left(\frac{\Omega\tau}{2}\right) \tag{2.63}$$

If we set the two frequency jumps ω_2 and ω_3 according to the first one ω_1 as:

$$\omega_2 = \omega_1 + k_{\text{eff}} a(T + 2\tau) \tag{2.64}$$

$$\omega_3 = \omega_2 + k_{\text{eff}} a(T + 2\tau) \tag{2.65}$$

we obtain the following expression:

$$\phi_{\text{continuous}} = a k_{\text{eff}} \left(T + 2\tau\right) \left[T + \frac{2}{\Omega} \tan\left(\frac{\Omega\tau}{2}\right)\right] \tag{2.66}$$

From that expression we extract the scale factor $S_{\text{continuous}}$ relying on a series of phase-continuous frequency jumps:

$$\frac{S_{\text{continuous}}}{k_{\text{eff}}} = \left(T + 2\tau\right) \left[T + \frac{2}{\Omega} \tan\left(\frac{\Omega\tau}{2}\right)\right] \tag{2.67}$$

In the case of an imbalanced interferometer where the effective Rabi frequencies are fluctuating and assuming perfect timings of the pulses, we deduce from Eq. 2.50:

$$\begin{aligned} \phi_{\text{continuous}} = \; & a k_{\text{eff}} \left(T + 2\tau\right) \left[T + \tfrac{2}{\Omega_3} \tan\left(\tfrac{\Omega_3\tau}{2}\right)\right] \\ & + \omega_1 \left[\tfrac{1}{\Omega_3} \tan\left(\tfrac{\Omega_3\tau}{2}\right) - \tfrac{1}{\Omega_1} \tan\left(\tfrac{\Omega_1\tau}{2}\right)\right] \end{aligned} \tag{2.68}$$

where Ω_1 and Ω_3 are the effective Rabi frequencies of respectively the first and third pulses of the atom interferometer and ω_1 is the frequency applied at the first pulse. We extract the scale factor as:

$$\frac{S_{\text{continuous}}}{k_{\text{eff}}} = \left(T + 2\tau\right) \left[T + \frac{2}{\Omega_3} \tan\left(\frac{\Omega_3\tau}{2}\right)\right] \tag{2.69}$$

where Ω_3 is the effective Rabi frequency of the third pulse of the atom interferometer.

Phase-discontinuous frequency jumps

In the context of the hybridization between the classical and the quantum accelerometer, we correlate the classical acceleration into the laser phase. The scheme operation of our hybrid accelerometer, explained in Section 2.3.2, requires to apply Doppler frequency correction without affecting the phase. For that, we reset the laser phase to zero at each pulse to not imprint a phase onto the wavefunction of the atoms as illustrated on Figure 2.10. Despite the reset of the phase for each pulse, the time-integral of the frequency between pulses, directly linked to the phase, is actually not zero. The contribution on the laser phase of the phase-discontinuous frequency jumps is determined as:

$$\phi_{\text{discontinuous}} = \int_{-\infty}^{+\infty} h(t)\phi(t)dt \tag{2.70}$$

$$= (\omega_1 - 2\omega_2 + \omega_3)t_d + (\omega_3 - \omega_1)\left[\frac{1}{\Omega}\tan\left(\frac{\Omega\tau}{2}\right) - \tau\right] \tag{2.71}$$

If we set the two frequency jumps ω_2 and ω_3 according to the first one ω_1 as Eqs. 2.65, the first term of Eq. 7.5 is canceled and the expression becomes:

$$\phi_{\text{discontinuous}} = 2k_{\text{eff}}a(T + 2\tau)\left[\frac{1}{\Omega}\tan\left(\frac{\Omega\tau}{2}\right) - \tau\right] \tag{2.72}$$

Additionally, by changing the pretrigger delay of the first and last pulses with respectively:

$$t_{d1} = t_d - \left(1 - \frac{2}{\pi}\right)\tau \tag{2.73}$$

$$t_{d3} = t_d + \left(1 - \frac{2}{\pi}\right)\tau \tag{2.74}$$

we obtain the following laser phase:

$$\phi_{\text{discontinuous}} = 2k_{\text{eff}}a(T + 2\tau)\left[\frac{1}{\Omega}\tan\left(\frac{\Omega\tau}{2}\right) - \frac{2}{\pi}\tau\right] \tag{2.75}$$

With the assumption that $\Omega\tau = \pi/2$, the resulting laser phase is zero:

$$\phi_{\text{discontinuous}} = 0 \tag{2.76}$$

However, in the case of an imbalanced interferometer where the effective Rabi frequencies are fluctuating and assuming perfect timings of the pulses, we deduce from Eq. 2.50:

$$\phi_{\text{discontinuous}} = 2k_{\text{eff}}a(T + 2\tau)\left[\frac{1}{\Omega_3}\tan\left(\frac{\Omega_3\tau}{2}\right) - \frac{2}{\pi}\tau\right] + \omega_1\left[\frac{1}{\Omega_3}\tan\left(\frac{\Omega_3\tau}{2}\right) - \frac{1}{\Omega_1}\tan\left(\frac{\Omega_1\tau}{2}\right)\right] \tag{2.77}$$

where Ω_1 and Ω_3 are the effective Rabi frequencies of respectively the first and third pulses of the atom interferometer and ω_1 is the frequency applied at the first pulse.

2.2 Atom accelerometer with a reference mirror

A configuration to operate the atom interferometer as an accelerometer is to retro-reflect the counter-propagating Raman laser with a reference mirror. The inertial phase $\phi_{\text{kin}} = -k_{\text{eff}} a T_{\text{eff}}^2$ depends on the relative acceleration a of the atoms relative to the reference mirror. It includes the projection $g_{\text{proj}} = g\cos(\theta)$ of the gravitational acceleration $\vec{g}$ forming a tilt θ with the effective wavevector $\vec{k_{\text{eff}}}$ and the projection $a_{\text{proj}} = a_{\text{mob}}\cos(\phi)$ of the acceleration $\vec{a_{\text{mob}}}$ of a moving frame forming an angle ϕ with the effective wavector $\vec{k_{\text{eff}}}$.

The phase information of the output interferometer is encoded into the probability transition ratio. The response of the Mach-Zehnder interferometer is sinusoidal as:

$$P(\Phi) = \frac{N_2}{N_1 + N_2} = P_0 - \frac{1}{2} C\cos(\Phi) \tag{2.78}$$

where P_0 is the offset, C is the contrast, N_1 and N_2 are the atomic population in energy states $|g\rangle$ and $|e\rangle$, and $\Phi = \phi_{\text{kin}} + \phi_{\text{laser}}$ is the phase output of the Raman interferometer. The central fringe is defined by $\phi_{\text{kin}} = \phi_{\text{laser}}$ when the imprinted laser phase is equal to the inertial phase. The scale factor $S_{\text{eff}} = k_{\text{eff}} T_{\text{eff}}^2$, controlled with the interrogation time T, determines the sensitivity of the atom interferometer.

Recoil direction

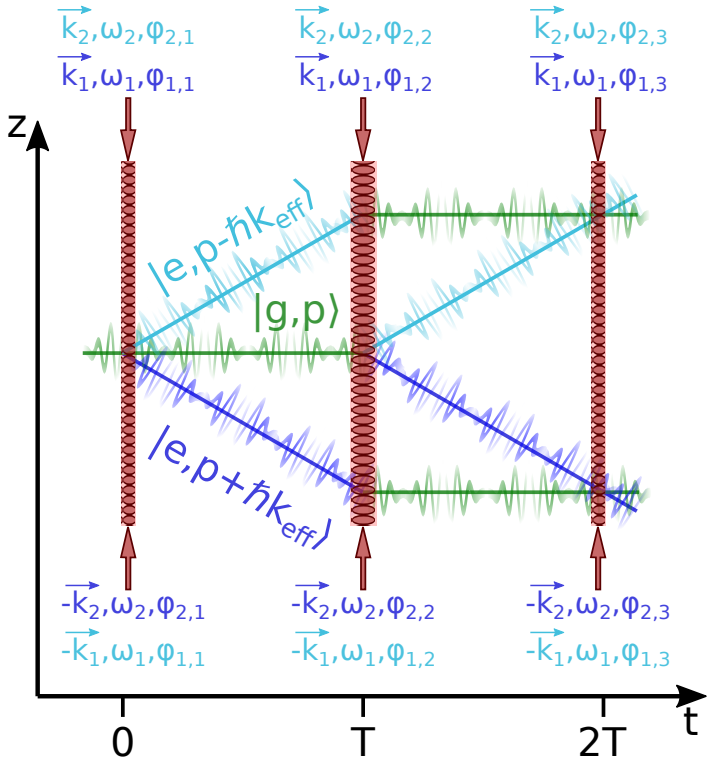

Figure 2.11: Matter-wave Mach-Zehnder interferometer with two different trajectories determined by the direction of the recoil $\pm k_{\text{eff}}$.

When the velocity of the atoms relative to the reference mirror is not zero, meaning that the momentum of the atoms $p_0 \neq 0$, we can operate single diffraction with two directions of the effective wavevector $+\vec{k_{\text{eff}}} = k_\uparrow$ or $-\vec{k_{\text{eff}}} = k_\downarrow$. The direction of the diffraction is controlled with the resonance detuning δ relying on the frequency difference of the Raman lasers $\omega_1 - \omega_2$ as $\pm\delta = \pm\omega_{\text{D}}(v) = \pm k_{\text{eff}} v$, assuming the light shifts are canceled. Figure 2.11 shows the trajectory of the atomic cloud for both cases, treated as a free particle. We can extract a "dependent" phase ϕ_{dep} and an "independent" phase ϕ_{ind} resulting from the two interferometer phases $\phi_\uparrow$ and $\phi_\downarrow$:

$$\phi_{\text{dep}} = \frac{\phi_\uparrow - \phi_\downarrow}{2} \tag{2.79}$$

$$\phi_{\text{ind}} = \frac{\phi_\uparrow + \phi_\downarrow}{2} \tag{2.80}$$

The "dependent" phase ϕ_{dep} contains the inertial phase ϕ_{kin} and reduces spatial dependant systematic shifts since a part of the path is common between the two interferometers. It also rejects some systematic effects dependant on the frequency shifts of optical transitions as first order light shifts or Zeeman shifts. The "independent"

phase ϕ_{ind} is not sensitive to the inertial phase, but extracts the systematic shifts rejected by the "dependent" phase ϕ_{dep}. The "independent" phase is interesting to isolate for studying those systematic effects.

2.3 Hybridization with classical accelerometers

The hybridization relies on data fusion between sensors with different and complementary performances and characteristics to optimize the sensing. In our case, we hybridize classical and quantum accelerometers. The classical accelerometer offers a broad-band continuous measurement with a high dynamic range, whereas the atom interferometer affords an absolute measurement with a controlled scale factor and predictable systematic shifts. The classical accelerometer is attached to the reference mirror to probe the same accelerations, precisely the gravitational acceleration and the acceleration displacement of the mirror.

2.3.1 Hybridization schemes

For an atomic gravimeter, the atom interferometer requires reduced mechanical vibrations provided by a rather calm environment. Indeed the response of the interferometer is sensitive to free fall of the atoms in the gravity field, but also to the reference mirror accelerations including parasitic mechanical vibrations which create phase noise and decrease the sensitivity. Figure 2.12(a) presents the open-loop operation of an hybrid gravimeter [29]. The hybrid gravimeter relies on the correction of the vibrations of the reference mirror, which are probed with the classical accelerometer by high-pass filtering its output. Since high dynamical range is not required, this hybrid gravimeter is optimized with a high sensitive classical accelerometer such as seismometer at the expense of low dynamical range. The resulting output of the hybrid gravimeter delivers a discrete measurement of the gravity with high sensitivity. When the direction of the measurement of the atom interferometer, determined by the effective wavevector $\vec{k_{\text{eff}}}$, is not along the vertical, the projection of the gravitational acceleration g_{proj} is probed. In addition, part of slow and continuous accelerations a_{proj} of the reference mirror which are filtered from the classical accelerometer are measured along the effective wavevector. In Chapter 5, we are referring to the hybrid gravimeter as the atom accelerometer since its operation is not possible without this hybridization for decent sensitivity and it measures as well acceleration of the mobile.

In the case of an accelerometer in strapdown operation, the relevant measurement is the acceleration of the mirror which relies on the acceleration of the moving mobile. Figure 2.12(b) describes the closed-loop operation of the hybrid accelerometer. The

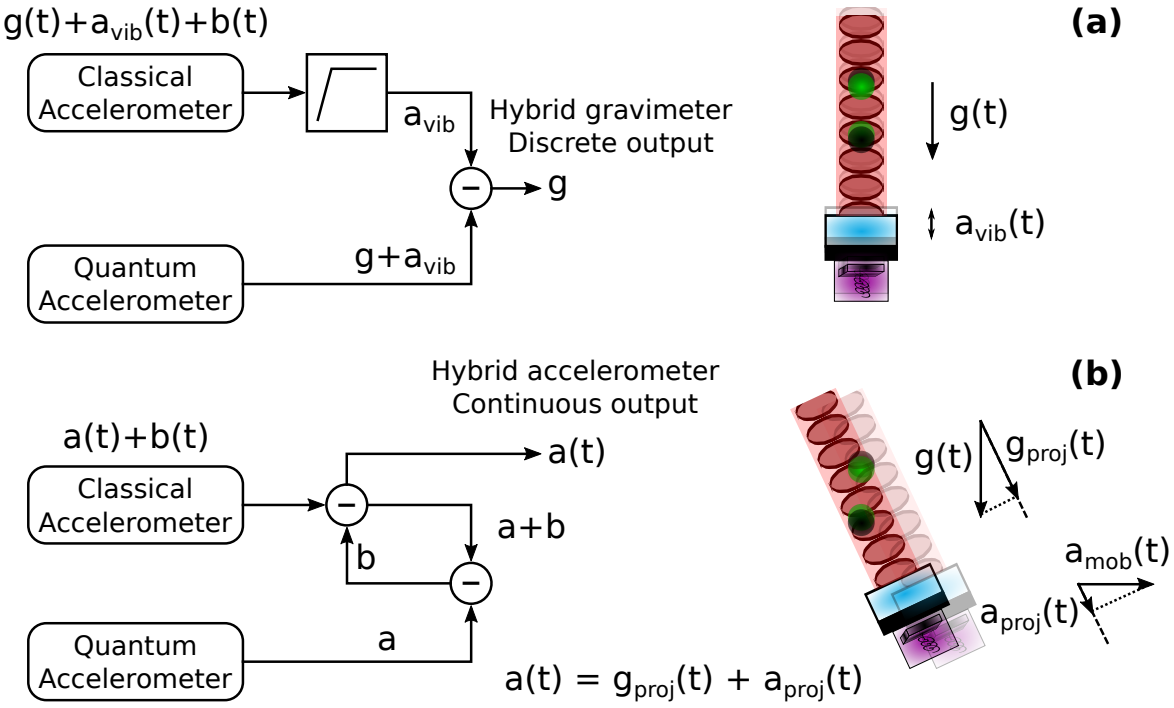

Figure 2.12: Hybridization schemes between the classical and atomic interferometer. (a) Open-loop operation of the hybrid gravimeter, labeled atom accelerometer in the manuscript, where the classical accelerometer output is filtered with a low-cut. (b) Closed-loop operation of the hybrid accelerometer where the bias of the classical accelerometer $b(t)$ is corrected by the absolute measurement of the atomic interferometer.

classical and atomic accelerometers measure the total acceleration a combining the projected gravitational acceleration g_{proj} and the projected acceleration a_{proj} of the mobile. The difference consists in the continuous measurement of the accelerations with the classical accelerometer, whereas the one from the atomic interferometer is discontinuous because of the dead-times between atomic shots. In addition, the classical accelerometer measurements include a time-dependant bias $b(t)$. The difference between the two outputs delivers an estimation of the bias $\tilde{b}$ of the classical accelerometer. When the loop is closed with the output of the classical accelerometer, the hybrid accelerometer delivers a continuous measurement of the acceleration $a(t)$. Beside the continuous measurement without dead-times, the hybrid accelerometer offers the high dynamic range of the classical accelerometer which particularly fits inertial sensing applications such as navigation. Here the long term bias drift of the classical accelerometer is not critical, but it requires a decent low-noise since it limits the sensitivity of the hybrid accelerometer output.

Additionally, for strapdown operation, the acceleration $a(t)$ of the mobile and the orientation of the atom interferometer are not known. To perform the atom interferometer, the Doppler frequency shift of the atomic transitions relative to the retro-reflected beams from the reference mirror need to be compensated. The other purpose

of the hybridization is to measure constantly and compensate during interferometry the Doppler shift with the classical accelerometer.

2.3.2 Real-time correlations

The response of the atom interferometer is sinusoidal. The sensitivity of the measurement depends on the area where the phase is measured on the fringe. It is maximal on the side of the fringe and minimal on the bottom and top. To control the phase measurement during the interferometer, it is important to retro-act in real-time the acceleration of the atoms relative to the reference mirror with the imprinted laser phase ϕ_{laser} [62]. Instead without correction, the phase measured would be random on the sinusoidal response and can degrade the sensitivity. We apply an additional laser phase ϕ_{mod} to operate the phase on a desired point of the fringe. All the laser phases are communicated to a direct digital synthesizer (DDS), which controls the phase of the Raman laser, and are applied before the last pulse of the atom interferometer.

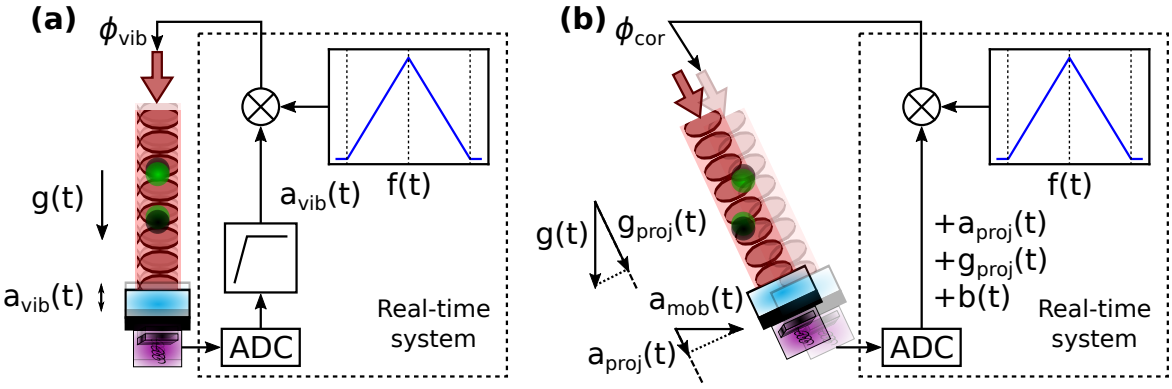

Figure 2.13: Correlation of the acceleration of the reference mirror with the atom interferometer in the case of an hybrid gravimeter (a) and an hybrid accelerometer (b). The real-time system is showed inside the dashed box including the analog-to-digital converter (ADC), the low-cut filter and the correlations calculated with the response function $f(t)$ of the atom interferometer.

Figure 2.13(a) illustrates the correlations between the classical accelerometer and the atom interferometer in the case of the hybrid gravimeter operating in open-loop. The measurements of the classical accelerometer are acquired by an analog-to-digital converter (ADC) and are low-cut filtered numerically to extract the mechanical vibrations $a_{\text{vib}}(t)$ from the reference mirror. To obtain the phase ϕ_{vib} derived from the mechanical vibrations, $a_{\text{vib}}(t)$ is correlated with the response function of the atom interferometer $f(t)$ as:

$$\phi_{\text{vib}} = \int_0^{2T} f(t) a_{\text{vib}}(t) dt \tag{2.81}$$

Here the inertial phase depends on the the gravitational acceleration g and the

vibrations of the mirror $a_{\text{vib}}(t)$ as $\phi_{\text{kin}} = -k_{\text{eff}}(g + a_{\text{vib}})T_{\text{eff}}^2$. By imprinting a phase $\phi_{\text{continuous}} = gk_{\text{eff}}T_{\text{eff}}^2$ during the interferometer with a series of phase-continuous frequency jumps, we finally obtain the imprinted laser phase equals to the inertial phase as $\phi_{\text{laser}} = \phi_{\text{continuous}} + \phi_{\text{vib}} = \phi_{\text{kin}}$.

Figure 2.13(b) illustrates the correlations between the classical accelerometer and the atom interferometer in the case of the hybrid accelerometer operating in closed-loop. Here the correlations are performed with the whole measurement of the classical accelerometer, including the projected gravitational acceleration $g_{\text{proj}}(t)$, the projected acceleration $a_{\text{proj}}(t)$ of the mobile and the bias $b(t)$, to extract a correlation phase ϕ_{cor} applied with the Raman laser as:

$$\phi_{\text{cor}} = \int_0^{2T} f(t)\left(a_{\text{proj}}(t) + g_{\text{proj}}(t) + b(t)\right) dt \tag{2.82}$$

The Doppler frequency shift compensation is applied with phase-discontinuous frequency jumps, meaning that the imprinted laser phase relies only on the correlation phase $\phi_{\text{laser}} = \phi_{\text{cor}}$. The sum of the inertial phase $\phi_{\text{kin}} = -k_{\text{eff}}(a_{\text{proj}} + g_{\text{proj}})T_{\text{eff}}^2$ and the laser phase ϕ_{laser} delivers the bias phase $\phi_b = k_{\text{eff}}bT_{\text{eff}}^2$.

2.4 Tracking algorithms

Different feedback schemes are convenient for non-linear response system to track measurements from an atom interferometer. Indeed since the response of the atom interferometer is sinusoidal and not linear, tracking the moving central fringe is critical. In addition, the bottom or top parts of the fringe are quadratic, whereas the side parts are linear at first order meaning the sensitivity is better [31]. The estimation of the phase of the central fringe is improved with mid-fringe measurements. The role of the tracking algorithm is then to control the imprinted laser phase ϕ_{laser} in order to measure the central fringe in the context of variation of the acceleration and set it on the side of the central fringe.

2.4.1 Kalman filter

In reference [14], we implement a Kalman filter to track the bias of the classical accelerometer with the atom interferometer. The experiment is achieved vertically. The algorithm is applied in post-process. It means that the experiment operates in free-running in open-loop, and the "loop is closed" numerically in post-process. Therefore, no feedback is applied to track and control the phase of the atom interferometer to address the central fringe or the mid-fringe. To apply the Kalman filter, the state

vector is defined with the fringe parameters:

$$x = \begin{bmatrix} \phi_b \\ \phi'_b \\ P_0 \\ C \end{bmatrix} \tag{2.83}$$

where P_0 is the offset, C is the contrast and ϕ'_b is the time derivative of the phase bias ϕ_b. The time derivative phase bias allows to cumulate shot-to-shot the measurements of the bias and is equivalent to the integral part of a PID controller. After each shot, the state vector is updated according to the current measurements and the state vector of the previous shot. The estimation of the fringe parameters propagates through the measurements with the Kalman filter and particularly, the Kalman filter delivers an estimation of the phase bias $\tilde{\phi}_b$ at each shot. An adaptive Kalman gain is applied to the state vector of the current measurement. This adaptive Kalman gain relies on the estimation and the uncertainty measurements of the previous state vector and also propagates between shots. The Kalman filter algorithm is further detailed in Chapter 1.

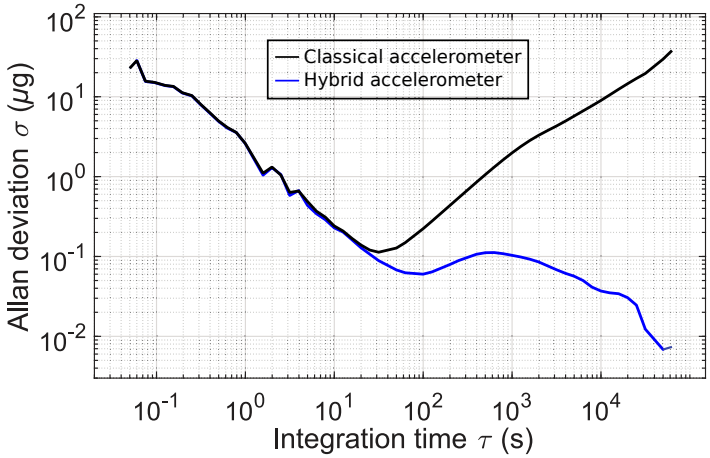

Figure 2.14: Allan deviation of the acceleration measurements from the classical accelerometer in black and the hybrid accelerometer operated with a Kalman filter in blue.

The state-space representation approach of the Kalman filter is strong because it allows versatile operations on the fringe parameters of the state vector. For instance we are able to estimate all the parameters of the state vector at each shot and their associated uncertainty. The resulting hybrid accelerometer achieves a continuous high-bandwidth measurement of the acceleration at $\simeq 100$ Hz with a bias reaching 10 ng of stability after 4×10^4 s of integration on the Allan deviation as shown on Figure 2.14.

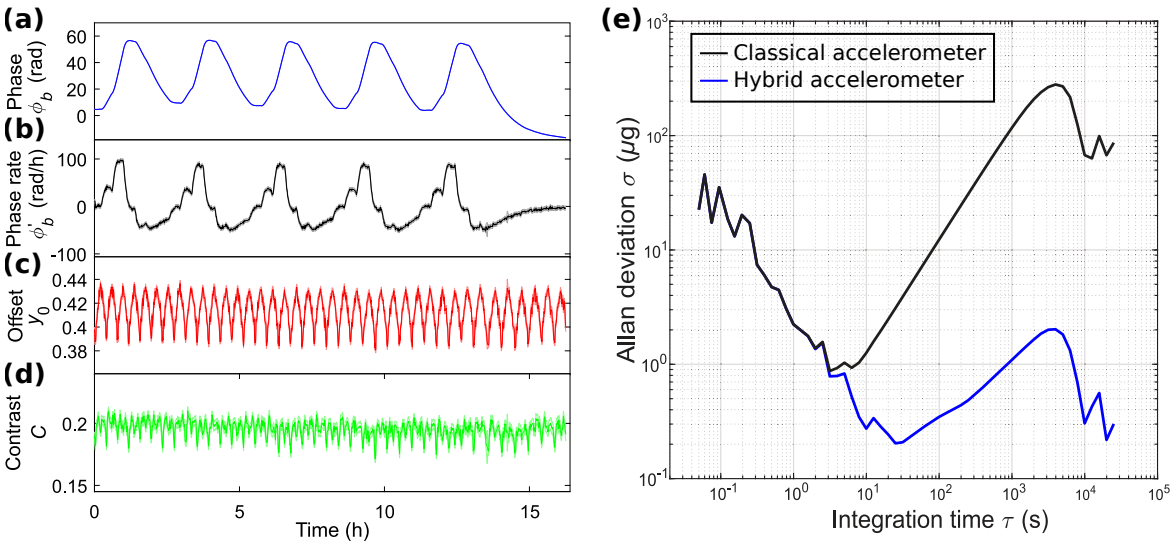

Figure 2.15: Performances of the Kalman filter in simulated harsh environment. On (a), (b), (c) and (d) each parameter of the state vector is tracked. (e) Allan deviation of the acceleration measurements from the classical accelerometer and the hybrid accelerometer.

Additionally the adaptive gain is interesting in the context of dynamical operation where the parameters can vary a lot. The parameters of the fringes have been voluntarily modulated to simulate a dynamical operation. The alteration of the phase bias ϕ_b is made by heating the classical sensor with 5 °C temperature modulation and the offset P_0 and contrast C are changed by modulating the power of the Raman lasers. Vibrations are also realized with a loud speaker fixed to the table where the experiment is standing. Within a run of 16 hours, the Kalman filter was able to track all the parameters of the state vector as shown on Figure 2.15. On the Allan deviation of Figure 2.15, the final acceleration output of the hybrid accelerometer gains 2 orders of magnitude on the stability of the bias compared to the classical accelerometer.

2.4.2 Mid-fringe lock algorithm

The mid-fringe lock algorithm relies on the optimization of the sensitivity of the measurements by proposing two different schemes: the two-points and three-points fringe tracking [31, 43]. A modulation phase $\phi_{\text{mod}} = +\pi/2$, $-\pi/2$ or 0 is applied to the laser phase ϕ_{laser}. The two-point fringe tracking, where $\phi_{\text{mod}} = \pm\pi/2$, focuses on the linear part of the fringe and allows to estimate the phase and the offset of the atom interferometer output. The three-point fringe tracking adds the bottom of the fringe with $\phi_{\text{mod}} = 0$ to estimate in addition the contrast.

Open-loop operation

The open-loop hybridization between the classical and atom interferometer is described in Sec. 2.3. The "open-loop" means that the acceleration measured by the atom interferometer is not feedbacked to the output of the classical accelerometer as the hybrid gravimeter depicted on Figure 2.12. Here we present the detailed operation with the mid-fringe lock algorithm. This protocol is adapted for probing the gravity in static situation since it provides a discrete and low bandwidth output acceleration. For instance we are using the open-loop operation in Chapters 5 and 6 to study and characterize respectively a vertical accelerometer and the 3-axis accelerometer. On the 3-axis accelerometer, each tilted axis is measuring the projection of the gravitational acceleration $g_{\text{proj}}(t)$ along its respective effective wavevector $\vec{k_{\text{eff}}}$.

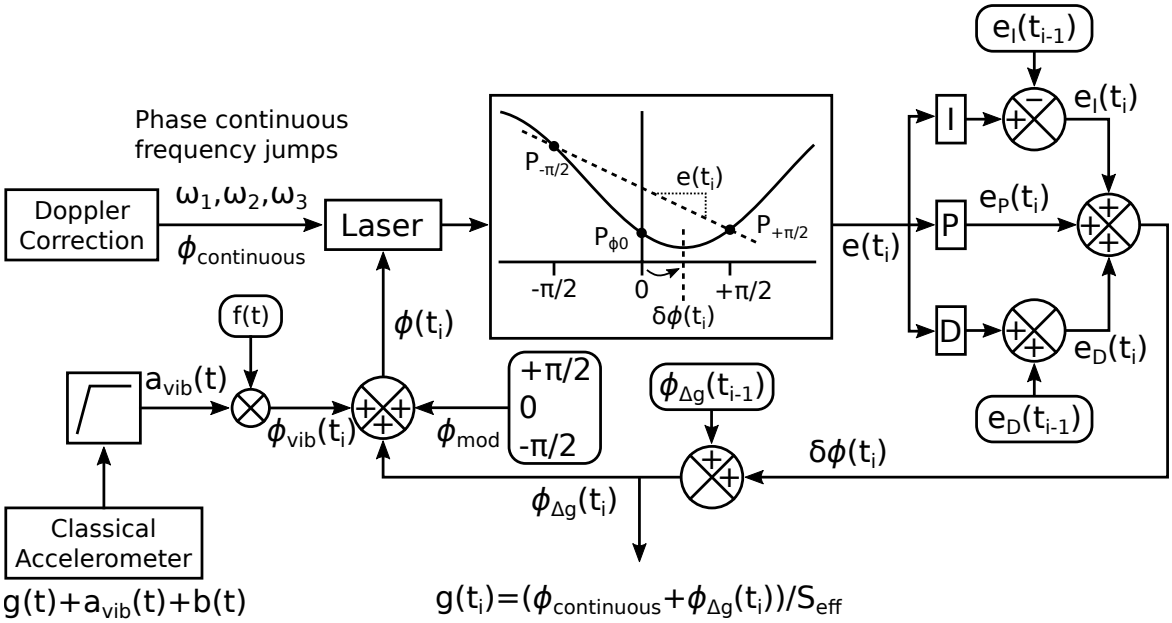

Figure 2.16: Mid-fringe lock algorithm in open-loop operation

Figure 2.16 presents the mid-fringe lock algorithm in open-loop operation. The RF chain generates an arbitrary series of phase-continuous frequency jumps ω_1, ω_2 and ω_3 to compensate the Doppler frequency shift so that the laser phase $\phi_{\text{continuous}}$ is:

$$\phi_{\text{continuous}} \approx g(t) k_{\text{eff}} T_{\text{eff}}^2 \tag{2.84}$$

Here the gravitational acceleration $g(t)$ (or the projected gravitational acceleration $g_{\text{proj}}(t)$) is varying over time. Indeed $g(t)$ and $g_{\text{proj}}(t)$, respectively in the case of a vertical accelerometer and tilted accelerometer, are subjected mostly respectively by the tides and the fluctuation of the tilt. In addition, any systematic shift varying in time probed by the atom interferometer will shift the fringes and can be characterized. The aim of the algorithm is to track and feedback a phase $\phi_{\Delta g}$ corresponding to the

remaining phase shift of the atom interferometer which provides the measurement of the time-varying gravitational acceleration $g(t)$ (or projected gravitational acceleration $g_{\text{proj}}(t)$) as:

$$g(t) = \frac{\phi_{\text{continuous}} + \phi_{\Delta g}(t)}{S_{\text{eff}}} \tag{2.85}$$

The classical accelerometer fixed to the reference mirror extracts parasitic vibrations $a_{\text{vib}}(t)$ by filtering slow accelerations (the gravity $g(t)$ and the biases $b(t)$). The corresponding parasitic shift from the vibrations $\phi_{\text{vib}}(t_i)$ is computed with the response function of the interferometer $f(t)$. Additionally, we generate a modulation $\phi_{\text{mod}} = +\pi/2$, $-\pi/2$ or 0 to locate the measurement of the interferometer respectively on the ascending linear region, descending linear region or bottom region of the fringe. The phase $\phi(t_i) = \phi_{\text{vib}}(t_i) + \phi_{\text{mod}} + \phi_{\Delta g}(t_i)$ is added before the last pulse of the atom interferometer. The laser phase imprinted onto the atom interferometer applied at $(i)^{\text{th}}$ shot is then:

$$\phi_{\text{laser}}(t_i) = \phi_{\text{continuous}} + \phi_{\text{vib}}(t_i) + \phi_{\text{mod}} + \phi_{\Delta g}(t_i) \tag{2.86}$$

The two-point modulation scheme generates an error signal $e(t_i)$ of the phase at the i^{th} shot:

$$e(t_i) = \frac{1}{C}(P_{-\pi/2}(t_i) - P_{+\pi/2}(t_{i-1})) \tag{2.87}$$

where C is the contrast of the fringe, $P_{+\pi/2}(t_{i-1})$ and $P_{-\pi/2}(t_i)$ are respectively the probability transitions of the $(i-1)^{\text{th}}$ shot with $\phi_{\text{mod}} = +\pi/2$ and the i^{th} shot with $\phi_{\text{mod}} = -\pi/2$. The algorithm requires to initialize for the first shot the phase $\phi_{\Delta g}(t_0)$, the offset $P_0(t_0)$ and the contrast $C(t_0)$ of the fringe. The estimation of the offset and the contrast are updated at each shot as:

$$\tilde{C}(t_i) = |P_{-\pi/2}(t_i) + P_{+\pi/2}(t_{i-1}) - 2P_{\phi_0}(t_{i-2})| \tag{2.88}$$

$$\tilde{P}_0(t_i) = \frac{P_{-\pi/2}(t_i) + P_{+\pi/2}(t_{i-1})}{2} \tag{2.89}$$

where $P_{\phi_0}(t_{i-2})$ corresponds to the probability transitions of the $(i-2)^{\text{th}}$ shot with $\phi_{\text{mod}} = 0$. It means that the three-point modulation scheme is required to track the contrast. Instead the contrast is taken as constant $C = C(t_0)$ in Eq. 2.87 and acts as a fixed gain on the error signal. We set the parameters P, I and D as respectively the proportional, integrative and derivative gains of the PID corrector. The error signal is treated as follow by the PID corrector:

$$e_P(t_i) = Pe(t_i) \tag{2.90}$$
$$e_I(t_i) = Ie(t_i) + e_I(t_{i-1}) \tag{2.91}$$
$$e_D(t_i) = De(t_i) - e_D(t_{i-1}) \tag{2.92}$$

The error signal treated by the PID corrector gives an estimate of the phase shift $\delta\phi(t_i)$ of the atom interferometer at the i^{th} shot:

$$\delta\phi(t_i) = e_P(t_i) + e_I(t_i) + e_D(t_i) \tag{2.93}$$

The cumulated phase shift is updated by adding the current estimate of the phase shift as:

$$\phi_{\Delta g}(t_i) = \phi_{\Delta g}(t_{i-1}) + \delta\phi(t_i) \tag{2.94}$$

The cumulated retroaction $\phi_{\Delta g}(t_i)$ guarantees the fringe of the interferometer to be centered and optimizes the operation by setting the modulations $\phi_{\text{mod}} = \pm\pi/2$ on the most sensitive part of the fringe. To better estimate the phase shift, it is convenient to measure the phase shift with the trajectory of the two atom interferometer defined by effective wavevectors $\pm k_{\text{eff}}$ ($k_\uparrow$ and $k_\downarrow$). It enhances the rejection of systematic biases by averaging the phase shifts over two trajectories as:

$$\phi_{\Delta g}(t_i) = \frac{\phi^{\uparrow}_{\Delta g}(t_i) - \phi^{\downarrow}_{\Delta g}(t_{i-1})}{2} \tag{2.95}$$

It requires different set of estimation for the phases $\phi^{\uparrow\downarrow}_{\Delta g}$, the offsets $\tilde{P_0}^{\uparrow\downarrow}$ and the contrasts $\tilde{C}^{\uparrow\downarrow}$ of the $k_\uparrow$ and $k_\downarrow$ parameters fringe and parameters for the proportional $P^{\uparrow\downarrow}$, integrative $I^{\uparrow\downarrow}$ and derivative $D^{\uparrow\downarrow}$ gains of the $k_\uparrow$ and $k_\downarrow$ PID correctors.

Closed-loop operation

The closed-loop operation relies on the measurement and the tracking of the bias of the classical accelerometer with the atom interferometer. This bias is feedbacked to the output of the classical accelerometer and allows to extract a high-bandwidth continuous acceleration bias-free without dead-times. We are using the closed-loop operation on the 3-axis hybrid accelerometer in Chapter 7.

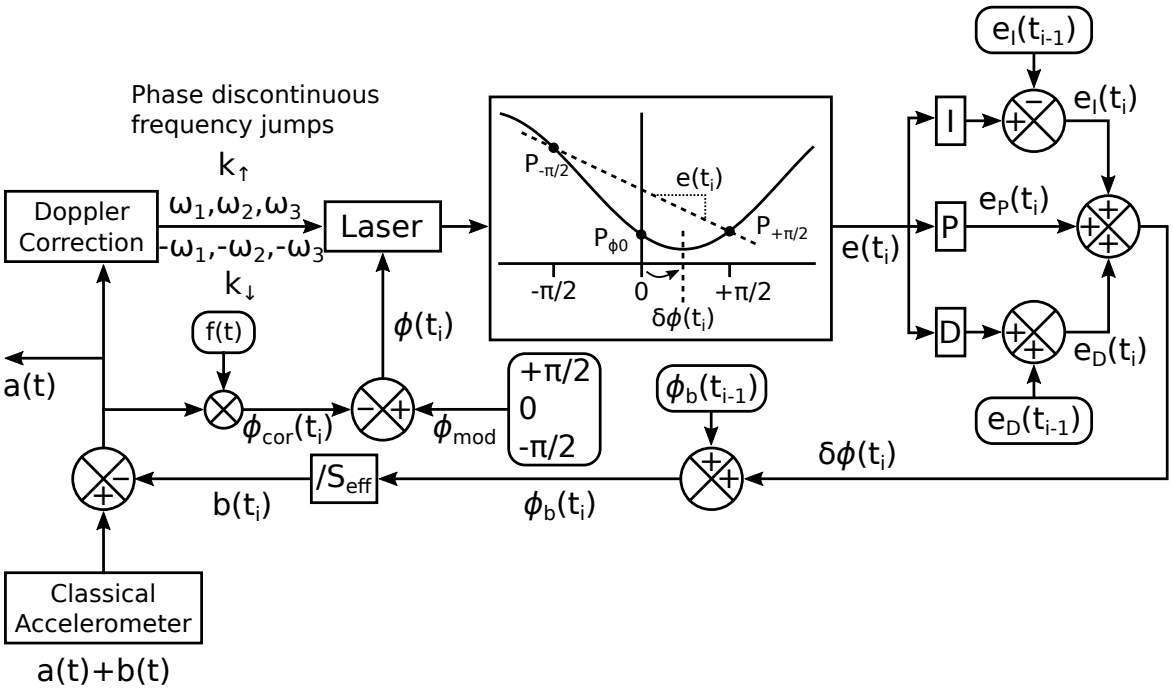

Figure 2.17: Mid-fringe lock algorithm in closed-loop operation

Figure 2.17 presents the closed-loop operation of the mid-fringe lock algorithm. The classical accelerometer is used to compensate the Doppler shift of the atomic transitions with a series of phase-discontinuous frequency jumps at each pulse. The phase imprinted onto the atoms from this correction is zero $\phi_{\text{discontinuous}} = 0$. The measurement of the classical accelerometer, containing the acceleration $a(t)$ and the bias $b(t)$, computes a correlation phase $\phi_{\text{cor}}(t_i)$ at the i^{th} shot with the response function $f(t)$. When the correlation phase is applied to the atom interferometer (before the last pulse), the remaining phase shift of the atom interferometer is the measurement of the bias $b(t_i)$ since the inertial phase measured by the atom interferometer contains only the acceleration as $\phi_{\text{kin}} = -k_{\text{eff}} a T_{\text{eff}}^2$.

The phase shift of the atom interferometer corresponds to the bias of the classical accelerometer and is noted $\phi_b(t_i)$ at the i^{th} shot. The estimation of the phase shift is governed by the error signal $e(t_i)$ defined by the two atom interferometers trajectory $k_\uparrow$ and $k_\downarrow$ as:

$$e(t_i) = \frac{e_\uparrow(t_i) - e_\downarrow(t_{i-1})}{2} \tag{2.96}$$

The error signal is treated by the PID corrector to obtain the correction phase shift $\delta\phi(t_i)$. The bias phase $\phi_b(t_i)$ is given by the cumulated phase shift of the atom interferometer:

$$\phi_b(t_i) = \phi_b(t_{i-1}) + \delta\phi(t_i) \tag{2.97}$$

The bias of the classical accelerometer $b(t_i)$ is obtained by computing the bias phase $\phi_b(t_i)$ with the effective scale factor S_{eff}. The bias is subtracted from the classical accelerometer output to deliver a bias-free measurement of the acceleration:

$$a(t) = a(t) + b(t) - b(t_i) \tag{2.98}$$

2.4.3 Sequential 3-axis hybrid accelerometer

In our apparatus, we choose to implement the two-point mid-fringe lock algorithm. It relies on a feedback loop with a proportional integrator (PI) corrector. The time-derivation correction (PID) can complete the correction but is not necessary for steady-state measurements. Indeed, it helps to decrease the time to lock the algorithm at the beginning when the bias is not estimated. The two-point mid-fringe lock algorithm estimates the phase and the offset of the fringes, whereas the three-point one estimates the contrast in addition. This three-point one is useful if the contrast is varying a lot. However if the contrast does not fluctuate strongly, the two-point mid-fringe lock algorithm is better since the sensitivity of the third point ($\phi_{\text{mod}} = 0$) is reduced and is not necessary. In fact the contrast acts as a global gain on the error signal and influences the sensitivity but is not critical for stability.

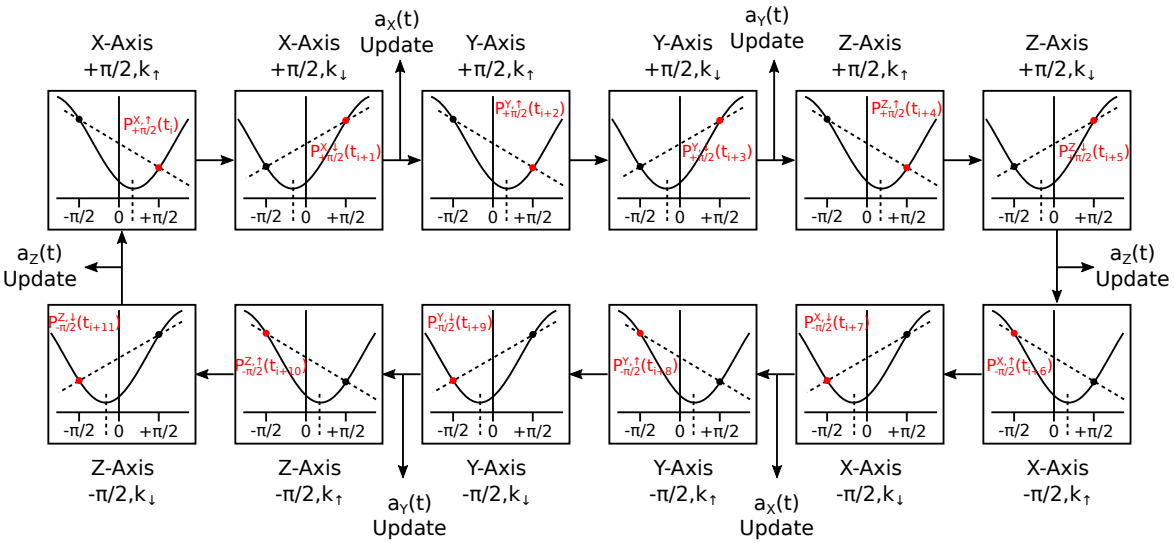

Figure 2.18: Operation of the sequential 3-axis hybrid accelerometer.

Figure 2.18 presents the operation of the 3-axis hybrid accelerometer. We alternate measurements between the three axes X, Y, Z, the two-point phase modulation $\phi_{\text{mod}} = \pm\pi/2$ and the trajectory of the atom interferometer $k_{\uparrow\downarrow}$ controlled with the sign of the Doppler frequency shift correction $\pm\omega_1$, $\pm\omega_2$ and $\pm\omega_3$. It requires 6 shots to measure the phase shift on each axis, $\phi_{\Delta g}$ in the case of open-loop operation and ϕ_b in the case of closed-loop operation. The total acceleration vector is defined as the vectorial sum of

the acceleration from each axis. Each time the acceleration bias on one axis is updated, every 2 shots, the norm of the total acceleration vector is updated as:

$$\|\mathrm{a}(t)\| = \sqrt{\mathrm{a_x}(t)^2 + \mathrm{a_y}(t)^2 + \mathrm{a_z}(t)^2} \tag{2.99}$$

In our apparatus, we choose to implement the mid-fringe lock rather than a Kalman filter. The mid-fringe lock is easier and straightforward to achieve since it relies on a simple feedback loop with a PI corrector. The Kalman filter goes further by estimating the uncertainties on each variable. In experiment from [14], real-time compensation of the phase was not implemented and the phase was running freely. Some points are located on non-linear parts of the fringes and are not optimized for sensitivity. With the real-time implementation, one can imagine combine the Kalman filter algorithm, where the adaptive Kalman gain corrector tracks and estimates the parameters of the fringe and their uncertainties, with the mid-fringe lock algorithm where the modulation phase $\phi_{\mathrm{mod}} = \pm\pi/2$ operates on the most sensitive part of the fringe.

Conclusion

We presented theoretical and practical tools for atom interferometry. The strength of the atom accelerometer relies on the accuracy of its scale factor and quantifying transfer function. A classical accelerometer, suffering from large time-varying biases, benefits from the absolute measurement of the quantum accelerometer by hybridization. Meanwhile, the classical accelerometer offers a continuous acceleration output essential to achieve interferometry for mobile operation.

We propose a tracking algorithm capable of tracking and rejecting the bias of the classical accelerometer. Despite a non-linear sinusoidal output, the tracking algorithm, coupled with a real-time hybridization with the classical accelerometer, allows to operate the atom interferometer on the linear part, favoring the sensitivity. Finally, we proposed a procedure to operate the 3-axis hybrid accelerometer to deliver a multi-axis continuous high-bandwidth measurement of the acceleration without biases.

Chapter 3

3-axis accelerometer apparatus

This chapter depicts the apparatus of the 3-axis hybrid accelerometer. It includes the description of the sensor head design, the classical accelerometers, the control system and the platforms dedicated to calibration and mobile operations. The laser system and the RF source are treated in a separate dedicated Chapter.

Contents

3.1 Design architecture 80

3.2 Sensor head 82

3.2.1 Vacuum chamber 83

3.2.2 Magnetic fields 83

3.2.3 Free-space optics 85

3.2.4 Liquid-crystal retardance waveplates 87

3.2.5 Fluorescence detection system 89

3.3 Classical accelerometers 90

3.3.1 Characteristics of the classical accelerometers 90

3.3.2 Temperature calibration 92

3.3.3 Triad calibration 94

3.4 Control system 97

3.4.1 Hardware elements 97

3.4.2 Software elements 99

3.4.3 Real-time system 100

3.4.4 Experimental sequence 101

3.4.5 Detection and signal extraction 103

3.5 Mobile and calibration apparatuses 105

3.5.1 Marble table 105

3.5.2 Rotational platform 105

3.5.3 Mobile platform 107

Introduction

A cold atom interferometer is an instrument with a high level of complexity. It is composed of an ultra-stable and low noise laser system which generates two phase coherent tunable frequencies, a non-magnetic vacuum system with a good optical access, a pure magnetic environment with shield and coils. Additionally the complete experimental sequence requires six beams for the cooling and trapping, one beam per axis for the interferometer (3 in total for a 3 axis measurement), one beam for state preparation, one for detection. For each function, it requires a specific frequency, power, polarization. It implies a strong complexity on the laser system, the vacuum chamber and the control system.

During the last 15 years, different techniques to simplify the system have been developed and tested. It is possible to generate all the required beams from a single one with the help of a pyramidal reflector [63]. This architecture is very suitable for atomic gravimeters and is at heart of the commercial systems developed by the start-up μQuans [20].

Small-sized apparatuses for atom interferometers represent a decisive challenge to transfer such technology into industry for transportable and mobile applications. A number of research teams have now developed transportable cold-atom gravimeters, meaning that the setup can be transported from one test site to another and installed within a few hours. However, these systems cannot be operated in movement and usually require a stable and quiet environment to operate at their nominal performances. AOsense [19] provides commercial products, as well as μQuans, in relatively compact packages weighting respectively 20 kg and 100 kg. In contrast to a transportable experiment, a very few mobile experiments are now truly mobile. The most mature mobile setups are the ICE double species experiment at LP2N and the ONERA mobile gravimeter, described briefly in Chapter 1.

In this chapter, we present the apparatus of our 3-axis hybrid accelerometer. The apparatus we present is designed specifically to realize a compact, three-axis atomic accelerometer for mobile applications and is able to operate in any orientation. Our apparatus is compatible for inertial navigation by offering an hybridization between classical and atom accelerometers along three directional axes. The quantum system is based on standard cold-atom technology and light-pulse atom interferometry using Raman transitions between two internal atomic states. It relies on the ability to produce all the steps required for 3-axis atom interferometry, including the cooling, trapping and interferometry, with the same three collimated beams. Furthermore, our apparatus uses the same laser system for all the stages of the experimental sequence,

which is possible because the laser source is completely agile. The laser system is not discussed in this chapter, but treated in detail in Chapter 4. When I began to work on the project, the sensor head was already built and under vacuum.

3.1 Design architecture

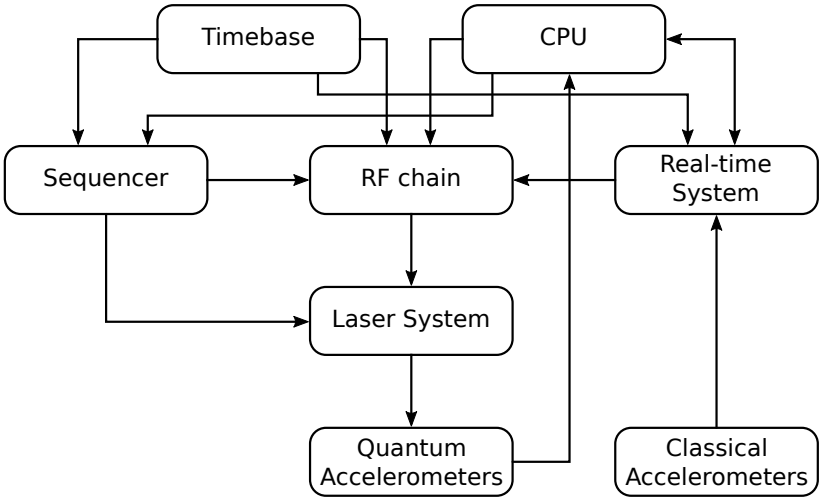

Figure 3.1: Block diagram of the 3-axis hybrid accelerometer design architecture. Arrows indicate the flow of information between hardware elements.

The 3-axis hybrid accelerometer design architecture consists of a number of hardware elements that communicate according to the block diagram shown in Fig. 3.1. The main hardware elements consist of a master timebase unit for synchronizing all subsystems to the same clock; a central processing unit (CPU); a sequencer for precise hardware timing and control; a radio-frequency (RF) chain for precise generation and control of specific radio and microwave frequencies required for the sensor head and laser system; a real-time (RT) control system for the hybridization between quantum and classical sensors; a laser system for the generation and control of a coherent light source used to cool and interrogate the atoms; quantum accelerometers (i.e. the three axes of the cold-atom sensor head); and classical accelerometers.

The operational principle of this architecture is as follows. The master timebase is continuously distributed to the sequencer, the RF chain and the RT system. The CPU first generates a matrix of timing and signal values that define the experimental sequence required to make an acceleration measurement from the 3-axis hybrid accelerometer. This matrix is sent to the sequencer, which converts it to a sequence of time-varying physical signals (both analog and digital). At the same time, the CPU initializes the RF chain and the RT system for the measurement via serial communication. Next, the sequencer triggers applicable hardware channels to output the predefined sequence, and these signals are sent to specific components in the RF chain, the RT system, and the laser system, which then act directly on the atoms via a sequence of optical pulses.

During the sequence, the RT system continuously acquires measurements from the classical accelerometers, which are attached to the reference mirrors of the atom

interferometers. They measure the acceleration of the reference frame in which the atomic motion is measured. At specified time intervals (corresponding to when the atoms are being interrogated), this system computes a correction that is applied to the atoms via the RF chain and the laser system at the end of the sequence.

To give a concrete example, the RF chain contains various switches and attenuators that receive digital and analog signals, respectively. These signals control the temporal profile of RF power entering an acousto-optic modulator that resides within the laser system, which controls the temporal profile of laser pulses that interact with the atoms. The RF chain and the laser system are studied specifically in Chapter 4.

Each quantum accelerometer, along a particular direction: X, Y, or Z, outputs an optical signal that is captured by a detection system. This signal is digitized and processed by the CPU to obtain a measurement of the acceleration. In the latter case, the bias of the classical accelerometer is corrected by comparison with the acceleration measured by the quantum accelerometer. This sequence of operations occurs once per measurement cycle, which is approximately 1 s. A minimum of two measurement cycles are required to obtain one acceleration component, hence the full acceleration vector can be obtained in 6 measurement cycles, or 6 s. However, in order to reject certain biases present in the quantum sensors, we performs four measurement cycles per axis, and hence one measurement of the full acceleration vector every 12 cycles.

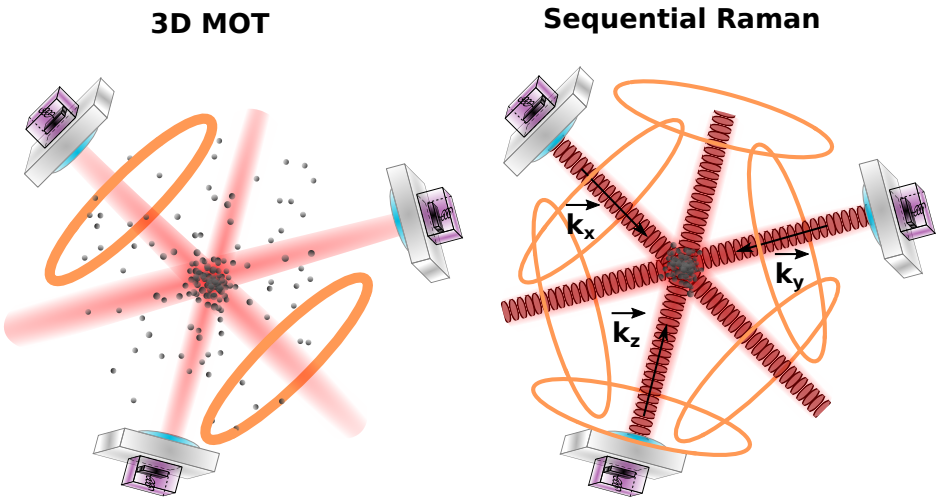

Figure 3.2: Illustration of the sensor head design where the laser beams operating the 3D MOT and the Raman interferometers are the same.

The innovative design of our sensor head is the operation of the 3D MOT and the Raman interferometry with the same retro-reflected laser beams as illustrated in Fig. 3.2. The 3D MOT is loaded directly from ambient vapor without 2D MOT preparation stages. Besides the cycling rate loss from missing 2D MOT stage, this architecture provides a much simpler design and does not need extra vacuum cell nor

lasers. Here the Raman transitions are achieved with a retro-reflected laser beam along a single axis where the axis is quantized with dedicated magnetic coils. The Raman interferometers can operate individually and sequentially on each axis. The switch between MOT and Raman beam is controlled with the polarization. An optical fiber switch commands the distribution of the laser beam for the 3D MOT or individual axis for Raman transitions.

3.2 Sensor head

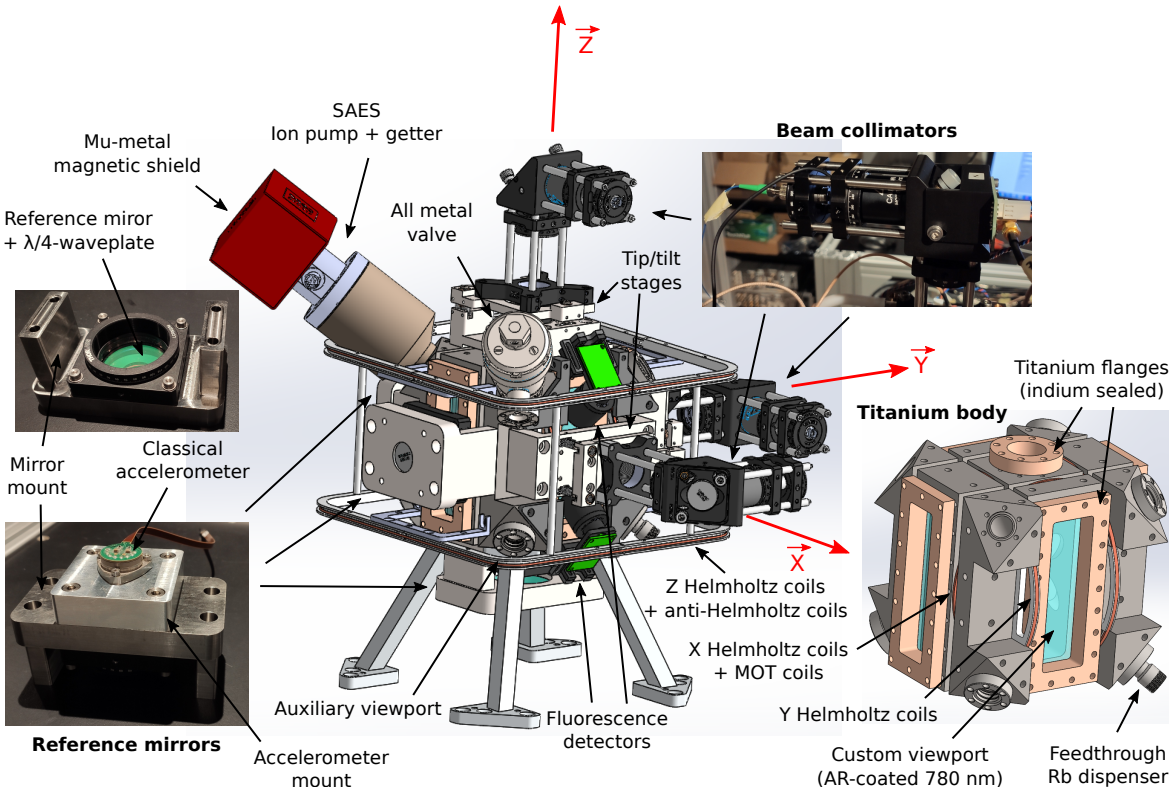

Figure 3.3: Description of the sensor head of the 3-axis hybrid accelerometer.

Figure 3.3 describes the sensor head of the 3-axis hybrid accelerometer. Three mutually-orthogonal laser beams are aligned through the central region of the chamber, and are retro-reflected by 2-inch-diameter reference mirrors where classical accelerometers are attached. These beams are ultimately used to cool, trap and interrogate 87-rubidium atoms. To trap the atoms in a MOT, a magnetic gradient of approximately 10 Gauss/cm is applied in the central region by a pair of anti-Helmholtz coils that are wound directly on the chamber body. Control of the DC magnetic field is facilitated by three pairs of mutually-orthogonal Helmholtz coils, two of which are wound on the chamber, and one square set of coils is attached externally on the vertical axis. These three pairs of coils are used to cancel the background magnetic field within the central

region, as well as to introduce a controlled bias field during the state preparation and interrogation stages. Detectors composed of photodiode detect the induced fluorescence of the atomic cloud at the end of the sequence to extract the measurement signal.

3.2.1 Vacuum chamber

The main body of the system was machined from a block of forged titanium (TA6V grade 5). This material has a high strength-to-weight ratio and has good vacuum properties. Compared to other high-strength materials like stainless steel, titanium is entirely non-magnetic. In addition, due to its low magnetic permeability (1.26×10^{-6} H/m), magnetically-induced Eddy currents are highly suppressed within the metal. These properties make titanium an ideal choice for vacuum systems used to produce cold atoms, which are extremely sensitive to inhomogeneous magnetic fields.

The vacuum chamber is sealed with a combination of copper gaskets on the CF16 316 stainless steel flanges for the auxiliary viewports and indium wire on the custom titanium flanges served to increase strength for sealing. A 316 stainless steel all-metal valve facilitates the initial pump out of the system with a commercial pumping stage. This valve is sealed and the internal pressure is maintained below 3×10^{-10} mbar by a commercial non-evaporable getter (NEG) + ion pump combination (SAES NEXTorr D100-5, 100 L/s H_2 pumping rate). A small mu-metal magnetic shield is installed around the ion pump magnet to limit its field strength within the vacuum chamber. Two alkali metal dispensers (one primary, one backup) are installed behind electrical feedthroughs on the lower-diagonal stainless steel flanges (only one is shown on the Fig. 3.3). Rubidium vapor is ejected into the vacuum by heating them with an electrical current (typically 4-5 A). Six custom-designed viewports (and their associated titanium flanges) give optical access to the chamber's interior. These viewports are rated with optical qualities of $\lambda/8$ flatness, 20/20 scratch/dig, 3 arcmin parallelism and are anti-reflection coated for our operational wavelength of 780 nm.

3.2.2 Magnetic fields

A pair of anti-Helmholtz coils is used to generate a gradient magnetic field in order to trap the atoms into a MOT. Figure 3.4 depicts the MOT coils located along the X-axis of the sensor head. Each coil is composed of $\simeq 90$ turn loops of 0.8 mm diameter copper wires (electrical resistivity of 1.68×10^{-8} Ω·m). They form respectively a disk of 63 mm inner radius and 75 mm outer radius with 5 mm of thickness and are separated by 58 mm. This geometry allows to produce theoretically a magnetic field gradient of 2 Gauss/cm/A at the center of the chamber. A MOSFET transistor circuit is used to

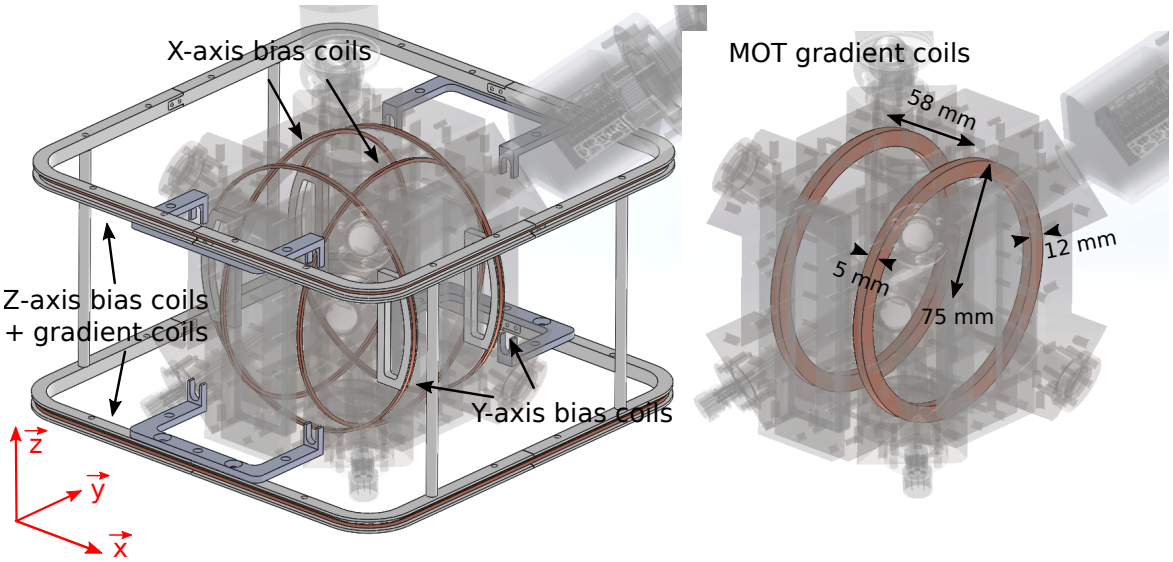

Figure 3.4: CAD view of the bias coils on the left and the MOT gradient coils on the right.

switch rapidly the current feed of the MOT coils with a TTL command. The circuit is composed of two diodes in opposite direction which are in parallel to the coils in order to generate a large back electro-magnetic field. The decay time of the magnetic field is then decreased to a few tens of μs [64].

The entire science chamber is installed inside a cube-shaped mu-metal shield with a base size of 660x660 mm^2 for a height of 515 mm (not shown in the figures). It is composed of two separated parts which are nested together and weighting individually 10 kg (bottom part) and 30 kg (upper part). This shield attenuates the ambient magnetic field, and simplifies the field control around the atoms when the system is in motion. Without this shield, active control of the magnetic field would be necessary in a dynamic environment, where the direction and magnitude of the field changes according to the system's orientation.

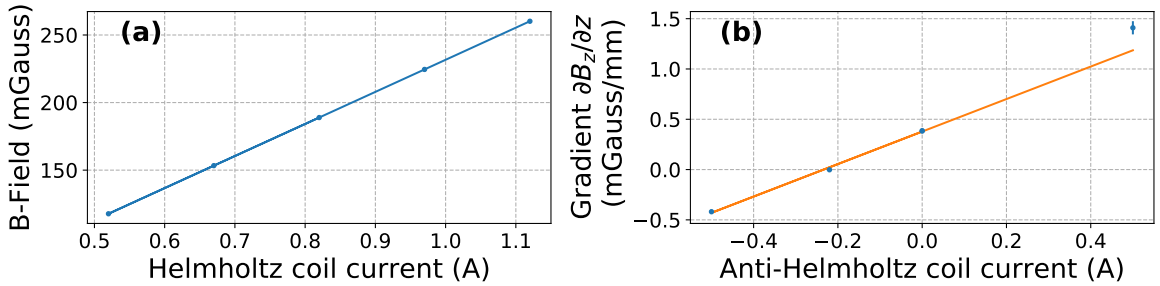

Figure 3.5: Magnetic field response of the current feeding Helmholtz (a) and anti-Helmholtz (b) coils on Z-axis. The orange plot is a linear fit. The magnetic field is measured with co-propagating Raman transitions spectroscopy.

As shown in Figure 3.4, the magnetic field is controlled on each axis with a dedicated pair of Helmholtz coils. They enable to cancel ambient non-zero magnetic field and

generate a bias field to define the quantization axis. Figure 3.5(a) presents the bias magnetic field produced by the pair of Helmholtz coil on Z-axis depending on the current injected. Here, the magnetic field is measured with a Raman spectroscopy where co-propagating Raman transitions are used to scan Zeeman frequency shift of the sub-magnetic levels sensitive to magnetic field. We observe a linear response of the field induced. An additional pair of anti-Helmholtz coils is set to cancel the magnetic field gradient along the Z-axis. Figure 3.5(b) displays the magnetic field gradient along the Z-axis depending on the electric current fed into the anti-Helmholtz coils. The trend is linear nearby the area where the magnetic field gradient is canceled, which is convenient for fast calibration. For the 3-axis atom interferometer study in Chapter 6, we calibrate the magnetic field gradient along the Z-axis when the sensor head is vertical. Then the gradient is not canceled correctly along each axis and for random orientation, nevertheless it helps to reduce it. One can imagine setting anti-Helmholtz coils along each axis to better control the gradient for 3-axis measurements.

3.2.3 Free-space optics

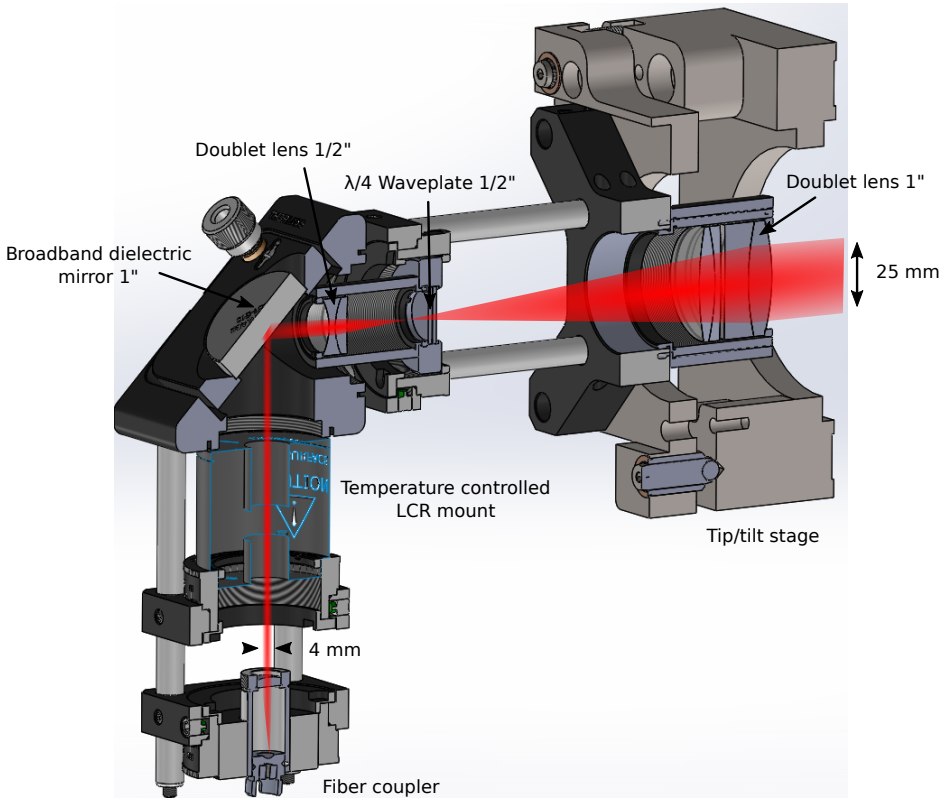

Figure 3.6: CAD side cut of the collimator used on each axis to form the optical beams addressing the atomic cloud.

The light is distributed onto the sensor head with a splitter/combiner stage described in Chapter 4. The light is sent through three custom beam collimators which expand

and collimate the light output from the fibers with a beam waist of 4 mm at the entrance to a beam waist of $\simeq$ 25 mm. Figure 3.6 shows the design of a collimator assembly, which also contains a tip/tilt stage to facilitate easy alignment through the center of the chamber. Since both the tip/tilt stage and the chamber mount below it are fixed within a few centimeters of the atoms, they are constructed from titanium to avoid detrimental magnetic field effects. Nevertheless we did not design all the components with titanium. For instance the collimator assembly is designed with standard Thorlabs kinematic components.

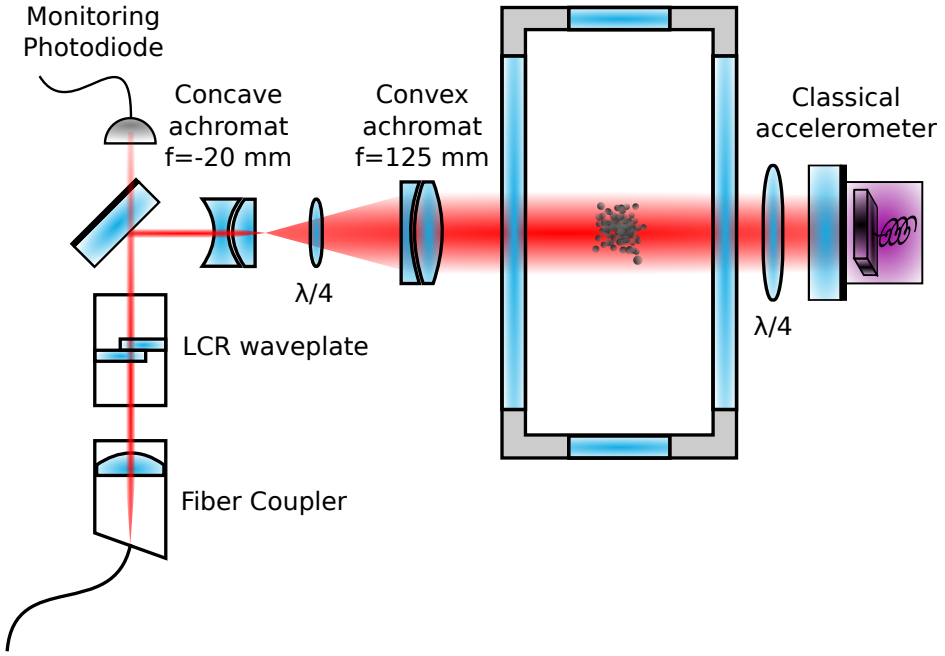

Figure 3.7: Schematic of the free-space optical beam used on each axis to realize the complete 3-axis atom interferometer.

Figure 3.7 presents the schematic of the beam light collimation to address the atomic cloud. After the fiber output coupler, the expanding light passes through a liquid-crystal retardance waveplate (LCR) (Thorlabs LCC1111T-B) which enables to dynamically change the light polarization during the measurement sequence. This is crucial for the sequential operation of MOT and Raman light with the same beams, because they require different polarization states (circular for the MOT, and linear for Raman interrogation). This component is mounted into a temperature controlled oven since it is sensitive to temperature. Then the light reflects off of an anti-reflection coated mirror with a polished backside. A small amount of light ($\simeq$ 1%) transmits through this mirror and is aligned onto a monitoring photodiode, which allows us to monitor the light level on each axis. The light reflected off the mirror passes through a concave achromat lens (f=-20 mm) followed by a convex achromat one (f=125 mm). This lens configuration makes a Galilean telescope producing a magnification of 6.25. A quarter-waveplate is placed between the two lenses to better control the polarization

of the light as described in Section 3.2.4. The light beam is retro-reflected by a 2 inches referenced mirror. A quarter-waveplate is placed between the atoms and the mirror to rotate the polarization of the light by 90 degrees to obtain $\sigma\pm/\sigma\pm$ configuration (for the MOT and co-propagating Raman transitions) and lin$\perp$lin configuration (for counter-propagating Raman transitions).

3.2.4 Liquid-crystal retardance waveplates

Since the light beams along each axis are used to produce all the steps for atom interferometry, we need to control the polarization during the sequence. Liquid-crystal retardance waveplates (LCR) are made of molecules able to change the optical birefringence when aa electrical potential difference is applied. The retardance due to the change of the ordinary and extraordinary indices creates a change in the resulted polarization of the light. Those components are convenient for rapid switch between different polarization states compared to rotating mechanical optics.

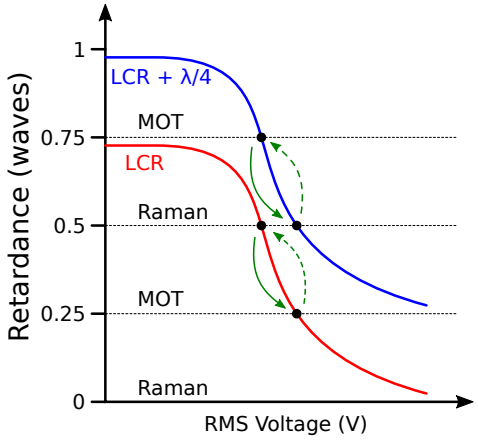

Figure 3.8: Operation of the LCR waveplate in red and with a quarter-waveplate added in the beam path in blue. Different retardances of the light authorize to produce MOT or Raman beams at respectively 0.25λ, 0.75λ and 0λ, 0.5λ. The plain green arrows depict fast time switching whereas dashed ones display slow time switching.

Figure 3.8 presents the response of the retardance of the light with an electrical square wave applied on the LCR. The polarization of the light at the output of the fiber is linear by default which is suitable to drive counter-propagating Raman transitions. A quarter retardance is required to obtain circular polarization to produce the MOT and generate co-propagating Raman transitions. We notice that different retardances allow to operate MOT or Raman beams. For instance, the counter-propagating Raman transitions do not differ from 0λ or 0.5λ retardance because it is the cross linear polarization with the retro-reflected beam which matters. However the MOT operation between 0.25λ and 0.75λ retardance influences the direction of the circular polarization

and needs to be chosen carefully to drive the MOT.

In our case, it is important to switch rapidly from the MOT configuration to the Raman one. The switch in reverse way is less critical since it is operated during dead times before restarting the sequence. We observe that the LCR is faster to decrease the retardance rather than increase it. Operating points are not convenient with the LCR alone because switching between the MOT configuration and the Raman one is slow. We implemented a quarter-waveplate into the optical scheme to increase the retardance and obtain appropriate switching scheme as shown in the Fig. 3.8.

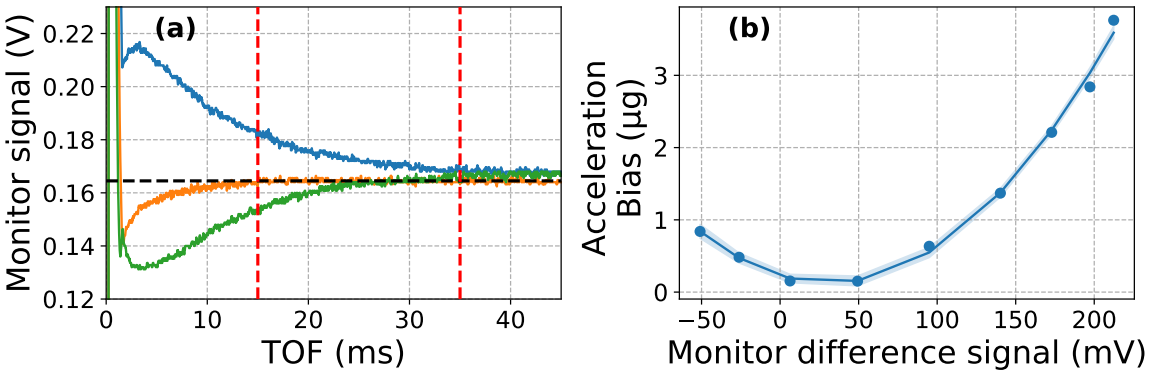

Figure 3.9: Characteristics of the polarization of the light depending on the burst applied. The polarization is measured with a monitoring photodiode placed through the mirror after the LCR waveplate. (a) Polarization response over time with a non-optimized burst (in blue and green) and an optimized one (in orange). The red dashed lines define a typical interferometer with a time-of-flight TOF=15 ms and a Raman interrogation time of T=10ms. (b) Acceleration bias measured on the atom interferometer depending on the voltage difference of the polarization measured by the monitoring photodiode on (a).

To operate optimally the LCR waveplates for switching rapidly between the MOT configuration and the Raman one, it is important to force the orientation of the liquid crystal molecules by applying a larger voltage during a short time (burst). For instance, the response time to switch the polarization can be tens of ms if no burst is applied. To correct that, we apply typically a burst of $\simeq 7.5$ V_{RMS} during 1.5 ms to switch from MOT to Raman state where voltages applied are respectively $\simeq 2.5$ V_{RMS} and $\simeq 4.5$ V_{RMS}. Figure 3.9 shows the behavior of the polarization depending on the burst applied. To study it, we use the monitoring photodiode placed after the mirror which is just after the LCR waveplate. Indeed the transmission of the light through the mirror depends on its polarization. Assuming constant power at that time scale, we measure directly the polarization behavior on the monitoring photodiode signal. Figure 3.9(a) displays an ideal transition of the polarization between the MOT and the Raman sequence in orange for a burst properly calibrated. The polarization signal is stabilized after $\simeq 15$ ms. When the polarization is not stable, any difference between the start and the end

of the interferometer leads to biases into the atom interferometer. In particular, the two-photon light shift (TPLS) is sensitive to this effect and is studied in Chapter 5. Figure 3.9(b) presents experimental measurements of acceleration biases generated by a differential polarization during the interferometer. The monitor difference signal corresponds to the voltage difference obtained on the monitoring photodiode and is produced by a change of the burst amplitude.

Since the LCR waveplate is sensitive to the temperature, it is important to control it. For that reason, the LCR waveplates are placed in a temperature controlled oven with a temperature setpoint of $\simeq 40$ °C. Furthermore, any change of the polarization angle at the entrance affects the polarization response. For instance, if the angle of the polarization is changing inside the fiber before the collimator, it impacts the measurements of the atom interferometer.

3.2.5 Fluorescence detection system

To detect the number of atoms remaining in each internal state at the output of the interferometer, we shine near-resonant light along a given axis with the Raman beam. This causes the atoms to emit 780 nm light in all directions as a result of spontaneous emission. To detect this light, we have fixed a series of imaging lenses and photodiodes around the atoms. Two detection configurations enable fluorescence imaging for two different situations. One is adapted for 3-axis atom interferometry and the other is optimized for atom interferometry along the vertical axis.

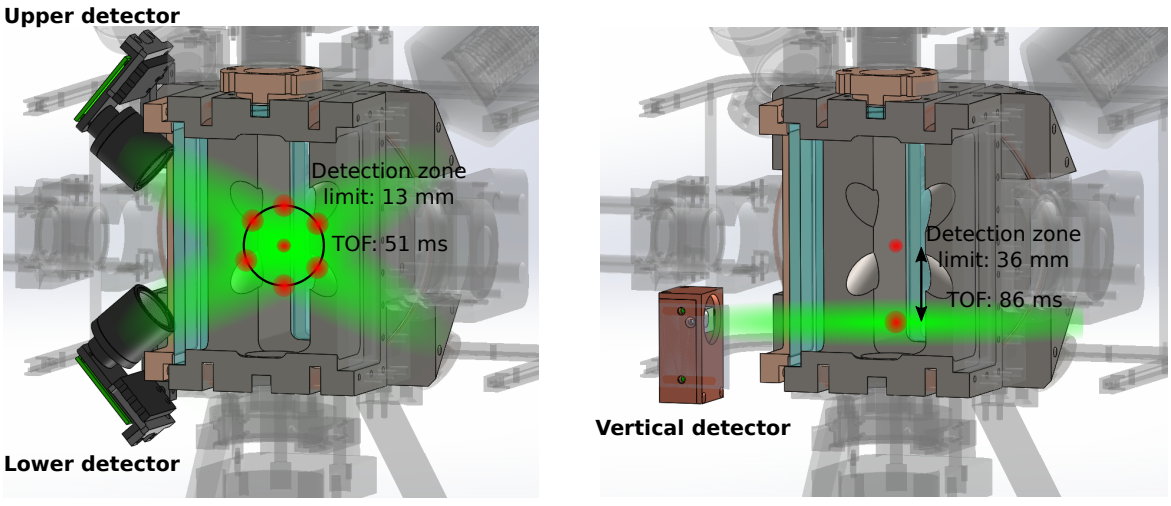

Figure 3.10: Two sets of detectors are installed on the sensor head depending the measurements to operate. On the left, the detection is adapted for 3-axis atom interferometry and on the right, it is optimized for atom interferometry along the vertical axis.

Figure 3.10(a) shows combinations of detection zones which can be used when

the system undergoes different motions (i.e. rotations or accelerations), which can cause the atoms to move in random directions relative to the chamber walls. The two detectors use a single 1 inch diameter aspheric lens with a focal length of 16 mm close to the photodiode, with a tube lens around it to avoid too much stray light from the background. They cover a large detection volume with a sphere of $\simeq$ 13 mm radius from the center of the chamber. Considering the gravitational acceleration along a random orientation and 1 inch diameter for the light beams used for fluorescence, the detection system offers an effective detection time-of-flight (TOF) of $\simeq$ 51 ms. Therefore, we can typically operate interferometers with Raman interrogation time of 10 ms. For instance, those two detectors are used in Chapters 6 and 7 where 3-axis atom interferometry is studied.

Figure 3.10(b) shows where the vertical Z-axis beam illuminates the atomic cloud and the "vertical detector" imaging the atoms in the center along the vertical axis. In this case, the partially-recessed viewports along this axis allow to implement an imaging system with a larger numerical aperture. The detector uses two back-to-back achromatic doublets with focal lengths of 75 mm and 30 mm, giving a magnification of 2.5. It images a volume 36 mm below the chamber center, where the atoms are located after a free-fall time of 86 ms. This detection configuration is ideal in the “gravimeter” configuration, where atoms fall along a vertical column offering a Raman interrogation time of 35 ms. This detector is used in Chapter 5 where the atom interferometer is studied along the vertical axis.

The photodiode used for each detector (S1223 Hamamatsu) presents a sensitivity of 0.52 A/W at 780 nm. The signal is treated with a transimpedance amplifier coupled with a JFET transistor in bootstrap configuration [65]. In such circuit, the operational amplifier (OPA656 Texas Instruments) combined with the JFET transistor allows a low noise and a high bandwidth output without compromising the high gain required to amplify the signal. Our circuit offers a bandwidth of $\simeq$ 10 MHz while obtaining a signal of $\simeq$ 1 V for the fluorescence of the total number of the atoms after interferometry.

3.3 Classical accelerometers

3.3.1 Characteristics of the classical accelerometers

Figure 3.11 presents the acceleration characteristics of the classical accelerometer (Thales EMA 1000-B1) used on the 3-axis hybrid accelerometer apparatus. We placed the sensor on a heavy marble table to isolate the sensor from ambient mechanical vibrations and recorded the signal during 10 minutes at 1 kHz sampling rate. The power spectral density (PSD) exhibits different features on specific frequency areas.

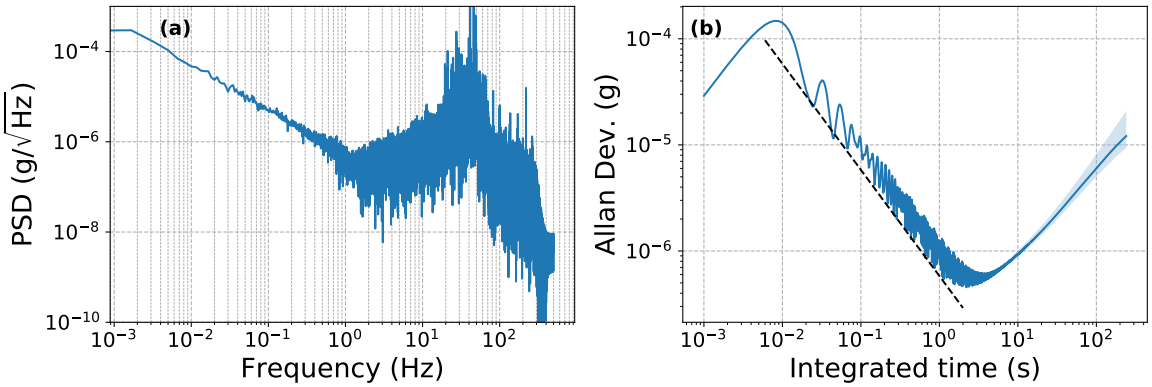

Figure 3.11: Acceleration characterization of the classical accelerometer under calm environment during 10 minutes at 1 kHz sampling rate. (a) Power spectral density and (b) Allan deviation with a $1/t$ slope integration in dashed line.

Below 1 Hz, the bias of the accelerometer is drifting and increases the PSD constantly in the lowest frequencies. Between 1 and 2 Hz the PSD reveals the noise floor of the sensor defining the region where the sensitivity is optimal. Above this frequency region, we observe mechanical vibration noises which are not compensated by the marble table with a peak at 30-40 Hz. Beyond 100 Hz, the bandwidth of the sensor declines and the PSD presents electro-magnetic noises.

On the Allan deviation plot, the acceleration measurements integrate as $1/t$ until 2 s corresponding to the quantization noise of the classical acceleration measurements. It results from the difference between the exact analog measurements and the nearest quantization value of the numerical conversion made by the analog-to-digital converter (ADC). It characterizes also the integration of a white phase noise representing the average of disparate and periodic ambient noises summed. The dashed line reveals an ultimate sensitivity of 600 ng/$\sqrt{\text{Hz}}$ for minimal noise. The Allan deviation reaches at best 450 ng after 2 s. Above that time, the measurements are instable due to bias drifts, primarily caused by temperature fluctuations.

The signal of the accelerometer is transmitted with an analog current signal. Current output is ideal for data transmission because of the very low sensitivity to electrical noise coming from EMI or RF noises. Moreover any drop of voltage, for example due to a bad wire termination or a long cable which increases the impedance, nearly does not affect the current signal since the charge quantity is conservative all over the current loop. This allows to use acceptable length of cables (2 or 3 meters) for wiring the accelerometers to the transimpedance electronic treatment inside the real-time system rack. Also shielded coaxial cables are used to prevent residual interferences with external fields.

3.3.2 Temperature calibration

The biases of the classical accelerometers derive mainly from their high sensitivity to the temperature. Classical accelerometers contain usually built-in temperature sensor to calibrate the response from temperature fluctuation. A simple model of the acceleration a experienced by the classical accelerometer can be defined as:

$$A = S(T)a + b(T) \tag{3.1}$$

where A is the measurement output, $S(T)$ and $b(T)$ are respectively the scale factor and the bias, both dependent on the temperature T. The dependency is mainly linear with the temperature which can be expressed at first order as:

$$S(T) = S_1 T + S_0 \tag{3.2}$$

$$b(T) = b_1 T + b_0 \tag{3.3}$$

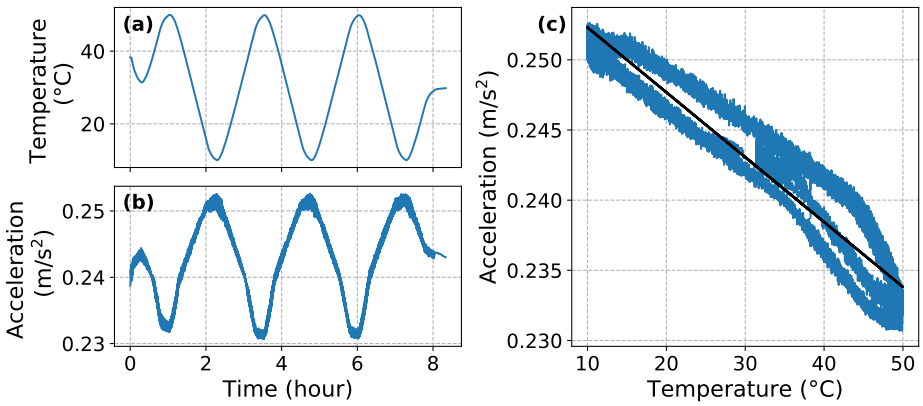

Figure 3.12: Classical accelerometer output behavior depending on the temperature. The accelerometer is placed horizontally, meaning that the acceleration measured is dominated by the bias error. (a) and (b) time-series of respectively the temperature and the acceleration. (c) correlations between the two with a linear fit in black.

To extract the parameters of the temperature dependence, the classical accelerometers are placed in a temperature controlled oven to operate ramps of temperature. To isolate the bias $b(T)$ from the scale factor $S(T)$, the accelerometers are placed horizontally to record no acceleration $a = 0$:

$$A_{\leftrightarrow} = b_1 T + b_0 \tag{3.4}$$

Here we assume that a slight tilt $\theta \ll 1$ from the perfect horizontal positions is not

affecting the measurements. Indeed $(b_1 + S_1 \cos(\theta - \pi/2)g)T \simeq (b_1 + S_1\theta g)T$ and since b_1 is at the same order of magnitude of S_1, we consider $S_1\theta g \ll b_1$ meaning negligible influence from the scale factor. Figure 3.12 presents the acceleration measurements of the classical accelerometer (EMA 1000-B1) placed horizontally into the oven. The variation of the acceleration under a temperature fluctuation between 10 and 50 degrees counts for 0.02 m/s^2. We observe slight non-linearities probably resulting from hysteresis response to the temperature or drifts which depend on other physical properties (pressure, humidity).

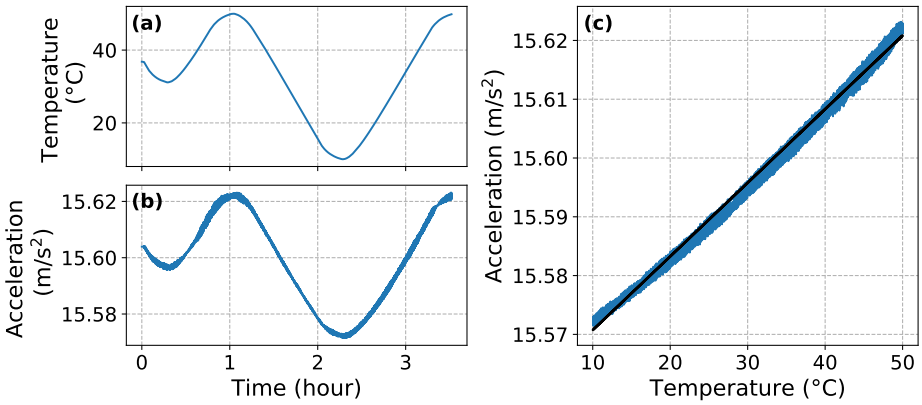

Figure 3.13: Classical accelerometer output behavior depending on the temperature. The accelerometer is placed vertically, meaning that the acceleration measured is dominated by the scale factor error. (a) and (b) time-series of respectively the temperature and the acceleration. (c) correlations between the two with a linear fit in black.

Conversely, to evaluate the scale factor dependence on the temperature, we maximize the acceleration experienced by the classical accelerometers by placing them vertically. Consequently, the accelerometer experiences the gravitational acceleration $a = g$ as:

$$A_{\updownarrow} = (S_1 g + b_1)T + S_0 g + b_0 \tag{3.5}$$

Knowing the parameters b_1 and b_0 determined with the accelerometer placed horizontally (see Eq. 3.4), we can deduce the parameters S_1 and S_0 related to the scale factor dependence on the temperature. Figure 3.13 displays the measurement of the classical accelerometer (EMA 1000-B1) placed vertically in the oven. We notice that the acceleration is off from the gravitational acceleration by $\simeq 0.5$ g meaning that the parameter S_0 is incorrect. It is not a concern at this stage since the response in temperature is not disturbed. The purpose of the hybridization with the quantum accelerometer is to correct the whole term $S_0 g + b_0$. Here the variation of the acceleration is 0.05 m/s^2, which is quite higher than the error induced by the bias alone. We notice a slight second order tendency on the measurements, meaning that the scale factor has

some quadratic dependence on the temperature.

Considering the correction of the classical accelerometer biases made by the atom accelerometers with the hybrid accelerometers, the first order calibration of the temperature is sufficient. However, slight mis-evaluation of the scale factor can disturb the correlations of the mechanical displacement from the referenced mirror with the atom interferometer measurements. This could result in biases at large time scale which are easily measured and rejected with the interferometer, but also in short term biases at time scale of the interferometer length which expand as noise on the atom interferometer shot-to-shot signal. This noise would decrease the sensitivity of the atom interferometer, specially at large Raman interrogation time, and eventually depreciate the precision of the hybrid accelerometer.

3.3.3 Triad calibration

A well known problem with inertial measurement units (IMU) is the misinformation regarding the orthogonality of the frame and lever arms between the centers formed by the triad of the sensors. It highly misleads the estimation of the total acceleration vector. To reconstruct the total acceleration vector, it is necessary to calibrate the alignment between the three axes of a triad of accelerometers. Indeed the frame defined by the direction of measurements of each accelerometer is not absolutely orthogonal. For instance, the angle alignment requires less than 0.1 μrad calibration to obtain 100 ng of precision on the total acceleration vector. This can be accomplished by varying the orientation of the triad between a set of positions and comparing the norm of the total gravity vector with a local measurement of the gravitational acceleration. A small deviation from the orthogonality between the axes can be modelled by multiplying the raw acceleration vector with a correction matrix. The method is detailed and applied on the 3-axis atom interferometer in Chapter 6 and relies on the work from reference [66].

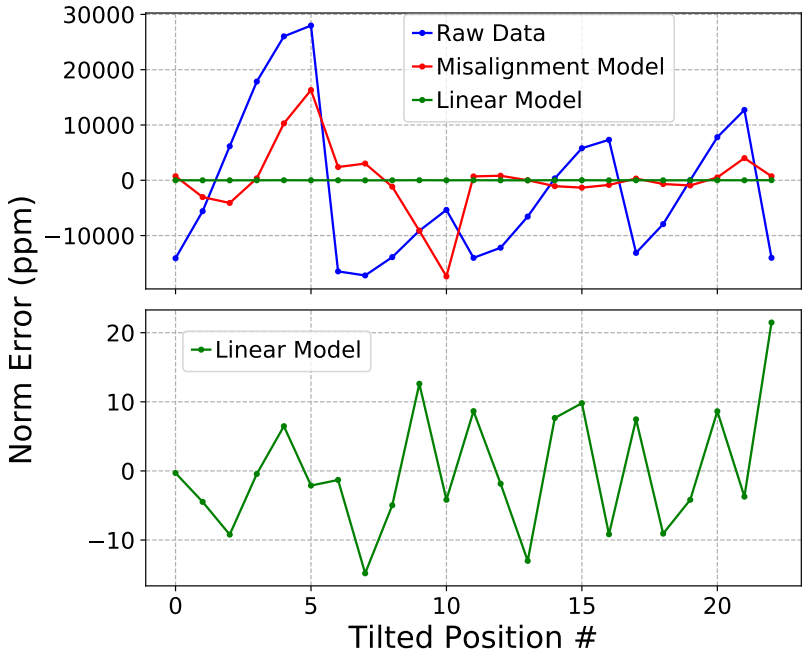

Figure 3.14: Calibration of the triad formed by the 3 classical accelerometers attached to the reference mirrors. The plots present the error on the norm of the total acceleration vector in blue. Corrections with the "misalignments" and the "linear" models are depicted respectively in red and green. The bottom graph focuses on the linear model results.

Figure 3.14 presents a brief misalignment calibration between the three classical accelerometers of our apparatus. By varying the orientation of the sensor head placed on a rotation platform presented in Section 3.5.2, the raw acceleration vector can be recast into a corrected base. The figure displays the measurements of the norm of the full acceleration vector in 23 different orientations. Two methods are applied to calibrate the misalignment angles which are detailed in Chapter 6. The "misalignment model" correspond to the calibration with a correction rotation matrix. The "linear model" is more advanced by including a correction on the scale factors and the biases of each accelerometer. This last approach is then more precise by discerning constant biases of the classical accelerometer, which does not depend on the acceleration experienced, and the error on the scale factors which depends directly on the acceleration measured. For instance, the "misalignment model" calibrates the norm at $\pm$ 6 mg of standard deviation, whereas the "linear model" reduces the uncertainty to $\pm$ 9 μg of standard deviation. This remaining uncertainty is certainly due to the time required to operate the calibration (manual rotational platform with heavy sensor head on it) during which the bias of the classical accelerometers is drifting, whereas the method assumes fixed biases. The correction parameters for the two models are depicted in Table 3.1.

In principle, this method is well suited to calibrate the triad of classical accelerometers where biases are roughly constant at short term and scale factors variation can

be corrected at first order with temperature modeling. Additionally increasing the number of measurements for different tilts provides more data for the algorithms and helps decreasing the uncertainties on the misalignments, whereas for the 3-axis atom interferometer it is more difficult and time consuming to generate a lot of data. In Chapter 6, we study the fact that biases of the 3-axis atom interferometer are strongly dependent on the orientation of the sensor head, which leads to a deep analysis of the systematic shifts to calibrate its misalignments.

$\mathbf{X}^{\text{Misalignment}}$	**Value**	$\mathbf{X}^{\text{Linear}}$	**Value**
$\tau_{y,x}$	$+0.0082712$	$\mathrm{k}_{a,yx}$	$+2.0238 \times 10^{-3}$
$\tau_{z,x}$	$+0.0334023$	$\mathrm{k}_{a,zx}$	$+1.7307 \times 10^{-3}$
$\tau_{z,y}$	$+0.0124671$	$\mathrm{k}_{a,zy}$	-5.431×10^{-4}
		$\mathrm{k}_{a,xx}$	1.0104456
$\tau_{y,y}$	1.0113919	$\mathrm{k}_{a,yy}$	1.0102423
$\tau_{z,z}$	0.9844584	$\mathrm{k}_{a,zz}$	0.9932359
		$p_{0,x}$ $(\mathrm{m.s}^{-2})$	-0.1889647
		$p_{0,y}$ $(\mathrm{m.s}^{-2})$	-0.0800065
		$p_{0,z}$ $(\mathrm{m.s}^{-2})$	$+0.0739956$

Table 3.1: Table of calibration parameters calculated with the misalignment and the linear model. The parameters of the matrices $\mathbf{X}^{\text{Misalignment}}$ and $\mathbf{X}^{\text{Linear}}$ are described in Chapter 6.

It is important to mention that the 3-axis hybrid accelerometer frame is governed by the axes formed by the triad of the classical accelerometers. Indeed, any misalignments between the classical accelerometer measurement axis and the atomic one is seen as a bias on the hybrid accelerometer output. Those misalignments correspond to second order shifts. The calibration of the 3-axis hybrid accelerometer is further discussed in Chapter 7.

3.4 Control system

3.4.1 Hardware elements

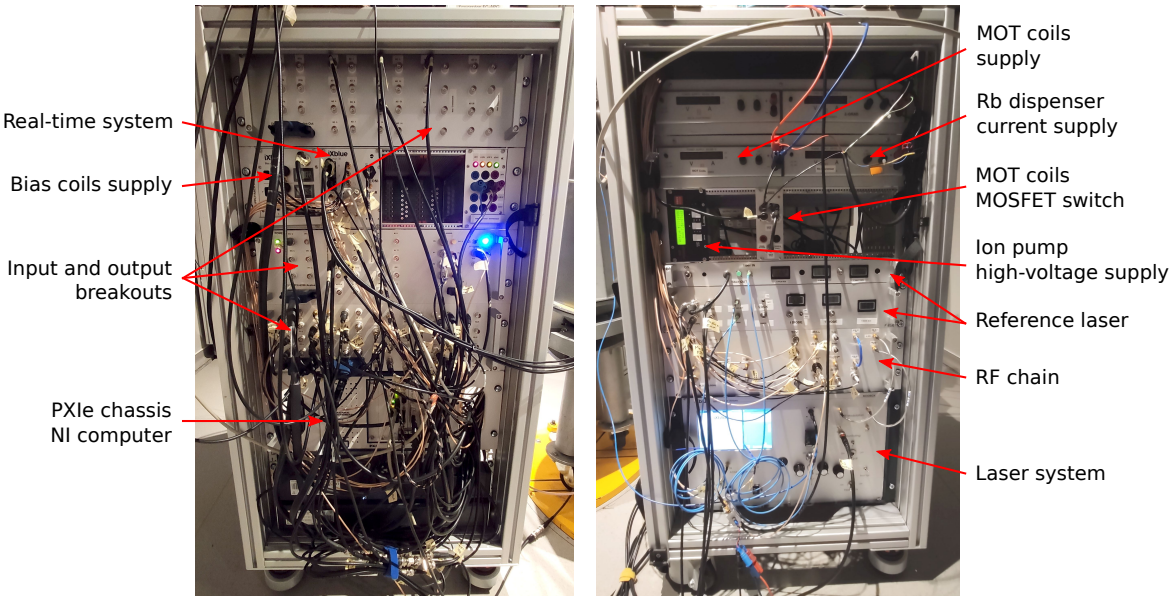

Figure 3.15: Photos of the front and the back of the 19" control rack of the experiment.

Figure 3.15 presents the rack involving all the components to operate the 3-axis hybrid accelerometer. It includes the control electronic, the CPU, the electrical supplies, the RF source and the laser system. The size of the rack is 565 mm large for a height of 950 mm and a depth of 900 mm, affording racks of 19" with a capacity of 18U on each side. The power consumption is $\simeq$ 770 W including $\simeq$ 170 W from the MOT coils current driver occurring only during the MOT loading.

The timebase system is derived from an oven-controlled quartz oscillator (OCXO O-CMR058IS-NS-R from NEL Frequency Controls company) and is included into the RF source. This clock has a relative temperature stability of 1 ppb/°C over a temperature range of 0-50 °C and a relative aging parameter of 100 ppb/year. This component delivers outputs of 10, 100 and 500 MHz which is convenient to distribute components requiring different clock frequency input (FPGA from real-time system and sequencer, frequency DDS, phase-lock oscillator). The CPU is composed of an embedded controller (PXIe-8820 National Instruments) included into a PXIe chassis offering 4 slots (PXIe-1071). A set of analog/digital input and output PXIe cards are used to send and acquire signal between the CPU and the experiment. Custom breakout racks for digital and analog inputs and outputs have been assembled with SMA and BNC connectors to link the National Instruments cards with the experiment. All the analog outputs are treated with a buffer circuit (BUF634 Texas Instruments)

to provide external current supply ($\simeq 250$ mA) with improved capacity load driving. It allows to drive signals with a reduced time response thanks to a very low output impedance. A FPGA (XEM3001 Opal Kelly) is integrated into a PXIe chassis to communicate the sequence with analog/digital output PXIe cards and is controlled by a dedicated software Cicero Word Generator.

Dedicated electrical supplies (from Delta Elektronics) generate electrical current for the MOT coils and the ^{87}Rb dispenser. A MOSFET circuit is used to switch rapidly the electric current supply for the MOT coils. The electrical current supply dedicated to the dispenser delivers typically 5 A. It is adjusted manually to deplete progressively the ^{87}Rb available on the dispenser. For instance, every month the current is increased by a few mA to activate deeper layers of ^{87}Rb. The quantity of Rubidium available on each dispenser lasts approximately 3-4 years. The time constant of the MOT loading if affected by the amount of current on the dispenser (quantity of Rubidium inside the chamber). Since the stability of number of atoms is not critical for us, we do not use any feedback to control this current. Indeed, the detection signal is normalized with the total number of atoms and does not depend on it. The warm-up of the dispensers can take tens of minutes and the heating of the chamber provided by the heat-dissipation of the MOT coils helps to diffuse atoms fixed on the walls.

The ion pump is running constantly with its dedicated high-voltage current supply provided by SAES. The pressure level inside the chamber can be monitored with an integrated Penning gauge and the current drove by the ion pump indicates the effective pumping speed. The ion pump is operated with a steady-state current supply of $\simeq 60$ nA for a voltage of 6 kV_{dc}.

The reference laser corresponds to the optical frequency etalon locked to a ^{87}Rb transition. It provides a frequency reference for the laser system which operates on the atoms. The RF chain generates two frequency modulations which are send to the laser system and is composed of connector mounted standard components. All those parts are presented in detail in Chapter 4.

3.4.2 Software elements

Figure 3.16: Screenshot of the two softwares operating the experiment. Cicero is used to control the sequence and LabVIEW to acquire signals and communicate via serial ports.

Figure 3.16 displays a screenshot of the two softwares used to control the experiment and acquire measurements. Cicero Word Generator (CWG) is a software collection dedicated to the control of atomic physics experiments developed by the MIT Center of Ultracold Atoms research group. The programs are free and adhere under the terms of the GNU General Public License. It is composed of Cicero, the graphical user-interface (GUI) for editing sequences, which communicates via .NET remoting to the back-end server Atticus to translate the sequences to the output buffers. It drives the National Instruments analog and digital outputs using an integrated FPGA where the sequence is loaded at each cycle. CWG is particularly optimized for experiments which do not expect high repetition rate. Indeed it suffers from large dead times between each cycle due to the loading of the sequence into the FPGA each time. Those dead times correspond to $\simeq 1$ s, which limits the cycling rate of the measurements at 1 Hz. Typically, considering a MOT loading of 250 ms and 50 ms for the rest of the sequence, our cycling time is $\simeq 1.3$ s. This technical limitation can be easily fixed by developing a dedicated solution with a FPGA where the sequence would be loaded only one time and repeated at each cycle. Nevertheless the CWG environment offers an advanced turnkey solution to control experiments with 1 μs precision timings.

On the other hand, LabVIEW is used to acquire the signal from the National Instruments analog input cards and communicate via serial port with frequency DDS and the real-time system. It controls as well parameters which modulate between sequences, including the directionality of the effective wavevector k_{eff}, the laser beam path to control the axis X, Y or Z, the LCR control voltages and the magnetic field biases required to switch the interferometry between axes. LabVIEW receives external digital triggers from Cicero to locate key timings during the sequence like the end of the optical molasses, or the detection. Additionally, LabVIEW runs the mid-fringe lock algorithm used to operate the atomic and hybrid accelerometers by receiving, extracting and treating the detection signals. LabVIEW communicates the parameters of the atom interferometer to the FPGA of the real-time system at the beginning of each sequence, including the timings of the interferometer. Those parameters are used to control in real-time the frequency and the phase difference of the Raman lasers during the interferometer.

3.4.3 Real-time system

We utilizes a real-time control system based on a field-programmable gate array (FPGA) to compensate for motion-induced frequency and phase shifts during the interferometer. These detrimental shifts can arise due to, for instance, mirror vibrations or changes in orientation. This limits the sensitivity of the interferometer as data can be taken at the top or the bottom of the fringe. It prevents the use of modulation schemes such as mid-fringe locks [31]. Furthermore, during the free fall time, the frequency difference between the Raman lasers needs to be adjusted at each light pulse to compensate for the varying Doppler shift due to gravity.

We address both of these issues by using a real-time system inspired by [29] based on an Artix7 FPGA. This system controls the classical accelerometer acquisition chain, computes the appropriate frequencies and phases, and acts on a frequency direct digital synthesizer (DDS) within the RF chain to ensure the correct frequencies and phases are applied during each Raman pulse. Between each pulse, the real-time system calculates the time integral of the acceleration and the corresponding Doppler shift. In addition, between the first and the last Raman pulse, the FPGA computes the expected inertial phase from the acquired classical accelerometer signal. A few microseconds before each pulse, the frequency DDS is updated to compensate the Doppler shift, and a phase opposite to the estimated inertial phase is applied for the last pulse. Finally, a laser phase controlled by the CPU is added at the last Raman pulse to operate the mid-fringe lock.

Serial communication between the CPU and the FPGA is made with Python.

The FPGA receives the parameters of the atom interferometer at the beginning of each sequence, including the measurement axis, the time-of-flight of the atom cloud before the interferometer, the Raman interrogation time and the Rabi pulse length. Those informations are stored into FPGA registers and are employed to compute corrections on the frequency and the phase in real-time. Triggers generated by the sequencer are addressed to the real-time FPGA to communicate specific timings of the sequence including the end of the optical molasses for instance. Additionally, the FPGA streams continuously to the CPU the high bandwidth measurements of the classical accelerometers.

The real-time system operates according to two different cases exposed in Chapter 2. The open-loop operation relies on the real-time system filtering numerically the acceleration of the classical sensor to remove any constant or slow-time-varying biases. It corrects parasitic vibrations of the referenced mirror during atom interferometry. The advantage of a numerical filter over an analog one is the straightforward switching to enable it or not. For instance, this case applies in Chapters 5 and 6 where the performances of the atom interferometers along respectively the vertical axis and the 3 axes are studied. On the other hand, the close-loop operation involves direct correlation of the classical accelerometer measurements with the atom interferometer without filter. This allows to extract the bias of the classical accelerometer and subtract it to the output by "closing the loop". This case is studied in Chapter 7 where the operation and the performances of the 3-axis hybrid interferometer are detailed.

3.4.4 Experimental sequence

Figure 3.17 describes the sequence to operate the atom interferometers composed of five main time-parts. The optical switch corresponds to a micro-mechanical fiber switch (Leoni EOL 1x4) which controls the beam paths with a TTL command to switch between the MOT configuration and individual axes X, Y or Z for Raman transitions. The laser power is controlled with a fiber acousto-optic modulator located into the laser system. The voltage controlled oscillator (VCO) and direct digital synthesizers (DDS) generate frequency modulations which are converted to optical sidebands via electro-optic modulation by the laser system. The VCO sets the frequency for atomic transitions $|F = 2\rangle \rightarrow |F'\rangle$, whereas the DDS achieves the repumper $|F = 1\rangle \rightarrow |F'\rangle$ used to repump the atoms into $|F = 2\rangle$ and the Raman DDS produces the phase coherent optical frequency for Raman transitions. All those components related to the laser system and the RF chain are detailed in Chapter 4.

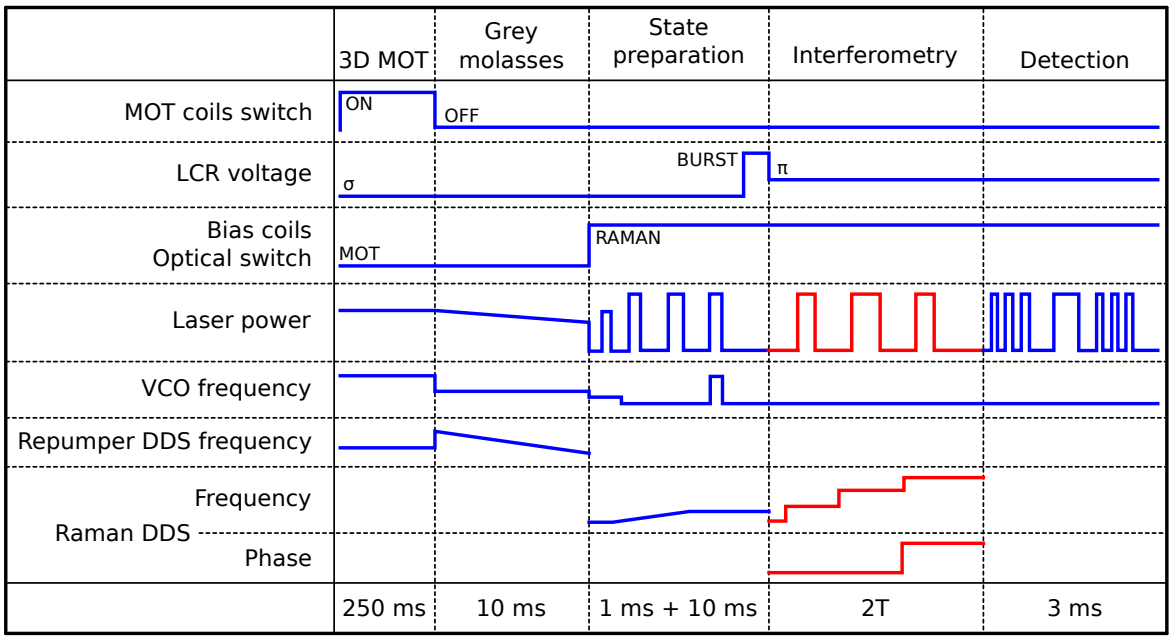

Figure 3.17: Overview of the experimental sequence operated for the atom interferometers. The red parts represent real-time controls ensured by the real-time FPGA. For more convenience, the LCR voltage, the bias coils and the optical switch are controlled by LabVIEW through the real-time FPGA to choose the Raman axis between the sequences.

Firstly, the 3D magneto-optical trap (MOT) loads the Rubidium evaporated by the heated dispenser. The MOT coils are driven with 5 A by the electric current supply and the laser power is at maximum to optimize the rate of atoms trapped per unit time. The optical switch enables the light from the laser system to distribute the 3 retro-reflected axes to drive the 3D MOT. The LCR waveplates configure the polarization of the light circularly on each axis. The bias coils are set along each axis to cancel ambient non-zero magnetic field. The frequencies of the laser are controlled with the VCO for the cooling frequency at the cycling transition $|F = 2\rangle \rightarrow |F' = 3\rangle$ slightly detuned to the red and the "repumper" DDS for the repumper frequency at transition $|F = 1\rangle \rightarrow |F' = 2\rangle$. This step is the longest of the sequence and lasts $\simeq 250$ ms. The length can be adjusted to control the number of atoms used for interferometry.

After the MOT loading, the grey molasses operate to cool down the atom cloud at sub-Doppler temperature [51]. The MOT coils current supply is disabled to release the magnetic trap. The principle of the grey molasses relies on the coupling between bright and dark states induced by the motion of the atoms. On our setup, grey molasses delivers slightly lower temperature ($\simeq 2$ μK) compared to red molasses (< 3.5 μK) but mostly they are more robust when the sensor head orientation is changing and the magnetic field is varying. To operate the grey molasses, the cooling frequency is set with the VCO at transition $|F = 2\rangle \rightarrow |F' = 2\rangle$ slightly detunned to the blue. At the same time, the repumper power is ramped down.

Subsequently, the pair of bias coils along the axis of measurement generate a magnetic bias to define the quantization axis and raise the degeneracy of magnetic states in order to drive the Raman transitions. Simultaneously the laser beam is switched from the 3 retro-reflected axes configuration used for the 3D MOT and the molasses, to the single retro-reflected axis configuration along the axis of measurement. The atoms are prepared into non-magnetic sensitive state $|F = 1, m_f = 0\rangle$. Now the repumper DDS, used to repump the atoms during cooling, is replaced by the Raman DDS. Here the state preparation is composed of successively one depump pulse to transfer all the atoms into state $|F = 1\rangle$, two selective pulses to transfer atoms from $|F = 1, m_f = \pm 1\rangle$ to $|F = 2, m_f = \pm 1\rangle$ and one blast pulse to remove the atoms in state $|F = 2\rangle$. After that, the remaining atoms are in state $|F = 1, m_f = 0\rangle$. The selection of the atomic states is made with non velocity-sensitive co-propagating Raman transition and last less than 1 ms. The state preparation is further detailed in Chapter 5. Additional time-of-flight (TOF) is operated to update switching components as the LCR switch, the Leoni fiber switch or the magnetic field bias. It adds 10 ms to this time-step. Further TOF can be added to increase the Doppler frequency shift with higher velocity atoms. For instance the effective TOF equals 20 ms when the sensor head is tilted in Chapters 6 and 7.

Once the atoms are prepared into non-magnetic sensitive states, the LCR waveplate switch the polarization of the laser beam along the measurement axis from circular to linear. A burst is applied to the voltage of the LCR to increase the switch speed. Because of the linear polarization of the retro-reflected beams and the quarter waveplate between the atoms and the reference mirror, the lin$\perp$lin configuration authorizes counter-propagating Raman transitions. The time-space Mach-Zehnder interferometer is composed of three successive velocity-sensitive Raman pulses that coherently splits ($\pi/2$ pulse), reflect (π pulse) and recombine ($\pi/2$ pulse) the atomic wavepackets. Each pulse is separated by an interrogation time T during which the atoms are in free fall. The sensitivity of the interferometer is adjustable by changing the interrogation time T which ranges from below 1 ms to 35 ms. During the interferometer, the real-time system controls the Raman DDS. It acquires measurements from the classical accelerometer to adjust the Doppler frequency shift before each pulse and corrects the phase for the last pulse. Finally, the detection step measures the population ratio between the two ground states $|F = 1\rangle$ and $|F = 2\rangle$ and is further detailed in Section 3.4.5.

3.4.5 Detection and signal extraction

After interrogating the atoms with Raman pulses during interferometry, the detection gives access to the population ratio between the two ground states. In our

apparatus, the measurements are made by fluorescence detection with discrete photodiodes. Compared to camera detection where a lot of informations can be collected with one image, extracting the signal with photodiode needs more steps, especially to reject parasitic background.

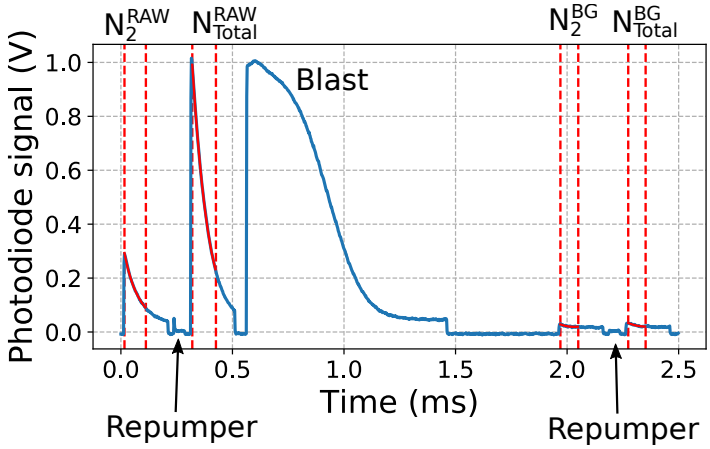

Figure 3.18: Detection signal at the end of the sequence.

Figure 3.18 presents an example of atomic detection signal. The laser is set on the transition $|F = 2\rangle \rightarrow |F' = 3\rangle$ to generate fluorescence by spontaneous emission from the atoms in state $|F = 2\rangle$. An exponential decay fit measures the number of atoms N_2^{RAW}. Afterwards the laser repumps all the atoms from $|F = 1\rangle$ to $|F = 2\rangle$. Again the laser produces fluorescence for the atoms in state $|F = 2\rangle$ and the total number of atoms N_{Total}^{RAW} is extracted with an exponential decay fit. This step is achieved within 0.5 ms. Then a blast is operated during $\simeq$ 1 ms with the laser set on the cycling transition $|F = 2\rangle \rightarrow |F' = 3\rangle$ to heat all the atoms participating to the interferometer and remove them from detection region. Subsequently a similar procedure permits to detect total number of remaining atoms N_{Total}^{BG} and the ones in $|F = 2\rangle$ state N_2^{BG}. They correspond to atoms from the background involved in the detection or residual light from the laser. Finally to extract the true signal of the population ratio performing the atom interferometer, we subtract the background signal to the raw one:

$$\frac{N_2}{N_{Total}} = \frac{N_2^{RAW} - N_2^{BG}}{N_{Total}^{RAW} - N_{Total}^{BG}} \tag{3.6}$$

3.5 Mobile and calibration apparatuses

3.5.1 Marble table

A marble table provides a very stable tilt and good isolation from ambient mechanical vibrations to the sensor head. However it does not afford any control of the tilt, meaning that it is adapted only for vertical interferometry. In that sense, the marble table is preferably used for vertical atom interferometer characterization and ultimate performance tests under calm environment. For instance, Chapter 5 studies the atomic accelerometer along the vertical axis where the sensor head is placed on the marble table.

3.5.2 Rotational platform

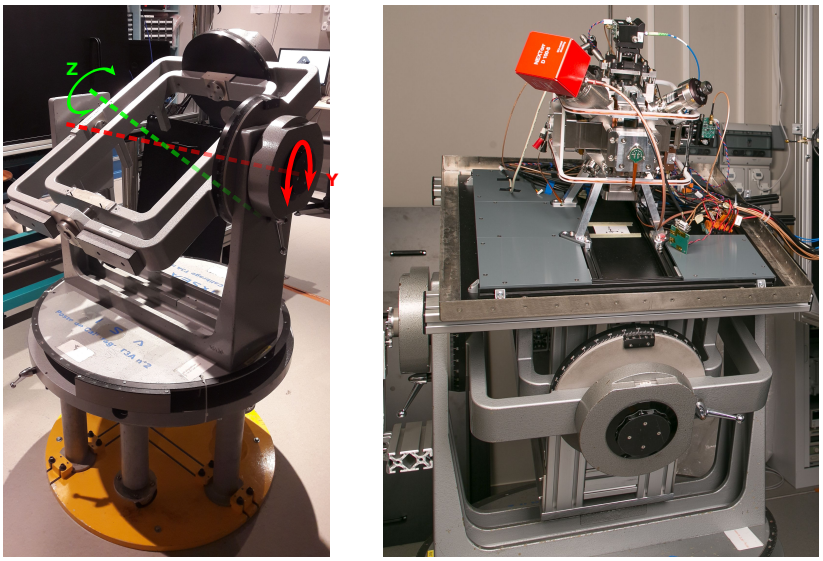

Figure 3.19: Photos of the rotational platform providing 2 axes of rotation.

Advanced tests for the 3-axis hybrid accelerometer require to control the orientation of the sensor head in order to calibrate and evaluate the performances. The rotational platform presented in Figure 3.19 affords two axes of rotation according to angles θ_X which can vary from -90 to +90 degrees and θ_Z which rotates the base of the sensor head. The angle θ_X is controlled manually with a pivot shaft where a break blocks the position. The angle θ_Z can be modified with the fixation of the base of the sensor head on the plate of the platform, allowing a complete turn of 360 degrees with increments of 15 degrees. To equilibrate the center of mass of the moving parts, four ballast composed of lead with a weight of $\simeq 20$ kg each has been built in and fixed bellow the sensor head. Additional steel plates adjust more finely the distribution of the weight.

The rotational platform serves as an ideal test bed to investigate the behavior of the free-falling atom interferometer under different static orientations as presented in Chapter 6, as well as to validate our hybridization schemes and analysis methods in Chapter 7. As a result, we achieve optimal operation of the hybrid sensor over a broad range of sensor orientations (±70 degrees relative to vertical). In the near-future, dynamic movements of the sensor head including rotations will be explored for mobile applications.

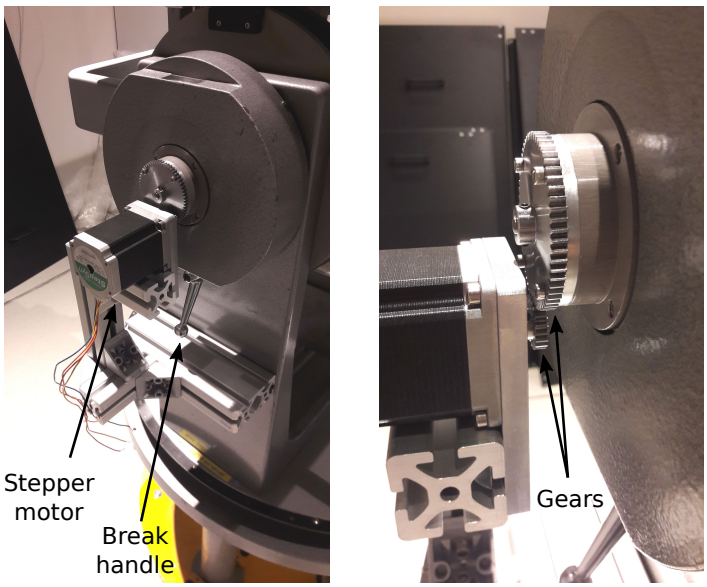

Figure 3.20: Photos of the motor installed for future automated rotations.

The control of the angle θ_X will be automated in the near future and will enable dynamical rotations. A bipolar stepper motor (Sanyo Denki 103H7126-5740), providing a holding torque of 1.6 N.m, is installed on the shaft of the rotational platform as shown in Fig. 3.20. It achieves an angle increment of $\beta = 1.8$ degree/step. The torque generated by the stepper motor decrease when the frequency step increase. For instance it produces 0.8 N.m at a frequency step of 1kHz. Hopefully the center of mass is centered at the level of the rotation axis, meaning there is almost no lever arm and the force required to rotate the sensor head is minimal. Two gears, an input gear (pinion) composed of 20 teeth and a larger output gear (wheel) of 60 teeth, transmit the motion of the motor to the shaft. In addition, an internal wheel into the rotational platform transmit the motion to the shaft with a gear ratio of 1/36. The total gear train decreases the input rotational speed by a gear ratio of $R = 20/(60 + 36) = 1/108$ and amplifies the input torque with a mechanical advantage of $1/R = 108$. A stepper motor requires a specific current driver controller (Sanyo Denki BS1D200P10) able to alternate synchronously the current between the coils to initiate the rotation of the central rotor. This controller authorizes a partition angle P which decreases the increment angle of the motor by a factor 1, 2, 4, 8 or 16. The rotation speed $\dot{\theta}$ delivered

by the system is controlled by the frequency step f of the stepper motor as:

$$\dot{\theta} = \frac{\beta R}{P} f \tag{3.7}$$

For example at $f = 1$ kHz of frequency step, we achieve a rotation speed of $\dot{\theta} = 16.7$ degrees/s.

3.5.3 Mobile platform

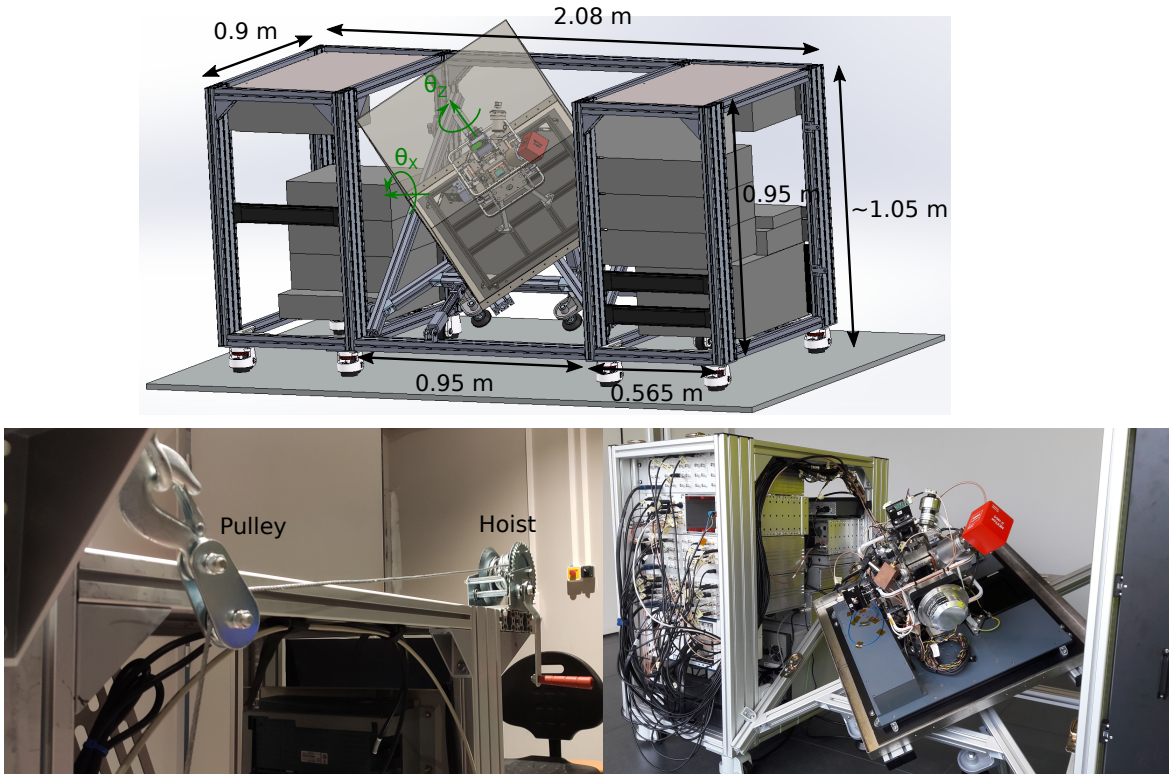

Figure 3.21: Capture of the mobile platform used to operate the 3-axis hybrid accelerometer. One photo shows a pair of hoist and pulley used to lift the sensor head central part and the other photo exhibits the sensor head with the control rack but without the magnetic shield.

The mobile platform is composed of three parts as shown in Fig. 3.21. One rack placed on four wheels contains all the electronic to operate the 3-axis hybrid accelerometer and described in Section 3.4.1. A second identical rack is used for additional equipment such as electronic test instruments (oscilloscope, spectrum analyser), spare backup equipments, uninterruptible power supply (UPS), electrical battery to operate the sensor for a few hours without external supply. A modular central part contains the sensor head with its magnetic shield. The orientation of this part can be adjusted with angles $\theta_X = 0$ to 50 degrees and a fixed angle $\theta_Z = 45$ degree. Two pairs of hoist and pulley are used to lift this part and control the angle θ_X. The whole structure measures 0.9x2.08 m^2 for a height of 1 m. The apparatus is easily movable with the

wheels installed. Besides, the wheels combine feet which are adjustable in height and allow the apparatus to rest on the floor.

This mobile platform offers a transportable as well as a mobile apparatus for static operation tests and future dynamic on-board applications. For instance the 3-axis hybrid accelerometer has been transported by a truck from the LP2N laboratory in Talence to the iXblue facilities in St-Germain-En-Laye. Half of a day has been required to operate on site the whole experiment and then conduct measurements of the local gravitational force by reconstructing the total acceleration vector. In Chapter 7, we detail the results obtained from the 3-axis hybrid accelerometer on this operation.

Conclusion

In this chapter, we have presented the apparatus of the 3-axis hybrid accelerometer. It offers a complete reliable system to operate 3-axis atom interferometry with the hybridization of classical accelerometers to measure ultimately continuous acceleration in the three spatial directions without biases. We demonstrated a reasonable compactness to operate outside of the laboratory. Strong integration of the instrument is required mainly for civil applications (commercial flight and marine). For strategic applications, the current technology (Frequency doubled telecom laser, compact vacuum system) is already compliant in terms of integration.

Technological developments to miniaturize each subsystem pave the way to more and more compact cold atom interferometers. The atom chip [67] is a compact solution to produce cold or ultracold atoms in magnetic traps. However the proximity of the surface is not ideal for atom interferometry. Complete integrated laser systems based on telecom components and frequency doubling, developed for compact gravimeter and cold atom interferometer experiments in microgravity [68], are compact and are now available commercially. Another approach by HUB [69], adopted for the sounding rocket BEC experiment (MAIUS), consists in miniaturization of semiconductor GaAlAs technology-based laser source. The next step to fully miniaturize the laser system requires other approaches such as Photonic Integrated Circuits (PIC). In this spirit, some developments of key components have been developed for optical clocks [70]. In addition, the development of mini vacuum cells to reduce the size of the sensor head is a necessary challenge [15]. One difficulty is to simplify the pumping system to remove or reduce the size of the ion pump. The company ColdQuanta develops Si/SiO2 technologies to build compact “all glass” compact systems [71].

The rotational platform is useful to tilt the sensor head in any orientation to calibrate the sensor. In particular, the calibration of the triad misalignment is a key procedure to reconstruct the total acceleration vector. Besides, the mobile platform allows to move the whole apparatus easily. For now, this platform is used to transport the sensor and to measure statically accelerations. In the near future, the 3-axis hybrid accelerometer will be used for mobile applications. Some improvements are still needed to operate dynamically, for instance the rotations need to be measured with gyroscopes. A full inertial navigation system (INS) integrating the 3-axis hybrid accelerometer will be operational with this apparatus by adding three gyroscopes on the apparatus to control and track the rotations.

Chapter 4

Agile integrated laser using advanced electro-optic modulation

This chapter presents the fiber laser system integrated into a compact rack and dedicated to our 3-axis atom interferometer. The architecture is based on a novel electro-optic modulation approach with an IQ modulator at 1560 nm and a second harmonic generation stage to reach 780 nm. This chapter describes as well the RF source adapted to this specific modulation and the fiber bench operating at 780 nm to split, switch and recombine the laser beams for the 3-axis atomic sensor head.

Contents

4.1 Agile laser system using advanced electro-optic modulation 114

4.1.1 Electro-optic modulation 114

4.1.2 CS-DSSB modulation with an IQ modulator 115

4.1.3 Laser architecture 119

4.1.4 Optical spectrum measurements of the modulated laser source 122

4.1.5 Resonant transitions produced by residual parasitic lines . . 125

4.1.6 Phase shift induced by parasitic lines 126

4.1.7 Splitting, recombining and switching fiber optical bench . . 130

4.1.8 Rack integration 132

4.2 RF Source 133

4.2.1 Architecture and spectrum 133

4.2.2 Phase noise 134

4.2.3 Frequency stability 135

4.2.4 Phase non-linearity of RF-filters 137

4.2.5 Hybrid coupler 138

4.3 Laser architecture improvements 140

4.3.1 IQ modulator operating at 780 nm 140

4.3.2 Single diode architecture based on a discrete lock 141

Introduction

Laser sources represent one of the most crucial and complex parts for atom interferometry. Since decades many efforts have been conducted to simplify, reduce size and power consumption of laser systems. In one hand, turn-key and straightforward laser systems depict an answer to facilitate development of complex experiments in science academy and in the other hand, a crucial and strategic side of supply-chain items dedicated to future industrial instruments based on atomic physics. Off-the-shelf telecom components benefits from a deep development since decades and are good candidates to fill this mission.

The use of telecom components and periodically-poled lithium-niobate crystal (PPLN) for laser cooling was first demonstrated in [72] and opened the field of telecom doubled laser architectures for atomic physics community. It affords the strength of reliable and robust off-the-shelf telecom components and can be frequency doubled by a PPLN to reach the wavelengths of atomic transitions. MuQuans developed a commercial solution based on that technology and proved its robustness for quantum gravimeters and fundamental physics instruments [18, 73]. Nonetheless, the use of two separate laser diodes, one operating at each frequency, requires an optical phase lock [74, 75]. Within the scope of all-fibered laser systems, the team of the ICE experiment [68] designed an architecture with phase modulation and frequency doubling for laser cooling and atom interferometry. Here, a frequency offset master-slave scheme offers frequency agility by controlling the current of the slave diode, but are typically limited in bandwidth and dynamic range by the electronics. Electro-optically generated sidebands in a servo-locked system can also achieve good frequency agility [76, 77, 5]. To simplify further such architectures, multiple-frequency electro-optic modulation generates multiple-frequency spectrum controlled by RF source with a single phase modulator [78]. However, the use of pure phase modulation generates parasitic sidebands that are detrimental to atom interferometers, as they produce both a systematic measurement bias and spatial variations in fringe contrast [79, 9]. Single-sideband (SSB) modulation using an IQ modulator has been shown to strongly reduce the effect of parasitic lines [80]. There, however, the carrier frequency was used as one of the Raman lasers, thus the tunability of laser source was realized by controlling the carrier.

The laser requires two frequencies with an accuracy of ~ 100 kHz. A typical atom interferometer sequence also demands tunability over a range of ~ 1 GHz near the atomic transition, and sub-ms response times. Specifically, for a Raman interferometer, the two optical frequencies must be phase coherent, with a relative phase noise below

60 dBc/Hz at 10 Hz offset.

In the frame of iXatom laboratory, we have developed a scheme for atom interferometry by using the IQ modulator as the key central component. A new 780 nm laser architecture is demonstrated based on carrier-suppressed dual single-sideband (CS-DSSB) modulation in an all-fibered IQ modulator operating at 1560 nm. Here, electro-optic modulation techniques are utilized to generate two "principal" optical sidebands, while suppressing the carrier frequency and other parasitic lines. These principal sidebands are controlled in frequency, phase and power in the RF domain—affording all the benefits of modern RF sources in terms of agility, stability and response time. With this system, we realize a complete interferometer sequence—including atom trap loading, sub-Doppler cooling, state preparation, interrogation, and detection—using only RF modulation while holding the carrier frequency of the laser fixed. We estimate the phase shift induced by parasitic lines from CS-DSSB by applying a model similar to [79] and prove its compatibility for inertial sensing.

4.1 Agile laser system using advanced electro-optic modulation

4.1.1 Electro-optic modulation

Electro-optic effect is an anisotropic effect describing the change of the refractive index in a crystal depending on an electric field. Lithium Niobate ($LiNbO_3$) is a commonly used crystal for electro-optic modulation applications. The phase modulator is a simple example. Two electrodes, placed at the surface of the crystal, transfer an AC electric field which modulates the light passing throw the component. It generates an optical-frequency comb controlled directly by the frequency modulation. This straightforward technic allows to convert electric field from microwave and RF band domain into optical frequency band.

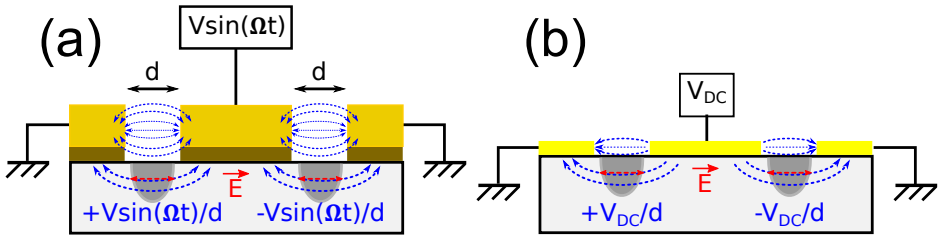

Figure 4.1: Side-cut view of (a) AC modulation electrodes and (b) DC phase bias electrodes of a $LiNbO_3$ electro-optic MZI in X-cut modulation.

Figure 4.1 displays a side-cut view of an electro-optic Mach-Zehnder Interferometer (MZI) in X-cut architecture. Anisotropic Pockels coefficient r_{33} of Lithium Niobate ($LiNbO_3$) in the X-cut crystallographic plane leads to a transverse modulation of optical electric field $\vec{E} = e^{i\frac{2\pi}{\lambda_0}ct}$, as $\overrightarrow{E}_{\text{output}} = \vec{E}e^{i\Delta\varphi}$ in one arm of the electro-optic MZI. Ellipsoid index formalism provides birefringent extraordinary index $n_e(E_{\text{mod}}(t)) = n_e(0) - \frac{1}{2}r_{33}n_e^3(0)E_{\text{mod}}(t)$ [81] where modulation electric-field $E_{\text{mod}}(t) = -\frac{V}{d}\sin(\Omega t)$ derives from the electric potential $V\sin(\Omega t)$ by considering a distance of d between the electrodes. The total phase induced by AC and DC electric fields in one arm of length L is then given by:

$$\begin{aligned}
\Delta\varphi &= \vec{k}\cdot\vec{r} \\
&= n(E)\tfrac{2\pi}{\lambda_0}L \\
&= n_e(0)\tfrac{2\pi}{\lambda_0}L + \pi\tfrac{L}{d}\tfrac{r_{33}n_e^3(0)}{\lambda_0}\left(V\sin(\Omega t) + V_{DC}\right) \\
&= \varphi_0 + \beta\sin(\Omega t) + \tfrac{\Delta\Phi}{2}
\end{aligned}$$

with $r_{33} = 30.9$ pm/V and $n_e = 2.2$. φ_0 represents an intrinsic phase induced by the material and is common to each arm of the electro-optic MZI. For that reason

this phase is generally not considered into calculation. Modulation depth is defined as $\beta = \frac{\pi}{2}\frac{V_{pp}}{V_\pi}$ where $V_{pp} = 2V$ is the peak-to-peak amplitude of the electric potential and $V_\pi = \frac{d}{L}\frac{\lambda_0}{r_{33}n_e^3(0)}$ is the half-wave voltage, which represents the voltage needed to shift the phase by π. $\frac{\Delta\Phi}{2}$ is a DC phase bias required to operate the electro-optic MZI over different modulation schemes. It allows to control where the modulation occurs in the sinusoidal response of the MZI. Typically four analog modulation schemes are used, $\pm\pi/2$ schemes to modulate linearly, 0 and π schemes to control the amplitude of the optical carrier. V_π is sensitive to the dimensions of the optical waveguides (width d and length L) and is optimized to be as small as possible in the design. Those waveguides are formed by Titanium diffusion into the $LiNbO_3$. The optical electric field and the electric field modulation have to be on the same spatial plane to perform correctly the electro-optic conversion.

4.1.2 CS-DSSB modulation with an IQ modulator

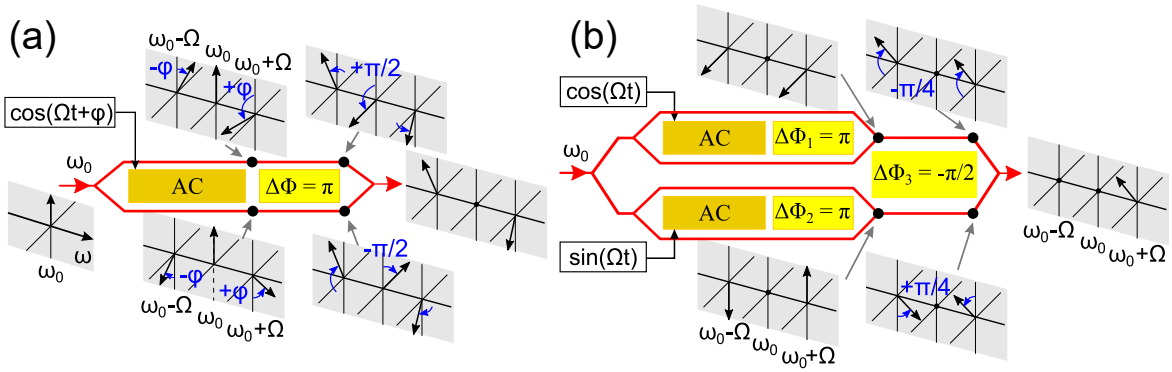

Figure 4.2: (a) Schematic of an electro-optic MZI operating in CS-DSB modulation. (b) Schematic of the IQ modulator operating in CS-SSB modulation.

Figure 4.2(a) presents the simple case of a MZI operating a carrier-suppressed dual sideband modulation (CS-DSB). The sidebands generated by the modulation are shifted by π between the two arms of the MZI because the direction of the electric field is inverted between the two arms (push-pull configuration). Then the condition $\Delta\Phi = \pm\pi$ on the DC electrodes guarantees destructive interferences of the carrier. The input RF phase φ determines the relative phase between the two remaining sidebands.

The In-phase and Quadrature (IQ) modulator consists of three optically-guided MZIs, two sub-MZIs nested inside a main one. A schematic of the IQ modulator, operating a carrier-suppressed single-sideband modulation (CS-SSB) [82, 83], is shown in Fig.4.2(b). The primary function of each sub-MZI is to suppress the optical carrier frequency, similarly to CS-DSB modulation with $\Delta\Phi_1$ and $\Delta\Phi_2 = \pm\pi$. The frequency Ω modulates the two sub-MZIs with $\cos(\Omega t)$ and $\sin(\Omega t)$, obtained by adjusting φ. This results in carrier-suppressed optical signals which are in-quadrature with one

another. These two signals are then combined in the main MZI, where the bias phase $\Delta\Phi_3$ determines the surviving harmonics. Specifically, the upper sideband (order $+1$) remains when $\Delta\Phi_3 = -\pi/2$, whereas the lower sideband (order -1) survives for $+\pi/2$. Some higher-order sidebands also constructively interfere but are strongly reduced in amplitude. CS-DSSB modulation is completely analogous to CS-SSB modulation, except two separate RF signals are injected into the IQ modulator—generating two independent sidebands. The relative phase between these optical signals is directly controlled by the RF source.

We present now the calculation of CS-DSSB modulation with an IQ modulator. The optical carrier at the input of the IQ modulator is defined as $E = E_0 e^{i(\omega_0 t + \phi_0)}$. RF modulation phases are set as ϕ_1 and ϕ_2. Their index of modulation are respectively $\beta_1 = \pi \frac{V_{\text{pp1}}}{V_\pi}$ and $\beta_2 = \pi \frac{V_{\text{pp2}}}{V_\pi}$ where V_{pp1} and V_{pp2} represent the amplitude of each modulation and V_π is the half-wave voltage of the two sub-MZI. We obtain the following electric fields at the output of the two sub-MZI:

$$E_1 = \frac{E}{4}\left[e^{i[\beta_1 \cos(\Omega_1 t+\phi_1)+\beta_2 \cos(\Omega_2 t+\phi_2)]} e^{i\frac{\Delta\Phi_1}{2}} + \text{C.C.}\right] \tag{4.1}$$

$$E_2 = \frac{E}{4}\left[e^{i[\beta_1 \sin(\Omega_1 t+\phi_1)+\beta_2 \sin(\Omega_2 t+\phi_2)]} e^{i\frac{\Delta\Phi_2}{2}} + \text{C.C.}\right] \tag{4.2}$$

The total electric field at the output of the IQ modulator is:

$$E^{\text{IQ}} = E_1 e^{i\Delta\Phi_3} + E_2 \tag{4.3}$$

By using the following rules, where $J_n(z)$ represents Bessel function of the first kind at nth order and evaluated in z:

$$e^{i\beta \sin(\theta)} = \sum_{n\in\mathbb{Z}} J_n(\beta) e^{in\theta} \tag{4.4}$$

$$e^{i\beta \cos(\theta)} = \sum_{n\in\mathbb{Z}} i^n J_n(\beta) e^{in\theta} \tag{4.5}$$

$$J_n(-\beta) = (-1)^n J_n(\beta) \tag{4.6}$$

we can develop the electric fields from the MZIs with CS-DSSB modulation parameters and we obtain:

$$E^{\mathrm{IQ}}_{\mathrm{CS-DSSB}} = E_0 \sum_{n,m\in\mathbb{Z}^2} A^{\mathrm{IQ}}_{n,m} e^{i\left[\Omega^{\mathrm{IQ}}_{n,m}t+\phi^{\mathrm{IQ}}_{n,m}\right]} \tag{4.7}$$

where amplitude, frequency and phase are:

$$A^{\mathrm{IQ}}_{n,m} = \sin\left((n+m)\frac{\pi}{2}\right)\sin\left((n+m+1)\frac{\pi}{4}\right)J_n(\beta_1)J_m(\beta_2) \tag{4.8}$$

$$\Omega^{\mathrm{IQ}}_{n,m} = \omega_0 + n\Omega_1 + m\Omega_2 \tag{4.9}$$

$$\phi^{\mathrm{IQ}}_{n,m} = \phi_0 + n\phi_1 + m\phi_2 + (3n+3m+1)\frac{\pi}{4} \tag{4.10}$$

Figure 4.3(a) shows an example of a theoretical spectrum obtained with an ideal IQ modulator. Sidebands $\Omega^{\mathrm{IQ}}_{1,0}$ and $\Omega^{\mathrm{IQ}}_{0,1}$ are the two main ones and are separated by the difference of the modulation frequencies $\Omega_2 - \Omega_1$ chosen to address the hyperfine transition of ^{87}Rb. According to Eq. 4.8, harmonics with sum $n+m$ even are suppressed, and odd-sum harmonics are reinforced by IQ modulator. For example, the two target harmonics in our case are $n(m) = 0, 1$ $(1, 0)$, both of which correspond to a sum of $n + m = 1$. The residual sidebands are suppressed by at least 28 dB. All other combinations of n and m correspond to a different output frequency $\Omega^{\mathrm{IQ}}_{n,m}$, with a reduced field amplitude $E_0 A^{\mathrm{IQ}}_{n,m}$ due to the higher order Bessel functions involved.

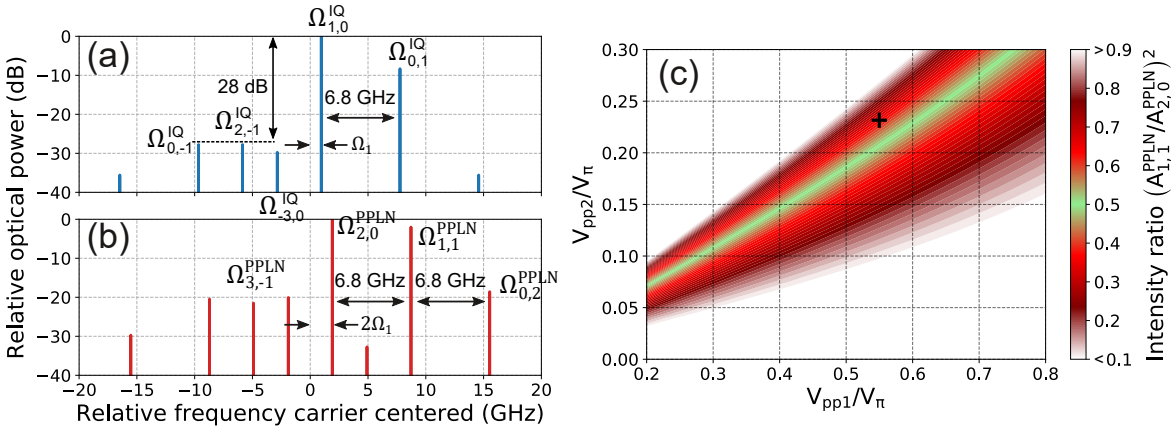

Figure 4.3: Optical spectra model for CS-DSSB modulation of an ideal IQ modulator at 1560 nm (a) and after a PPLN at 780 nm (b). (c) Intensity ratio of the two main lines after the PPLN driving Raman transitions depending on the modulation depths of the RF modulations. The contour scale is centered for an intensity ratio of 1/2 between the two main lines. The cross displays the modulation depths $V_{\mathrm{pp1}}/V_\pi = 0.55$ and $V_{\mathrm{pp2}}/V_\pi = 0.23$ used for the two spectra in (a) and (b), it is chosen to cancel constant light shifts and reduce parasitic interferometers in our experiment.

Electric field after second-harmonic generation (SHG) is deduced from the square of Eq. 4.7 weighted by the efficiency of the PPLN. We suppose the quasi phase-matching

fulfilled and we ignore the frequency dependency of the efficiency:

$$E^{\mathrm{PPLN}}_{\mathrm{CS-DSSB}} = \epsilon_0 \chi^2 E_0^2 \sum_{N,M\in\mathbb{Z}^2} A^{\mathrm{PPLN}}_{N,M} e^{i\left[\Omega^{\mathrm{PPLN}}_{N,M} t + \phi^{\mathrm{PPLN}}_{N,M}\right]} \tag{4.11}$$

where ϵ_0 is the permittivity of vacuum, χ is the susceptibility of the medium of the PPLN. Here the amplitude $A^{\mathrm{PPLN}}_{N,M}$, frequency $\Omega^{\mathrm{PPLN}}_{N,M}$ and phase $\phi^{\mathrm{PPLN}}_{N,M}$ resulted from SHG are:

$$\begin{aligned} A^{\mathrm{PPLN}}_{N,M} = \sum_{n,m\in\mathbb{Z}^2} & \sin\left((n+m)\frac{\pi}{2}\right)\sin\left((N+M-n-m)\frac{\pi}{2}\right) \\ & \sin\left((n+m+1)\frac{\pi}{4}\right)\sin\left((N+M-n-m+1)\frac{\pi}{4}\right) \\ & J_n(\beta_1)J_{N-n}(\beta_1)J_m(\beta_2)J_{M-m}(\beta_2) \end{aligned} \tag{4.12}$$

$$\Omega^{\mathrm{PPLN}}_{N,M} = 2\omega_0 + N\Omega_1 + M\Omega_2 \tag{4.13}$$

$$\phi^{\mathrm{PPLN}}_{N,M} = 2\phi_0 + N\phi_1 + M\phi_2 + (3N+3M+1)\frac{\pi}{4} \tag{4.14}$$

Figure 4.3(b) presents a theoretical spectrum of CS-DSSB modulation followed by SHG. Three main sidebands derived from the two main sidebands of the CS-DSSB spectrum: the doubling parts $\Omega^{\mathrm{PPLN}}_{2,0} = 2\Omega^{\mathrm{IQ}}_{1,0}$ and $\Omega^{\mathrm{PPLN}}_{0,2} = 2\Omega^{\mathrm{IQ}}_{0,1}$ and the sum part $\Omega^{\mathrm{PPLN}}_{1,1} = \Omega^{\mathrm{IQ}}_{1,0} + \Omega^{\mathrm{IQ}}_{0,1}$. We want to maximise the sidebands $\Omega^{\mathrm{PPLN}}_{2,0}$ and $\Omega^{\mathrm{PPLN}}_{1,1}$, separated by $\Omega_2 - \Omega_1$, and minimize the others. Equation 4.12 informs us how to adjust the modulation depths $\beta_1 = \pi\frac{V_{\mathrm{pp1}}}{V_\pi}$ and $\beta_2 = \pi\frac{V_{\mathrm{pp2}}}{V_\pi}$. For instance, Figure 4.3(c) exhibits the intensity ratio between the two main lines and offers various conditions to cancel constant light shifts at first order [7].

As explained in Section 4.1.6, pair of lines separated by $\Omega_2 - \Omega_1 = \Omega^{\mathrm{PPLN}}_{N+1,M+1} - \Omega^{\mathrm{PPLN}}_{N+2,M}$ induces Raman transitions and involve coupling between electrical fields $E^{\mathrm{PPLN}}_{N+1,M+1}$ and $E^{\mathrm{PPLN}}_{N+2,M}$. The main pair of sidebands $\Omega^{\mathrm{PPLN}}_{2,0}$ and $\Omega^{\mathrm{PPLN}}_{1,1}$ drives the atom interferometer, whereas the other pairs create parasitic interferometers and can lead to large phase bias. We proved in Section 4.1.6 that it exists an ideal ratio to nearly cancel the effect of the two largest parasitic contributions, coming from the pair $\Omega^{\mathrm{PPLN}}_{2,0}$ and $\Omega^{\mathrm{PPLN}}_{3,-1}$ and the pair $\Omega^{\mathrm{PPLN}}_{1,1}$ and $\Omega^{\mathrm{PPLN}}_{0,2}$. The modulation depths used in Fig. 4.3 are the ones used in our experiment. They are optimized to simultaneously cancel the first order light shifts and minimize the contribution from parasitic lines.

Furthermore, for atom interferometry, the relative phase of the two Raman lines has to be precisely controlled. It can be deduced from Eq. 4.14:

$$\phi^{\mathrm{PPLN}}_{N+1,M+1} - \phi^{\mathrm{PPLN}}_{N+2,M} \quad = \quad \phi_2 - \phi_1 \tag{4.15}$$

This key property allows to control very precisely the relative phase of Raman lines directly with the relative phase of the two frequency modulations.

4.1.3 Laser architecture

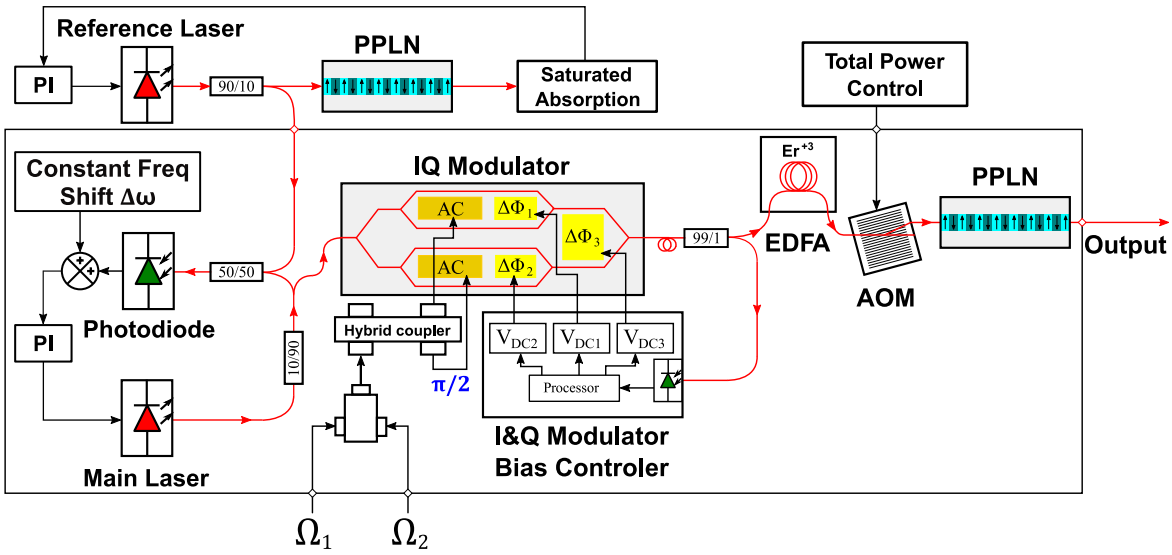

Figure 4.4: Scheme of the laser architecture. The laser system rack is delimited into the square black box. The reference laser with the saturated absorption is integrated into an external rack. PI: Proportional Integrator controller ; EDFA: Erbium-Doped Fiber Amplifier ; AOM: Acousto-Optic Modulator ; PPLN: Periodically-Poled Lithium-Niobate crystal

The architecture of the laser system is presented in Fig. 4.4. The telecom-domain IQ modulator (iXblue MXIQER-LN-30) is operating in CS-DSSB modulation. Each MZI has a broad modulation bandwidth of 30 GHz. An RF signal, containing the two frequencies Ω_1 and Ω_2, is sent through a hybrid coupler, which equally splits the signal and phase shifts one arm by $\pi/2$. The resulting two RF signals are sent to the AC electrodes of each sub-MZI. The modulator bias voltage controller (iXblue IQ-MBC-LAB) delivers three continuous voltages to the DC electrodes to control and stabilize in real time the bias phases of each MZI ($\Delta\Phi_1$, $\Delta\Phi_2$, and $\Delta\Phi_3$). This DC bias lock is realized by modulating the light passing through each sub-MZI with two orthogonal frequencies around 1 kHz, and deriving an error signal from the FFT of the corresponding optical signals. This control is critical since these phases can drift dramatically due to temperature sensitivity and internal charge dynamics. The optical loss in the IQ modulator ($\sim$ 12 dB in our case) depends on the total injected RF

power. The remaining 500 μW of optical power is sufficient to saturate the double-stage erbium-doped fiber amplifier (EDFA) after the modulator. The EDFA then outputs 2 W at 1560 nm with a $\sim$ 1% power stability. This light subsequently undergoes second-harmonic generation (SHG) to 780 nm in a periodically-poled lithium-niobate (PPLN) crystal waveguide. A fibered acousto-optic modulator (AOM), located between the EDFA and the PPLN waveguide, controls the total output power, which is 485 mW at maximum.

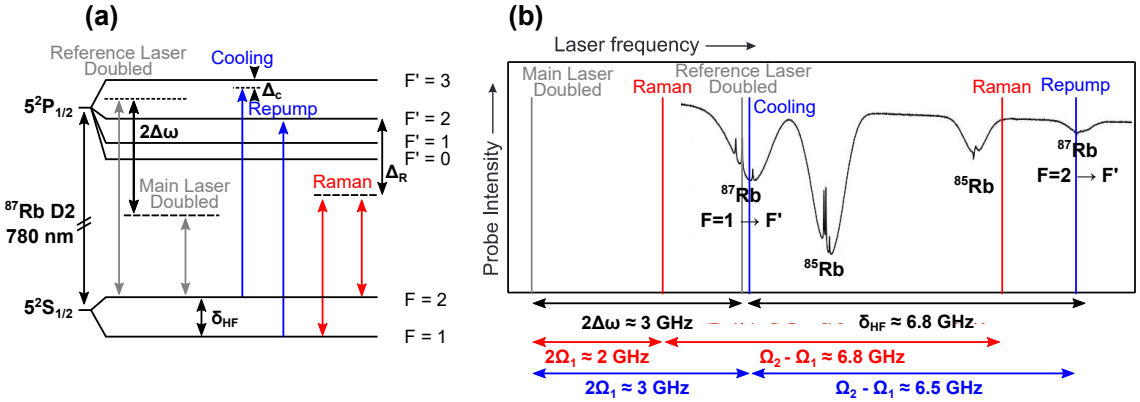

Figure 4.5: (a) Hyperfine structure and (b) spectroscopy of ^{87}Rb D2 transitions with frequency operations for cooling (in blue) and Raman interferometry (in red). In grey, the frequency of the reference laser and the main laser are frequency doubled reaching the atomic transitions at 780 nm.

Figure 4.5 presents the frequency operations for cooling and atom interferometry on ^{87}Rb. The reference laser diode is locked on the $F = 2 \rightarrow F' = (2, 3)$ crossover D2 transition of ^{87}Rb using saturated absorption spectroscopy. The main laser (Redfern Integrated Optics external-cavity diode laser at 1560 nm, 20 mW output power) is frequency locked to the red of the reference laser via an optical beatnote at $\Delta\omega \simeq 2\pi\times1.5$ GHz. For the laser-cooling phase, two principal sidebands are generated on the main laser at frequencies $\Omega_1 = \Delta\omega + (\delta_{32}/2 + \Delta_C)/2$ for cooling and $\Omega_2 = \Omega_1 + (\delta_{HF} - \delta_{32})$ for repumping, both of which are blue-shifted from the reference laser. Here, $\delta_{32}/2\pi \simeq 266$ MHz is the splitting between excited states $F' = 2$ and $F' = 3$, $\delta_{HF}/2\pi = 6.834$ GHz is the ground-state hyperfine splitting, and $\Delta_C/2\pi \simeq -20$ MHz is the optical detuning from the cycling transition used for laser cooling. Similarly, for Raman interferometry, $\Omega_1 = \Delta\omega + (\Delta_R - \delta_{32}/2)/2$ and $\Omega_2 = \Omega_1 + \delta_{HF}$, where Δ_R is the detuning of the Raman beams from $F = 2 \rightarrow F' = 2$.

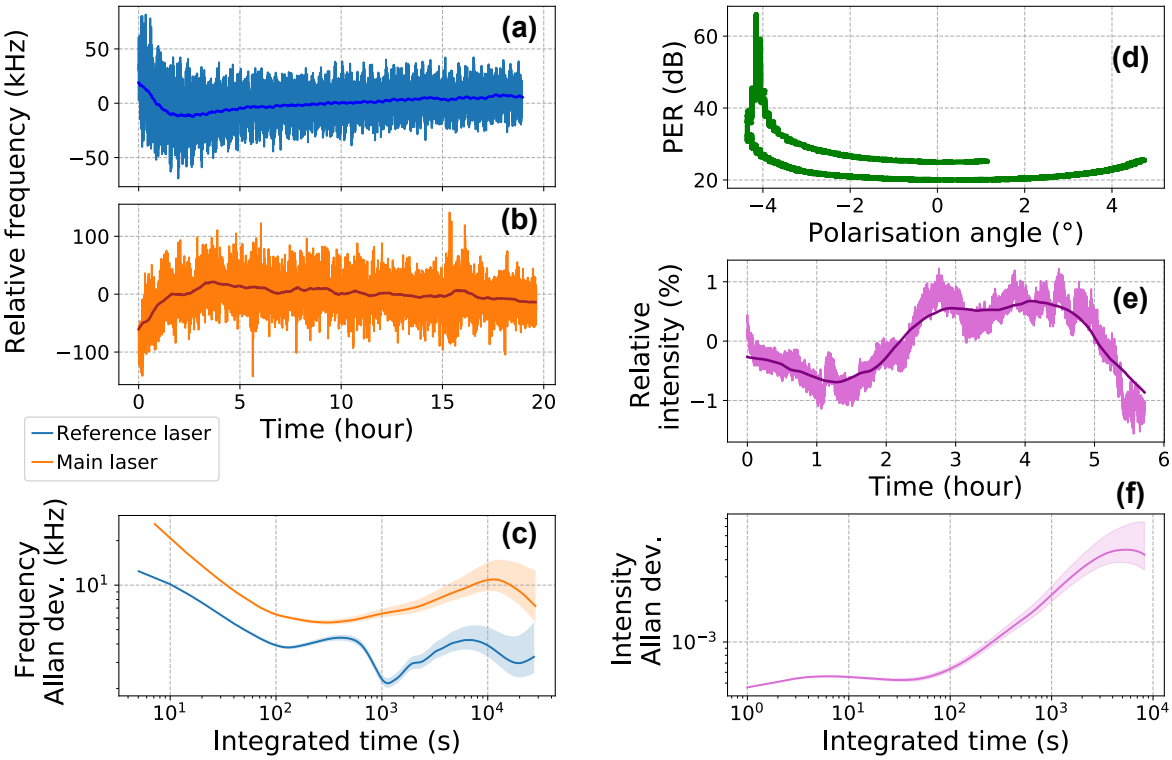

Figure 4.6: Frequency, intensity and PER stability of the laser source. The frequency measurements are recorded at 1560 nm and the PER and intensity ones at 780 nm. On time-series graphs ((a), (b) and (e)), the darker lines expose a one hour moving averaged of the data. On Allan deviation graphs ((c) and (f)), the lighter fills correspond to the confidence interval. The polarization diagram (d) presents the PER as a function of the angle of the polarization for different axes of the fiber bench.

Figure 4.6 shows the long term performances in frequency, intensity and PER of the laser source. The frequency measurements are recorded with a beatnote at 1560 nm with a laser stabilized on a saturated absorption of ^{87}Rb which have been validated with a stable optical comb (1.5 kHz after 10^3 s). The reference and main lasers present a 10 kHz long-term stability, corresponding to 20 kHz after SHG. The relative intensity at 780 nm is stable at 1% and the polarization extinction ratio (PER) at 780 nm is 20 dB. The polarization profile on Fig. 4.6 presents the PER as a function of the angle of the polarization. Due to the non-optimized optical injection into PM fiber, the polarization varies between elliptical polarization when PER $\simeq$ 20 dB and linear polarization when PER $\rightarrow \infty$ dB. This profile is similar to a circle on the Poincaré sphere. Consequently, the polarization angle swaps between -4° and +6° corresponding to the two purely linear polarization states. It can be critical for sensitive components to the linear polarization (*e.g.* LCR waveplates, see Chapter 3 for more details).

4.1.4 Optical spectrum measurements of the modulated laser source

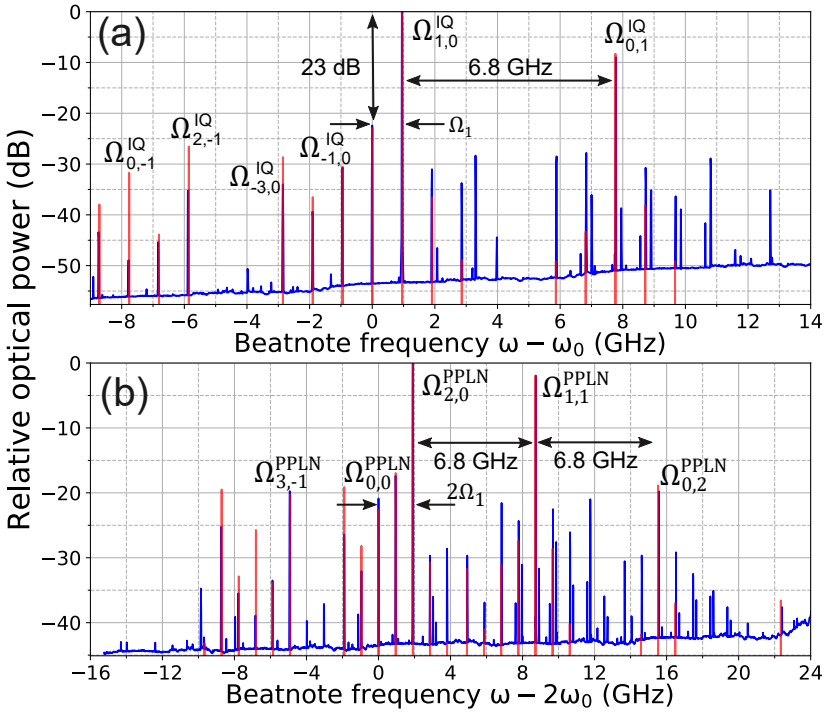

Figure 4.7: Frequency spectrum after CS-DSSB modulation at 1560 nm (a) and 780 nm (b). Blue lines show measured spectra obtained with a beatnote with a stable local oscillator at 1560 nm and 780 nm, respectively. To suppress the light shift at first order, the input RF power is 17 dBm and 9 dBm for Ω_1 and Ω_2, respectively, corresponding to modulation depths of 0.55 and 0.23. Red lines correspond to the numerical model.

Figure 4.7(a) shows an example of the spectrum obtained after CS-DSSB modulation at 1560 nm using a beatnote with the reference laser. Due to the limited bandwidth of the photodiode ($\sim$ 10 GHz), we combined several truncated frequency scans. In each scan, we shifted the local oscillator such that the peaks lied within the sensitivity band, and we renormalized the spectrum by the detector's transfer function. This had the effect of increasing the noise floor at certain frequencies. Before the SHG, we demonstrate a suppression of the carrier ω_0 by $\sim$ 23 dB and all other parasites below 25 dB. The two principal sidebands $\Omega_{1,0}^{\mathrm{IQ}} = \omega_0 + \Omega_1$ and $\Omega_{0,1}^{\mathrm{IQ}} = \omega_0 + \Omega_2$, are offset from the carrier by $\Omega_1/2\pi \approx 1$ GHz and are separated by $\Omega_2 - \Omega_1 = \delta_{\mathrm{HF}}$. Similarly, the optical spectrum at 780 nm (*i.e.* after the PPLN) is shown in Fig. 4.7(b). Here, the primary laser lines used for cooling and interferometry are labelled $\Omega_{2,0}^{\mathrm{PPLN}} = 2\omega_0 + 2\Omega_1$ and $\Omega_{1,1}^{\mathrm{PPLN}} = 2\omega_0 + \Omega_1 + \Omega_2$. These two frequencies are mainly generated by doubling $\Omega_{1,0}^{\mathrm{IQ}}$ and by summing $\Omega_{1,0}^{\mathrm{IQ}} + \Omega_{0,1}^{\mathrm{IQ}}$, respectively. The highest parasitic line $\Omega_{1,0}^{\mathrm{PPLN}}$ is suppressed by 17 dB and the carrier $\Omega_{0,0}^{\mathrm{PPLN}}$ by 21 dB.

Several effects are taken into account in the numerical model shown in Fig. 4.7. The

level of carrier suppression is determined by the accuracy of bias phases $\Delta\Phi_1$ and $\Delta\Phi_2$. The suppression of all other sidebands is influenced by a combination of the bias phase $\Delta\Phi_3$, and the phase and amplitude imbalance caused by the hybrid coupler. These imbalances are measured and input into the model. The IQ modulator can also exhibit several manufacturing defects, such as asymmetries between the arms of the MZIs and irregularities in the electrodes, which can produce additional lines. The PPLN then mixes all the lines through the process of SHG. Finally, we observe several lines in the spectra that are not predicted by the model. These are due to spurious frequencies generated by the RF source coming from harmonic distortion and mixing residues not completely suppressed by filters (see Section 4.2).

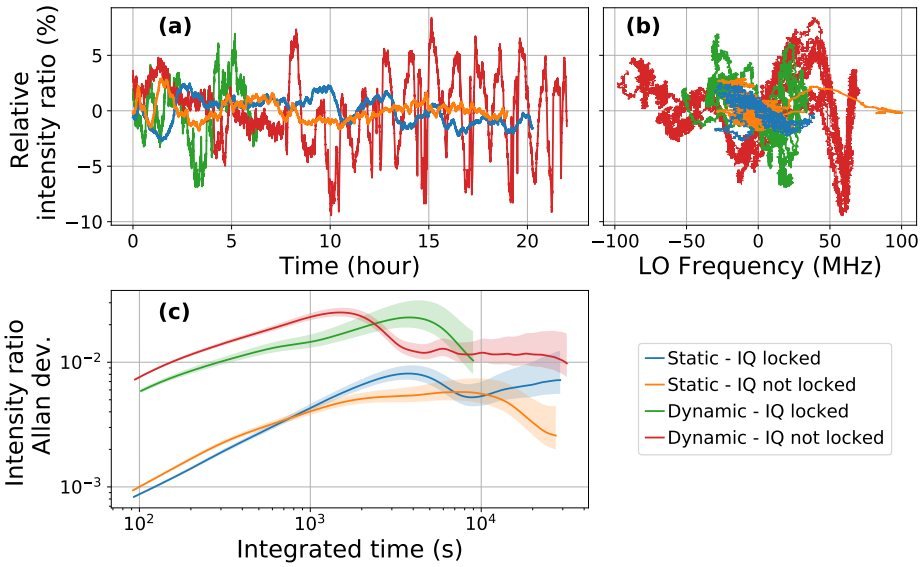

Figure 4.8: Intensity ratio stability of the two main lines $\Omega_{1,1}^{\mathrm{PPLN}}/\Omega_{2,0}^{\mathrm{PPLN}}$ at 780 nm after the PPLN in different conditions. The static case stands for no change of RF modulations, the dynamic one states for changes in frequency, power and phases of RF modulations during Raman interferometry experiments. These two cases are evaluated with and without the lock of the IQ modulator by the MBC. (a) Time series and (c) Allan deviation of measurements. (b) Correlations of the intensity ratio measurements with the frequency of the local oscillator (LO).

In Figure 4.8 and 4.9, we tracked the intensity of the sidebands from the optical spectrum obtained at 780 nm after the PPLN over a long period. We compare the efficiency of the lock of the modulator bias controller (MBC) when the experiment is running, meaning that the RF modulations are changing in amplitude, frequency and phase (dynamic) and at rest (static). Those measurements have been obtained by beating the light with a local oscillator (LO) at the same wavelength, as the experimental spectra from Fig. 4.7. We exhibit the intensity ratio between the two primary lines $\Omega_{2,0}^{\mathrm{PPLN}}$ and $\Omega_{1,1}^{\mathrm{PPLN}}$. Instability of this intensity ratio can lead to light shift instability. However, the correlation graph from Fig. 4.8(b) shows clear correlations

with the frequency of the local oscillator. This is due to the fact that our local oscillator cannot be frequency locked on a workable frequency for the optical beatnote. As a result, the intensity is changing because of the non flat response of the photodiode and the acquisition chain. Correction of the response with the transfer function is difficult because it fluctuates over time at small scale (10% fluctuation corresponds to $\simeq 0.4$ dB). Therefore, the instability measurements are over estimated. We can nevertheless state an upper limit of few % of intensity ratio stability.

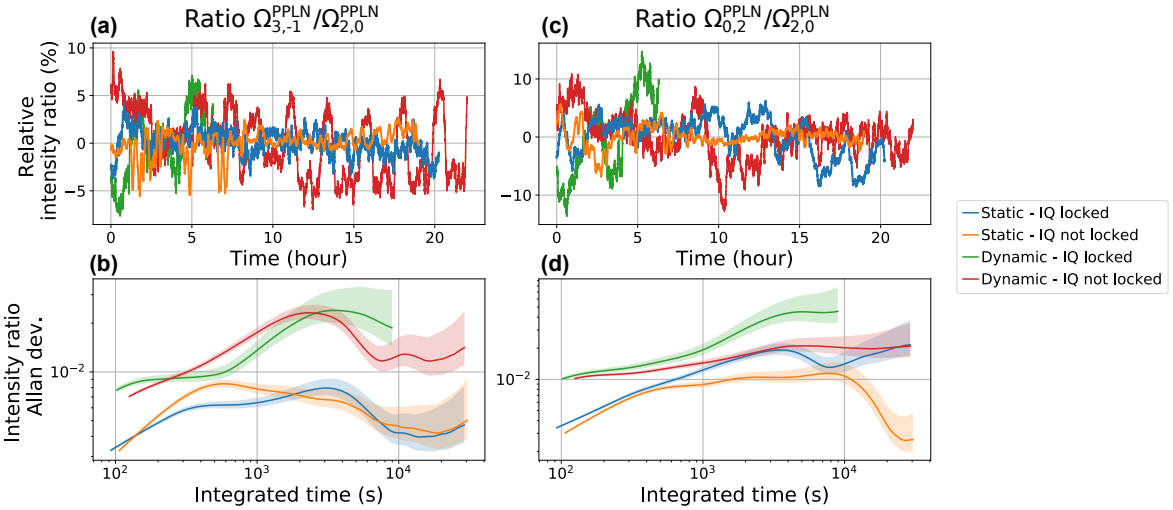

Figure 4.9: Intensity ratio stability of the sidebands $\Omega_{3,-1}^{PPLN}$ ((a) and (b)) and $\Omega_{0,2}^{PPLN}$ ((c) and (d)) compared to the highest one $\Omega_{2,0}^{PPLN}$ at 780 nm after the PPLN in different conditions.

Within the same frame, we measured the intensity ratio of the parasitic sidebands $\Omega_{3,-1}^{PPLN}$ and $\Omega_{0,2}^{PPLN}$ with the highest line $\Omega_{2,0}^{PPLN}$. These two parasitic lines are separated by the hyperfine transition from the two main lines and are the most responsible of parasitic interferometers by driving parasitic Raman transitions. This effect is studied in Section 4.1.6. As described earlier, due to the frequency change of the local oscillator, these measurements are over estimated but give an upper limit of few % of intensity ratio stability.

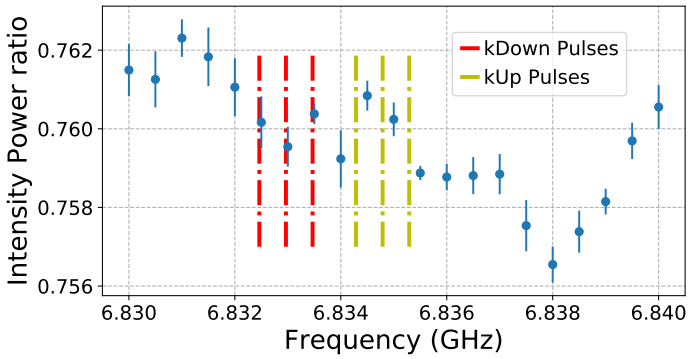

Figure 4.10: Intensity ratio at 780 nm between the two main sidebands in the frequency area of chirping. The frequency corresponds to the relative frequency between those two lines. The pulses are specified for an interferometer of T=20 ms and TOF=16 ms.

We investigated the effect of a frequency chirp during the atom interferometer on the intensity ratio between the two sidebands driving Raman transitions. Figure 4.10 presents this intensity ratio at 780 nm against the relative frequency in the area of the frequency chirp. We obtain a fluctuation below 0.2 %, which represents a negligible impact on light shifts compared to the influence of ratio instability in time.

4.1.5 Resonant transitions produced by residual parasitic lines

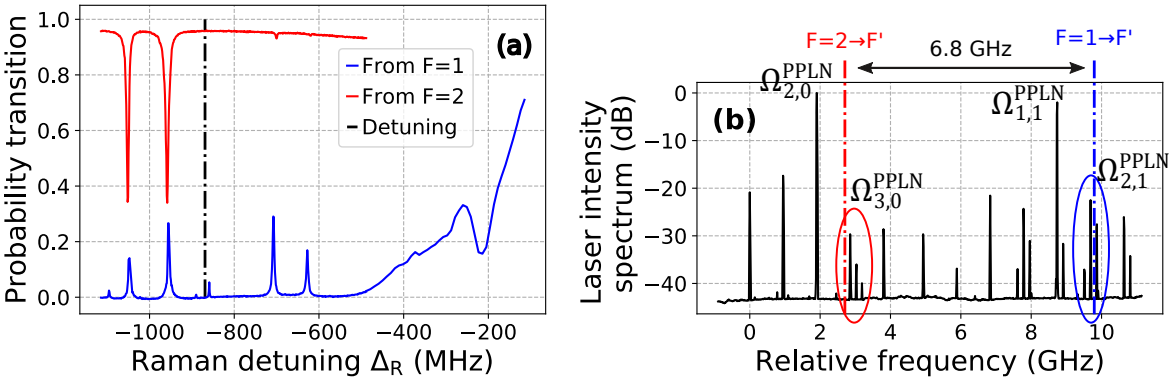

Figure 4.11: (a) One-photon parasitic resonant transitions experienced by the atomic cloud prepared in states $|F = 1\rangle$ and $|F = 2\rangle$ (blue and red respectively) for different Raman detuning Δ_R from $|F' = 2\rangle$. The black dashed line indicates the Raman detuning $\Delta_R = -870$ MHz used on the experiment. (b) Relative intensity spectrum of the laser where parasitic lines responsible for spontaneous emission are showed.

Residual parasitic lines, generated by the modulated laser source, can cross atomic transitions and create spontaneous emission during the Raman pulses, as shown in Fig. 4.11. To measure it, we set the resonance detuning δ at 10 MHz to not transfer atoms with 2-photon Raman transitions. We scan the Raman detuning Δ_R and evaluate

the parasitic one-photon transitions. Figure 4.11(a) displays the residual resonant transitions for different Raman detuning of the atomic cloud prepared in states $|F = 1\rangle$ and $|F = 2\rangle$. When the atoms are in state $|F = 2\rangle$, the parasitic transitions are coming from the residual line $\Omega_{3,0}^{\mathrm{PPLN}}$ and nearby residuals. For $|F = 1\rangle$ state, the line $\Omega_{2,1}^{\mathrm{PPLN}}$ and nearby residuals are responsible for the residual transitions. Figure 4.11(b) displays the intensity spectrum of the light and indicates the lines causing parasitic transitions. Additionally, for Raman detuning $\Delta_{\mathrm{R}} > -500$ MHz, the main Raman lines $\Omega_{2,0}^{\mathrm{PPLN}}$ and $\Omega_{1,1}^{\mathrm{PPLN}}$ are close to the atomic transition and produce spontaneous emission. We chose a Raman detuning $\Delta_{\mathrm{R}} = -870$ MHz to remove any one-photon parasitic transition during Raman interferometry.

4.1.6 Phase shift induced by parasitic lines

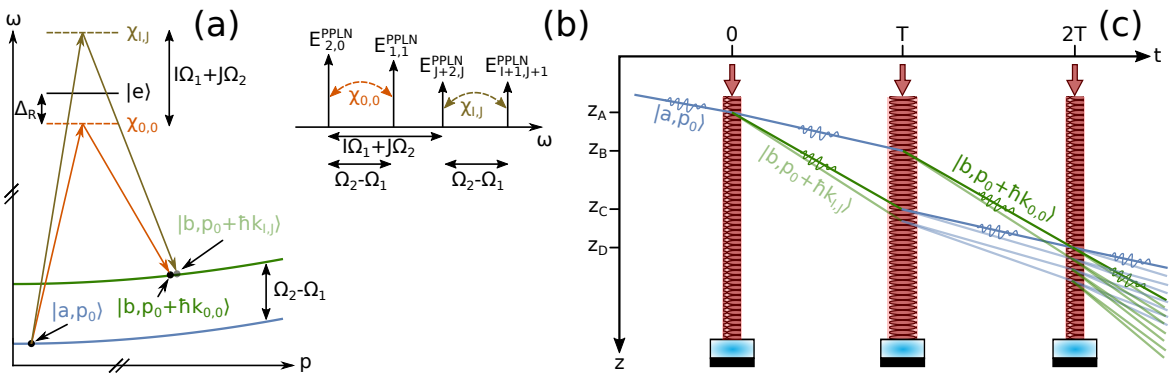

Figure 4.12: Illustration of the influence of a parasitic Rabi oscillation on atomic interferometer. The parasitic wavevector $k_{I,J}$ is defined as $k_{\mathrm{eff}} + I\Delta k_1 + J\Delta k_2$. (a) Frequency momentum dispersion of two hyperfine states coupled by Raman transition with the main Rabi oscillation $\chi_{0,0}$ and a parasitic one $\chi_{I,J}$. (b) Illustration of the pairs of lines contributing to the phase shift. (c) Spatio-temporal scheme of parasitic paths.

The impact on the interferometer phase shift with phase modulation has been studied in [79] and the model is adapted here for CS-DSSB modulation. We consider an atom interferometer in a gravimeter configuration where a mirror facing upward retro-reflects counter-propagating beams to drive velocity-sensitive Raman transitions. Pairs of lines $E_{I+2,J}^{\mathrm{PPLN}}$ and $E_{I+1,J+1}^{\mathrm{PPLN}}$ are separated by $\Omega_2 - \Omega_1 = \delta_{\mathrm{HF}}$ and generate Raman transitions between the two hyperfine states as illustrated in Fig. 4.12. The main pair $E_{2,0}^{\mathrm{PPLN}}$ and $E_{1,1}^{\mathrm{PPLN}}$ leads the atom interferometer, whereas the other pairs create parasitic paths and lead to parasitic interferometers converted into a phase shift. The effective Rabi frequency $\chi_{I,J}$ quantify the strength of coupling between the pair $E_{I+2,J}^{\mathrm{PPLN}}$ and $E_{I+1,J+1}^{\mathrm{PPLN}}$. Δ_{R} defines the Raman detuning of the main Rabi oscillation $\chi_{0,0}$ from the excited state $F' = 2$ and $\Delta_{\mathrm{R,I,J}} = \Delta_{\mathrm{R}} + I\Omega_1 + J\Omega_2$ for each parasitic Raman

transition. We ignore the contribution from the excited state $F' = 3$, which is three times smaller. Effective Rabi frequency can be expressed as:

$$\chi_{I,J} = \sqrt{\Lambda^{\mathrm{PPLN}}_{I+1,J+1}(\Lambda^{\mathrm{PPLN}}_{I+2,J})^* + (\Delta_{\mathrm{R,I,J}})^2} - |\Delta_{\mathrm{R,I,J}}| \tag{4.16}$$

where $\Lambda^{\mathrm{PPLN}}_{I+1,J+1}$ and $\Lambda^{\mathrm{PPLN}}_{I+2,J}$ are Rabi frequencies associated to single-photon transition. According to Equation 4.15, the relative phase between $E^{\mathrm{PPLN}}_{I+1,J+1}$ and $E^{\mathrm{PPLN}}_{I+2,J}$ depends only on the relative phase of the two RF modulations. Furthermore, for high Raman detuning $\Delta_{\mathrm{R,I,J}} \gg \Gamma$, effective Rabi frequency can be simplified as:

$$\chi_{I,J} \approx \chi_{0,0} \frac{A^{\mathrm{PPLN}}_{I+1,J+1} A^{\mathrm{PPLN}}_{I+2,J}}{\Delta_{\mathrm{R,I,J}}} \frac{\Delta_{\mathrm{R}}}{A^{\mathrm{PPLN}}_{1,1} A^{\mathrm{PPLN}}_{2,0}} \tag{4.17}$$

The amplitude of the sidebands generated after the SHG $A^{\mathrm{PPLN}}_{N,M}$ are defined in Eq. 4.12. The optical intensities are evaluated experimentally from the experimental spectrum showed in Fig. 4.7(b). Figure 4.14(c) presents the weight of each effective Rabi frequency. The key feature is coming from sidebands $\Omega^{\mathrm{PPLN}}_{3,-1}$ and $\Omega^{\mathrm{PPLN}}_{0,2}$ respectively, which are suppressed by 20 dB. These lines are coupled with the primary Raman lines $\Omega^{\mathrm{PPLN}}_{2,0}$ and $\Omega^{\mathrm{PPLN}}_{1,1}$ respectively as illustrated in Fig. 4.13, driving the Rabi oscillations $\chi_{1,-1}$ and $\chi_{-1,1}$ respectively which account for almost all of the systematic shift due to parasitic lines in Raman interferometers employing electro-optic phase modulators [79, 9].

Despite the low amplitude of $A^{\mathrm{PPLN}}_{3,0}$ and $A^{\mathrm{PPLN}}_{2,1}$ as shown in the spectrum of Fig. 4.7(b), the Rabi oscillation generated $\chi_{1,0}$ is larger than $\chi_{1,-1}$ or $\chi_{-1,1}$ in our case. This is due to their frequencies $\Omega^{\mathrm{PPLN}}_{3,0}$ and $\Omega^{\mathrm{PPLN}}_{2,1}$ which are nearby the excited state $F' = 2$, resulting in a small detuning $\Delta_{\mathrm{R},1,0} = \Delta_{\mathrm{R}} + \Omega_1 \simeq 0$ where in our case $\Delta_{\mathrm{R}}/2\pi \approx -1$ GHz and $\Omega_1/2\pi \approx 1$ GHz. This results in a singularity for the parasitic Raman transitions $\chi_{1,0}$ in Eq. 4.17 which is no longer valid. For that particular case, Eq. 4.16 is used. It is important to change the Raman detuning $\Delta_{\mathrm{R},1,0}$ to exclude the contribution from this parasitic Raman transition. For instance varying $\Omega_1 = \Delta\omega + (\delta_{32}/2 + \Delta_{\mathrm{C}})/2$, where $\Delta\omega$ is the relative frequency between the main laser and the reference laser, can increase the detuning $\Delta_{\mathrm{R},1,0}$ and remove the impact of $\chi_{1,0}$. However we characterized the effect from parasitic lines without changing it.

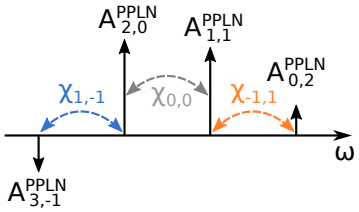

Figure 4.13: Illustration of the amplitude of the lines contributing to the largest parasitic Rabi oscillations $\chi_{1,-1}$ and $\chi_{-1,1}$. $A^{\mathrm{PPLN}}_{3,-1}$ and $A^{\mathrm{PPLN}}_{0,2}$ are in opposite sign according to Eq. 4.12, which leads to compensate their impact on the phase shift.

The parasitic recoil shift induced by the parasitic Raman transition is derived from the wavevector $k_{I,J} = k_{\mathrm{eff}} + I\Delta k_1 + J\Delta k_2 = k_{\mathrm{eff}} + \frac{2(I\Omega_1 + J\Omega_2)}{c}$. We consider an atomic cloud sufficiently cold (<3 μK), so that the atomic coherence length is much higher than the spatial separation between parasitic paths. Therefore the parasitic phase shift induced at each pulse for a given position relative to the mirror z can be expressed as:

$$\Delta\varphi(z) \quad = \quad \mathrm{Arg}\left(\sum_{I,J}\chi_{I,J}e^{i(I\Delta k_1 + J\Delta k_2)z}\right) \tag{4.18}$$

We notice that $\Delta\varphi(z)$ does not depend on $\chi_{0,0}$ (the argument of a positive real is null), which means that the phase shift resulting from parasitic interferometers is independent from the laser intensity.

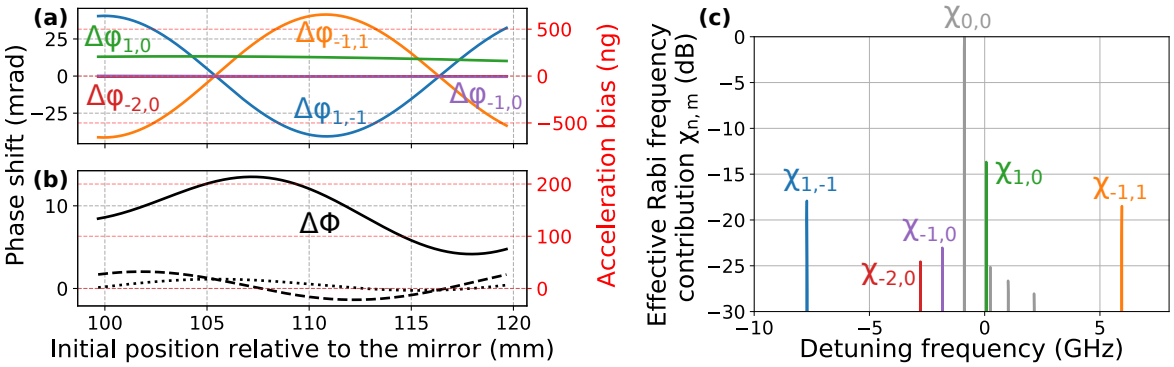

Figure 4.14: (c) Contribution of each parasitic Rabi oscillation with their respective impact on the phase shift as a function of the atom-mirror distance z_M on (a). (b) Predicted atom interferometer phase shift due to residual parasitic lines in solid line, with optimized parameters Ω_1 in dashed line and with optimized index modulations β_1 and β_2 in dotted line. Atom interferometer parameters: TOF=15 ms, T = 20 ms, $\Delta_{\mathrm{R}}/2\pi$=-877 MHz.

The total phase shift cumulated over the interferometer path is given by:

$$\Delta\phi = \Delta\varphi(z_{\mathrm{A}}) - \Delta\varphi(z_{\mathrm{B}}) - \Delta\varphi(z_{\mathrm{C}}) + \Delta\varphi(z_{\mathrm{D}}) \tag{4.19}$$

with, for a gravimeter as showed in Fig. 4.12(c):

$$z_{\mathrm{A}} = z_0 - \frac{1}{2} g \mathrm{TOF}^2 \tag{4.20}$$

$$z_{\mathrm{B}} = z_{\mathrm{A}} - \frac{p_0}{\mathrm{M}} T - \frac{1}{2} g T^2 \tag{4.21}$$

$$z_{\mathrm{C}} = z_{\mathrm{A}} - \frac{p_0 + \hbar k_{\mathrm{eff}}}{\mathrm{M}} T - \frac{1}{2} g T^2 \tag{4.22}$$

$$z_{\mathrm{D}} = z_{\mathrm{A}} - \frac{2p_0 + \hbar k_{\mathrm{eff}}}{\mathrm{M}} T - \frac{1}{2} g (2T)^2 \tag{4.23}$$

where M is the mass of ^{87}Rb, k_{eff} is the effective wavevector, T is the interrogation time of the interferometer, z_0 is the initial MOT position of the atomic cloud relative to the mirror and p_0 is the initial mean momentum of the atomic cloud influenced by the time of flight (TOF). The contribution of each parasitic Rabi oscillation on the phase shift of the interferometer corresponds to:

$$\Delta\varphi_{I,J} = \Delta\varphi_{I,J}(z_{\mathrm{A}}) - \Delta\varphi_{I,J}(z_{\mathrm{B}}) - \Delta\varphi_{I,J}(z_{\mathrm{C}}) + \Delta\varphi_{I,J}(z_{\mathrm{D}}) \tag{4.24}$$

with:

$$\Delta\varphi_{I,J}(z) = \mathrm{Arg}\left(\chi_{I,J} e^{i(I\Delta k_1 + J\Delta k_2)z}\right) \tag{4.25}$$

We estimated the theoretical phase shift induced by parasitic lines with optical intensities obtained from the experimental spectrum showed in Fig. 4.7(b). Figure 4.14(a) shows the resulted phase shift for each effective Rabi frequency. The amplitude sign of each line is obtained from CS-DSSB modulation theory in Eq. 4.12. It results that $A^{\mathrm{PPLN}}_{3,-1} < 0$, $A^{\mathrm{PPLN}}_{2,0} > 0$, $A^{\mathrm{PPLN}}_{0,2} > 0$ and $A^{\mathrm{PPLN}}_{1,1} > 0$ as illustrated in Fig. 4.13. In consequence their contributions $\Delta\varphi_{1,-1}$ and $\Delta\varphi_{-1,1}$ are in opposite sign and mostly cancel each other as showed in Fig. 4.14(b).

We notice a phase shift pattern with a periodicity of $d_{I,J} = \frac{\pi c}{I\Omega_1 + J\Omega_2}$ observed by the atoms. This is due to the retro-reflection configuration of the beams, where the parasitic Raman transitions, driven by the straight and the retro-reflected beam, interfere constructively or destructively at each pulse depending on the position of the cloud relative to the mirror. For an atom interferometer with interrogation time of T=20 ms and small TOF (<15 ms), the length of the spatial path between z_{A} and z_{D} is $\simeq$ 10 mm, which corresponds to the half of the period of $d_{1,-1} = d_{-1,1} \simeq 21.9$ mm. It means that the Raman pulses occur over a large spatial part of the oscillation according to Eq. 4.19. Whereas for $d_{1,0} \simeq 157$ mm, corresponding to the parasitic Raman transitions derived from Rabi frequency $\chi_{1,0}$, the Raman pulses cover a small

spatial part of the oscillation leading to a small impact on the phase shift.

The resulted phase shift $\Delta\phi$ evaluated with Eq. 4.19 is shown in Fig. 4.14(b) depending on the initial MOT position of the atomic cloud relative to the mirror z_0. It has been calculated with an interferometer of T=20 ms and TOF=15 ms. We experimentally measured $z_0 = 111.6$ mm in Section 5.3.5 for our interferometer. With those parameters, we estimate the phase shift of parasitic interferometers at 12.4 mrad, leading to an acceleration bias of 195 ng. The zone of the position of the cloud chosen for Fig. 4.14(a) and (b) is the same as scanned experimentally in Chapter 5 to evaluate the model.

The resulted bias shift, depicted in Fig. 4.14(b) in plain line, corresponds to 148 ± 51 ng depending on the position of the atomic cloud relative to the mirror. The main contribution of this shift derives from the Rabi coupling $\chi_{1,0}$ where the detuning $\Delta_{R,1,0}/2\pi = 60$ MHz is small. Adjusting the frequency Ω_1 by adding +150 MHz decreases the bias shift to 19 ± 5 ng. Furthermore, finetuning the parameters β_1 and β_2 allows to optimize the extinction from $\chi_{-1,1}$ and $\chi_{1,-1}$, reducing the bias to 7 ± 6 ng.

4.1.7 Splitting, recombining and switching fiber optical bench

The laser architecture presented above delivers one optical output and need an additional optical bench to split, switch and recombine the beam to supply the 3 axes sensor head. Figure 4.15 presents the 780 nm optical fiber bench used on our experiment. A micro-mechanical fiber switch (Leoni EOL 1x4) controls the beam paths with a TTL command to switch between the MOT configuration and individual axes X, Y or Z for Raman transitions. The settling time of the switch is between 2 and 10 ms depending which axis is switched. The MOT splitter is composed of cascaded 50/50 fiber splitters (Thorlabs PN780R5A1) and benefits of an extra port for monitoring power. A near future architecture will be optimized by using a splitter 1x3 to not loose extra power in the monitor port. Fiber polarization combiners (Thorlabs custom PBC780PM-APC) recombine Raman and MOT beams on fast and slow axis of propagation inside the fibers distributing the sensor head. Those combiners afford complete power transmission from the two entrance ports compared to classic combiners which divide the power by 2. Moreover it filters the polarization at the output of the component. However, the polarization filtering is converted into power fluctuation and can degrade it. All the connections between fibers are spliced in order to maximize power transmission. Table from Fig. 4.15 sums up the optical power and minimum PER of the fast-axis of fibers for each output.

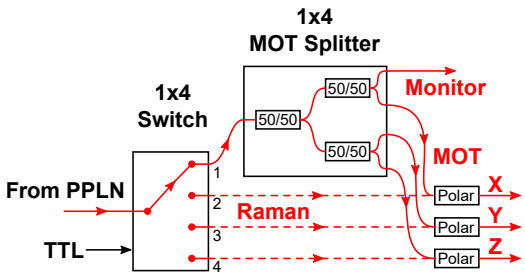

Maximal power and PER delivered

	X	Y	Z
MOT (mW)	45	55	56
Raman (mW)	253	256	290
PER (dB)	> 27	> 24	> 24

Figure 4.15: Scheme of the all fibered optical bench working at 780 nm and table presenting maximal power and PER delivered on fast-axis for the atomic source. Polar: fiber polarization combiner.

We have placed the fiber bench in an oven to qualify it for field-deployed performances. Temperature ramps between 20 °C and 50 °C with cycles of 20 minutes have been conducted and the results are showed in Fig. 4.16. Due to the polarization filtering of the combiner, at the expense of better performances in polarization, the intensity is fluctuating in consequence. For instance, the X-axis presents a high PER but suffers of intensity instability with temperature, whereas the Y and Z-axes display better intensity stability but less PER. Furthermore, slow-axis propagation, which has a better PER than fast-axis, delivers higher instability of the intensity than the fast-axis. The polarization profile on Fig. 4.16 presents the PER as a function of the angle of the polarization for different axes of the fiber bench. As explained in Fig. 4.6 the polarization varies between elliptical polarization when the PER is low and linear polarization when PER $\rightarrow \infty$ dB. It reveals a polarization angle swap of 6° for Y and Z-axis corresponding to purely linear polarization states. This is due to the non optimal fiber injection into the polarization combiner component, leading to high angle fluctuations into PM fibers output. This effect can lead to non optimized polarization treatment into LCR waveplate and impact the two-photon light shift (TPLS) as explained in Chapter 5.

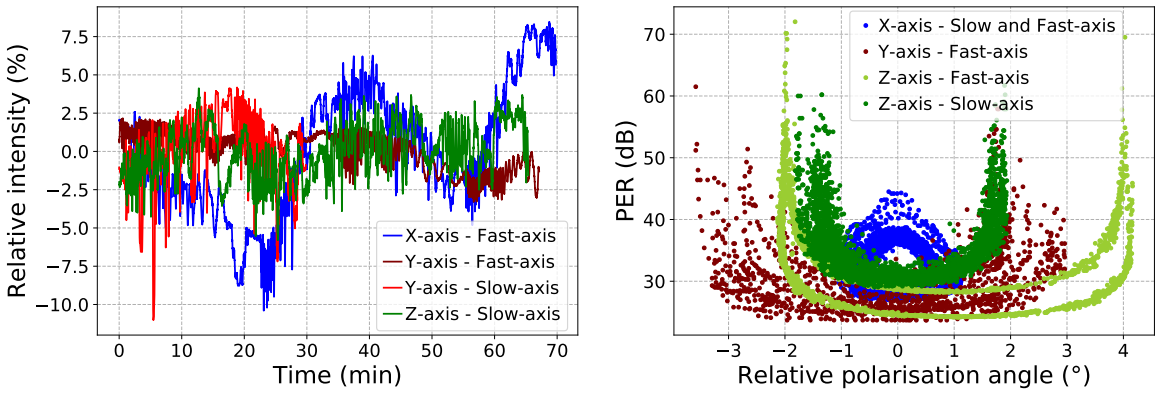

Figure 4.16: Intensity and polarization stability under temperature ramps of 20 °C to 50 °C. The polarization diagram presents the PER as a function of the angle of the polarization for different axes of the fiber bench.

4.1.8 Rack integration

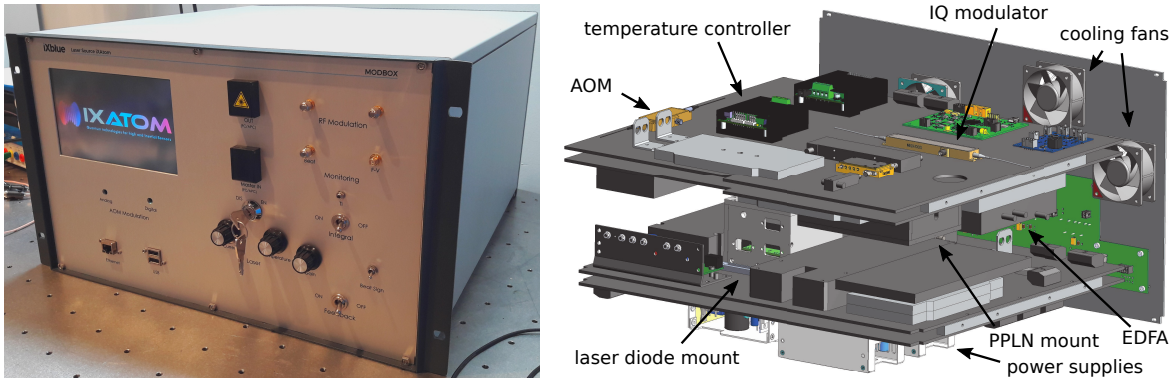

Figure 4.17: Picture of the laser source for iXatom and a CAD view of the inside.

The laser system is integrated into a 6U rack of 19" and is controlled with a graphical user interface (GUI), as showed in Fig. 4.17. Its inner architecture is displayed in Fig 4.4 into the square black box. This laser system provides a compact turn-key solution for atom cooling and interferometry. In our case, a reliable and mobile system is a key feature for field-deployable inertial sensor. For instance the laser diode and the PPLN are placed into a temperature controlled box since they are sensitive to temperature fluctuations.

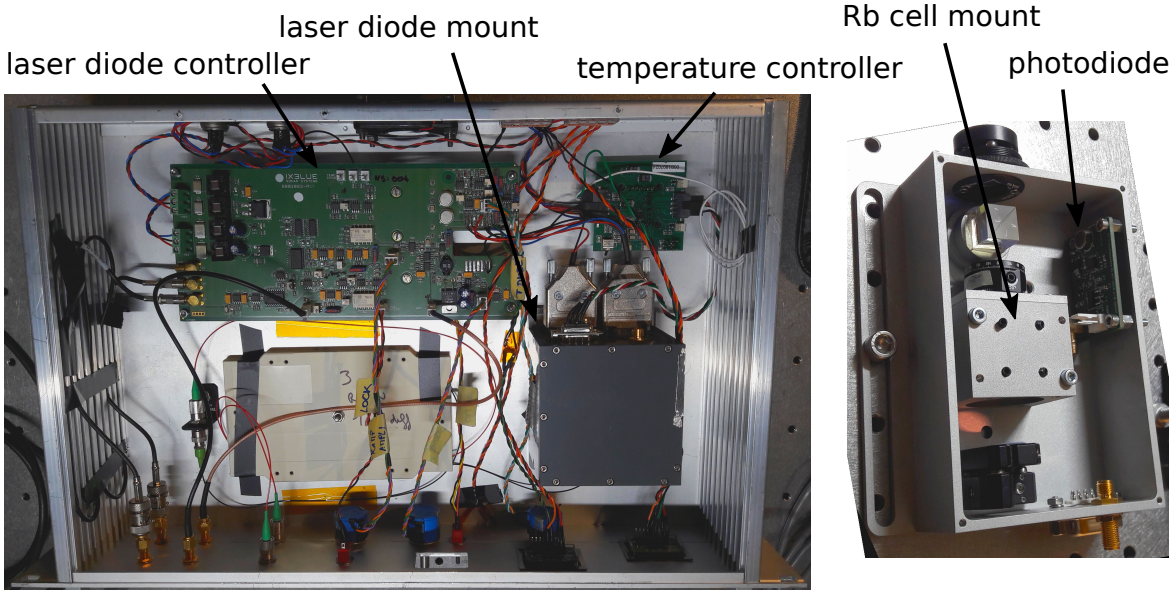

Figure 4.18: On the left, the 2U rack of the reference laser with electronics. The laser diode is placed in an oven. On the right, free space saturated absorption integrated into a separated 1U rack with a PPLN.

Figure 4.18 presents the reference laser with the free space part of the saturated absorption. They are respectively integrated into a 2U and a 1U rack, for a total dimension of 3U, consistently with the optic of a compact and mobile laser system. As

the main laser system presented above, the laser diode and the PPLN are placed into a temperature controlled box for field-deployable applications. The Rubidium vapor cell is placed into a temperature isolated box with heat-tapes in order to maintain a relatively high and homogeneous temperature compared to usual external temperature. The temperature has to be sufficient to obtain a decent vapor pressure ($\simeq$ 30 °C). Its homogeneity is also critical to avoid cold spot on the surface where Rubidium clusters can be created and block the optical path or not being used for the saturated absorption.

4.2 RF Source

4.2.1 Architecture and spectrum

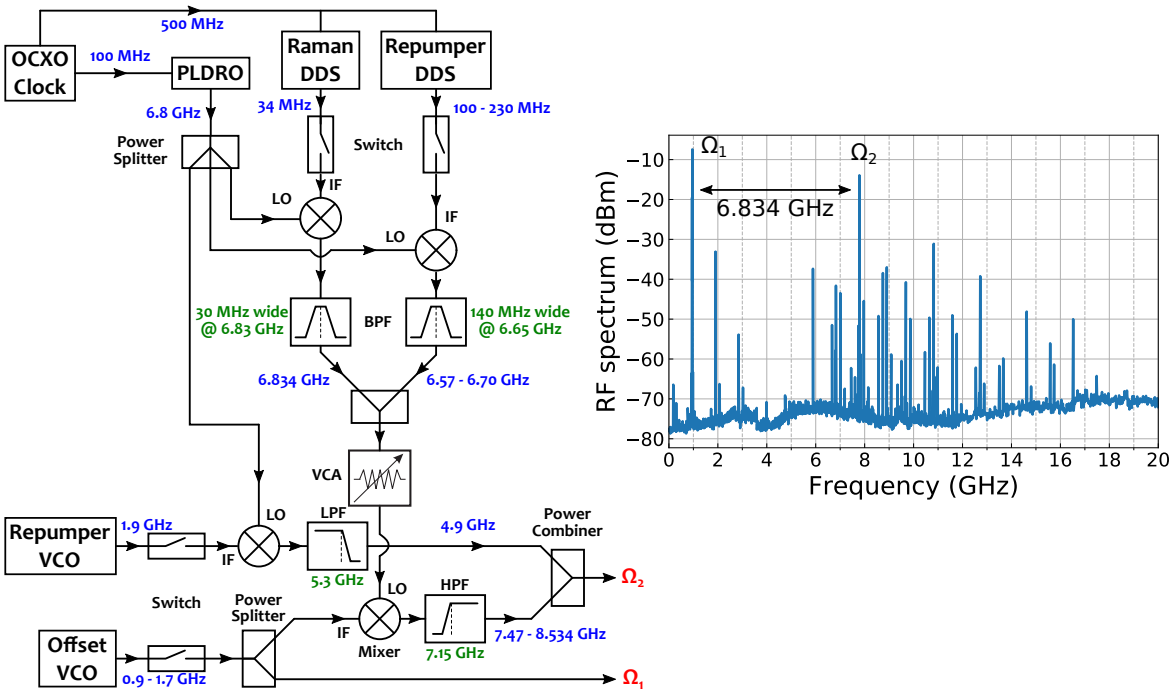

Figure 4.19: RF Source and RF spectrum generated during Raman interferometry. OCXO: Oven Controlled X-tal(Crystal) Oscillator ; PLDRO: Phase Locked Dielectric Resonator Oscillator ; VCO: Voltage Controlled Oscillator ; DDS: Direct Digital Synthesizer ; VCA: Voltage Controlled Attenuator; BPF: Band-Pass Filter ; LPF: Low-Pass filter ; HPF: High-Pass Filter.

Figure 4.19 presents the architecture of the custom-built RF source and the spectrum generated by the RF source for Raman interferometry where the two outputs Ω_1 and Ω_2 are combined. Both frequency modulations are controlled at the sub-Hz level and treated by the hybrid coupler before being injected into IQ modulator. The offset voltage-controlled oscillator (VCO) is used to generate Ω_1. A low-noise phase-locked dielectric resonator oscillator (PLDRO, Polaris model SPLDRO-RE100-6800-P13-CP)

with low phase noise generates 6.8 GHz and is mixed with the VCO to produce Ω_2. Similar to the architecture described in [84], the differential frequency and phase between Ω_1 and Ω_2 is controlled by two direct digital synthesizer (DDS) (Analog Devices AD9959) mixed with the PLDRO. The PLDRO and DDS are locked to the timebase frequency clock of the experiment (NEL Frequency Controls OCXO O-CMR058IS-NS-R 10/100/500 MHz). The power ratio between the two frequencies is controlled using voltage-controlled RF attenuators (VCA) enabling us to suppress constants light shifts during the interferometer [7], and to optimize the optical molasses, state preparation and detection phases of the sequence. The repumper DDS and Raman DDS are used to generate Ω_2 during cooling and interferometry respectively. The Repumper VCO ($\simeq$ 2 GHz) provides a single frequency to address transitions $F = 1 \rightarrow F'$. For that, we select the down-mixed harmonic with the PLDRO ($6.8 - 2 \simeq 4.8$ GHz) and by CS-SSB modulation with the optical IQ modulator, we generate a frequency $\simeq \omega_0 + 9.6$ GHz after the SHG to address only transitions $F = 1 \rightarrow F'$. This frequency allows us to optimize preparation and detection steps and to set up different optical pumping schemes.

Residual parasitic lines from the RF spectrum, as shown in Fig. 4.19, are imprinted into optical spectrum from Fig. 4.7 and explain the slight differences with the numerical simulation. IQ RF modulators present high rejection of residuals (>30 dB) and can replace mixers and band-pass filters in the architecture [85].

4.2.2 Phase noise

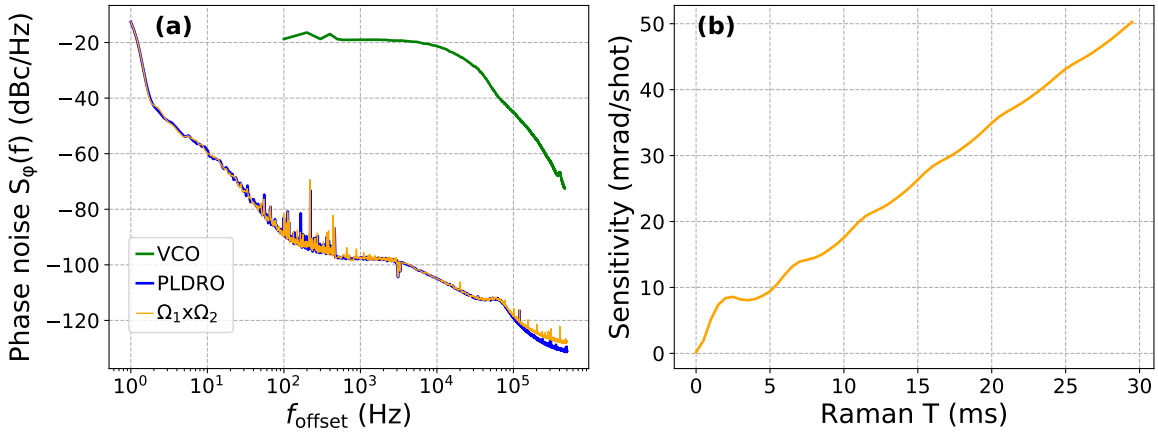

Figure 4.20: (a) Phase noise of the VCO, the PLDRO and the mixed output $\Omega_1 \otimes \Omega_2 = \delta_{\mathrm{HF}}$. (b) Estimation of the sensitivity of the atom interferometer generated by the phase noise of the mixed output $\Omega_1 \otimes \Omega_2$ for different interrogation time T and a Raman π-pulse of 6 μs.

The phase noise, derived from the relative phase between the two Raman frequencies, impacts the sensitivity of the atom interferometer [7]. In our architecture, it depends mostly on the performances of the OCXO clock and the PLDRO. Figure 4.20(a) shows phase noise measurements of the VCO, the PLDRO and the mixed output between Ω_1 and Ω_2 which corresponds to the phase difference of the atom interferometer. According to the RF source scheme in Fig. 4.19, the offset VCO is common between Ω_1 and Ω_2, therefore its relatively large phase noise does not affect the differential phase between Ω_1 and Ω_2. The measurements have been taken with a spectrum analyser (N9010A EXA) and the phase noise floor is actually reached. Nevertheless it gives us an upper limit of the phase noise of the RF source.

The estimation of the sensitivity of the atom interferometer deriving from the phase noise of the RF source can be evaluated as [58]:

$$\left(\sigma_\phi^{\text{rms}}\right)^2 = \int_0^{+\infty} |H(\omega)|^2 S_\phi(\omega) d\omega \tag{4.26}$$

where $H(\omega)$ is the phase transfer function of the interferometer defined in Chapter 2 and $S_\phi(\omega)$ is the phase noise of the RF source in rad^2/Hz. Figure 4.20(b) shows the estimation of the sensitivity per shot of the atom interferometer for different interrogation time T. For T=20 ms, we obtain a sensitivity of 35 mrad/shot which correspond to 550 ng/shot. This estimation of the sensitivity deriving from the relative phase noise of the RF source gives an upper limit and is actually smaller than the sensitivity to the mechanical vibrations.

4.2.3 Frequency stability

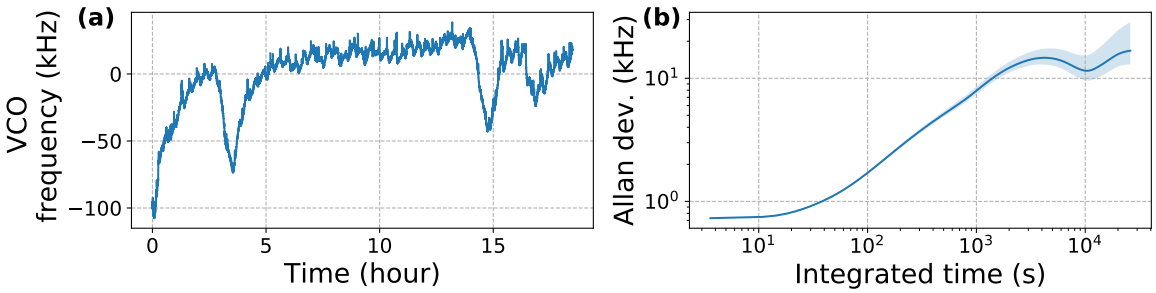

Figure 4.21: Frequency stability of the offset VCO with time series on (a) and Allan deviation on (b).

The offset VCO controls the frequency of the laser sidebands. Frequency stability measurements, presented in Fig. 4.21, are reaching 20 kHz, which offer 40 kHz after optical SHG. It is worse than the stability of the main laser by a factor of two, which constitutes the limitation in frequency stability for the system. VCO is an affordable

and easy handling component but is sensitive to environnement. A temperature controlled box would improve the performances.

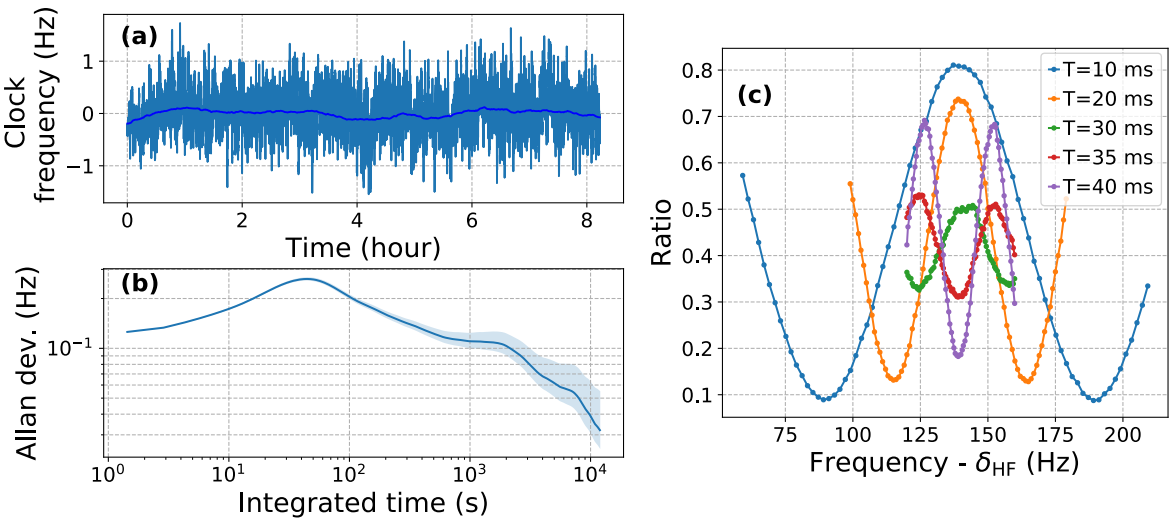

Figure 4.22: Ramsey interferometer fringes (c) centered with the hyperfine transition frequency δ_{HF} for different interrogation time T. Time series (a) and Allan deviation (b) of the frequency stability at mid-fringe for T=40 ms. The dark blue curve on time series graph shows a moving average of 1 hour.

To measure the frequency stability of the timebase clock, we performed a Ramsey interferometer composed of two successive $\pi/2$ co-propagating Raman pulses, with the atomic sensor head. Figure 4.22(c) presents the fringes obtained by scanning the relative frequency between the two Raman lines. The interrogation time T separates the two Raman pulses and controls the sensitivity, scaled as 1/T for the period of a fringe. We observe a strong modulation on the contrast and an inversion of the fringes. This is due to the retro-reflection configuration of the beams, where the co-propagating Raman transitions are driven competitively between the straight and the retro-reflected beams, leading to interferences depending on the position of the cloud relative to the mirror. This effect is more detailed in Chapter 5.

At that time, the experiment was not optimized for high performances in frequency measurements, including light shifts and magnetic fields compensation [36]. That is why the central fringe is shifted by 139 Hz from the hyperfine transition, which represents a relative accuracy of 2×10^{-8}. This inaccuracy is large compared to atomic clocks used for metrology.

The frequency stability measurements on Fig. 4.22(a) and (b) have been obtained by setting the frequency at mid-fringe with an interrogation time of T=40 ms. We achieve a long-term frequency stability of 40 mHz offering a relative stability of 6×10^{-12}.

4.2.4 Phase non-linearity of RF-filters

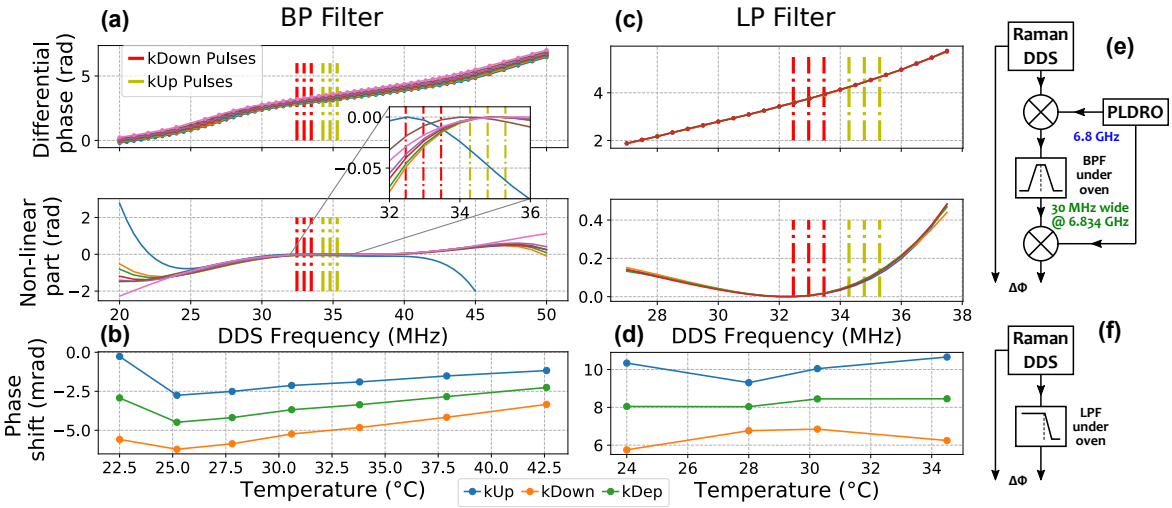

Figure 4.23: Non-linearity of the phase of filters in the RF chain. On (a) and (c), differential phase vs frequency of the DDS at different temperature of a band-pass filter (BP filter) and a low-pass (LP filter). On (b) and (d), estimation of the interferometer phase shift for kUp, kDown and kDep cases ; kDep being the half sum between kUp and kDown. KUp and kDown pulses are specified for an interferometer with T=20 ms and TOF=16 ms. The test benches are presented on (e) and (f).

The phase coherence between the two Raman frequencies is crucial for atom interferometry. The laser phase, controlled with the Raman DDS, is imprinted onto the output signal of the interferometer as:

$$\phi_{\text{laser}} = \phi_1 - 2\phi_2 + \phi_3 \tag{4.27}$$

where ϕ_{i} corresponds to the relative phase at each pulse. During the interferometer, this relative frequency follows the doppler frequency of the atomic cloud relative to the sensor head frame. Therefore the phase has to be linear with frequency to not impact the imprinted laser phase ϕ_{laser} as shown by Equation 4.27.

Figure 4.23 shows the relationship between the relative phase and the frequency of the filters inside the RF chain at different temperature. By extracting the non-linear part of a polynomial fit, we observe quite non-linearity which has an impact on the phase shift of the interferometer. We estimated the phase shift for different configurations depending on the direction of the effective wavevector $\pm k_{\text{eff}}$ (kUp and kDown) and the rejection case corresponding to the mean of the two directions (kDep). Depending the component, an interferometer with an interrogation time of T=20 ms can reach 10 mrad of phase shift which is not negligible.

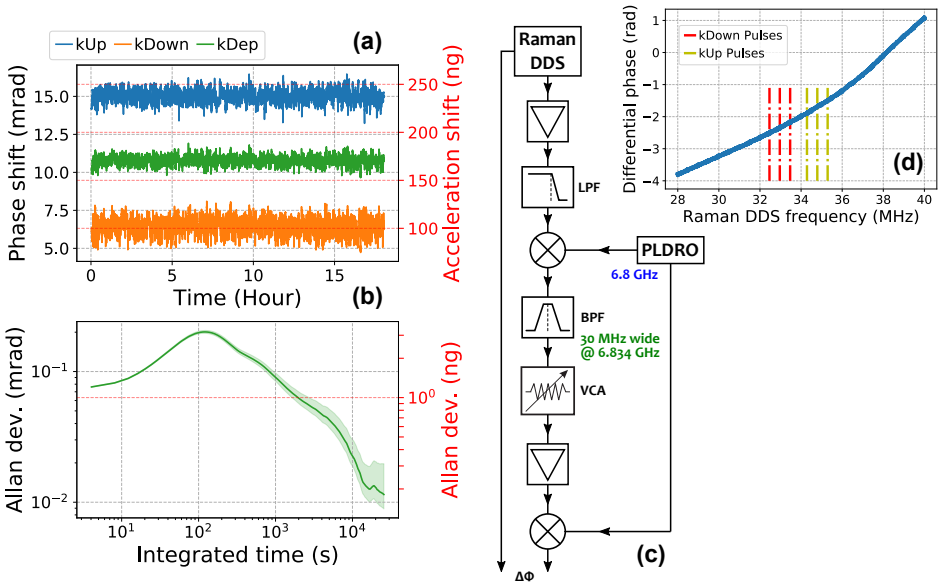

Figure 4.24: Stability of the phase difference from the RF chain. (a) Times series of the estimated phase shift contribution from the non linearity of the phase difference with frequency, as shown on (d). (b) Allan deviation of the estimated phase shift of the half sum between kUp and KDown cases. KUp and kDown pulses are specified for an interferometer with T=20 ms and TOF=16 ms. The test bench is presented on (c).

On Figure 4.24, we measured the stability of the relative phase of the RF source over time and estimate the impact on the phase shift of the interferometer. By repetitively scanning the DDS frequency and fitting the measurements as shown on Fig. 4.24(d), we obtained an estimation of 170.9 ± 0.2 ng systematic phase shift for an interferometer with an interrogation time of T=20 ms.

To improve the RF architecture, one could replace the mixers and band-pass filters with an IQ RF modulator [85]. The rejection of residuals are better and reach 30 dB. However, the phase linearity has not been yet study with this component and should raise interest for atom interferometry.

4.2.5 Hybrid coupler

The hybrid coupler is a critical component which equally splits the RF signal to produce the quadrature phase part required for CS-DSSB modulation. Fig. 4.25 presents the imbalance in phase and amplitude of our hybrid coupler (KRYTAR model number 1230) measured with a network analyser. The performances allow to operate CS-DSSB modulation between 1 GHz and 13 GHz. However one can ask if this treatment on the phase impacts the relative phase output of the interferometer due to non-linearity as in Section 4.2.4.

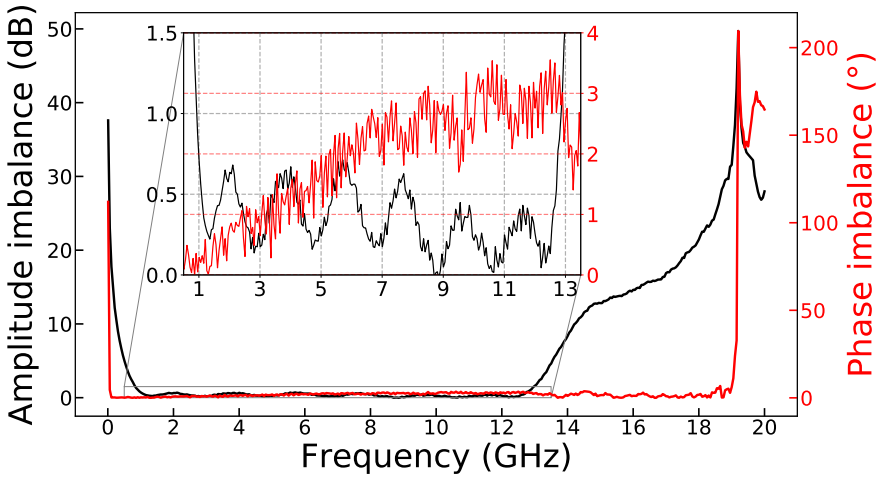

Figure 4.25: Amplitude and phase imbalance between the I and Q parts of the hybrid coupler.

The residual phase imbalances on RF signal of frequencies Ω_1 and Ω_2 are modeled respectively as $\Delta\phi_{1\mathrm{HC}}$ and $\Delta\phi_{2\mathrm{HC}}$. We obtain a different form of Eq. 4.1:

$$E_1 = \frac{E}{4}\left[e^{i[\beta_1\cos(\Omega_1 t+\phi_1+\Delta\phi_{1\mathrm{HC}})+\beta_2\cos(\Omega_2 t+\phi_2+\Delta\phi_{2\mathrm{HC}})]}e^{i\frac{\Delta\Phi_1}{2}}+\mathrm{C.C.}\right] \quad (4.28)$$

The resulting amplitude and phase output of the IQ modulator changes as following:

$$A^{\mathrm{IQ}}_{n,m} = \sin\left((n+m)\frac{\pi}{2}\right)\sin\left((n+m+1)\frac{\pi}{4}+n\frac{\Delta\phi_{1\mathrm{HC}}}{2}+m\frac{\Delta\phi_{2\mathrm{HC}}}{2}\right) J_n(\beta_1)J_m(\beta_2) \quad (4.29)$$

$$\phi^{\mathrm{IQ}}_{n,m} = \phi_0+n\phi_1+m\phi_2+n\frac{\Delta\phi_{1\mathrm{HC}}}{2}+m\frac{\Delta\phi_{2\mathrm{HC}}}{2}+(3n+3m+1)\frac{\pi}{4} \quad (4.30)$$

According to the amplitude expression from Eq. 4.29 the phase quadrature imbalance does not affect all sidebands. Furthermore we can deduce the impact on the phase after the SHG process:

$$\phi^{\mathrm{PPLN}}_{N,M} = 2\phi_0+N\phi_1+M\phi_2+N\frac{\Delta\phi_{1\mathrm{HC}}}{2}+M\frac{\Delta\phi_{2\mathrm{HC}}}{2} + (3N+3M+1)\frac{\pi}{4} \quad (4.31)$$

The resulting relative phase between lines separated by the hyperfine splitting frequency is affected by the phase quadrature imbalance as follow:

$$\phi^{\mathrm{PPLN}}_{N+1,M+1} - \phi^{\mathrm{PPLN}}_{N+2,M} = \phi_2 - \phi_1 + \frac{\Delta\phi_{2\mathrm{HC}} - \Delta\phi_{1\mathrm{HC}}}{2} \tag{4.32}$$

The impact produced by the phase quadrature imbalance can be determined by injecting results obtained in Fig. 4.25 into Eq. 4.32 and into the relative phase output of the atom interferometer Eq. 4.27. Hopefully the estimation of the acceleration shift is below 0.1 ng which is insignificant.

4.3 Laser architecture improvements

4.3.1 IQ modulator operating at 780 nm

The parasitic lines are largely increased due to the non-linearity of second-harmonic generation. One can ask for the benefit of an IQ modulator operating at 780 nm without using a PPLN. The CS-DSSB modulation presents advantages that could be transposed to 780 nm laser architectures. We simulated the impact of an IQ modulator at 780 nm on the phase shift of the atom interferometer, assuming similar defects and properties from IQ modulator at 1560 nm as the spectrum measured in Fig. 4.7(a).

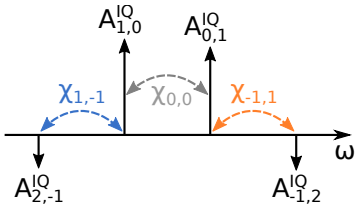

Figure 4.26: Illustration of the amplitude of the sidebands obtained by CS-DSSB modulation with an IQ modulator contributing to the largest parasitic Rabi oscillations $\chi_{1,-1}$ and $\chi_{-1,1}$.

The theory is quite similar to the one developed in Section 4.1.6. Here we consider pairs of lines $E^{\mathrm{IQ}}_{i+1,j}$ and $E^{\mathrm{IQ}}_{i,j+1}$ separated by $\Omega_2 - \Omega_1 = \delta_{\mathrm{HF}}$ generating Raman transitions. The Rabi oscillation driven by each pair is given by:

$$\chi_{i,j} = \sqrt{\Lambda^{\mathrm{IQ}}_{i+1,j}(\Lambda^{\mathrm{IQ}}_{i,j+1})^* + (\Delta_{\mathrm{R,i,j}})^2} - |\Delta_{\mathrm{R,i,j}}| \tag{4.33}$$

which can be approximated for large detuning $\Delta_{\mathrm{R,i,j}} = \Delta_{\mathrm{R}} + i\Omega_1 + j\Omega_2 \gg \Gamma$ by:

$$\chi_{i,j} \approx \chi_{0,0} \frac{A^{\mathrm{IQ}}_{i+1,j} A^{\mathrm{IQ}}_{i,j+1}}{\Delta_{\mathrm{R,i,j}}} \frac{\Delta_{\mathrm{R}}}{A^{\mathrm{IQ}}_{1,0} A^{\mathrm{IQ}}_{0,1}} \tag{4.34}$$

Figure 4.27(c) presents the weight of each effective Rabi frequency. As for the case of an IQ modulator operating at 1560 nm with a PPLN, $\chi_{1,-1}$ and $\chi_{-1,1}$ are the largest parasitic Rabi frequencies. The amplitude sign of each sideband is obtained from CS-DSSB modulation calculation in Eq. 4.8. It results that $A^{\mathrm{IQ}}_{2,-1} < 0$, $A^{\mathrm{IQ}}_{1,0} > 0$, $A^{\mathrm{IQ}}_{0,1} > 0$ and $A^{\mathrm{IQ}}_{-1,2} < 0$ as illustrated in Fig. 4.26. Here the amplitude signs are different from the case of CS-DSSB modulation at 1560 nm with a PPLN as shown in Fig. 4.13. In consequence, their impact is added and not substracted as displayed on Fig. 4.27(b). Fig. 4.27(a) estimates the predicted parasitic phase shift for an atom interferometer in gravimeter configuration with T=20 ms and TOF=15 ms. Assuming the position of the atomic cloud relative to the mirror and the acceleration are not known, the uncertainty is estimated at ± 500 ng at T = 20ms and is actually worse than the current combination of an IQ modulator operating at 1560 nm with a PPLN.

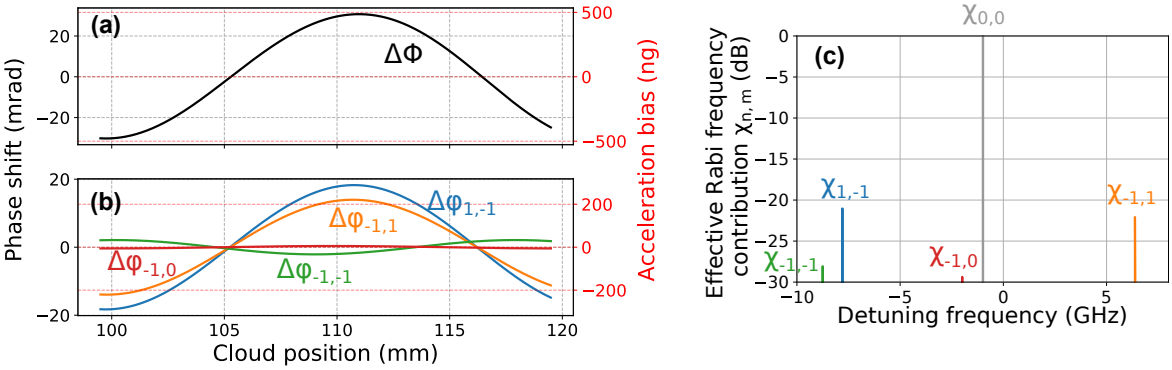

Figure 4.27: (a) Estimation of the phase shift of the atom interferometer with an IQ modulator operating at 780 nm. (c) Contribution of each parasitic Rabi oscillation with their respective impact on the phase shift on (b). The parameters of the interferometer are TOF=15 ms, T=20 ms.

4.3.2 Single diode architecture based on a discrete lock

The frequency of the optical carrier is fixed in the CS-DSSB modulated laser architecture. One can imagine a complete laser system employing only one laser diode as main source without additional external reference [5, 86]. The atom species used for frequency reference is present in the sensor head and could be used to recalibrate the offset VCO of the RF source by saturated absorption between every shot. However a continuous lock on frequency reference delivers high performances in frequency stability and phase noise by correcting temperature fluctuations and low-frequency current noise. Therefore, free running performances offered by the laser diode should be decent in phase noise and short term frequency stability. Redfern Integrated Optics (RIO) external-cavity diode laser is a good candidate to fill those specifications. In addition, the frequency of the diode should not drift excessively in long term not to reach the limit on the feedback of the frequency lock for the VCO. A temperature controlled box

as used in the laser system and visible in Section 4.1.8 prevents from large drifts in frequency from temperature changes in random environment.

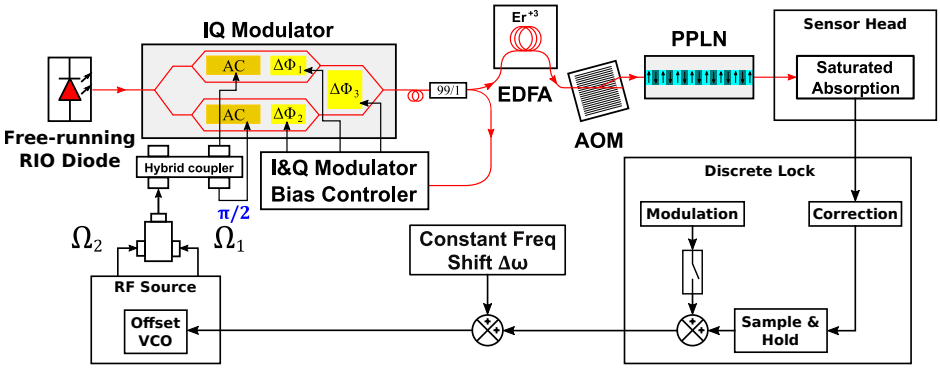

Figure 4.28: Discrete lock scheme suggestion to simplify further the laser architecture. The laser is using directly the atom species available in the sensor head to operate the saturated absorption during dead times and retroacts the correction on the RF source. The switch bench between the laser and the sensor head is not showed.

Figure 4.28 proposes an architecture where the RIO diode is running without frequency feedback lock. The stability of the frequency is regulated with a discrete lock where the feedback frequency correction is applied on the RF source. The discrete lock system would be composed by a sample and hold circuitry to operate the saturated absorption during dead times and maintain a constant correction feedback otherwise. The modulation is activated to perform the saturated absorption and stopped otherwise. A constant frequency shift is added to generate the sidebands out from the optical carrier. This technique offers the possibility to use the atom species available in the sensor head to perform the saturated absorption. It avoids the need of an external frequency reference which requires an auxiliary laser or an additional PPLN in the case of single diode architecture.

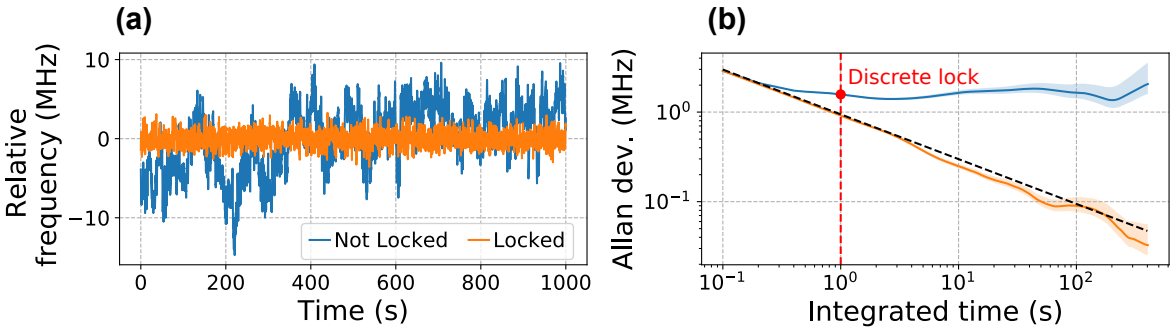

Figure 4.29: (a) Time series and (b) Allan deviation of short-term frequency stability of RIO diode with and without frequency lock in blue and orange respectively. The time series are plotted with a moving average of 1s. The black dashed line indicates white noise integration which comes from the analog acquisition chain. The red dot indicates the typical time period of the discrete lock which would be 1 s.

We compared short term frequency stability performances of a RIO diode when it is locked to a frequency reference and when it derives freely. The results, presented in Fig. 4.29(a) and (b), have been obtained by beating the RIO diode with an external frequency reference and treated by a frequency to voltage conversion analog circuit. It reveals a relative frequency stability of $\simeq 1$ MHz at 1 s for the free running RIO diode, whereas the frequency lock is more stable than the measurement setup at this time range (the Allan variance integrates until reaching 10 kHz level). The norm of the effective wavevector $\|\vec{k_{\text{eff}}}\| = \|\vec{k_1}\| + \|\vec{k_2}\|$ is affected and the scale factor of the atom interferometer is changing as:

$$\delta S = T^2 \delta k_{\text{eff}} \tag{4.35}$$

$$= \frac{2\pi T^2}{c} 2\delta\nu \tag{4.36}$$

where $\delta\nu$ is the frequency shift from the reference of the diode at 1560 nm before SHG. The relative error on the scale factor increases linearly with the frequency shift as:

$$\frac{\delta S}{S_{\text{eff}}} \propto 2\frac{\delta\nu}{\nu} < 10^{-8} \tag{4.37}$$

The frequency lock would bring an uncertainty below 10 ng on the atom accelerometer.

The effective Rabi frequency χ of Raman transitions are slightly affected by a frequency shift of the order of $\delta\Delta_R \simeq 1$ MHz considering a Raman detuning of $\Delta_R \simeq 1$ GHz. It represents a relative drift of:

$$\frac{\delta\chi}{\chi} \propto \frac{\delta\Delta_R}{\Delta_R} \simeq 10^{-3} \tag{4.38}$$

In addition, atom cooling and preparation are affected by a change of the frequency. The natural linewidth of the D_2 transition of ^{87}Rb is $\simeq 6$ MHz, which is in the same order of $2\delta\nu$ for a free running RIO diode.

At that time, the cycling rate of our experiment is limited at $\simeq 1$ Hz and can be easily improved. Increasing it would improve the frequency shift between each shot of the discrete lock.

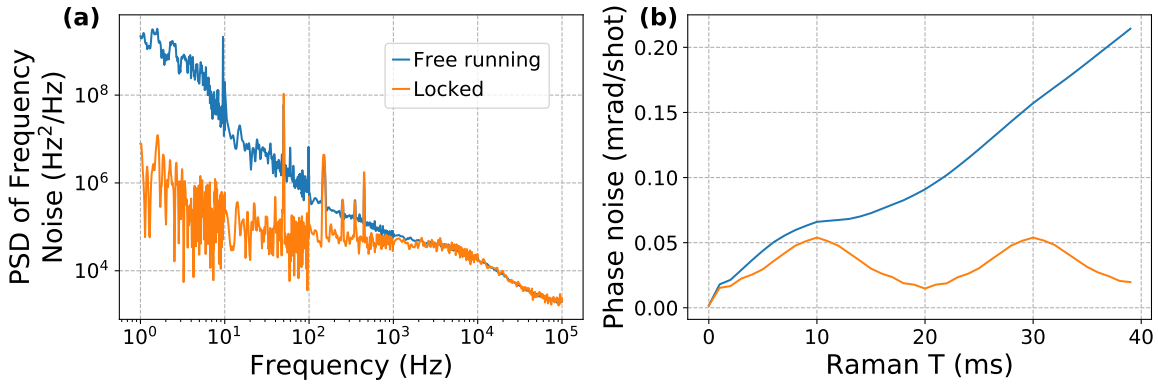

Figure 4.30: (a) PSD of the frequency noise of the reference RIO laser diode running freely in blue and frequency locked to a saturate absorption in orange. (b) Estimation of the phase noise contribution to an atomic interferometer with L=15 cm and $\tau = 6$ μs for different interrogation time T.

The phase spectral density (PSD) of the frequency noise of the laser, which determine the linewidth of the laser, is intrinsic to the design and technology of the laser diode. Besides, the PSD is affected by the noise of the current feeding the diode and is reduced with a frequency lock. Figure 4.30(a) shows the PSD of the frequency noise of a RIO diode with a clean current supply providing noise at $\simeq 1$ μA. The RIO diode running freely exhibits good performances especially for large frequencies.

In the configuration of retro-reflected Raman beams with a mirror, Reference [87] studies the effect of the frequency noise on the sensitivity of the interferometer and expresses the impact as:

$$\sigma_\Phi^2 \approx t_d^2 \int_0^{+\infty} |H(\omega)|^2 S_\nu(\omega) \frac{d\omega}{2\pi} \tag{4.39}$$

where σ_Φ is the variance of the phase fluctuation , t_d=2L/c is the retro-reflection delay with L the relative distance between the mirror and the atomic cloud, $H(\omega)$ is the phase transfer function of the interferometer described in Chapter 2 and $S_\nu(\omega)$ is the PSD of the frequency noise presented in Fig. 4.30(a). Figure 4.30(b) reports the phase noise estimation of the atom interferometer at different Raman interrogation time T. The impact of the RIO diode running freely is small thanks to the high intrinsic performances of the RIO diode, clean current supply and small distance L<15 cm between the mirror and the position of the cloud.

Conclusion

We have presented a dual-frequency, electro-optically modulated laser source with reduced parasitic sidebands, where the control of two independent optical signals is realized using only RF components. We verified its performances and proved its compliance for atom interferometry and inertial sensing applications. By suppressing parasitic lines by 20 dB, we estimate the residual acceleration bias due to parasitic interferometers below 200 ng. The simplicity of our architecture, along with the dramatic improvement in accuracy, represents a suitable alternative with a trade-off on the complexity and frequency agility from systems employing two phase-locked laser diodes [74, 75]. With agility over tens of GHz and very fast electro-optic conversion, this architecture can be employed for many applications like atom launching, chirping to compensate high accelerations, compensation of zero-velocity atom for interferometry [56]. The architecture can also be easily modified for use with other atomic species, such as potassium [68] or cesium [37], which makes it promising for several applications.

We explored new configurations and improvements of the laser architecture to reduce and simplify evermore. The current architecture is using an extra laser diode referenced on ^{87}Rb transition. Because the carrier agility of the main laser is not required, this approach opens the field of laser architectures operating with only one laser diode frequency locked on a reference [5]. Futhermore, we demonstrated high performances of the RIO diode and its compatibility for single diode architectures with discrete locking of the RF source on the atoms inside the sensor head between shots. In this way, no additional saturated absorption layout or PPLN is needed and the compactness can be even more improved. In addition, through a fiber IQ modulator operating at 780 nm, one can transfer the benefit of the CS-DSSB modulation to laser architectures entirely operating at 780 nm.

Chapter 5

Characterization of the atom accelerometer along the vertical axis

This chapter reports the performances and systematic effects of our atom interferometer prototype on the vertical axis. Specifically, we analyse the characteristics of the atom cooling, the preparation of the atomic states for interferometry, the stability and the bias of the atomic accelerometer which operates as a gravimeter.

Contents

5.1 Operation of the atom accelerometer along the vertical axis 149

5.1.1 Raman transitions 149

5.1.2 Atom interferometer 150

5.2 Preparation of the atomic source 151

5.2.1 Temperature of the atomic source 151

5.2.2 Preparation into non-magnetic states 151

5.3 Performances of the atom interferometer 153

5.3.1 Acceleration sensitivity 153

5.3.2 Long-term stability with the tracking algorithm 154

5.3.3 Magnetic field 155

5.3.4 Light shifts 157

5.3.5 Cloud position dependence of Rabi frequencies 160

5.3.6 Scale factor error 162

5.3.7 Other systematic effects 164

5.3.8 Summary of systematic effects 168

5.3.9 Relative accuracy 168

Introduction

Laser cooling and trapping has led to a good control and manipulation of cold atoms by increasing the de Broglie wavelength. In 1989, Christian Bordé discusses the use of light to diffract atoms between internal energy states to split an atomic path with the atomic recoil [88]. Mark Kasevich and Steven Chu demonstrate in 1992 the use of counter-propagating velocity selective Raman transitions to perform a cold atom interferometer sensitive to inertial effects [6, 54]. Since then, many efforts have been conducted to develop atomic gravimeters and to reach high sensitivity level while reducing the systematic effects, which affect the accuracy of the sensor. In particular, the SYRTE laboratory achieved impressive performances of 6 ng/$\sqrt{\text{Hz}}$ of sensitivity with an unprecedented stability of 2 ng for their atomic gravimeter [89, 7]. Cold-atom gravimeters are easier to achieve and operate compared to an accelerometer. Indeed a gravimeter can be calibrated by comparison with a known reference, a local value of the gravitational acceleration. On the other hand a cold-atom accelerometer requires deep analysis of the systematic effects to be characterized and no such work has been done yet.

The characterization and qualification of our atom interferometer prototype along a single-axis is a necessary step in the quest of developing the 3-axis hybrid accelerometer. Indeed we want to measure the intrinsic performances of the sensor. In this chapter, the atom interferometer is configured as a three-pulse Mach-Zehnder-type gravimeter, with vertically-oriented Raman beams that are retro-reflected by the reference mirror. The classical accelerometer fixed to the mirror corrects the parasitic vibrations by reconstructing the fringes with a high-pass filter to reject any bias. Our sensor head is compact and made for mobile applications which limits the free-fall time for the atoms to not drop out from the laser beams and the detection zone. Therefore, the study of the systematic effects is made at rather small interrogation time of $T = 20$ ms compared to gravimeters, where interrogation time reaches $T > 100$ ms. We aim for a sensitivity below $2\mu\text{g}/\sqrt{\text{Hz}}$ with a long-term stability reaching ~ 10 ng level and a relative accuracy of ~ 100 ng.

5.1 Operation of the atom accelerometer along the vertical axis

5.1.1 Raman transitions

In Chapter 2, we identifies the probability transition of the atoms subjected to Raman transitions as:

$$P(\tau, \delta, r, v) = \frac{\Omega_{\text{eff}}^2(r)}{\omega^2(\delta, v, r)} \sin^2\left(\frac{\omega(\delta, v, r)\tau}{2}\right) \tag{5.1}$$

where τ is the length of the Rabi pulse, Ω_{eff} is the effective Rabi frequency, $\omega(\delta, v, r) = \sqrt{\Omega_{\text{eff}}^2(r) + (\delta - \omega_{\text{D}}(v) - \omega_{\text{R}} - \omega_{\text{AC}})^2}$ is the exact Rabi frequency depending on the controlled resonance detuning δ between the lasers, the Doppler frequency $\omega_{\text{D}}(v) = k_{\text{eff}} v$ with the velocity v relative to the reference mirror, the recoil frequency $\omega_{\text{R}} = \hbar k_{\text{eff}}^2 / 2M$ and the light shift ω_{AC}.

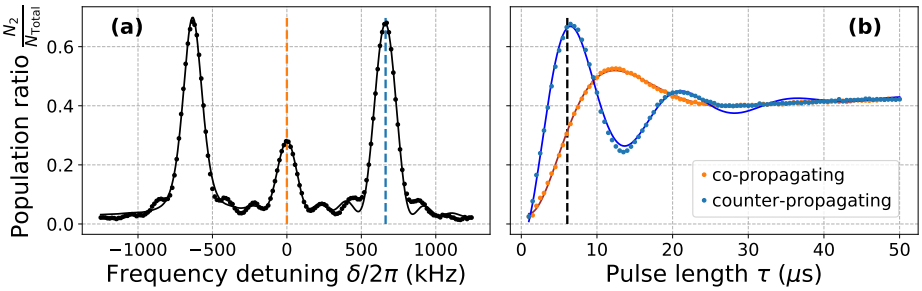

Figure 5.1: (a) Raman spectrum with lin⊥lin polarized Raman beams after a TOF of 25 ms with a Rabi pulse length of 6 μs. (b) Rabi oscillations of the co-propagating and counter-propagating Raman transitions.

Figure 5.1 presents a Raman spectroscopy and Rabi oscillations of co-propagating and counter-propagating Raman transitions. Here, the measurements are operated with a lin⊥lin polarization on the Raman beams to drive counter-propagating velocity-selective Raman transitions. The PER of the light is > 24 dB where residual circular polarizations σ^+/σ^+ and σ^-/σ^- induce parasitic co-propagating Raman transitions on the central peak. The Doppler frequency shift is different as $\pm\omega_{\text{D}}(v)$ depending on the pair of counter-propagating Raman beams. It raises a degeneracy on the transition, as depicted on the figure with two main peaks, and transfers a momentum recoil on opposite directions according to $\pm k_{\text{eff}}$. The sign of the detuning resonance $\pm\delta$ allows to select between the two.

5.1.2 Atom interferometer

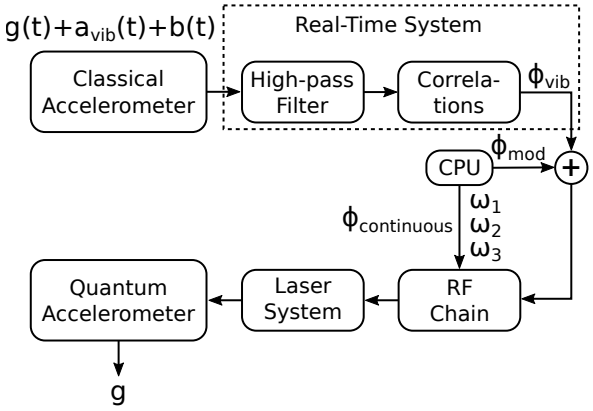

Figure 5.2: Operation scheme in open-loop of the atom accelerometer along the vertical axis.

The atom interferometer is configured as a three-pulse Mach-Zehnder-type gravimeter, with vertically-oriented Raman beams that are retro-reflected by the reference mirror. Figure 5.2 presents the operation scheme of the atom interferometer in this Chapter. The scheme has been detailed in Chapter 2, called hybrid gravimeter in open-loop. To track the time-varying gravitational acceleration $g(t)$, the two-point mid-fringe algorithm is employed.

The classical accelerometer monitors and extracts the vibrations of the reference mirror by filtering its output with a high-pass filter. The resulted vibrations $a_{\text{vib}}(t)$, measured during the interferometer, are correlated with the response function of the interferometer $f(t)$ to generate the correction phase ϕ_{vib}. The CPU commands the Raman DDS to generate a series of phase-continuous frequency jumps ω_1, ω_2 and ω_3 to correct the Doppler shift, which imprints the phase $\phi_{\text{continuous}}$ on the atomic wavefunction. In addition a modulation phase ϕ_{mod} is used as a free parameter to operate the mid-fringe algorithm or to scan Raman fringes.

The resulting transition probability of the interferometer is measured by detecting the number of atoms N_2 in energy state $|F = 2\rangle$ and the total number of atoms N_{total} as:

$$P = \frac{N_2}{N_{\text{total}}} = P_0 - \frac{1}{2} C \cos\left(\phi_{\text{kin}} + \phi_{\text{laser}}\right) \tag{5.2}$$

where C is the contrast, P_0 is the offset, $\phi_{\text{kin}} = -(g + a_{\text{vib}}) k_{\text{eff}} T_{\text{eff}}^2$ is the inertial phase corresponding to the acceleration of the atoms relative to the reference mirror and $\phi_{\text{laser}} = \phi_{\text{continuous}} + \phi_{\text{vib}} + \phi_{\text{mod}}$ is the phase imprinted onto the atomic wavefunction.

5.2 Preparation of the atomic source

5.2.1 Temperature of the atomic source

A vapor-loaded 3D magneto-optical trap (MOT) accumulates $\simeq 5 \times 10^8$ atoms in 250 ms. This is followed by a 10 ms stage of optical grey molasses where the atoms are cooled down at sub-Doppler temperatures [51]. The probability transition function distributed over velocity classes is $\overline{P}(\tau) = \int G(v)P(\tau, v)dv$, where the velocity distribution is Gaussian [54]:

$$G(v) = \frac{1}{\sigma_v\sqrt{\pi}} e^{-\frac{(v-v_0)^2}{\sigma_v^2}} \tag{5.3}$$

with σ_v the dispersion of the velocity classes and v_0 the central velocity of the distribution.

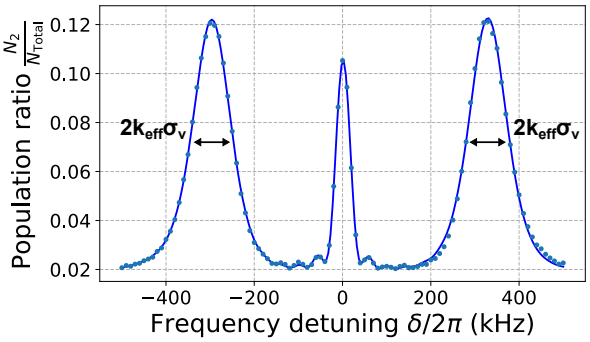

Figure 5.3: Raman spectroscopy with π polarized Raman beams at a pulse length of 25 μs after 17 ms of TOF.

Figure 5.3 presents a Raman spectroscopy with counter-propagating Raman transitions after 17 ms of time-of-flight (TOF). The power used for the spectroscopy is low, with a duration of the Raman pulse equals to 25 μs. By averaging the velocity dispersion between the right peak ($+k_{\text{eff}}$) and the left peak ($-k_{\text{eff}}$), we find a temperature of 2.5 μK, equivalent to a velocity dispersion of 22 mm/s.

5.2.2 Preparation into non-magnetic states

Quantum purity is necessary to operate properly a Raman interferometer. It relies on the preparation of the atoms onto a common energy state before the interferometer. The common energy state level should be non-magnetic in order to avoid sensitivity to ambient magnetic field.

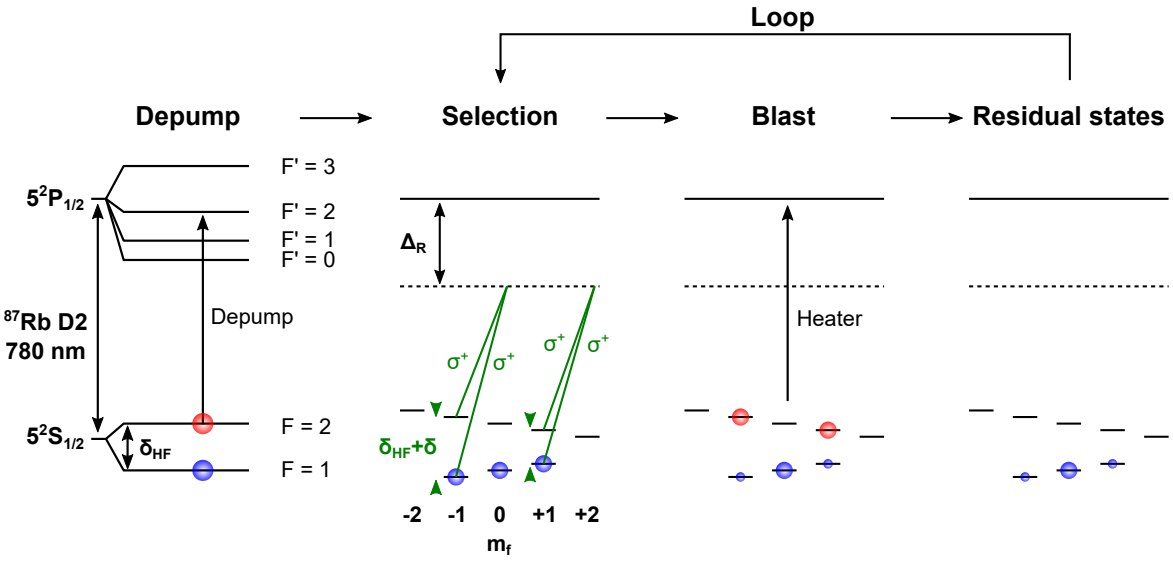

Figure 5.4: Scheme of the preparation of the atoms into non-magnetic sensitive energy state $|F = 1, m_f = 0\rangle$.

For atom interferometry, we prepare the atoms into non-magnetic sensitive state $|F = 1, m_f = 0\rangle$ with the scheme illustrated on Fig. 5.4. This scheme allows to preserve the third of the atoms available. After the molasses, we depump all the atoms into state $|F = 1\rangle$. The bias magnetic field is set to split in energy the magnetic sub-levels by Zeeman shift and to quantize the axis along the light beams. Then we use co-propagating Raman transitions to transfer atoms from states $|F = 1, m_f = \pm 1\rangle$ to $|F = 2, m_f = \pm 1\rangle$ by controlling the resonance detuning δ. Atoms transferred in $|F = 2\rangle$ are removed by heating them with the $|F = 2\rangle \rightarrow |F' = 3\rangle$ cycling transition. To optimize this blast, we ramp slightly the optical frequency to the blue to address all the velocity classes. We repeat the sequence to remove residual atoms in bad magnetic states.

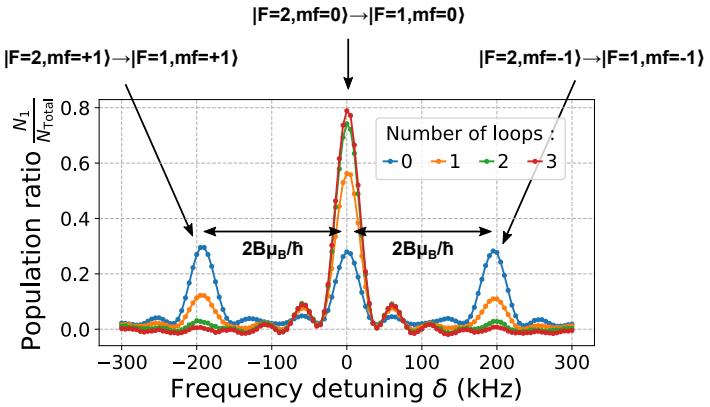

Figure 5.5: Raman spectroscopy with circularly polarized beams scanning the magnetic energy states of the hyperfine transition. Looping the selection reduces the remaining atoms in $|F = 1, m_f = \pm 1\rangle$ and increases quantum states purity.

Figure 5.5 shows a Raman spectroscopy with co-propagating Raman transitions

for different number of loops of the preparation sequence. The transitions scanned are between magnetic energy states. The magnetic states are split in frequency by $2B\mu_B/\hbar$ where μ_B is the Bohr magneton and $B = 68.5$ mGauss is the field generated by the pair of Helmholtz coils. Three loops are sufficient to maximize the quantity of atoms in energy state $|F = 1, m_f = 0\rangle$.

5.3 Performances of the atom interferometer

In this Section, we want to measure the intrinsic performances of the atom interferometer on a gravimeter configuration, including the sensitivity, the stability and the systematic shifts. Despite the compensation of the ambient mechanical vibrations achieved with the measurements of the classical accelerometer, the sensor head is set on the marble table to reduce them. The other purpose of the marble table is to stabilize the angle between the acceleration measurements of the atom interferometer determined by $\vec{k_{\text{eff}}}$ and the gravitational acceleration vector $\vec{g}$.

5.3.1 Acceleration sensitivity

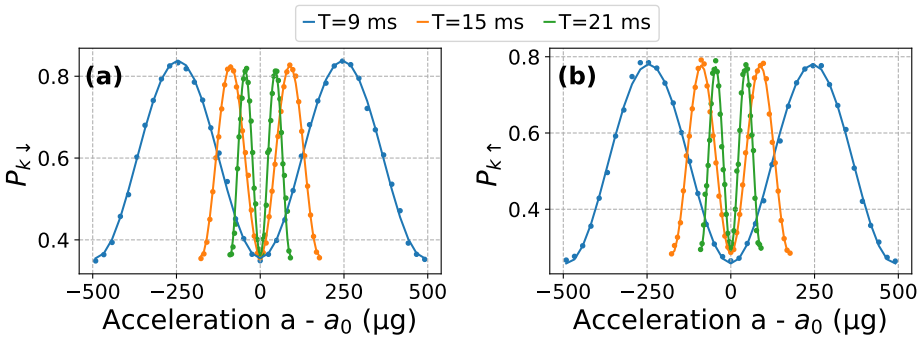

Figure 5.6: Raman fringes of the atom interferometer for different interrogation time T obtained by varying the series of frequency jumps. The Raman transitions are resonant with Doppler velocities classes of direction $-k_{\text{eff}}$ on (a) and $+k_{\text{eff}}$ on (b).

In Chapter 2, we described the operation of the atom interferometer with a series of phase-continuous frequency jumps ω_1, ω_2 and ω_3 at each pulse. The frequency jumps compensate the frequency Doppler shift and imprint a laser phase $\phi_{\text{continuous}} = ak_{\text{eff}}T_{\text{eff}}^2$ when the frequency jumps are set according to the first jump as:

$$\omega_2 = \omega_1 + k_{\text{eff}}a(T + 2\tau) \tag{5.4}$$

$$\omega_3 = \omega_2 + k_{\text{eff}}a(T + 2\tau) \tag{5.5}$$

where a is an arbitrary acceleration we choose and τ is the Rabi pulse length. Figure 5.6 presents Raman fringes where a is varying arbitrarily by controlling the frequency jumps and $a_0 \simeq 9.805642$ m.s^{-2} is an independent measured value of local gravitational acceleration [18]. The phase output of the interferometer is $\Phi = \phi_{\text{kin}} + \phi_{\text{laser}}$, with the inertial phase $\phi_{\text{kin}} = -(a_0 + a_{\text{vib}})k_{\text{eff}}T_{\text{eff}}^2$ and the imprinted laser phase $\phi_{\text{laser}} = \phi_{\text{continuous}} + \phi_{\text{vib}}$.

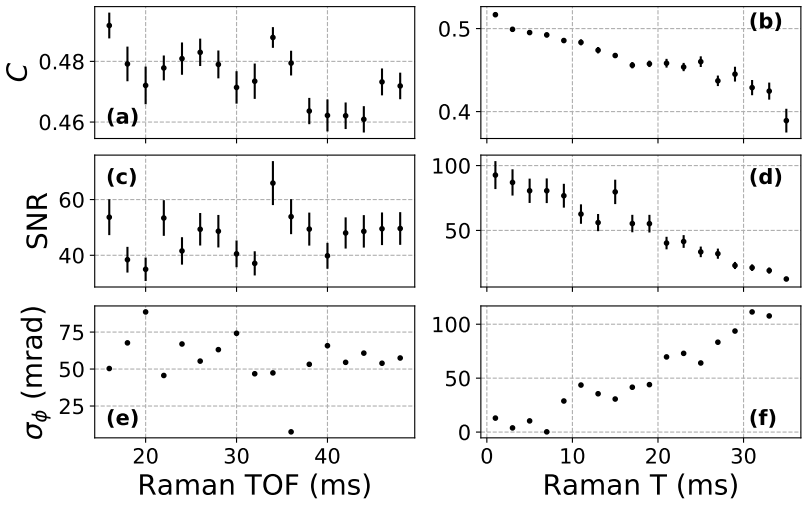

Figure 5.7: Estimation of the contrast (a) (b), the SNR (c) (d) and the phase noise in mrad/shot (e) (f), for different TOF at T=20 ms (a) (c) (e) and for different interrogation time T at TOF=16 ms (b) (d) (f).

Figure 5.7 shows the fit estimations of Raman fringes for different interrogation time T and time-of-flight TOF. The signal to noise ratio (SNR) is defined as SNR $= C/r_{\text{std}}$, where r_{std} is the standard deviation of the residuals from the fit estimation $r_i = P_i - \tilde{P}_i$. The phase noise σ_ϕ is estimated by a Bayesian approach with negative log-likelihood fit model [90]. When the TOF is varying, the contrast and the SNR are rather stable with a mean value of respectively $C = 0.47$ and SNR=47 for an interrogation time of $T = 20$ ms. The mean value of the phase noise gives us a phase sensitivity of $\sigma_\phi = 59$ mrad/shot, corresponding to a sensitivity to acceleration of $\sigma_a = 1.1\ \mu\text{g}/\sqrt{\text{Hz}}$. Aside from a slight reduction of the contrast, the atom interferometer is more sensitive when the interrogation time T is increased. Residual mechanical vibrations not compensated with the hybridization of the classical interferometer intensify the phase noise. Indeed the classical accelerometer is reaching a sensitivity of $\simeq 1\ \mu\text{g}/\sqrt{\text{Hz}}$.

5.3.2 Long-term stability with the tracking algorithm

The mid-fringe tracking algorithm is used to measure the stability of the atom interferometer. We alternate the sign of $\vec{k_{\text{eff}}}$ between each measurement to obtain an estimation of the acceleration along the two interferometric paths $a_\uparrow$ and $a_\downarrow$. We

compute the "dependant" acceleration $a_{\text{Dep}} = \frac{a_\uparrow + a_\downarrow}{2}$ and 'independent' acceleration $a_{\text{Ind}} = \frac{a_\uparrow - a_\downarrow}{2}$ from the sign of $\vec{k_{\text{eff}}}$. Therefore, a_{Dep} represents the true acceleration observed by the atoms and reject most of systematic effects including first order light shifts and quadratic Zeeman shift. Those rejected systematic effects are present in a_{Ind} and contain informations relative to their stability.

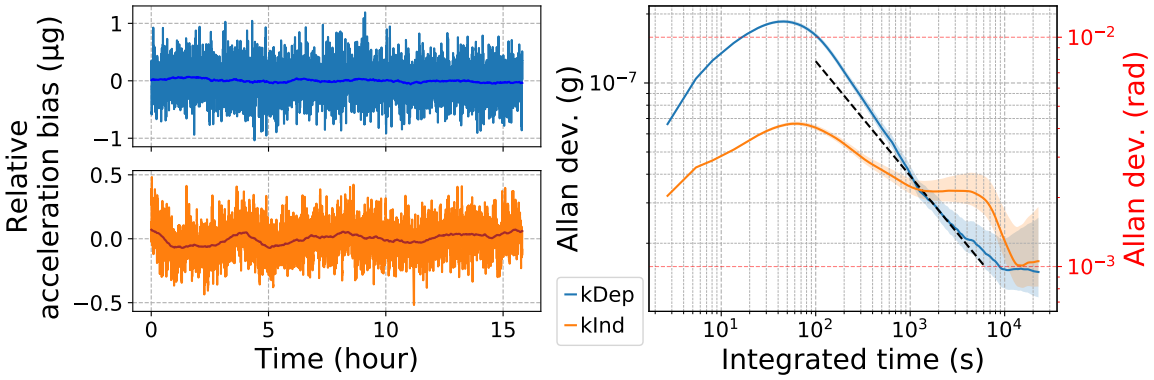

Figure 5.8: Stability in time of the acceleration measurements a_{Dep} dependent on the sign of $\vec{k_{\text{eff}}}$ in blue with rejected systematic effects and a_{Ind} independent on the sign of $\vec{k_{\text{eff}}}$ in orange. The interrogation time of the atom interferometer is 20 ms. The tides have been removed from the acceleration measurements in the a_{Dep} part. The darker colors on the time-series graphs expose a one hour moving average. The dashed line on the Allan deviation graph represents a $1/\sqrt{t}$ time integration of uncorrelated measurements.

Figure 5.8 presents the relative stability of the acceleration measured by the atom interferometer over 15 hours with an interrogation time T=20 ms. The tidal effects are visible after 10^3 s and have been removed from the measurements. The bump on the Allan deviation at 50 s corresponds to oscillations of the mid-fringe lock where the integrator part struggles to compensate several types of noise and averages it after the bump at a scale between correlated noises $1/t$ and uncorrelated noises $1/\sqrt{t}$. We use the measurements integrated as $1/\sqrt{t}$ after 10^3 s to determine a sensitivity of $\sigma_a = 1.24$ $\mu\text{g}/\sqrt{\text{Hz}}$ corresponding to a phase sensitivity of $\sigma_a = 68$ mrad/shot. After 1 hour, the measurements reach the level of mrad and stop integrating. Here, we assume that the stability is limited by the two-photon light shift (TPLS) where the co-propagating Raman interaction is unstable due to residual polarization variation. This effect is later detailed in Sec. 5.3.4. The stability of the acceleration stabilizes at 10 ng level after 5h30 of integration.

5.3.3 Magnetic field

Figure 5.9 presents the stability of the magnetic field in time and its spatial dependency. It has been measured with spectroscopies of co-propagating Raman

transitions. As a result of the magnetic shield made from μ-metal isolating the atoms from external magnetic fluctuations, we obtain a magnetic field stability of 10 μGauss after 8 hours of integration. Efforts have been made in the design of the sensor head to avoid magnetic components and prevent time-dependent Eddy currents. We use pairs of Helmholtz and anti-Helmholtz coils to respectively generate a Zeeman shift for magnetic states degeneracy and suppress residual magnetic gradient field. However, a residual 1 mGauss spatial magnetic field is present over the free-fall trajectory of the atoms due to magnetic materials nearby the sensor head inside the magnetic shield.

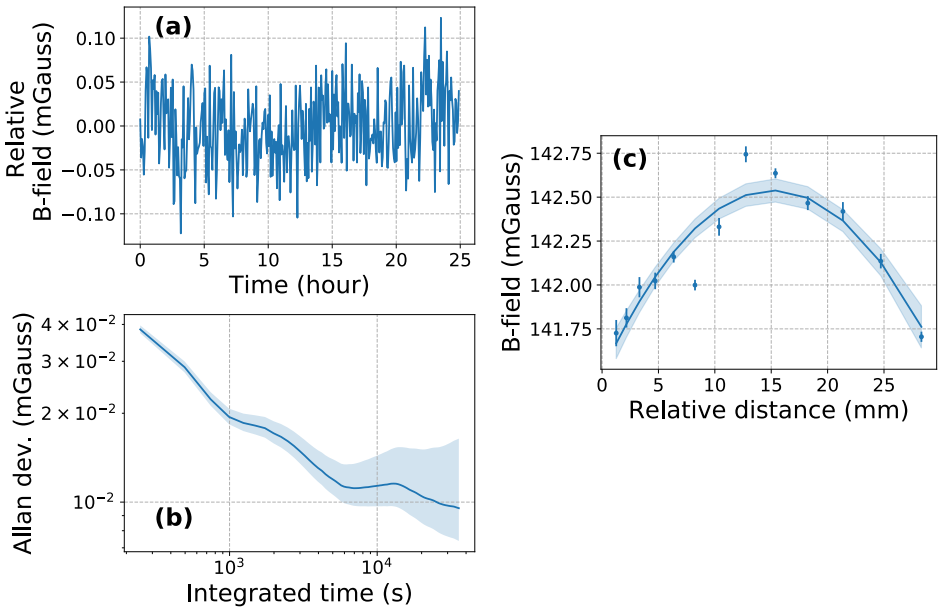

Figure 5.9: (a) (b) Time stability and (c) spatial dependence along the atomic free-fall path of the magnetic field. The measurements are obtained with spectroscopies of co-propagating Raman transitions.

The frequency of the hyperfine transition is sensitive to the magnetic field. The tensor light shift also participates to the shift of the energy state transitions and has not been included or calculated. The second order Zeeman frequency shift affects frequency of the clock transition by $\omega_B(z) = 2\pi K|B(z)|^2$, with $K = 575.15$ Hz/G^2 the clock transition Zeeman shift and $B(z)$ the magnetic field at position z. The fit estimation of the spatial part on Fig. 5.9(c) shows a remaining spatial curvature. The resulted phase shift from the Zeeman frequency shift is computed with the sensitivity function $g(t)$ as:

$$\phi_B = \int g(t)\omega_B(t)dt = 2\pi K \int g(t)\left(|B(z(t))|^2 - |B(z(0))|^2\right)dt \tag{5.6}$$

The trajectory of the atom interferometer influences the magnetic field experienced by the atoms. In consequence the resulted phase shift is highly rejected with the two interferometers alternating the recoil direction according to $\pm k_{\text{eff}}$. For an atom

interferometer of interrogation time T=20 ms and a TOF=15 ms, we obtain a residual acceleration shift of $\phi_B = 5.3 \pm 0.7$ ng thanks to the $\pm k_{eff}$ rejection.

5.3.4 Light shifts

AC Stark shift

The one-photon light shift (OPLS) (or AC Stark shift) ω_{AC} is common to two interferometers with trajectory determined by $\pm k_{eff}$. It means that the calculation of the 'dependent' acceleration $a_{Dep} = \frac{a_\uparrow + a_\downarrow}{2}$ allows to nearly cancel OPLS [89, 7]. Moreover, the cancellation of the OPLS have been optimized by modifying the intensity ratio between the Raman lines of the laser and have been adapted for the Raman detuning $\Delta_R = -877$ MHz. For this reason we consider negligible the impact of the OPLS on the atom interferometer.

Two-photon light shift

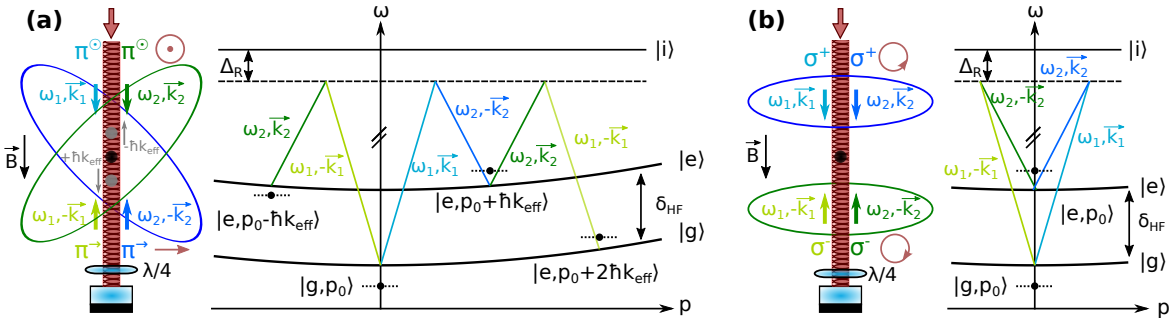

Figure 5.10: Illustration of the two-photon light shift for counter-propagating Raman transitions (a) and residual co-propagating Raman transitions (b).

The two-photon light frequency shift (TPLS) is expressed as [91]:

$$\omega_{TPLS\pm} = \omega^{counter}_{TPLS\pm} + \omega^{co}_{TPLS\pm} \tag{5.7}$$

where $\omega^{counter}_{TPLS\pm}$ and $\omega^{co}_{TPLS\pm}$ are the TPLS frequency shifts induced respectively by counter-propagating and co-propagating Raman transitions:

$$\omega^{counter}_{TPLS\pm} = \frac{\Omega^2_{eff}}{\pm 8\omega_D} + \frac{\Omega^2_{eff}}{\pm 8\omega_D + 16\omega_R} \tag{5.8}$$

$$\omega^{co}_{TPLS\pm} = \frac{\Omega^2_{co}}{4(\pm\omega_D + \omega_R)} \tag{5.9}$$

with ω_D the Doppler frequency shift and ω_R the recoil frequency shift. The sign of the Doppler frequency is determined by the direction of the selected Raman

transitions $\pm k_{\text{eff}}$. Figure 5.10 illustrates the frequency shifts on the energy states induced by counter-propagating and co-propagating Raman transitions. The TPLS co-propagating frequency shift is caused by slight residue of elliptical polarization of the light. Here we consider only the transitions between magnetic states $|F = 1, m_f = 0\rangle$ and $|F = 2, m_f = 0\rangle$ and ignore the impact of the transitions involving magnetic states $|m_f = \pm 2\rangle$ where the impact is at least three times lower. The phase shift induced by the TPLS depends on the frequency shift and effective Rabi frequency at the first (1) and last pulse (3):

$$\phi_{\text{TPLS}} = \frac{\omega^{(1)}_{\text{TPLS}}}{\Omega^{(1)}_{\text{eff}}} \tan\left(\frac{\Omega^{(1)}_{\text{eff}}\tau}{2}\right) - \frac{\omega^{(3)}_{\text{TPLS}}}{\Omega^{(3)}_{\text{eff}}} \tan\left(\frac{\Omega^{(3)}_{\text{eff}}\tau}{2}\right) \tag{5.10}$$

For a Rabi frequency nearly optimized $\Omega_{\text{eff}} \approx \pi/2\tau$ and a negligible contribution of the TPLS from the co-propagating transitions $\omega^{\text{co}}_{\text{TPLS}\pm}$, the resulted phase shift is linear with the power and scales as $\phi^{\text{counter}}_{\text{TPLS}}(\Omega_{\text{eff}}, \omega_{\text{D}}) \propto \Omega_{\text{eff}}/4\omega_{\text{D}}$. By modulating the power of the laser [89], one can obtain the TPLS phase shift for two different intensities I_1 and I_2 and reject mostly the effect with the expression:

$$\frac{r\phi^{\text{counter}}_{\text{TPLS}}(\Omega^{\text{P1}}_{\text{eff}}, \omega_{\text{D}}) - \phi^{\text{counter}}_{\text{TPLS}}(\Omega^{\text{P2}}_{\text{eff}}, \omega_{\text{D}})}{r - 1} \approx 0 \tag{5.11}$$

where $r = \Omega^{\text{P2}}_{\text{eff}}/\Omega^{\text{P1}}_{\text{eff}} \approx I_2/I_1$ is the ratio between the two Rabi frequencies at two different laser power.

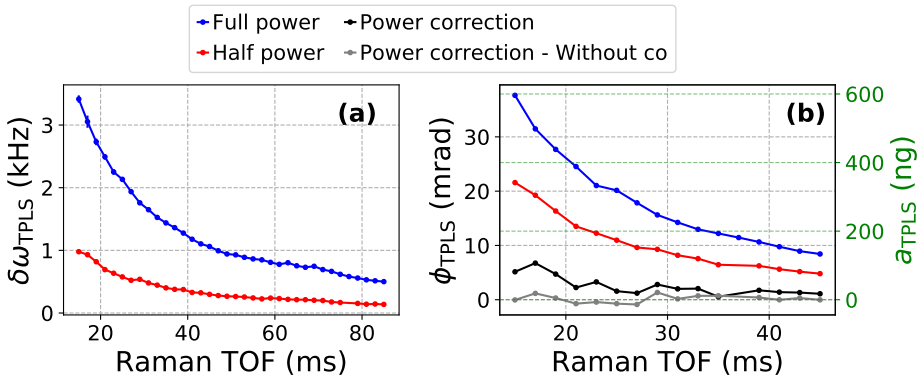

Figure 5.11: Estimation of the frequency shift (a) and the phase shift (b) of the TPLS for different TOF at two laser power. The phase and acceleration shift of the TPLS is estimated for a Raman interrogation time T=20 ms. The expression from Eq. 5.11 is used to correct the total phase shift ϕ_{TPLS} in black and the phase shift involving only the counter-propagating transitions $\phi^{\text{counter}}_{\text{TPLS}}$ in grey.

We measured the Rabi frequencies of the counter-propagating transitions Ω_{eff} and co-propagating transitions Ω_{co} (exposed in Sec. 5.3.5) to estimate the phase shift of the interferometer. Figure 5.11 shows the frequency shift and the phase shift induced by the TPLS for two laser power. We notice that the power correction with expression

from Eq. 5.11 is efficient for counter-propagating transitions, but is affected by the residual co-propagating transitions and the rejection of the TPLS is not complete. We obtain residuals of 80 ng at TOF=15 ms and 20 ng at TOF=45 ms.

Influence of the polarization on the stability

To control the polarization of the light in our experiment, we are using a liquid-crystal retardance waveplate (LCR) which is temperature sensitive. On Chapter 3, we described its operation and impact on the phase shift of the atom interferometer. For that, we calibrated a monitoring photodiode sensitive to the polarization to measure the difference of the polarization between the first and last pulse of the interferometer. We correlated the stability of the co-propagating Raman transitions over time and its impact on the phase shift.

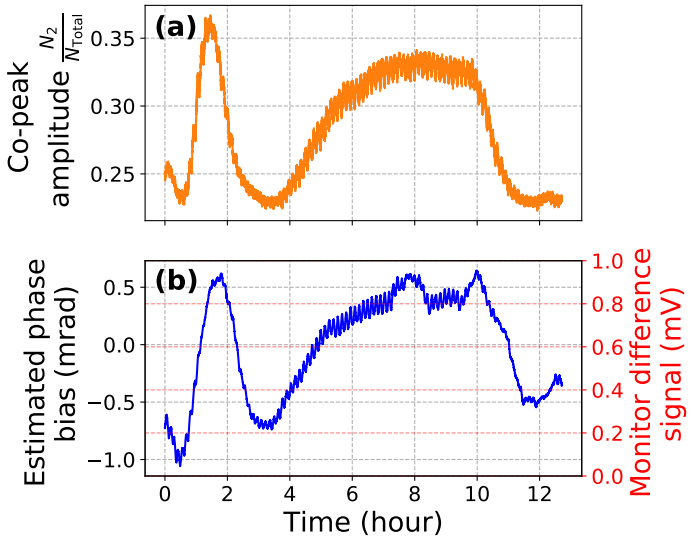

Figure 5.12: (a) Amplitude of the peak of the residual co-propagating Raman interaction. (b) Signal of the monitor photodiode measuring the difference polarization after the LCR waveplate.

Figure 5.12(a) shows the evolution of the amplitude of the co-propagating Raman transitions peak. We depict the signal difference of the monitoring photodiode and we estimated the resulted phase shift on the interferometer as shown in Fig. 5.12(b). The resulted estimated phase shift reaches a standard deviation of 0.5 mrad. This corresponds to an acceleration error of 8 ng at T=20 ms. Since it is a pure phase shift, the effect can be dramatic at low interrogation time, reaching for example 3 μg at T=1 ms.

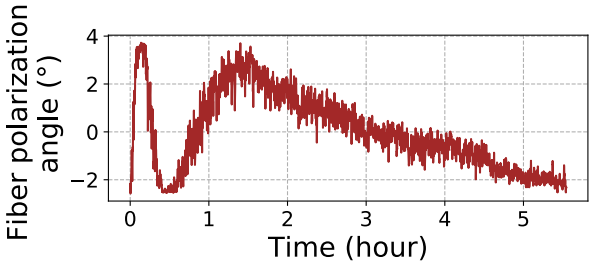

Figure 5.13: Angle of the linear polarization of the Raman laser.

In Chapter 4, we described the 780 nm optical fiber bench used to switch and recombine the light to the sensor head. We identified an instability of the angle of the polarization at the output of the fiber bench as depicted on Fig. 5.13. We suspect that the variation of this angle affects the polarization switch efficiency of the LCR waveplate and provokes instability on the co-propagating Raman transitions as shown on Figure 5.12.

5.3.5 Cloud position dependence of Rabi frequencies

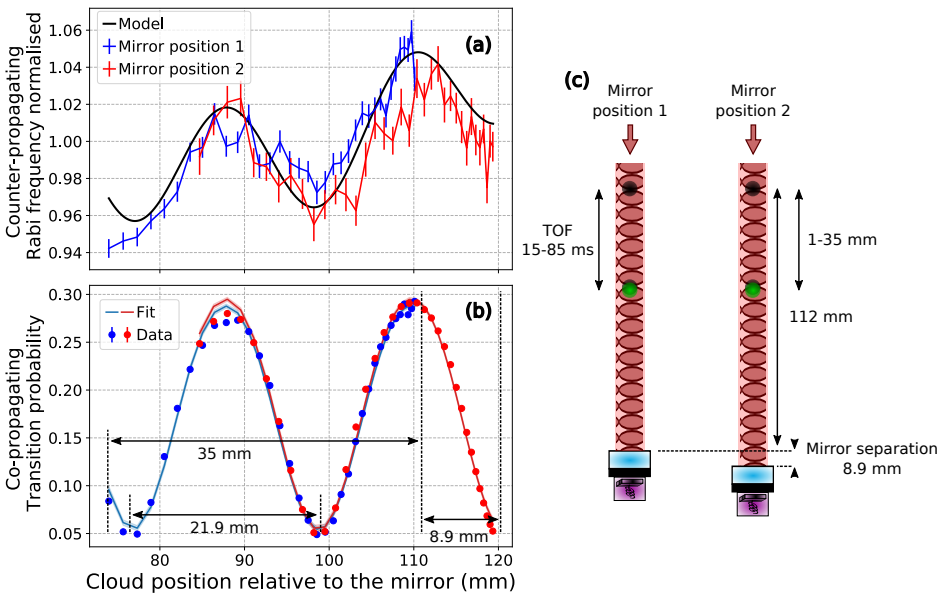

Figure 5.14: Rabi frequency of counter-propagating Raman transition (a) and amplitude of the peak of co-propagating Raman transitions spectroscopy (b) at different positions of the cloud relative to the reference mirror obtained by varying the TOF. (c) Spatial scheme of the measurements illustrating the mirror displacement.

Counter-propagating Raman transitions

In Chapter 4, we evaluated the effective Rabi frequency deriving from a Raman spectrum with parasitic lines. The effective Rabi frequency is defined by the modulus of the sum of each Raman transition occurring as:

$$\Omega_{\text{eff}}^{\text{model}}(z) = |\sum_{I,J} \chi_{I,J} e^{i(I\Delta k_1 + J\Delta k_2)z}| \tag{5.12}$$

where $\chi_{I,J}$ is the effective Rabi frequency associated to a pair of parasitic lines, with corresponding parasitic momentum recoil of $I\Delta k_1 + J\Delta k_2$.

In Figure 5.14(a) we measured the Rabi frequencies at different positions over the atomic path by letting drop the atoms (TOF variation). We also moved the position of the mirror to broaden the scanned region. We compared the measurements with the model and observed good accordance. The periodicity of the Rabi frequencies are determined by the distance $d_{I,J} = \frac{\pi c}{I\Omega_1 + J\Omega_2}$, where $\Omega_1/2\pi \approx 1$ GHz and $\Omega_2/2\pi \approx 7.8$ GHz are the frequency modulations used for CS-DSSB modulation. The highest parasitic Rabi frequencies are $\chi_{1,-1}$, $\chi_{-1,1}$ and $\chi_{1,0}$ and lead respectively to periodicities of $d_{1,-1} = d_{-1,1} = 21.9$ mm and $d_{1,0} = 157$ mm.

Co-propagating Raman transitions

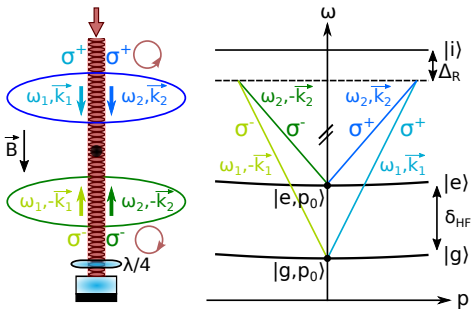

Figure 5.15: Illustration of the co-propagating Raman transitions where the light has to be σ polarized.

We determined very precisely the position of the atomic cloud relative to the reference mirror and the relative position of the mirror between the two cases. We took advantage of the co-propagating Raman transitions generated by two pairs of Raman beams, one from the straight path and the other from the reflected path, as shown in Figure 5.15. Indeed the transitions interfere constructively or destructively and are in competition between the straight co-propagating Raman transitions and the retro-reflected ones, depending on the position of the cloud relative to the mirror. On Figure 5.14(b), the period of the oscillations is directly dependent on the hyperfine transition and create a spatial periodicity of $\frac{\pi c}{\delta_{\text{HF}}} = 21.9$ mm. The fit estimation gives an initial position of the MOT cloud relative to the reference mirror of 111.6 ± 0.2 mm in standard position (mirror position 1), a relative distance of the reference mirror between the two cases of 8.9 ± 0.3 mm and an initial velocity of 26(4) and 5(3) mm/s for respectively the mirror position 1 and 2. The variation of the initial velocity between

the two cases can be explained by the phase behavior spatially-dependant affecting the grey molasses.

5.3.6 Scale factor error

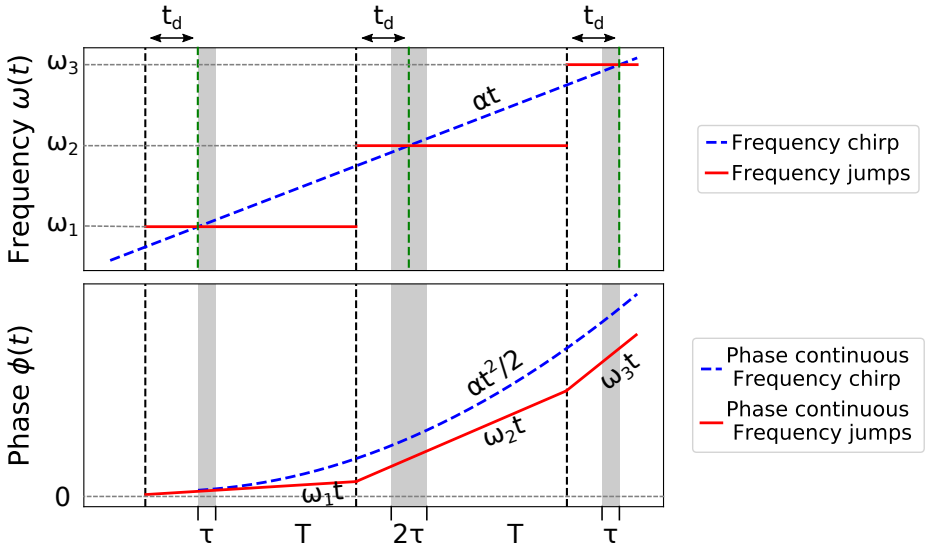

Figure 5.16: Comparison between phase continuous frequency chirp (in dashed blue) and phase continuous frequency jumps (in red) during Raman interferometer. The resulted phase for the first case follows the kinetic path of the atomic cloud. Whereas for the second case, the slope of the phase changes at each frequency update and impacts differently the scale factor.

The phase output of the interferometer depends on the inertial phase ϕ_{kin}, corresponding to the acceleration of the atoms relative to the reference mirror, and the imprinted laser phase ϕ_{laser} induced by the Raman laser phase. The imprinted laser phase is specific when a series of phase-continuous frequency jumps is applied. Figure 5.16 illustrates the frequency and the associated Raman laser phase of a chirp, usually used for gravimeters, and for a series of phase-continuous frequency jumps. On Chapter 2 we determined the associated scale factors from the inertial and the phase parts as:

$$\frac{S_{\text{kin}}}{k_{\text{eff}}} = (T+2\tau)\left[T+\frac{1}{\Omega_{\text{eff}}^{(1)}}\tan\left(\frac{\Omega_{\text{eff}}^{(1)}\tau}{2}\right)+\frac{1}{\Omega_{\text{eff}}^{(3)}}\tan\left(\frac{\Omega_{\text{eff}}^{(3)}\tau}{2}\right)\right] \tag{5.13}$$

$$\frac{S_{\text{continuous}}}{k_{\text{eff}}} = (T+2\tau)\left[T+\frac{2}{\Omega_{\text{eff}}^{(3)}}\tan\left(\frac{\Omega_{\text{eff}}^{(3)}\tau}{2}\right)\right] \tag{5.14}$$

where $\Omega_{\text{eff}}^{(1)}$ and $\Omega_{\text{eff}}^{(3)}$ correspond to Rabi frequencies respectively at the first and last pulse of the interferometer and τ is the Rabi pulse length at $\pi/2$-pulse. By defining the scale factor error as $\delta S = S_{\text{continuous}} - S_{\text{kin}}$, the phase output of the atom interferometer

is:

$$\begin{aligned} \Phi &= \phi_{\text{kin}} + \phi_{\text{laser}} && (5.15)\\ &= -aS_{\text{kin}} + aS_{\text{continuous}} && (5.16)\\ &= a\delta S && (5.17) \end{aligned}$$

where a is the acceleration of the atoms relative to the reference mirror and the acceleration defined by the arbitrary frequency jumps. We define the phase shift induced by the scale factor error as ϕ_{SF}. It is calculated as:

$$\begin{aligned} \phi_{\text{SF}} &= a\delta S && (5.18)\\ &= ak_{\text{eff}}\left(T+2\tau\right)\left[\frac{1}{\Omega_{\text{eff}}^{(3)}}\tan\left(\frac{\Omega_{\text{eff}}^{(3)}\tau}{2}\right) - \frac{1}{\Omega_{\text{eff}}^{(1)}}\tan\left(\frac{\Omega_{\text{eff}}^{(1)}\tau}{2}\right)\right] && (5.19)\\ &\simeq ak_{\text{eff}}\left(T+2\tau\right)\left(\Omega_{\text{eff}}^{(3)} - \Omega_{\text{eff}}^{(1)}\right)\left(\frac{\pi}{2}-1\right)\left(\frac{2\tau}{\pi}\right)^2 && (5.20) \end{aligned}$$

where the last expression is a first order approximation. The resulted acceleration bias due to the error on the scale factor is $\delta a_{\text{SF}} = \phi_{\text{SF}}/S_{\text{kin}} = a\delta S/S_{\text{kin}}$. The phase shift from the scale factor error has the same dependence on the effective Rabi frequencies as the phase shift induced by the TPLS from Eq. 5.10. Consequently, we apply the method from Eq. 5.11 to reject the effect of the scale factor error by measuring the phase with two different powers.

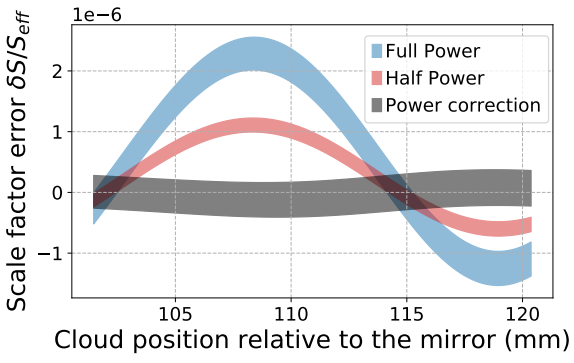

Figure 5.17: Estimation of the error on the effective scale factor due to parasitic Rabi oscillations for two different laser power. The power correction is using the expression from Eq. 5.11 to reject the effect from the error on the scale factor.

In Section 5.3.5, we measured the Rabi frequencies of the counter-propagating Raman transitions for different position of the cloud relative to the reference mirror. We detected fluctuations, as shown on Figure 5.14(a), deriving from the parasitic

lines of the laser spectrum induced by the CS-DSSB modulation. In consequence, it generates a phase shift from the scale factor error ϕ_{SF}. The scale factor error $\delta S/S_{\mathrm{kin}}$ is estimated in Fig. 5.17 for two different laser powers. We used the model of parasitic Rabi frequencies induced by parasitic lines for the calculations, which are shown in Fig. 5.14(a). It generates an error at the order of μg on the measurements. By using the expression from Eq. 5.11 with measurements between two different laser powers, we reject largely the error from the scale factor.

5.3.7 Other systematic effects

Alignment of the laser beams

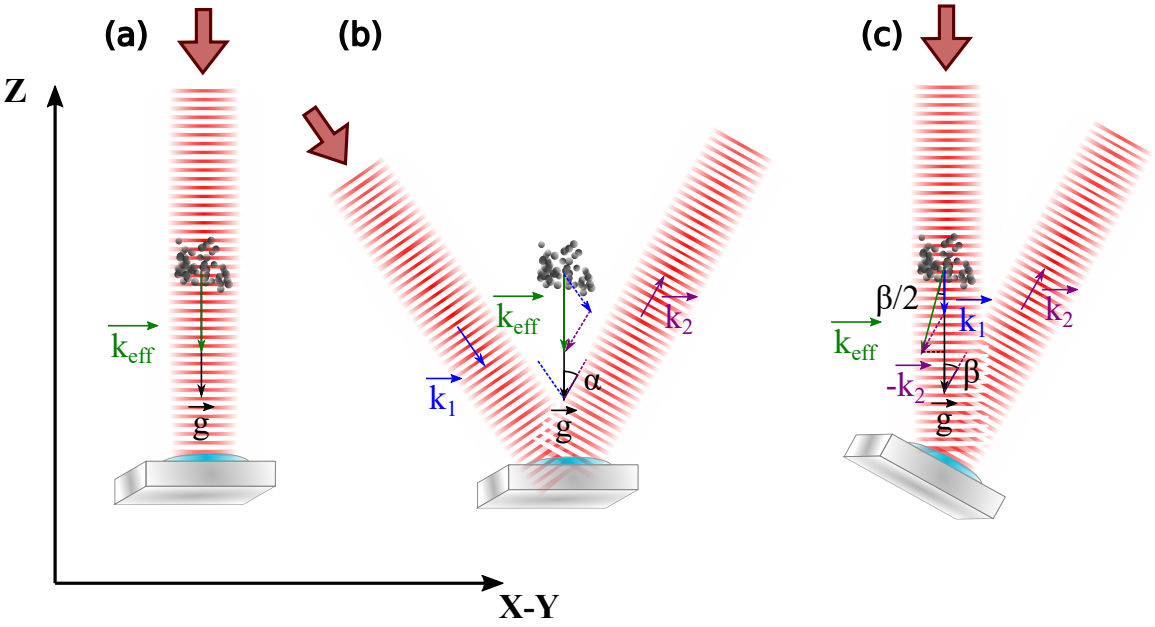

Figure 5.18: Illustration of the different misalignments of the effective wavevector $\vec{k_{\mathrm{eff}}}$. The angles are exaggerated for better comprehension and the laser beams should cross the atomic cloud for each case. (a) Ideal alignment. (b) Tilt of the collimator. (c) Tilt of the mirror relative to the collimator.

The effective wavevector $\vec{k_{\mathrm{eff}}}$ is affected when the retro-reflected laser beam is not aligned with the straight path. Figure 5.18 illustrates the different cases of misalignment when the reference mirror or the collimator are tilted. When the mirror is tilted, the effective wavevector k_{eff} is not aligned with the acceleration vector we want to measure as:

$$\vec{g} \cdot \vec{k_{\mathrm{eff}}} = g k_{\mathrm{eff}} \cos(\beta/2) \tag{5.21}$$

where β is the tilt angle of the mirror. In addition the scale factor is impacted when the collimator is tilted with respect to the reference mirror as:

$$k_{\text{eff}} = \vec{k_1} \cdot \vec{k_2} = k_1 k_2 \cos(2\alpha + \beta) \tag{5.22}$$

where α is the tilt angle of the collimator. The resulted measurement is affected at the second order by a shift of:

$$1 - \cos(2\alpha + \beta)\cos(\beta/2) \sim 2\alpha^2 + 2\alpha\beta + \frac{5}{8}\beta^2 \tag{5.23}$$

The alignment of the collimator is adjusted by checking the round trip of the laser beam through a pinhole placed at the output of the collimator. We evaluate the precision of this technique precise at $\alpha < 0.5$ mrad. The angle of the reference mirror from the gravitational vector is not known, we consider it at zero for the calculus. The resulted shift is estimated at -500 ng. No particular effort has been conducted to reduce this effect and explains this high shift.

Gravity gradient

Gravity gradient is affecting the interferometric path of the atomic cloud. The phase shift induced is determined by [92]:

$$\phi_\Gamma = \pm k_{\text{eff}} \Gamma_{zz} (vT + \frac{7}{12} g T^2) T^2 \tag{5.24}$$

where v is the initial velocity of the atoms and Γ_{zz} is the component of the gravity gradient tensor along the atomic interferometric path. The sign of the shift is determined by the direction of $\vec{k_{\text{eff}}}$. For T=20 ms, $\phi_\Gamma \simeq 100\mu$rad corresponding to a negligible acceleration bias of 1.6 ng.

Coriolis shift

The three-pulse Mach-Zehnder atom interferometer is sensitive to inertial effects, including Coriolis acceleration. The phase shift induced by the Coriolis acceleration depends on the cross product between the effective wavevector k^i_{eff} along each axis with the initial velocity v^i_0 and the acceleration of the atoms a^i along each axis. In this Chapter, the only source of rotation is the Earth rotation rate Ω_{rot}. The phase shift can be expressed as [93]:

$$\phi_\Omega = \mp 2 \left[k^i_{\text{eff}} \times (v^i_0 + a^i T) \right] \cdot \Omega_{\text{rot}} T^2 \tag{5.25}$$

where the sign is determined by the direction of $\vec{k_{\text{eff}}}$. Here, we consider only an acceleration of g along the vertical axis. The initial velocity $v_0 = 26(4)$ mm/s of the atoms along the vertical axis has been determined in Sec. 5.3.5. Along the two other

axes, the initial velocity is not known and is considered null with an uncertainty of 30 mm/s. In those conditions, the resulted phase shift induced by the Coriolis acceleration is estimated at $\phi_\Omega = 0 \pm 315$ ng.

Mach-Zehnder interferometer asymmetry

The transition probability of the Mach-Zehnder interferometer from Eq. 5.2 is valid when each Rabi pulse of the interferometer is optimal and the laser frequency detuning δ is set on the center of the counter-propagating velocity distribution. According to Ref. [94], and by assuming a Gaussian velocity distribution $G(v)$ for the atomic cloud ($\simeq 3$ μK), we can estimate the phase shift ϕ_{MZA} induced by an asymmetry of the Mach-Zehnder interferometer as:

$$\overline{P} = \int G(v)P(v)dv \simeq P_0 - \frac{1}{2}C\cos(\phi_0 + \phi_{\mathrm{MZA}}) \tag{5.26}$$

with:

$$\phi_{\mathrm{MZA}} = \frac{1}{C}\int G(v)C(v)\Delta\Phi_{\mathrm{MZA}}(v)dv \tag{5.27}$$

Here, $C(v)$ and $\Delta\Phi_{\mathrm{MZA}}(v)$ represent respectively the contrast and the phase shift of the interferometer depending on the velocity distribution of the atoms. Whether the direction chosen for $\vec{k_{\mathrm{eff}}}$ is positive ($\uparrow$) or negative ($\downarrow$), the frequency of the counter-propagating transition depending on the velocity v of the atomic velocity distribution $G(v)$ is given by:

$$\delta_{\downarrow,\uparrow}(v) = k_{\mathrm{eff}}v + \omega_{\mathrm{R}} + \omega_{\mathrm{OPLS}} + \omega_{\mathrm{B}} \pm \omega_{\mathrm{D}} \pm \omega_{\mathrm{TPLS}}^{\mathrm{Counter}} - \delta_{\downarrow,\uparrow} \tag{5.28}$$

where $\delta_{\downarrow,\uparrow}$ is the laser frequency detuning and the frequency shifts are detailed in Sec. 5.1.1. We define the total Rabi frequency at pulse n of the interferometer as $\omega_{\downarrow,\uparrow}^{(n)}(v) = \sqrt{\delta_{\downarrow,\uparrow}(v)^2 + (\Omega_{\mathrm{eff}}^{(n)})^2}$. Reference [94] provides the expressions of the contrast $C(v)$ and the phase shift $\Delta\Phi_{\mathrm{MZA}}(v)$ as follow:

$$\begin{aligned}\Delta\Phi_{\downarrow,\uparrow}(v) = \arg\left(\cos\left(\frac{\omega_{\downarrow,\uparrow}^{(1)}(v)\tau}{2}\right) - \frac{i\delta_{\downarrow,\uparrow}(v)\sin\left(\frac{\omega_{\downarrow,\uparrow}^{(1)}(v)\tau}{2}\right)}{\omega_{\downarrow,\uparrow}^{(1)}(v)}\right) \\ + \arg\left(\cos\left(\frac{\omega_{\downarrow,\uparrow}^{(3)}(v)\tau}{2}\right) + \frac{i\delta_{\downarrow,\uparrow}(v)\sin\left(\frac{\omega_{\downarrow,\uparrow}^{(3)}(v)\tau}{2}\right)}{\omega_{\downarrow,\uparrow}^{(3)}(v)}\right)\end{aligned} \tag{5.29}$$

$$C_{\downarrow,\uparrow}(v) = \frac{4\Omega_{\text{eff}}^{(1)}(\Omega_{\text{eff}}^{(2)})^2\Omega_{\text{eff}}^{(3)}\sin^2\left(\omega_{\downarrow,\uparrow}^{(2)}(v)\tau\right)\sin\left(\frac{\omega_{\downarrow,\uparrow}^{(1)}(v)\tau}{2}\right)\sin\left(\frac{\omega_{\downarrow,\uparrow}^{(3)}(v)\tau}{2}\right)}{\left(\omega_{\downarrow,\uparrow}^{(1)}(v)\omega_{\downarrow,\uparrow}^{(2)}(v)\omega_{\downarrow,\uparrow}^{(3)}(v)\right)^2}$$
$$\times\left[\delta_{\downarrow,\uparrow}(v)\sin\left(\frac{\omega_{\downarrow,\uparrow}^{(1)}(v)\tau}{2}\right)\sin\left(\frac{\omega_{\downarrow,\uparrow}^{(3)}(v)\tau}{2}\right)+\omega_{\downarrow,\uparrow}^{(1)}(v)\omega_{\downarrow,\uparrow}^{(3)}(v)\cos\left(\frac{\omega_{\downarrow,\uparrow}^{(1)}(v)\tau}{2}\right)\cos\left(\frac{\omega_{\downarrow,\uparrow}^{(3)}(v)\tau}{2}\right)\right] \tag{5.30}$$

Since the Rabi frequencies are varying during the interferometer according to Figure 5.14(a), we expect a shift of 22±2 ng on the measurement of the acceleration.

Wavefront distortion shift

The phase profile of the wavefront Raman beams contains optical aberrations. The phase imprinted onto the atoms at each pulse is not homogeneous, which induces a phase shift. The curvature of the wavefront of a Gaussian beam can be characterized by the Rayleigh distance z_R at a distance z as:

$$R(z) = \frac{z^2 + z_R^2}{z^2} \tag{5.31}$$

In addition the path of the Raman beams between the straight and retro-reflected trajectory contains the window, the quarter-waveplate and the reference mirror, which will participate to the optical aberrations respectively as $\delta\phi_{\text{W}}$, $\delta\phi_{\lambda/4}$ and $\delta\phi_{\text{m}}$. The resulted phase shift on the atom interferometer is [95, 96]:

$$\phi_{\text{WD}} = k_{\text{eff}}\frac{(\sigma_v T)^2}{R} + 2\delta\phi_{\text{W}} + 2\delta\phi_{\lambda/4} + \delta\phi_{\text{m}} \tag{5.32}$$

The effect from the curvature of the Gaussian beam is evaluated at a distance $z = 330$ mm from the collimator to the atoms with the retro-reflected path and a Rayleigh distance $z_R = 100$ mm. We calculate a bias shift of 6 ± 1 ng on the measurement of the acceleration.

The complete characterization of the phase profile of the beam is difficult [89]. Especially, since the window is sealed to the sensor head, we can not quantify individually each impact. In consequence we did not characterize optical aberrations caused by the optics. Further study is required to quantify the impact of the wavefront distortion on the bias of the interferometer. For that reason, we increase the uncertainty of the wavefront distortion by $\simeq 100$ ng.

5.3.8 Summary of systematic effects

Systematic effect (ng)	Bias shift	Uncertainty	Section
Two-photon light shift	+81	10.2	5.3.4
Quadratic Zeeman	+5.3	0.7	5.3.3
Scale factor error	-130	50	5.3.6
Parasitic lines	+195	5	4.1.6
RF non-linearity	+170.9	0.2	4.2.4
MZ Asymmetry	+22	2	5.3.7
Gravity gradient	+1.6	4×10^{-3}	5.3.7
Coriolis effect	0	315	5.3.7
Beams misalignments	-	500	5.3.7
Wavefront distortion	6	100	5.3.7
Total	+351.8	983.1	-

Table 5.1: Table of systematic effects of the atom interferometer with an interrogation time of $T = 20$ ms.

Table 5.1 summarizes the acceleration biases induced by the systematic effects on the atom interferometer. We estimates the acceleration biases with two rejection techniques: change of the sign of $\vec{k_{\text{eff}}}$ and modulation of the power to reject widely the TPLS and the error on the scale factor. We consider an interrogation time of $T = 20$ ms and a time-of-flight of TOF=15 ms, corresponding to an initial position of the atomic cloud relative to the mirror of 111.6 mm at the start of the interferometer. The total bias shift on the measurement of the acceleration is estimated at 351.8 ± 983.1 ng. We note that this number is misjusdged due to the non-complete calculation of the wavefront distortion effect and the beams misalignments. Also the uncertainty on the initial velocity along the other axes raises the Coriolis effect estimation.

5.3.9 Relative accuracy

We characterized the accuracy of the acceleration measurements for different positions of the atomic cloud relative to the reference mirror. In particular, we want to verify the effect of the parasitic lines from the CS-DSSB modulation on the bias shift. We evaluated this impact on Chapter 4.

To scan different positions of the atomic cloud, we let drop the atoms by changing the TOF and move the mirror to broaden the region. We apply a series of phase-continuous frequency jumps according to $a_0 = 9.805642$ m.s^{-2}, an independent measured value of local gravitational acceleration [18]. In addition, we measure the acceleration

for different laser power to reject the TPLS and the scale factor error. For each measurement, we operate 45 minutes of tracking to reach around 20 ng of confidence according to the Allan deviation from Fig. 5.8.

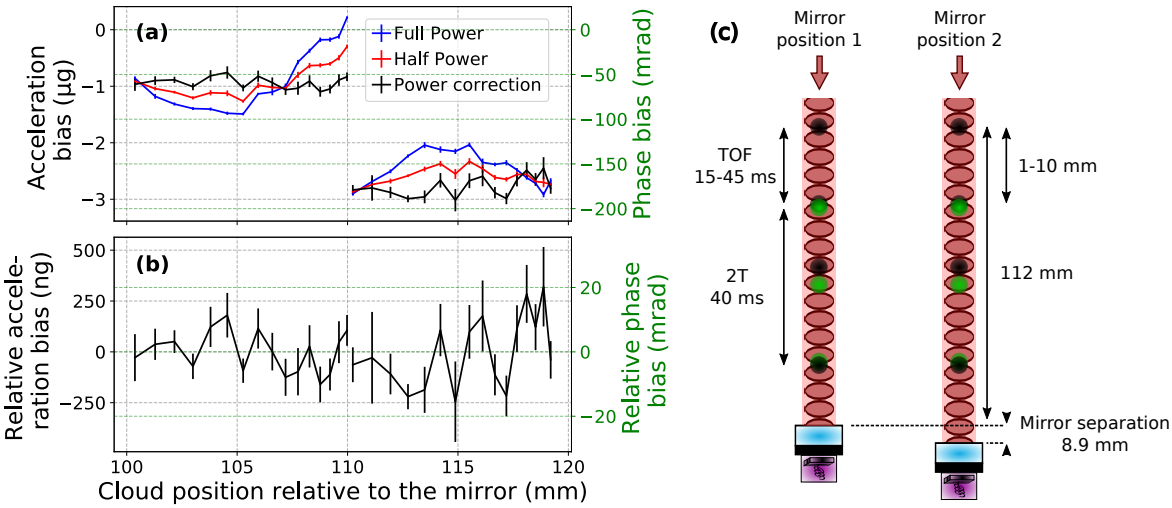

Figure 5.19: (a) Acceleration measurements for different positions of the atomic cloud at the start of the interferometer relative to the reference mirror. The interrogation time of the interferometer is T=20 ms. (b) Relative measurements of the power corrected accelerations. (c) Illustration of the atom interferometer with the mirror displacement and the TOF variation.

Figure 5.19 presents the measurements where the tides are corrected. By using the expression from Eq. 5.11, the power correction graph allows to reject the TPLS and errors from the scale factor. We obtain a relative accuracy depending on the position of the mirror of standard deviation $\simeq$ 100 ng. This uncertainty is coming from the noise of the measurements at half power, where the contrast and the SNR of the interferometer are lower, which decreases the precision. The measurements for a distance between 110 and 120 mm are more noisy. This is due to the position of the cloud during the state preparation and the grey molasses, which occurs at 120 mm from the reference mirror and corresponds to a destructive interferences spot for the co-propagating Raman transitions according to Fig. 5.14(b).

The acceleration biases are different by an amount of -0.937 and -2.771 μg from a_0 at respectively the position 1 and 2 of the reference mirror. This is a result of the systematic effects, where the uncertainty is rated at 0.983 μg in Table 5.1, and the tilt of the sensor head according to the gravitational acceleration vector. In addition, a relative acceleration offset between the two positions of the reference mirror is coming from a tilt of the mirror due to spacers used to move the mirror. We suspect also that the Coriolis effect is different between the two cases, since the initial velocity of the atoms is affected differently along the other axes.

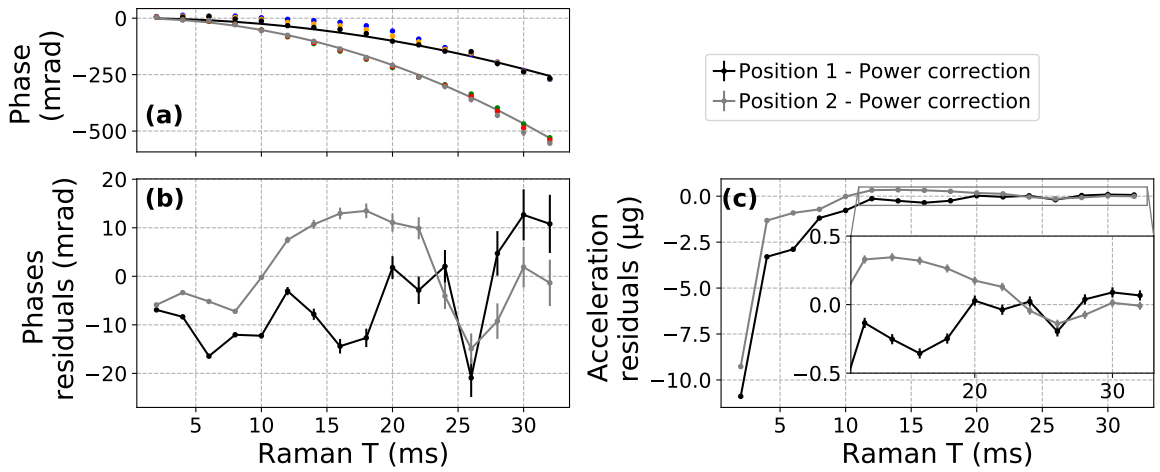

Figure 5.20: Gravity measurements for different interrogation time T. (a) Raw measurements for two different positions of the reference mirror with two different powers and the power corrected measurements. (b) Residuals of the fit from the measurements on (a) to remove the acceleration offset. (c) Same residuals as graph (b) expressed in acceleration.

We repeat similar measurements on the Figure 5.20 where the interrogation time T is varying for a fixed TOF=20 ms. To remove the acceleration offset on the phase measurements, we extract the residuals of the fit estimates giving an offset from the reference acceleration a_0 of -0.880 and -2.58 μg at respectively the position 1 and 2 of the reference mirror. The difference obtained from measurements in Fig. 5.19 is due to variations of the interrogation time T affecting systematic effects differently. The measurements are precise at ± 20 mrad. At low interrogation time $T < 10$ ms, the acceleration bias is large due to pure phase systematic effects dominated by the TPLS. Another reason is the duration of $T \simeq 10^{-3}$ s becoming closer to the Rabi pulse length $\tau \simeq 10^{-5}$ s which affects the estimation of the scale factor and decrease the rejection of the error on the scale factor made with the power correction.

The noise of the measurements for different position of the atomic cloud is higher than the effect of the parasitic lines estimated on Chapter 4. Indeed we predicted an oscillation with a standard deviation of $\simeq 58$ ng of bias depending the position of the atomic cloud. Consequently, the model of the parasitic lines can not be demonstrated here. Nevertheless, an upper limit of standard deviation $\simeq 100$ ng of relative accuracy is guaranteed.

Conclusion

We demonstrated that the performances of the atom interferometer along one-axis are in accordance with our expectations. Specifically, for an interrogation time of $T = 20$ ms, the stability of the bias is reaching 10 ng level after 1 hour of integration. We estimated the sensitivity of the acceleration at 1.24 $\mu g/\sqrt{\text{Hz}}$. We also validated the laser source to perform all the steps required for the atom accelerometer, including atom trapping and cooling, states preparation, interferometry and fluorescence for detection. We proved the compatibility of the CS-DSSB modulation to reach < 200 ng level of relative accuracy wherever the position of the atoms relative to the reference mirror.

Chapter 6

3-axis atomic accelerometer

This chapter reports the study of the 3-axis atomic accelerometer prototype. The optimization of cooling, state preparation and detection are operated. We also study the acceleration sensitivity, stability and the systematic effects depending on the tilt of the sensor head. In particular, the misalignments of the orthogonality of the 3-axis frame lead to errors on the norm of the full acceleration vector and need to be calibrated.

Contents

6.1 Operation of the 3-axis atomic sensor 175

6.2 Tilt of the sensor head 177

6.2.1 Axes quantization and states preparation 177

6.2.2 Temperature along the direction of each axis 177

6.3 Performances of the 3-axis atom interferometer 178

6.3.1 Acceleration sensitivity on each axis 178

6.3.2 Long-term stability of the 3-axis atomic accelerometer . . . 180

6.4 Calibration of the 3-axis atom accelerometer 181

6.4.1 Protocol for the calibration of the 3-axis atomic accelerometer 181

6.4.2 Rabi oscillations along the 3 laser beams profile 182

6.4.3 3D mapping of the magnetic field 182

6.4.4 Systematic effects 183

6.4.5 Correction of the 3-axis frame misalignments 187

Introduction

Whereas atomic gravimeters have been studied since decades and have lead to a mature technology [18], multi-axis atomic accelerometers need to be explored [33, 34, 47]. In particular, the acceleration along three axes has never been measured within a compact setup dedicated to inertial navigation. Furthermore, the full study of the systematic effects on multi-axis interferometry is novel and particular efforts are required, notably on the orientation of the instrument which needs high degrees of freedom.

In this chapter, we perform measurements on the 3-axis atom interferometer. We report the performances of each atom accelerometer in terms of sensitivity and stability. A well known problem with inertial navigation systems is the slight non-orthogonality of the triad formed by the measurement axes of the three accelerometers. A calibration is required to measure and correct the misalignments from the triad formed by the 3-axis atom accelerometer. We propose a method to calibrate the 3-axis atom accelerometer to evaluate and increase the accuracy.

6.1 Operation of the 3-axis atomic sensor

The 3-axis atom accelerometer is operated in the same spirit as the one-axis atom accelerometer performed in Chapter 5. However here we achieve sequentially the measurements along each of the three axes. Figure 6.1 presents the open-loop operation scheme of our 3-axis atom accelerometer. The classical accelerometers monitor the mechanical vibrations a_{vib} of the reference mirrors and a corresponding correlated phase ϕ_{vib} is imprinted onto the atom interferometer phase. In addition a series of phase-continuous frequency jumps is applied to compensate the Doppler frequency shift, where the phase imprinted $\phi_{\text{continuous}} = ak_{\text{eff}}T_{\text{eff}}^2$ correspond to the acceleration a along the chosen axis. Furthermore a modulation phase ϕ_{mod} serves to scan Raman fringes or to operate the mid-fringe lock algorithm. To select the axis of measurement, the CPU commands the real-time system and controls a numerical switch to select the classical accelerometer. In parallel, the optical fiber switch controls the path of the laser onto the sensor head.

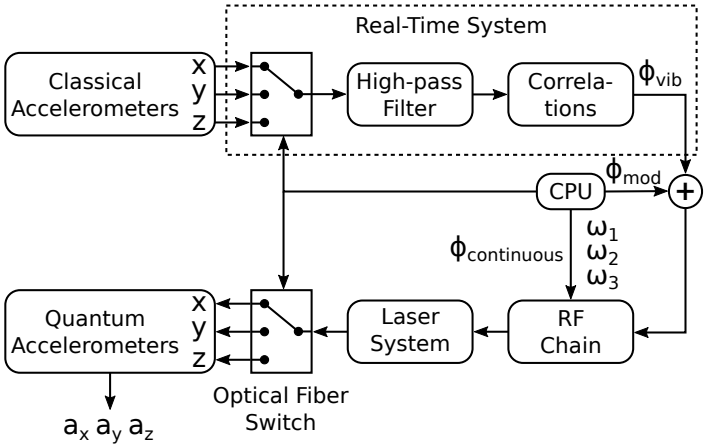

Figure 6.1: Principle of operation in open-loop of the sequential 3-axis atom interferometer. The selection of the classical accelerometer is made by the CPU and the laser beams addressing each quantum accelerometers are controlled with the fiber-bench laser.

Since the Raman laser beams are retro-reflected, two velocity selective Raman transitions are allowed according to $\pm k_{\text{eff}}$. We want to avoid those two simultaneous transitions and select between them by raising the degeneracy with Doppler effect. For gravimeters, the gravitational force accelerates the atoms through the vertical laser beams. Several technics are used when the Doppler shift is too small due to the horizontal orientation of the laser beams or due to micro-gravity. A momentum kick induced by the light or magnetic field can generate moving molasses and delivers a velocity to the atomic cloud. Another approach is to use the double single diffraction, which employs a long Raman pulse to select between two different narrow velocity

classes [16]. A novel technique is simulating a Doppler shift from the retro-reflected laser beams by applying a fast frequency chirp [56]. To operate our 3-axis atomic accelerometers, we decided to tilt the sensor head and benefit from the projection of the gravitational acceleration along each axis.

The trajectory of the atoms along the gravitational force vector brings them out of the laser beam during free fall. Therefore due to the limited size of the laser beams, the free falling time of the atoms can not exceed $\simeq$ 50 ms to stay inside. For that reason, we have to limit the interrogation time of the interferometer to 10 ms.

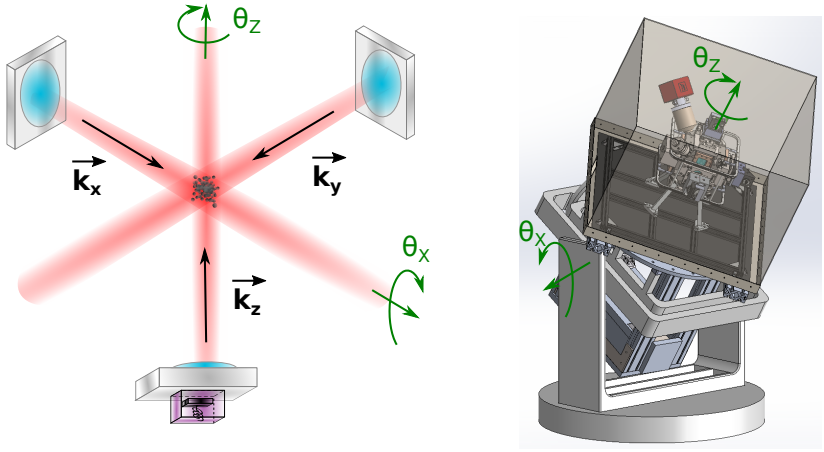

Figure 6.2: Scheme of the 3-axis atom interferometer where the sensor head is placed on the rotational platform allowing to tilt with two angles θ_X and θ_Z.

The experiment is set up on the rotational platform as displayed in Fig. 6.2. We define the direction of each axis of the three axis accelerometer by $\vec{\mathbf{x}}$, $\vec{\mathbf{y}}$ and $\vec{\mathbf{z}}$. The rotational platform allows to tilt the sensor head according to two independent axes $\vec{X}$ and $\vec{Z}$. The rotation matrix $R(\theta_X, \theta_Z) = R_Z(\theta_Z) \cdot R_X(\theta_X)$ predicts the resulted vector obtained by tilting the sensor head with:

$$R_X(\theta_X) = \begin{bmatrix} 1 & 0 & 0 \\ 0 & \cos(\theta_X) & -\sin(\theta_X) \\ 0 & \sin(\theta_X) & \cos(\theta_X) \end{bmatrix} \tag{6.1}$$

$$R_Z(\theta_Z) = \begin{bmatrix} \cos(\theta_Z) & -\sin(\theta_Z) & 0 \\ \sin(\theta_Z) & \cos(\theta_Z) & 0 \\ 0 & 0 & 1 \end{bmatrix} \tag{6.2}$$

$$\tag{6.3}$$

We obtain the following acceleration vector:

$$\mathbf{a} = \begin{bmatrix} a_x \\ a_y \\ a_z \end{bmatrix} = R(\theta_X, \theta_Z) \cdot \begin{bmatrix} 0 \\ 0 \\ g \end{bmatrix} = g \begin{bmatrix} \sin(\theta_X)\sin(\theta_Z) \\ -\sin(\theta_X)\cos(\theta_Z) \\ \cos(\theta_X) \end{bmatrix} \tag{6.4}$$

To obtain a balanced acceleration on each axis of $a_x = a_y = a_z = g/\sqrt{3}$, the tilts need to be $\theta_X = 54.7$ deg and $\theta_Z = 45$ deg.

6.2 Tilt of the sensor head

6.2.1 Axes quantization and states preparation

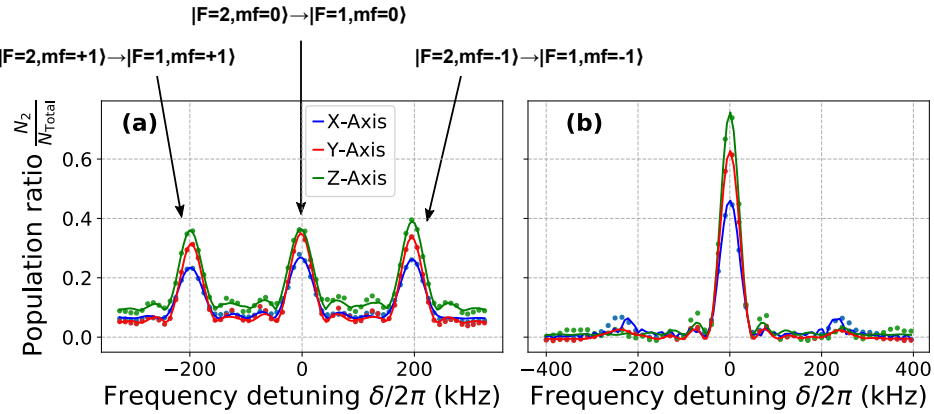

Figure 6.3: Raman spectroscopy with co-propagating Raman transitions on each axis with states preparation on (b) and without on (a).

We want to prepare the atoms into non-sensitive magnetic energy state $|F = 1, m_f = 0\rangle$. A magnetic field equal to $\simeq 145$ mGauss is applied with the Helmholtz coils from each axis to raise the degeneracy of magnetic sub-levels along one axis per shot. It also defines the quantization axis to drive the Raman transitions. Figure 6.3 presents a Raman spectroscopy with circularly polarized beams ($\sigma^{\pm}/\sigma^{\pm}$) after the molasses. The state preparation is similar to the one used for the vertical axis accelerometer in Chapter 5.

6.2.2 Temperature along the direction of each axis

We raise the degeneracy of the velocity sensitive counter-propagating Raman transitions with the Doppler frequency shift by tilting the sensor head. Figure 6.4 presents a Raman spectroscopy with linearly polarized Raman beams (lin⊥lin) on each axis. Here the sensor head is tilted with angles $\theta_X = 42$ deg and $\theta_Z = 45$ deg. This explains the same velocity of the atomic cloud on X and Y axes and the higher velocity on Z-axis. The atoms are cooled down with grey molasses, as for the vertical atom

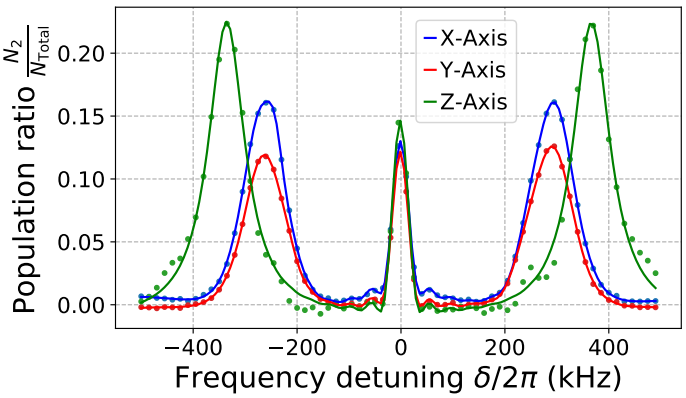

Figure 6.4: Raman spectroscopy with linearly polarized Raman beams (lin⊥lin) on each axis to measure the temperature along each direction. The TOF is 15 ms, which is enough to separate in frequency the counter-propagating transitions from the residual co-propagating transitions.

interferometer presented in Chapter 5. We obtained temperatures for the atomic cloud along X, Y and Z directions of respectively 2.1 μK, 2.0 μK and 1.8 μK.

6.3 Performances of the 3-axis atom interferometer

6.3.1 Acceleration sensitivity on each axis

Similarly to the one axis accelerometer case, we apply a series of phase-continuous frequency jumps during interferometry to compensate the Doppler frequency shift. The resulting phase imprinted onto the atoms is $\phi_{\text{continuous}} = ak_{\text{eff}}T_{\text{eff}}^2$ where the acceleration a is controlled with the frequency jumps. In addition, the classical accelerometers attached to the reference mirrors of each axis monitor the mechanical vibrations a_{vib} and a correlation phase ϕ_{cor} is calculated. The phase measured at the output of the atom interferometer is:

$$\Phi = \phi_{\text{kin}} + \phi_{\text{laser}} \tag{6.5}$$

where $\phi_{\text{kin}} = -(a_i + a_{\text{vib}})k_{\text{eff}}T_{\text{eff}}^2$ is the inertial phase with a_i is the acceleration along axis x (a_x), y (a_y) or z (a_z) and $\phi_{\text{laser}} = \phi_{\text{continuous}} + \phi_{\text{cor}}$ is the laser phase. In this Chapter for static operation, the accelerations measured correspond to the projection of the gravitational acceleration along each effective wavevector $\vec{k_x}$, $\vec{k_y}$ and $\vec{k_z}$.

Figure 6.5 presents Raman fringes on each axis by scanning the quantity a with the frequency jumps. The measurements are made with the sensor head tilted with angles $\theta_X = 54.7$ deg and $\theta_Z = -45$ deg to equivalently balance the gravitational force along each axis. Depending on the sign of the series of frequency jumps $\pm\omega$, we are able to address velocity classes of the atoms where the degeneracy is raised by the Doppler

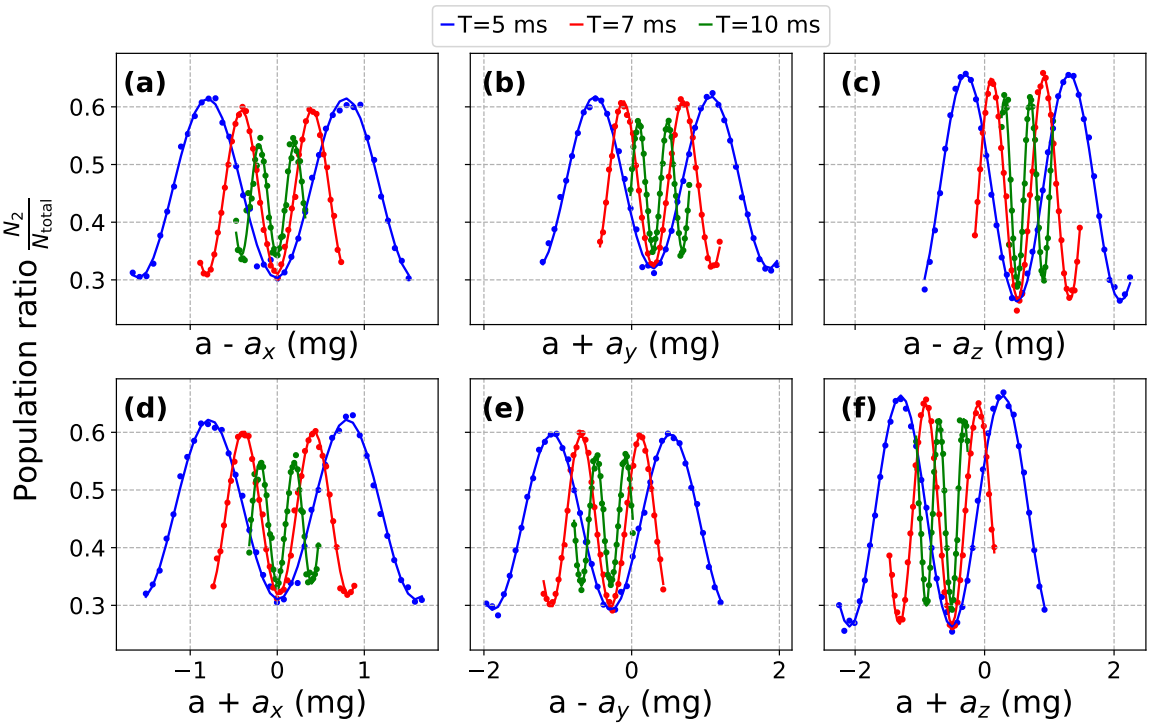

Figure 6.5: Raman fringes obtained by varying the series of frequency jumps on each axis sequentially for different interrogation time. The sign of the accelerations a_x, a_y and a_z corresponds to the direction of $\vec{k_{\text{eff}}}$ depending if the atoms are falling outward or forward the reference mirror.

frequency shift induced by the velocity of the atoms relative to the laser beams. We define the directions $k_\uparrow$ and $k_\downarrow$ when the atom are falling respectively outward and toward the reference mirror.

Figure 6.6 summarizes the fit estimation of the fringes obtained in Fig. 6.5. We notice a difference in the contrast of the fringes from the axis z compared to the others. This is probably due to the fact that we optimized the optical parameters (light intensities and durations) of the molasses and the state preparation with the z-axis and we are using the same for each axis. In addition we observed in Chapter 5 a competition between the two pairs of co-propagating Raman transitions with σ^+/σ^+ and σ^-/σ^-. Those transitions interfere periodically and depend on the position relative to the reference mirror. Therefore we think that the efficiency of the state preparation is affected by this interference effect on x and y-axis and limits the contrast.

The sensitivity of each axis are estimated respectively at $\sigma_x = 13.8\ \mu g/\sqrt{\text{Hz}}$, $\sigma_y = 4.8\ \mu g/\sqrt{\text{Hz}}$ and $\sigma_z = 5.9\ \mu g/\sqrt{\text{Hz}}$. We believe that the sensitivity on the x-axis is inferior due to the correlations with the classical accelerometer. Indeed the classical accelerometer fixed on the reference mirror was maybe not well calibrated or the signal on the acquisition chain interferes with a parasitic field.

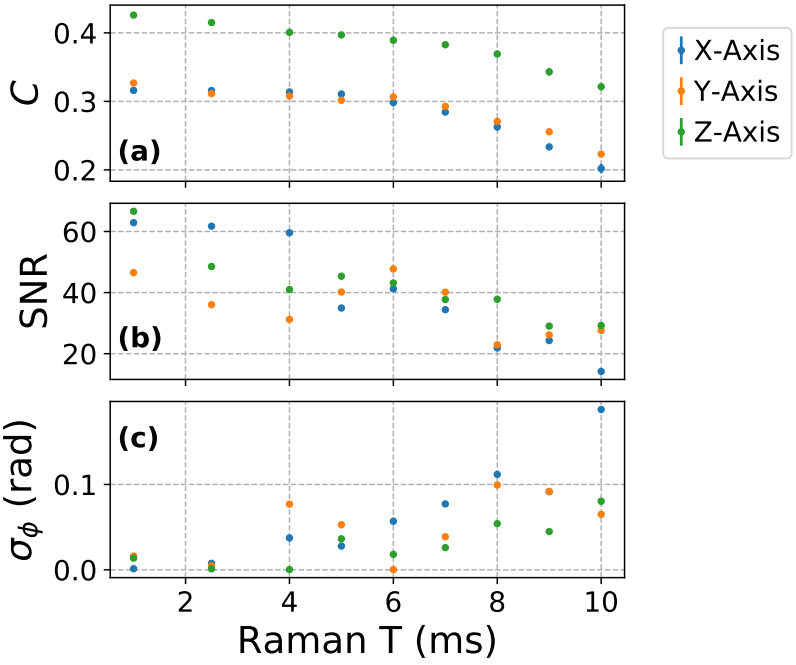

Figure 6.6: Analysis of the fringes obtained on each axis at different interrogation time T. Estimation of the contrast (a), the SNR (b) and the phase noise in rad/shot (c). The results correspond to a mean between the estimation on $k_\uparrow$ and $k_\downarrow$ cases.

6.3.2 Long-term stability of the 3-axis atomic accelerometer

We measured the stability of the measurements on each of the three axes of the atom accelerometer. We operated the mid-fringe tracking algorithm described on Chapter 2. Figure 6.7 presents the measurements with an interrogation time T=10 ms and the sensor head tilted with angles $\theta_X = 54.7$ deg and $\theta_Z = -45$ deg. We computed the norm of the total acceleration vector as $\|\mathrm{a}\| = \sqrt{\mathrm{a_x}^2 + \mathrm{a_y}^2 + \mathrm{a_z}^2}$. We observe a large drift of the acceleration on each axis whereas the norm is stable and reach 200 ng level after 9 hours of integration. This is due to the rotation of the sensor head or the laboratory estimated at $\simeq 30$ μrad over 30 hours. It impacts individually the acceleration of each axis but not the total acceleration vector, measuring the gravitational acceleration.

We notice slight instabilities at 200 ng level after 10 hours of integration of the norm. We suspect the two-photon light shift to vary widely at interrogation time of 10 ms on each interferometer axis, as a result of the temperature fluctuation affecting the polarization quality. We described those instabilities in Chapter 5.

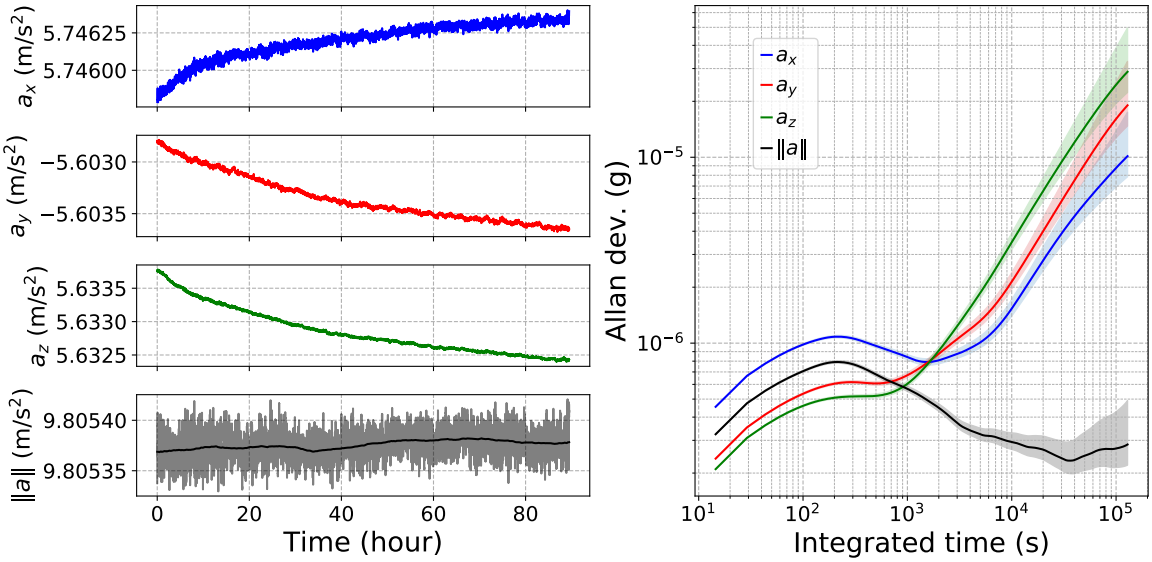

Figure 6.7: Stability of the acceleration of each interferometer axis and the norm of the full acceleration vector ‖a‖ over 90h. The time-series plot of the norm includes a 9 hours moving average in darker color.

6.4 Calibration of the 3-axis atom accelerometer

6.4.1 Protocol for the calibration of the 3-axis atomic accelerometer

A well known problem with inertial navigation systems is the misalignments of the triad formed by the 3-axis accelerometer. For our 3-axis atom interferometer, the effective wavevectors $\vec{k_x}$, $\vec{k_y}$ and $\vec{k_z}$ of the Raman laser beams define the direction of the measurement and are neither perfectly orthogonal. Those directions are mostly defined by the reference mirrors. The total acceleration vector is affected at first order by those misalignments. For instance, a realistic misalignment of $\epsilon = 100$ μrad between two axes generates an error of $\cos(\pi/2 - \epsilon) \sim \epsilon \simeq 100$ μg on the norm. Methods have been developed to correct this issue with classical sensors on inertial measurement units (IMU) by conducting a series of measurements in different orientations and comparing the norm of the accelerations with a local measurement of the gravitational acceleration as a reference. This approach is new in the field of atomic inertial sensing and needs to be explored.

Whereas the scale factor and the bias of classical sensors are rather constant depending on the orientation, the atomic accelerometer suffers from strong variation of the systematic effects depending on the orientation of the sensor head. In particular, the interactions of the atoms with magnetic fields and Raman laser beams depend strongly on the tilt of the sensor head and the position of the atomic cloud inside the

beam, which contribute widely to the systematic effects. Thus the systematic effects are specific for each axis of the 3-axis atomic interferometer and depend highly on the tilt of the sensor head. Besides, the method used to calibrate the classical sensors allows to correct constant shifts. For that reason, to apply accurately the method on the 3-axis atomic accelerometer, it is important to remove the systematic biases for each orientation on each axis. Then we compare the norm of the full acceleration vector from the measurements with an independent measured value of the local gravitational acceleration $g = 9.805642$ m/s^2.

6.4.2 Rabi oscillations along the 3 laser beams profile

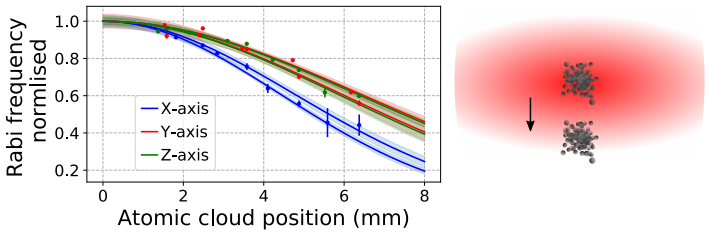

Figure 6.8: Estimation of the Rabi frequencies along the beam profile for each axis. Straight lines correspond to Gaussian fits with the assumption of centered initial position of the atomic cloud inside the molasses.

The exposition time of the atomic cloud through the tilted laser beams is limited and leads to a drop of the power on the edges. Figure 6.8 shows normalized Rabi frequencies along the Gaussian profile of the laser beams for each axis. The measurements have been done for two different orientations of the sensor head. The angles of the two positions are respectively $\theta_X = 54.7$ deg, $\theta_Z = -45$ deg and $\theta_X = 45$ deg, $\theta_Z = -30$ deg. The position is corrected with the rotation matrix $R(\theta_X, \theta_Z)$ to obtain a radial position from the center of the beam as illustrated on Figure 6.8. We notice different profiles for the two different orientations. We suspect that the initial position of the atomic cloud in the molasses is not centered with the laser beams. This leads to a shift of the Gaussian profile of the laser beams relative to the atomic cloud. Further study is required to fully characterize the Rabi frequencies inside the laser beam.

6.4.3 3D mapping of the magnetic field

By tilting the sensor head with various angles for θ_X and θ_Z, we probed the magnetic field along the trajectory of the atoms, corresponding to the vertical on the laboratory frame Z_{lab}, over 26 different orientations. Due to the generation of the magnetic field bias with the Helmholtz coils along each axis, the profile of the magnetic field probed is different for each axis. Figure 6.9 presents the measurements of the magnetic field

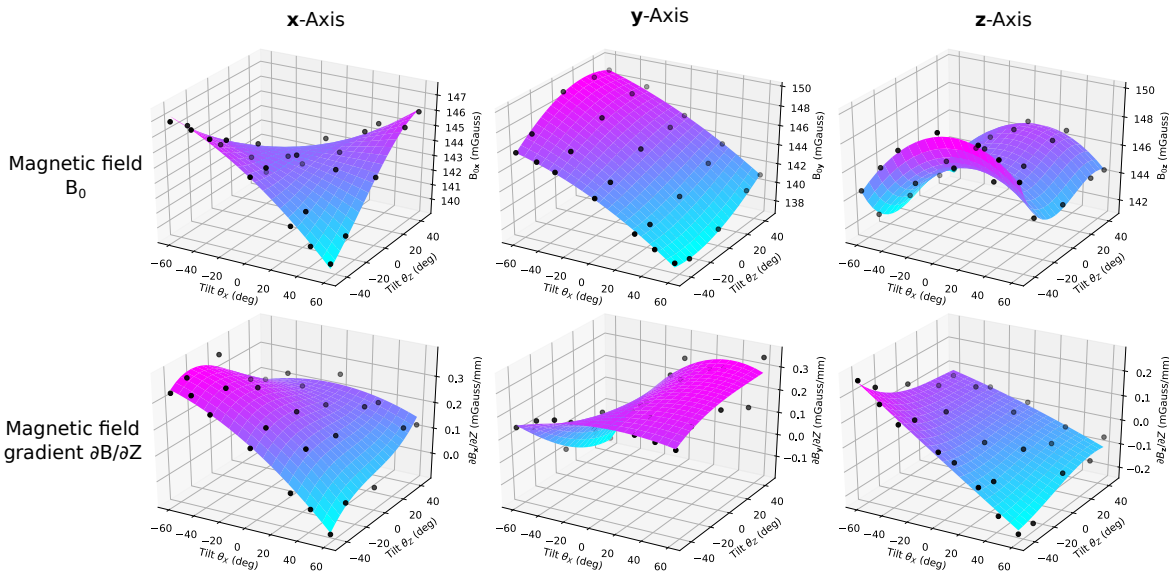

Figure 6.9: Mapping of the magnetic field B_0 (in mGauss) on each axis and the magnetic field gradient $\partial B/\partial Z_{\text{lab}}$ (in Gauss/m) along the vertical for different tilt. The magnetic field have been measured with co-propagating Raman spectroscopies for 26 different orientations of the sensor head. The 2D surface plots are third order polynomial fits estimation.

obtained with co-propagating Raman spectroscopies. The Zeeman frequency shift created by the magnetic field is measured and gives the measurement of the magnetic field. B_0 corresponds to the magnetic field at the initial position of the atomic cloud inside the molasses. The magnetic field gradient $\partial B/\partial Z$ is determined for each axis along the trajectory of the atomic path, corresponding to the vertical on the laboratory frame Z_{lab}. A two-dimensional third order polynomial fit estimates the magnetic field for any orientation of the sensor head. The anti-Helmholtz coils on the z-axis allow to cancel the gradient field along the z-axis $\partial B_z/\partial Z \simeq 0$ at tilt $\theta_X = \theta_Z = 0$ and reduce it for the other axes and orientations of the sensor head.

We mention that the tensor light shift influences the measurements of the magnetic field and has not been fully evaluated. This frequency shift is measured at first order from the non-magnetic states transition $|F = 1, m_f = 0\rangle$ to $|F = 2, m_f = 0\rangle$ and corresponds to a few kHz (equivalent to an error of a few mGauss).

6.4.4 Systematic effects

On Table 6.1, we report the systematic effects calculated on each axis and the impact on the norm of the total acceleration vector. We estimated the systematic shifts for an interrogation time of $T = 10$ ms at a position where the sensor head is tilted with angles $\theta_X = 54.7$ deg and $\theta_Z = -45$ deg. All those systematic effects have been studied for the vertical interferometer in Chapter 5. Due to the tilt of atom interferometers compared to a gravimeter, some effects are exacerbated. In particular,

the Rabi frequencies preliminary studied in Section 6.4.2 are fluctuating largely and impact highly the bias shifts. We conducted the study by alternating the direction of the interferometer according to $k_\uparrow$ and $k_\downarrow$. We estimated the systematic biases for the k_{dep} case where shifts depending on the trajectory are highly rejected. Modulating the power of the measurements like we did with the vertical axis characterization would decrease the uncertainty and reject mostly the scale factor error and the TPLS, but it was not operated for this study.

Systematic effect (μg)	**X-axis bias**	**Y-axis bias**	**Z-axis bias**	**Norm bias**
Scale factor error	58.9 (6.4)	-31.3 (1.6)	30.3 (0.9)	73.3 (6.6)
TPLS	3.762 (6)	-3.091 (5)	3.26 (3)	5.861 (9)
MZ Asymmetry	1.064 (27)	-0.124 (10)	0.345 (9)	1.125 (31)
Coriolis effect	0.65 (44)	-2.42 (37)	-1.77 (26)	3.07 (63)
RF non-linearity	0.060 (23)	0.057 (23)	0.058 (23)	0.101 (40)
Parasitic lines	-0.048 (40)	0.030 (72)	0.046 (5)	0.098 (50)
Quadratic Zeeman	0.003 (21)	-0.007 (19)	0.010 (22)	0.007 (77)
Beams misalignments	0.00 (0.50)	0.00 (0.50)	0.00 (0.50)	0.00 (0.87)
Total	64.4 (7.4)	-36.8 (2.6)	32.3 (1.7)	83.6 (8.0)

Table 6.1: Table of systematic effects of the 3-axis atom interferometer with an interrogation time of $T = 10$ ms and the sensor head tilted with angles $\theta_X = 54.7$ deg and $\theta_Z = -45$ deg. The measurements correspond to the k_{dep} case and they are expressed in μg with the uncertainties in parentheses. The norm bias stands for the bias of the norm of the total acceleration vector.

Scale factor error

The difference of scale factors between the inertial phase ϕ_{inertial} and the imprinted laser phase $\phi_{\text{continuous}}$ from the series of phase-continuous frequency jumps leads to a parasitic shift of:

$$\phi_{\text{SF}} = a\delta S \tag{6.6}$$

where $\delta S = S_{\text{continuous}} - S_{\text{kin}}$ is the scale factor error and is calculated in Chapter 5. It depends on the Rabi frequency of the first and last pulses of the interferometer. Due to the drop of the Rabi frequencies at the edge of the laser beams, this effect is very large, leading to tens of μg of bias. Most importantly, the uncertainty on this systematic shift is wide (several μg) because the beam profile of each axis laser has not been fully characterized.

Two-photon light shift

The two-photon light shift (TPLS), as the scale factor error, depends on the Rabi frequencies of the first and last pulses of the interferometer. The TPLS is also impacted by the inverse of the Doppler frequency shift. Here the Doppler shift is smaller due to the tilt of the laser beams. The acceleration shift induced is at $\simeq 3$ μg level. However the uncertainty is low and the effect is determined at some ng of confidence.

Mach-Zehnder asymmetry

The Mach-Zehnder asymmetry (MZ asymmetry) is likewise affected by the large variation of the Rabi frequencies during interferometry. The interferometric path is altered by the imbalance of the Rabi pulses and the atomic wavepackets are not fully recombined at the end. The resulted bias is at hundreds of ng level and can reach 1 μg on the x-axis. The confidence is at ten ng level which is due to the incomplete characterization of the Rabi frequencies along the beam profile.

Coriolis effect

The atom interferometer is a gyroscope and measures rotation rates. In static operation, Coriolis accelerations occurs due to the rotation of the Earth. For a vertical trajectory of the atomic cloud on gravimeter, the effect is canceled when there is no transverse velocity. However here, the laser beams are tilted, which induce a transverse trajectory. The Coriolis effect is estimated at μg level with a confidence of several hundreds of ng, resulted from an uncertainty of 30 mm/s on the initial velocities of the atoms along each axis.

RF non-linearity

In Chapter 4, we observed slight non-linearities in the RF chain nearby the frequencies operated on the interferometer. They are induced by dispersions from filters. The resulted bias is calculated with the model developed empirically. It depends on the series of frequency jumps employed during the interferometer and varies marginally.

Parasitic lines

Parasitic lines are generated by the CS-DSSB modulation operated by the laser system. A full model has been established in Chapter 4. We were able to evaluate the theoretical shift induced on each axis. However this shift depends on the distance of the atoms relative to the reference mirror. This distance has been calculated very accurately in Chapter 5 along the z-axis, which reduces the uncertainty to 5 ng. For x

and y axes, this distance is evaluated roughly with the mechanical design of the sensor head and raises an uncertainty of tens of ng.

Quadratric Zeeman shift

The magnetic field and magnetic field gradients have been mapped in Section 6.4.3 and serve to estimate the quadratic Zeeman effect. For that, the magnetic fields measured are projected along the quantization axis of the measurement. The direction of the recoil velocity, determined by the wavevector for each axis, influences the trajectory of the atomic cloud. Thanks to the rejection performed by alternating the sign of the wavevector on each axis, we highly reduce the impact of the quadratic Zeeman, achieving a residual shift between -7 and 10 ng depending the orientation of the sensor head. Due to the uncertainty in the fit estimation of the magnetic fields probed, the confidence on the biases are at $\simeq 20$ ng. Additionally, the tensor light shift induces a slight frequency shift of a few kHz impacting slightly the estimation of the quadratic Zeeman shift by a few ng.

Other systematic effects

The beams misalignments correspond to the alignment between the collimator and the reference mirror. We estimated in Chapter 5 an uncertainty of 500 ng on this effect for z-axis. Since we calibrated the collimators equivalently and the mechanical structure of the mirror are the same on the other axes, we assume the same confidence on this bias for the other axes. No particular effort has been conducted to reduce these effects.

The wavefront distortion has not been evaluated. We explained in Chapter 5 that the optics have not been characterized. We expect a non-negligible bias from the optical aberrations which in addition, should be exacerbated at the edge of the laser beams. Because the sensor head is tilted, optical aberrations are intensified with the transverse trajectory of the atomic cloud relative to the wavefront of the laser beams.

The gravity gradient is negligible compared to the other effects. In addition, transverse components of the gravitational field tensor can slightly impact the bias for tilted interferometers, but they are not known and should be still negligible.

Summary of the systematic shifts

The systematic shifts of the 3-axis atom accelerometer are difficult to estimate. In particular, the Rabi frequencies have not been correctly characterized and nonetheless are critical to the calculations. The uncertainties are exacerbated by this partial model. The largest bias and uncertainty comes from the scale factor error induced

by the difference between the phase imprinted by the phase-continuous frequency jumps and the inertial phase. In consequence, the biases increased by more than 2 orders of magnitude compared to the vertical atom interferometer. We finally obtain a systematic bias of 83.6 ± 8.0 μg on the norm of the total acceleration vector.

We mention that the tides are usually measured and corrected for gravimeters along the vertical. However for tilted accelerometers, transverse tides should be taken into account.

6.4.5 Correction of the 3-axis frame misalignments

We want to measure and calibrate the misalignments of the triad formed by the 3-axis atom accelerometer. The direction of measurement along each axis is determined by the effective wavevectors $\vec{k_x}$, $\vec{k_y}$ and $\vec{k_z}$ of the Raman laser beams. The method described in Ref. [66] allows to determine the misalignments of the non-orthogonal frame and calibrate the value of the norm of the full acceleration vector. Figure 6.10 illustrates the approach. The non-orthogonal sensor head frame $(\vec{x_0}, \vec{y_0}, \vec{z_0})$ is transformed by angles $\theta_{i,j}$ to obtain an orthogonal sensor head frame $(\vec{x_1}, \vec{y_1}, \vec{z_1})$, where $i = x_1$, y_1 or z_1 and $j = x_0$, y_0 or z_0. The rotation matrix $R(\theta_X, \theta_Z)$ allows to convert the orthogonal sensor head frame onto the unitary laboratory frame $(\vec{x_2}, \vec{y_2}, \vec{z_2})$ where the local measured gravitational acceleration g is projected as $\vec{g} = g\vec{z_2}$.

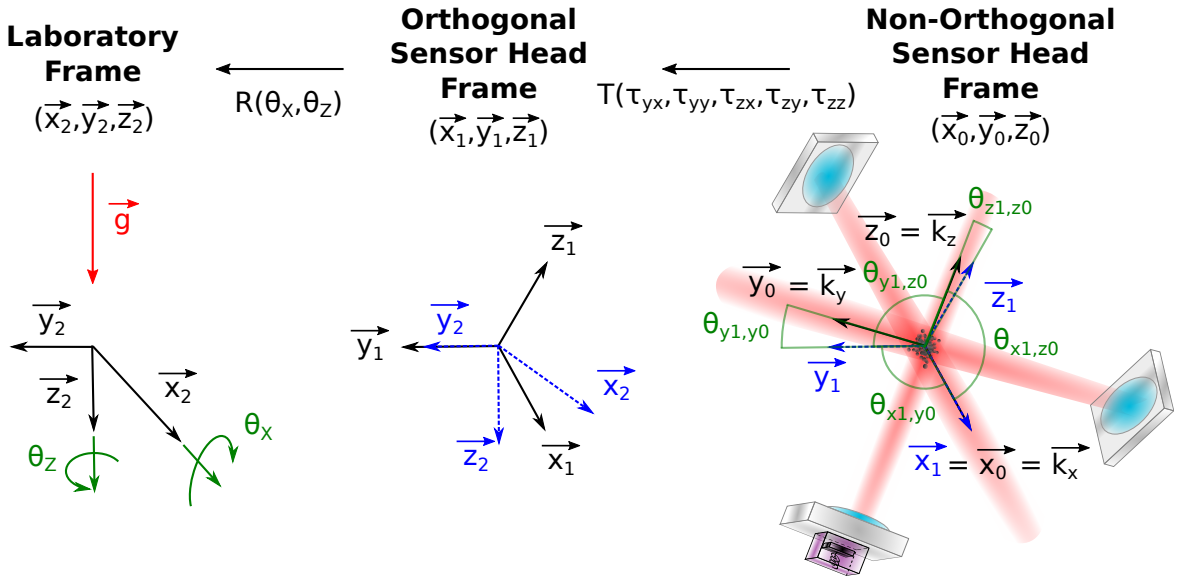

Figure 6.10: 2D projection of the 3D coordinate system of the laboratory frame, the orthogonal sensor head frame and the real non-orthogonal sensor head frame.

The misalignment model of the 3-axis frame can be modeled as:

$$\mathbf{a} = \mathbf{k_a} \cdot T \cdot R \cdot \mathbf{g} + \mathbf{p_0} \tag{6.7}$$

where $\mathbf{a} = \begin{bmatrix} \mathrm{a}_x \\ \mathrm{a}_y \\ \mathrm{a}_z \end{bmatrix}$ is the raw output of the 3-axis accelerometer, $T = \begin{bmatrix} 1 & 0 & 0 \\ \tau_{y,x} & \tau_{y,y} & 0 \\ \tau_{z,x} & \tau_{z,y} & \tau_{z,z} \end{bmatrix}$ is the non-orthogonal transformation of the sensor head frame as $\tau_{i,j} = \cos(\theta_{i,j})$, $R(\theta_X, \theta_Z) \cdot \mathbf{g} = g \begin{bmatrix} \sin(\theta_X)\sin(\theta_Z) \\ -\sin(\theta_X)\cos(\theta_Z) \\ \cos(\theta_X) \end{bmatrix} = \begin{bmatrix} r_1 \\ r_2 \\ r_3 \end{bmatrix} = \mathbf{r}$ is the transformation of the local gravitational vector with the rotation matrix from the laboratory frame to the sensor head frame, $k_a = \begin{bmatrix} k_{a,x} & 0 & 0 \\ 0 & k_{a,y} & 0 \\ 0 & 0 & k_{a,z} \end{bmatrix}$ and $\mathbf{p_0} = \begin{bmatrix} p_{0,x} \\ p_{0,y} \\ p_{0,z} \end{bmatrix}$ are respectively scale factors and biases corrections for each axis.

By solving Eq. 6.7 with a series of measurements, the goal is to extract two sets of parameters $\mathbf{X}^{\text{Misalignment}}$ and $\mathbf{X}^{\text{Linear}}$. $\mathbf{X}^{\text{Misalignment}}$ corresponds to the set of parameters where only the matrix of misalignments is considered and the scale factors and biases corrections are ignored:

$$\mathbf{X}^{\text{Misalignment}} = \begin{bmatrix} \tau_{y,x} & \tau_{z,x} & \tau_{z,y} & \tau_{y,y} & \tau_{z,z} \end{bmatrix} \tag{6.8}$$

$\mathbf{X}^{\text{Linear}}$ corresponds to the full linear model from Eq. 6.7 including scales factors and biases corrections:

$$\mathbf{X}^{\text{Linear}} = \begin{bmatrix} k_{a,yx} & k_{a,zx} & k_{a,zy} & k_{a,xx} & k_{a,yy} & k_{a,zz} & p_{0,x} & p_{0,y} & p_{0,z} \end{bmatrix} \tag{6.9}$$

where $k_{a,yx} = k_{a,y}\tau_{y,x}$, $k_{a,zx} = k_{a,z}\tau_{z,x}$, $k_{a,zy} = k_{a,z}\tau_{z,y}$, $k_{a,xx} = k_{a,x}$, $k_{a,yy} = k_{a,y}\tau_{y,y}$ and $k_{a,zz} = k_{a,z}\tau_{z,z}$. To estimate the calibration parameters, we need to perform a series of measurements $\mathbf{a_k} = \begin{bmatrix} \mathrm{a}_{k,x} \\ \mathrm{a}_{k,y} \\ \mathrm{a}_{k,z} \end{bmatrix}$ at different tilted positions leading to a set of parameters $\mathbf{r_k} = \begin{bmatrix} \mathrm{r}_{k,x} \\ \mathrm{r}_{k,y} \\ \mathrm{r}_{k,z} \end{bmatrix}$. We define the model functions $\mu_k^{\text{Misalignment}}$ and μ_k^{Linear} for the axes frame calibration as:

$$\mu_k^{\text{Misalignment}}(\mathbf{X}^{\text{Misalignment}}, \mathbf{r_k}) = T \cdot \mathbf{r_k} \tag{6.10}$$

$$\mu_k^{\text{Linear}}(\mathbf{X}^{\text{Linear}}, \mathbf{r_k}) = k_a \cdot T \cdot \mathbf{r_k} + \mathbf{p_0} \tag{6.11}$$

A maximum likelihood estimation method allows to estimate the set of parameters $\mathbf{X}^{\text{Misalignment}}$ and $\mathbf{X}^{\text{Linear}}$ as:

$$(\hat{\mathbf{X}}^{\text{Model}}, \hat{\mathbf{r}}) = \text{argmin} \left(\sum_k \| \mathbf{a_k} - \mu_k^{\text{Model}}(\mathbf{X}^{\text{Model}}, \mathbf{r_k}) \|^2 \right) \tag{6.12}$$

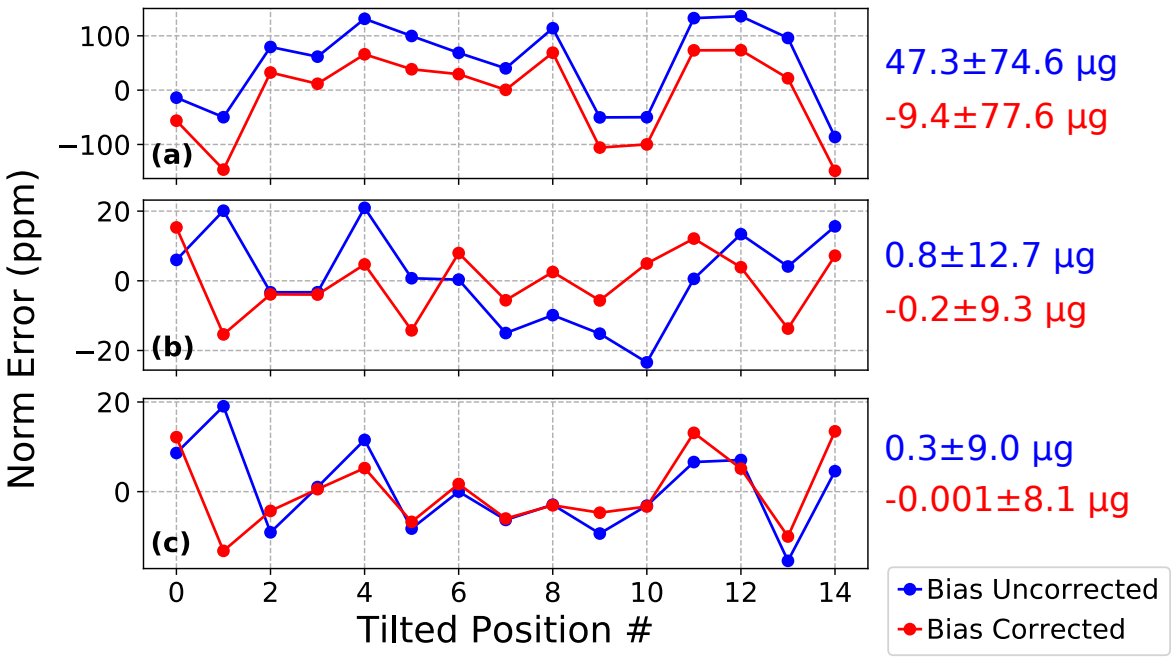

Figure 6.11: Error on the norm of the total acceleration vector compared to the local measured gravitational force $g = 9.805642$ m/s^2 for different tilted positions. In blue, the measurements used are the raw ones at the output of the interferometer. In red, the measurements used are corrected with the systematic effects. The mean value and the standard deviation are indicated on the right. (a) Raw measurements. (b) Measurements corrected with the misalignment model $\mathbf{X}^{\text{Misalignment}}$. (c) Measurements corrected with the linear model $\mathbf{X}^{\text{Linear}}$.

Figure 6.11 presents 15 measurements obtained for different orientations of the sensor head where θ_X varies between ±60 deg and θ_Z between -45, -30, -15 and 30 deg. The raw measurements in Fig. 6.11(a) are used to estimate the set of parameters for the two models $\mathbf{X}^{\text{Misalignment}}$ and $\mathbf{X}^{\text{Linear}}$ by solving Eq. 6.12. Figure 6.11(b) and (c) shows the measurements with the parameters obtained with respectively the misalignment and the linear model. Those parameters are reported in Table 6.2 for the case where the systematic biases of the atom interferometers are corrected (in red).

The systematic shifts, evaluated in Section 6.4.4 for one orientation, are evaluated for each 3 axes at each 15 orientations. The difficulty of such calibration is to remove accurately those systematic shifts. Otherwise the algorithm can not discriminate true misalignments from individual systematic biases on the different axes. We compared the raw measurements obtained at the output of the interferometer (in blue on the Figure) with the ones where the systematic shifts are removed (in red on the Figure). We notice that the uncertainty with the data where the biases are corrected are slightly better. We gain roughly 3.5 and 1 μg on the uncertainty for respectively the misalignment and the linear model. We observe also a better calibration with linear model than the misalignment model, because the scale factor correction $\mathbf{k_a}$ and biases correction $\mathbf{p_0}$ tend to compensate systematic biases of the atom interferometer. We finally obtained

an uncertainty of 8.1 μg on the measurements where systematic biases are removed on each axis with the linear model calibration. It corresponds to the uncertainty on the norm of the total acceleration vector 8.0 μg from Table 6.1. A better calibration can be made by improving the systematic shifts estimation where the effects depending on the Rabi oscillations are misjudged.

$\mathbf{X}^{\text{Misalignment}}$	**Value**	$\mathbf{X}^{\text{Linear}}$	**Value**
$\tau_{y,x}$	$+1.807 \times 10^{-4}$	$\mathrm{k}_{a,yx}$	$+1.807 \times 10^{-4}$
$\tau_{z,x}$	$+1.519 \times 10^{-4}$	$\mathrm{k}_{a,zx}$	$+1.519 \times 10^{-4}$
$\tau_{z,y}$	-1.706×10^{-4}	$\mathrm{k}_{a,zy}$	-1.706×10^{-4}
		$\mathrm{k}_{a,xx}$	1.0000062
$\tau_{y,y}$	1.0000000	$\mathrm{k}_{a,yy}$	1.0000485
$\tau_{z,z}$	1.0000000	$\mathrm{k}_{a,zz}$	1.0001302
		$p_{0,x}$ $(\mathrm{m.s}^{-2})$	$+2.327 \times 10^{-4}$
		$p_{0,y}$ $(\mathrm{m.s}^{-2})$	$+2.878 \times 10^{-4}$
		$p_{0,z}$ $(\mathrm{m.s}^{-2})$	-1.1711×10^{-3}

Table 6.2: Table of calibration parameters calculated with the misalignment and the linear model. They have been calculated with the systematic biases removed from the output of the atom interferometer (in red on Figure 6.11)

We compute the new acceleration vector $\mathbf{a}' = \begin{bmatrix} \mathrm{a}'_x \\ \mathrm{a}'_y \\ \mathrm{a}'_z \end{bmatrix}$ with the calibration parameters $\mathbf{X}^{\text{Linear}}$ from the raw output $\mathbf{a}$ as:

$$\begin{aligned}
\mathrm{a}'_x &= \frac{1}{k_{a,xx}}(\mathrm{a}_x - p_{0,x}) \\
\mathrm{a}'_y &= -\frac{k_{a,yx}}{k_{a,xx}k_{a,yy}}(\mathrm{a}_x - p_{0,x}) + \frac{1}{k_{a,yy}}(\mathrm{a}_y - p_{0,y}) \\
\mathrm{a}'_z &= \frac{k_{a,yx}k_{a,zy} - k_{a,yy}k_{a,zx}}{k_{a,xx}k_{a,yy}}(\mathrm{a}_x - p_{0,x}) - \frac{k_{a,zy}}{k_{a,yy}k_{a,zz}}(\mathrm{a}_y - p_{0,y}) + \frac{1}{k_{a,zz}}(\mathrm{a}_z - p_{0,z})
\end{aligned} \tag{6.13}$$

Conclusion

A full study of a 3-axis atomic accelerometer has never been conducted so far and this work opens new fields in multi-axis atomic inertial sensors. We studied the performances of our sequential 3-axis atom interferometer by measuring the acceleration sensitivity, the systematic shifts on each axis and the stability of the norm of the total acceleration vector. We obtained acceleration sensitivities of $\sigma_x = 13.8\ \mu g/\sqrt{\text{Hz}}$, $\sigma_y = 4.8\ \mu g/\sqrt{\text{Hz}}$ and $\sigma_z = 5.9\ \mu g/\sqrt{\text{Hz}}$. We observed the rejection of the tilt of the sensor head, affecting the acceleration on each axis during long-term measurements, on the norm of the total acceleration vector. We achieved a relative stability on the norm of the total acceleration vector of $\simeq 200$ ng, reached after 9 hours of integration, and demonstrated the stability over 36 hours.

We also performed a misalignment calibration to correct the non-orthogonalities between the effective wavevectors on each axis $\vec{k_x}$, $\vec{k_y}$ and $\vec{k_z}$. For that, we conducted a series of measurements at different orientations, where the systematic shifts have been removed, and applied a method used for IMU misalignments calibration. We obtained an accuracy of 8.1 μg on the norm of the full acceleration vector depending on the tilted positions. Further work needs to be done to improve the systematic shifts model to decrease the uncertainty. This step is important to correctly operate the misalignment calibration by removing the biases of each axis at each orientation. Modulate the power at each measurement and characterize the Rabi frequencies at the edges of the laser beams will help to decrease the biases on each axis. Another solution is to produce flat-top laser beams to flatten the intensity profiles [97].

The calibration has been made in a laboratory with a stabilized temperature environment. For field-deployable applications, the variation of the temperature can raise instabilities of the misalignments between the reference mirrors of the sensor head. The material and the size of the sensor head determines the stability of the structure and influences the stability of the misalignments. The sensor head is made of titanium which observes a low thermal expansion coefficient. Further study through simulations or under temperature controlled environment will be required to evaluate the stability of the misalignments.

Chapter 7

3-axis real-time hybrid accelerometer

This chapter reports the study and the performances of the 3-axis hybrid accelerometer, which affords continuous accelerations, provided by the classical accelerometers whose biases are tracked and removed by the atom interferometers. In particular, real-time feedback correlations of the reference mirrors and the angle dependant Doppler frequency shift compensation during interferometry are demonstrated. Finally, the 3-axis hybrid accelerometer is validated to operate on its mobile platform outside of the laboratory.

Contents

7.1 Operation of the 3-axis real-time hybrid accelerometer . . 195

7.2 Real-time hybridization 197

7.2.1 Correlations with the classical accelerometer 197

7.2.2 Doppler frequency shift compensation 197

7.2.3 Bias tracking of the classical accelerometer 199

7.3 Performances of the real-time hybridization 200

7.3.1 Long-term stability of the 3-axis hybrid accelerometer . . . 200

7.3.2 Limits of the real-time correlations to the sensitivity 201

7.3.3 Residual discontinuous phase from the frequency jumps . . 204

7.3.4 Systematic effects and calibration of the 3-axis hybrid accelerometer 208

7.3.5 3-axis hybrid accelerometer outside of the laboratory 212

Introduction

The correlations between an atomic gravimeter and a seismometer fixed to the reference mirror has established an alternative to anti-vibration platform by measuring and correcting in phase parasitic mechanical vibrations [62]. This technique paved the way of hybridization between classical and quantum gravimeter [27, 29, 17, 18].

Classical accelerometers suffer from biases which are not constant and from the alteration of the scale factor due to physical surrounding fluctuations such as temperature, magnetic fields, humidity, pressure. Real-time data fusion processing is necessary in inertial navigation systems to increase positioning and navigation efficiency by combining multiple sensors and has been recently employed for quantum sensors [14, 30]. Indeed the atom interferometer benefits from an absolute measurement of the acceleration, thanks to a predictable scale factor, and can correct the classical accelerometer. In addition, the dead-times of $\simeq 1$ Hz and the limited dynamic range of $\simeq \pm 2$ g of atom interferometers are solved by profiting from the high-data rate > 1 kHz and large dynamic range of ± 20 g from the classical accelerometers. Furthermore, the knowledge of the acceleration is mandatory to operate the atom interferometer by correcting the Doppler frequency shift, induced by the relative velocity between the atoms and the Raman laser beams.

We present in this chapter a novel 3-axis real-time hybrid accelerometer, which delivers a continuous and bias-free measurement of the acceleration in the 3 dimensions. 3 classical accelerometers are fixed to 3 orthogonal atom interferometers to form 3 hybrid accelerometers.

The hybridization allows mobile operations, which represent another challenge in the quest of onboard quantum sensors. Static operation of our transportable sensor in an arbitrary environment is one of the key first step to qualify the system. In this chapter, we demonstrated and exhibit performances of the 3-axis hybrid accelerometer outside of the laboratory on its mobile platform. We validated the proper running of the experiment in a random environment including the laser system, the electronics and the sensor head. We also certified the mobile platform for transporting safely and efficiently the whole system.

7.1 Operation of the 3-axis real-time hybrid accelerometer

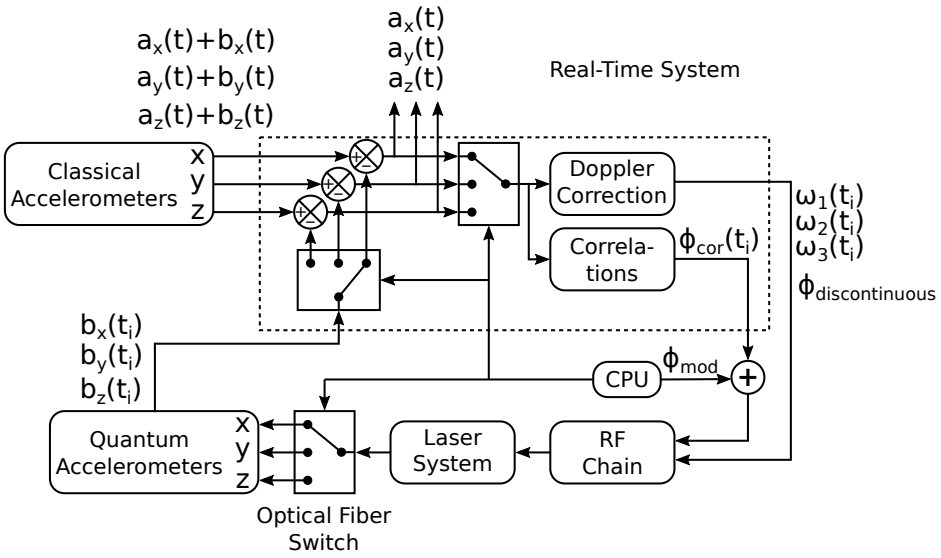

Figure 7.1: Closed-loop operation scheme of the 3-axis hybrid accelerometer.

Figure 7.1 presents the closed-loop operation scheme of the 3-axis hybrid accelerometer described in Chapter 2. The CPU commands numerical switches inside the real-time system and the optical fiber switch to select the axis to measure. The classical accelerometer measures the biased acceleration $a(t) + b(t)$. The measurements of the classical accelerometer are correlated with the response function $f(t)$ of the atom interferometer to obtain the correlation phase $\phi_{\text{cor}} = \phi_a + \phi_b$. The measurements are also used to generate a series of phase-discontinuous frequency jumps to compensate the Doppler frequency shift, delivering an imprinting phase $\phi_{\text{discontinuous}} = 0$. In addition, the CPU controls a modulation phase ϕ_{mod} to operate the mid-fringe lock algorithm or to scan the phase arbitrarily. The resulting phase output of the interferometer is the sum of the inertial phase $\phi_{\text{kin}} = -ak_{\text{eff}}T_{\text{eff}}^2$ and the imprinted laser phase $\phi_{\text{laser}} = \phi_{\text{cor}} + \phi_{\text{discontinuous}} + \phi_{\text{mod}}$, resulting in $\Phi = \phi_{\text{kin}} + \phi_{\text{laser}} = \phi_b + \phi_{\text{mod}}$. The measured bias is fedback to the output of the accelerometer to deliver a continuous measurement without bias.

The closed-loop mid-fringe algorithm presented in Chapter 2 is used to track the bias of the classical accelerometer measured by the atom interferometer. In order to track conveniently the biases, the Raman interrogation time should be adapted depending on the variation of the biases. For example, at the beginning of the tracking algorithm, the interrogation time should be short (T=2 ms) to track large biases ($\simeq$ 5 mg) and then can be increased to gain in sensitivity when the biases are removed

progressively. If the biases are varying abruptly during the tracking (change in the tilt typically), the interrogation time should be reduced, to not jump from the central Raman fringe and lock the algorithm on the wrong Raman fringe.

To analyse the performances of the 3-axis hybrid accelerometer, the sensor head is placed on the rotational platform as in Chapter 6. It allows to control the orientation of the sensor head with rotation angles θ_X and θ_Z. In that way, we can test the real-time compensation by generating a random acceleration with the projection of the gravitational force along each axis. We can also vary the biases of the classical accelerometers with a tilt. Indeed the bias is strongly affected by the scale factor error and consequently depends on the acceleration. The mobile platform described in Chapter 3 is used to operate and transport the 3-axis hybrid accelerometer outside the laboratory. The racks contain all the system to perform the 3-axis hybrid accelerometer including laser system, electronic, CPU, real-time system and power supplies. The sensor head is oriented to provide an acceleration projected on each axis required to operate atom interferometers.

7.2 Real-time hybridization

7.2.1 Correlations with the classical accelerometer

The correlation phase $\phi_{\text{cor}} = \phi_a + \phi_b$, obtained from the classical accelerometer fixed to the reference mirror, and the inertial phase $\phi_{\text{kin}} = -ak_{\text{eff}}T_{\text{eff}}$ are measured by the atom interferometer. The resulted output corresponds to the phase bias ϕ_b. The acceleration measured a contains also mechanical vibrations which are compensated on the atom interferometer output thanks to the correlations.

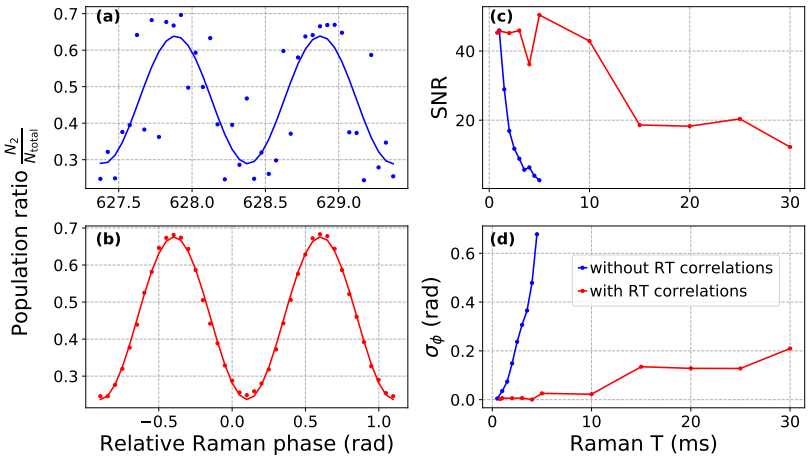

Figure 7.2: Raman fringes obtained without (a) and with (b) the real-time correlations for a Raman interrogation time of T=5 ms. (c) and (d) display respectively the SNR and the phase noise (in rad/shot) for different T when the real-time correlations are active (red) and when they are inactive (blue).

Figure 7.2 presents Raman fringes with SNR and phase noise estimations when the real-time correlations is active and inactive. We obtain the bias of the classical accelerometer when the real-time correlations are active. The phase noise induced by the mechanical vibrations on the reference mirror at T=5 ms is $\simeq 0.7$ rad. The real-time correlations correct those vibrations which increase the sensitivity. Such sensitivity is necessary for the atom interferometer to operate at interrogation time $T > 3$ ms.

7.2.2 Doppler frequency shift compensation

During the free-fall of the atoms, the velocity of the atomic cloud relative to the Raman laser beam induces a Doppler frequency shift. To stay on resonance to drive the velocity-sensitive counter-propagating Raman transitions, the Doppler frequency shift is corrected in real-time during interferometry.

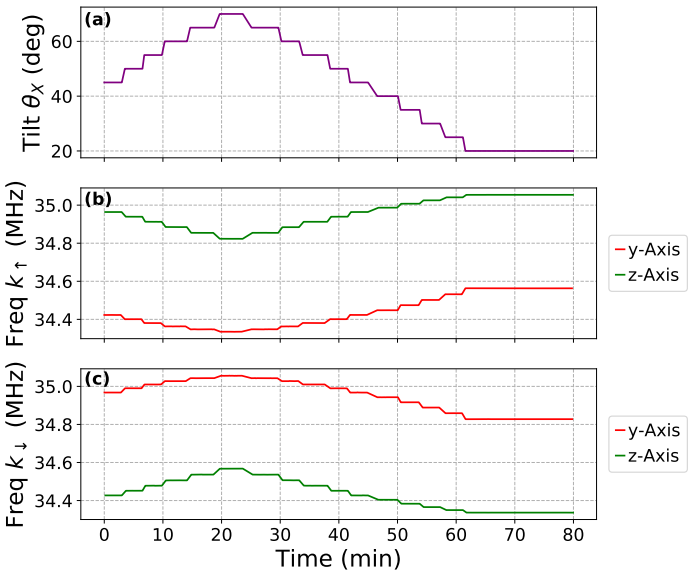

Figure 7.3: Correction of the Doppler frequency shift measured by the classical accelerometer and applied in real-time to the DDS. (a) Tilt of the sensor head operating on the rotational platform. (b) and (c) DDS frequency for the first pulse of the interferometer of Y and Z-axis for respectively $+k_{\text{eff}}$ and $-k_{\text{eff}}$ directions.

Here, we demonstrate the ability of the real-time system to compensate the Doppler frequency shift for an arbitrary velocity. We placed the sensor head onto the rotational platform and used the gravitational acceleration to generate a random projected velocity by tilting the sensor head. Figure 7.3 presents the real-time frequency compensation of Y and Z axes at different angles θ_X for $\pm k_{\text{eff}}$ ($k_\uparrow$ and $k_\downarrow$). We tilted the sensor head with steps of 5 deg every 2-3 min. The frequencies are updated at each step according to the acceleration measured by the classical accelerometers. This frequency compensation is done in the same way for the two other pulses of the atom interferometers.

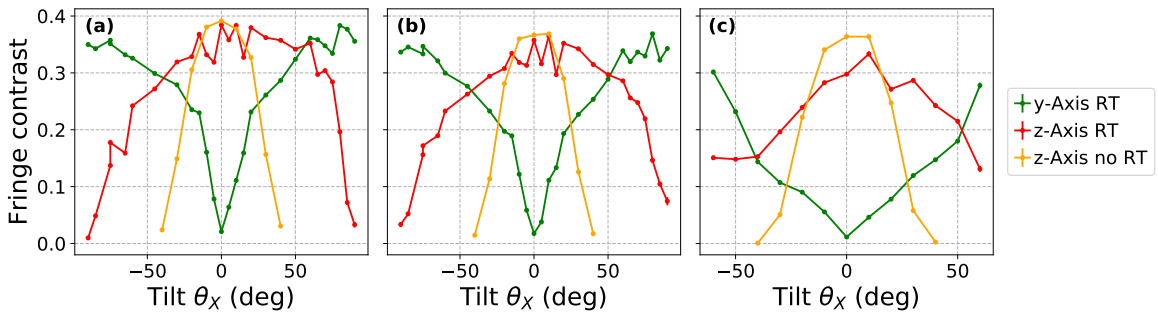

Figure 7.4: Contrast of the Raman fringes depending on the tilt of the sensor head along Y-axis (green) and Z-axis (red) and when the real-time compensation of the Doppler frequency shift is disabled (yellow). The Raman interrogation times used are T=2.5 ms (a), T=5 ms (b) and T=10 ms (c).

Figure 7.4 compares the contrast of Raman fringes when the Doppler frequency shift is corrected and when it is not. When the Doppler frequency shift is not corrected,

the contrast of the interferometer drops quickly with the tilt (a higher angle θ_X induces a lower velocity on Z-Axis). When the real-time compensation is activated, the contrast is no longer limited by the Doppler frequency shift compensation. However we notice a decrease of the contrast when the Raman beams approach horizontality ($\theta_Z = 0$ deg for Y-axis and $\theta_X = 90$ deg for Z-axis). This is mainly due to the overlap of the frequencies from the counter- and co-propagating Raman transitions. Also the drop of Rabi frequencies through the edge of the Raman beams reduces the contrast.

7.2.3 Bias tracking of the classical accelerometer

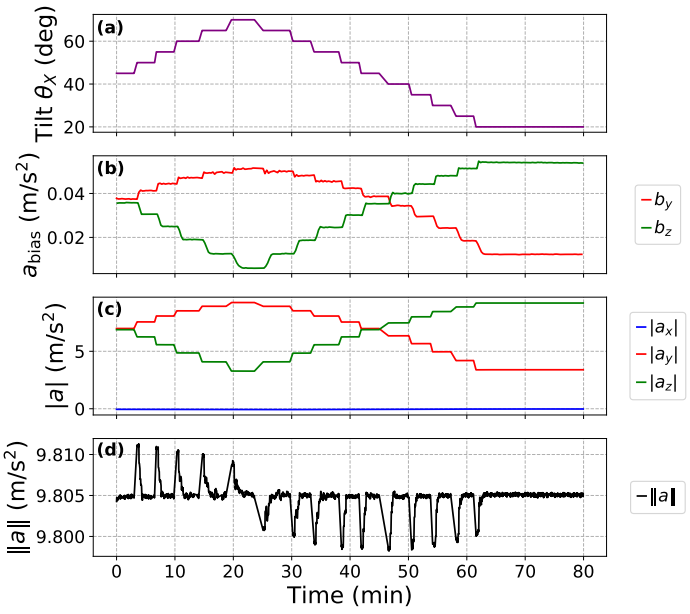

Figure 7.5: Measurements of the 3-axis hybrid accelerometer where the biases of the classical accelerometers are tracked. (a) Tilt of the sensor head operating on the rotational platform. (b) Acceleration measured by the atom interferometer corresponding to the bias of the classical accelerometer. (c) Acceleration measured by the 3-axis hybrid accelerometer. (d) Norm of the full acceleration vector.

Figure 7.5 presents acceleration measurements of the 3-axis hybrid accelerometer, using the closed-loop operation scheme described in Figure 7.1 and the mid-fringe tracking algorithm developed in Chapter 2. To demonstrate the tracking of the classical accelerometers biases, we tilted the sensor head on the rotational platform with steps of 5 deg every 2-3 min. The accelerations measured by the atom interferometers on Fig. 7.5(b) correspond to the difference between the acceleration experienced by the atoms, from the inertial phase ϕ_{kin}, with the one from the classical accelerometer, from the correlation phase ϕ_{cor}. Then only the biases of the classical accelerometers are left. By comparing the atom interferometers measurements to the classical accelerometers ones,

we obtain the measurements from Fig. 7.5(c), corresponding to the accelerations of the hybrid accelerometers, where the biases of the classical accelerometers are removed. Figure 7.5(d) displays the norm of the total acceleration vector of the 3-axis hybrid accelerometer.

We observe that at each change of the tilt of the sensor head, the biases of the classical accelerometers are varying abruptly and can reach $\simeq 700$ μg. The biases are tracked and are removed from the classical accelerometers after a few tens of seconds at each change of the tilt. Here the PI controller of the mid-fringe lock algorithm is optimized to correct large fluctuations (high proportional gain and medium integrator gain). The Raman interrogation time of the interferometer is T=5 ms. To avoid to lock the tracking on the wrong Raman fringe, the biases should not exceed $\pm\pi$ rad which corresponds to $\simeq \pm 800$ μg for T=5 ms.

7.3 Performances of the real-time hybridization

7.3.1 Long-term stability of the 3-axis hybrid accelerometer

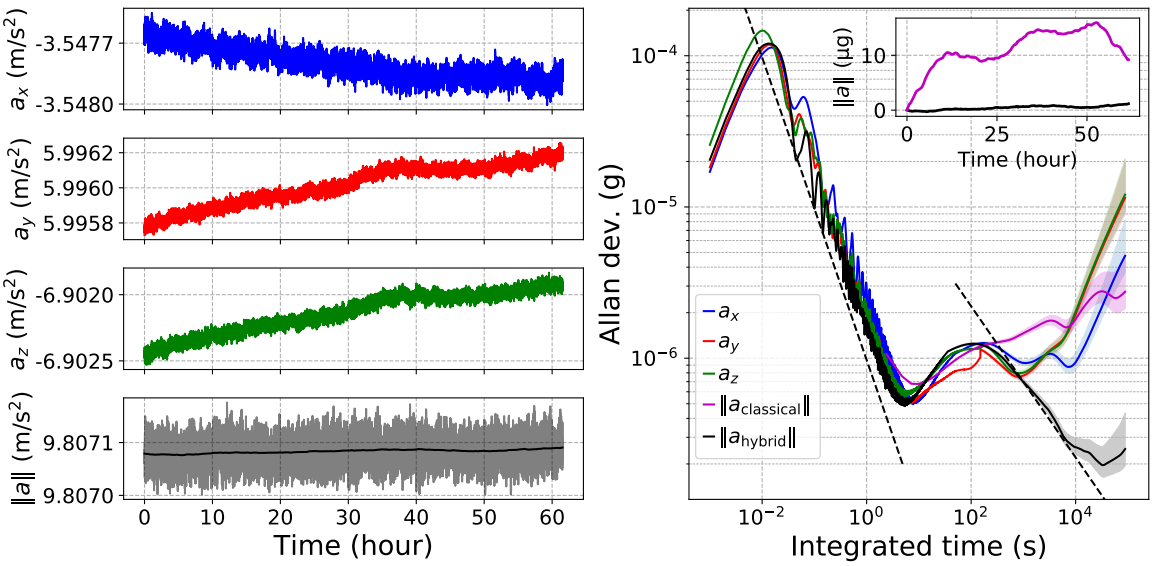

Figure 7.6: Stability of the acceleration on each hybrid accelerometer and on the norm of the total acceleration vector $\|a\|$ over 60h. The Raman interrogation time of the interferometers is T=10 ms and the sensor head is tilted by $\theta_X = 45$ deg and $\theta_Z = -30$ deg. The time-series plots show measurements at the cycling rate of the atom interferometer and the norm $\|a\|$ includes a 9 hours moving average in darker color. The Allan deviation of the norm $\|a_{\text{classical}}\|$ in purple derives from the outputs of the classical accelerometers when the biases are not removed. Dashed lines represent time integrations of $1/t$ and $1/\sqrt{t}$.

The 3-axis hybrid accelerometer benefits from a 1kHz bandwidth, thanks to the classical accelerometers high data-rate output, and a high stability of the bias, due to the correction applied by the atomic accelerometers. Figure 7.6 presents measurements of the 3-axis hybrid accelerometer with the closed-loop mid-fringe tracking algorithm described in Chapter 2. The Raman interrogation time is T=10 ms. The sensor head is set up on the rotational platform with a tilt of $\theta_X = 45$ deg and $\theta_Z = -30$ deg. Each output of the hybrid accelerometers a_x, a_y and a_z is unstable due to the rotation of the sensor head, estimated at $\simeq 10$ μrad after 30 hours. In the mean time the norm of the full acceleration vector $\|a\| = \sqrt{{a_x}^2 + {a_y}^2 + {a_z}^2}$ reaches and stabilizes at 200 ng after 9 hours of integration. We assume that this limitation corresponds to the 3-axis atom interferometer bias drifts as studied in Chapters 5 and 6. We observed that the polarization of the lasers was drifting and affects the two-photon light shifts, which tend to drift in time. The norm of the full acceleration vector of the uncorrected classical accelerometers $\|a_{classical}\| = \|a + b\|$ is drifting at the level of 2 μg. This instability is directly correlated with the biases of the classical accelerometers. The 3-axis hybrid accelerometer finally gains one order of magnitude on the stability of the norm bias compared to the 3-axis classical accelerometer triad.

On the Allan deviation plot, the acceleration measurements integrate as $1/t$ until 4 s corresponding to the quantization noise of the classical acceleration measurements. It results from the difference between the exact analog measurements and the nearest quantization value of the numerical conversion made by the analog-to-digital converter (ADC). It characterizes also the integration of a white phase noise representing the average of disparate and periodic ambient noises summed. Starting at that time scale, the biases of the classical accelerometers are drifting. It corresponds to the timing rate of the biases correction of the 3 classical accelerometers by the 3-axis atom interferometer. In other words, the hybridization starts to be effective at that time scale. The bump at 100 s time scale corresponds to oscillations of the mid-fringe lock where the integrator part struggles to average different types of noise on each atom interferometer. We notice a $1/\sqrt{t}$ time integration on the norm. It corresponds to white frequency noise on the measurements of the atom interferometers integrated.

7.3.2 Limits of the real-time correlations to the sensitivity

Field-programmable gate array (FPGA) benefits from almost zero latency processing which justify a logical option for real-time applications. In our hybrid accelerometer, the FPGA represents the central part of the real-time system to control the frequency and the phase of the laser with a dedicated direct digital synthesizer (DDS). However real-time processing brings some limitations due to inherent latency from the classical

accelerometer.

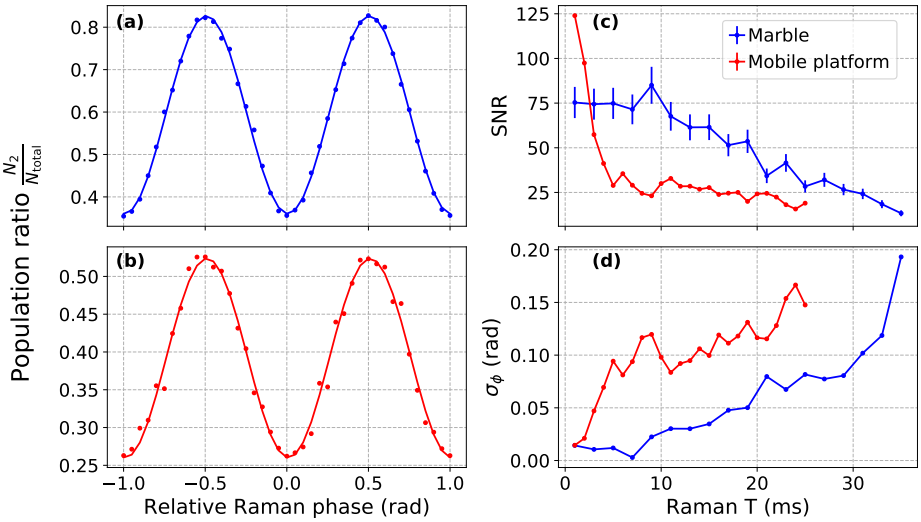

Figure 7.7: Raman fringes obtained with the sensor head placed on a marble table (a) and on the mobile platform (b) for a Raman interrogation time T=15 ms. (c) and (d) display respectively the SNR and the phase noise (in rad/shot) for different T when the sensor head is placed on the marble table (blue) and on the mobile platform (red).

We compared the sensitivity of the hybridized accelerometer in two different vibrational environments. To focus the analysis on the sensitivity of the atom interferometer, we filtered the bias of the classical accelerometer to not be disturbed by the bias. In addition, the series of frequency jumps is operated in phase continuous similarly to Chapters 5 and 6. In Figure 7.7(a), the sensor head is placed on a heavy marble table where ambient mechanical vibrations are widely attenuated. In Figure 7.7(b), the sensor head is placed on the mobile platform where no precautions are made to isolate it from any mechanical vibrations. Figures 7.7(c) and (d) show respectively the SNR and phase noise in those two situations for different Raman interrogation time T. The atom interferometer is more sensitive to mechanical vibrations from the reference mirror at high Raman interrogation time T. We observe that the phase noise is better when the sensor head is placed on the marble table. The efficiency of the correlations depends on the regime of the vibrations.

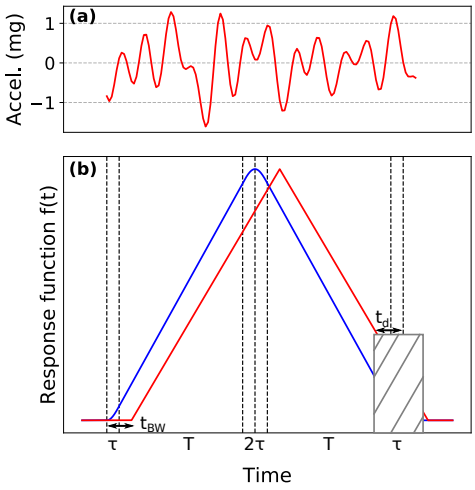

Figure 7.8: (a) Example of acceleration measured during atom interferometer by the classical accelerometer where its output is filtered. (b) Response function of the atom interferometer with the exact one in blue and the one applied by the real-time FPGA in red. The hatched grey area corresponds to the timezone where acceleration is missing because of the real-time.

Figure 7.8(b) shows the response function of the atom interferometer used to correlate the measurements with the classical accelerometer. Figure 7.8(a) displays an example of mechanical vibrations measured during atom interferometry. The response function used by the real-time FPGA is not the exact one but a simplified one approximated by a triangle-shaped function. Such function is easier to implement into the real-time FPGA and the difference on the estimation of the phase correction from the exact form should be negligible because $T \gg \tau$. However, the real-time correction induces a slight latency $t_{\mathrm{BW}} \simeq 1$ ms to compute the acceleration measurements with the response function. It corresponds to the bandwidth of the classical accelerometer. Furthermore, the vibrations occurring after the phase update for the last pulse can not be measured. It corresponds to a timezone of $t_d + t_{\mathrm{BW}} \simeq 1$ ms, where $t_d = 5$ μs corresponds to the pretrigger delay of the phase update from the last pulse. The last known acceleration is used as an estimation of the missing information.

Temperature modeling of the scale factor of the classical accelerometer, as described in Chapter 3, improves the estimation of the vibrations. To go further, measuring a more precise transfer function of the classical accelerometers would improve the estimation of the mechanical vibrations. We suspect that some non-linearity of the scale factor of the classical accelerometer emphasize when the vibrations are larger and make difficult to evaluate a simple transfer function. Another limitation can be the frequency dependence of the propagation delay of the mechanical vibrations inside the materials between the reference mirror and the classical accelerometer. Concretely high frequency mechanical vibrations propagate faster than low frequency ones. The mechanical bounds between the mirror, its mount and the classical accelerometer play

a role in the transmission efficiency to measure correctly the vibrations from the mirror.

7.3.3 Residual discontinuous phase from the frequency jumps

To correlate the measurements of the classical accelerometer with the atom interferometer experiencing an acceleration a_0, mechanical vibrations a_{vib} and a bias b, we compute the correlation phase $\phi_{\text{cor}} = \phi_{a_0} + \phi_{\text{vib}} + \phi_b$. For that reason, when we correct the Doppler frequency shift, we do not want to impact the imprinted phase onto the interferometer. We apply a series of phase-discontinuous frequency jumps, delivering an imprinted phase $\phi_{\text{discontinuous}} \approx 0$. The resulted output of the atom interferometer is:

$$\begin{aligned} \Phi &= \phi_{\text{kin}} + \phi_{\text{laser}} && (7.1)\\ &= -(a_0 + a_{\text{vib}})k_{\text{eff}}T_{\text{eff}}^2 + (a_0 + a_{\text{vib}} + b)k_{\text{eff}}T_{\text{eff}}^2 + \phi_{\text{discontinuous}} && (7.2)\\ &= bk_{\text{eff}}T_{\text{eff}}^2 + \phi_{\text{discontinuous}} && (7.3) \end{aligned}$$

where ϕ_{kin} is the inertial phase and $\phi_{\text{laser}} = \phi_{\text{cor}} + \phi_{\text{discontinuous}}$ is the imprinted laser phase.

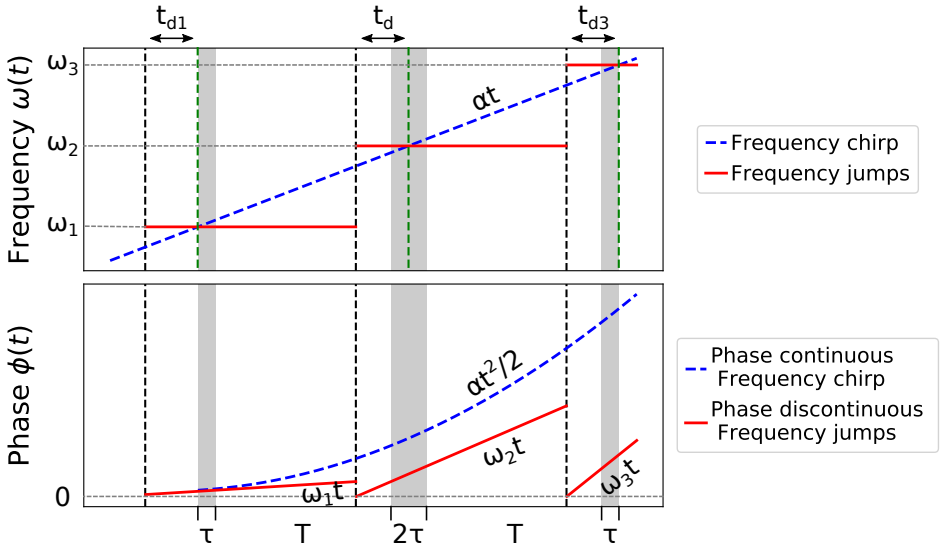

Figure 7.9: Comparison between phase continuous frequency chirp (in dashed blue) and phase discontinuous frequency jumps (in red) during Raman interferometer. The resulting phase for the first case follows the kinetic path of the atomic cloud. Whereas for the second case, the phase is reset at zero at each frequency update and a residual cumulating phase appears.

Figure 7.9 illustrates the method of the series of phase-discontinuous frequency jumps and compares it with a frequency chirp, usually applied for gravimeters. The resulted imprinted phase $\phi_{\text{discontinuous}}$ has been calculated in Chapter 2 as:

$$\phi_{\text{discontinuous}} = \int_{-\infty}^{+\infty} h(t)\phi(t)dt \tag{7.4}$$

$$= (\omega_1 - 2\omega_2 + \omega_3)t_d + \omega_3\left[\frac{1}{\Omega_{\text{eff}}^{(3)}}\tan\left(\frac{\Omega_{\text{eff}}^{(3)}\tau}{2}\right) - \tau\right] - \omega_1\left[\frac{1}{\Omega_{\text{eff}}^{(1)}}\tan\left(\frac{\Omega_{\text{eff}}^{(1)}\tau}{2}\right) - \tau\right] \tag{7.5}$$

where $h(t)$ is the phase sensitivity function, ω_1, ω_2 and ω_3 are the frequency jumps respectively during the first, second and last pulses, t_d is the pretrigger delay to update the frequency jumps, τ is the Rabi pulse length of the first and last pulse and $\Omega_{\text{eff}}^{(1)}$ and $\Omega_{\text{eff}}^{(3)}$ are respectively the Rabi frequencies of the first and the last pulse. If we set the two frequency jumps ω_2 and ω_3 according to the first one ω_1 with an arbitrary acceleration a as:

$$\omega_2 = \omega_1 + k_{\text{eff}}a(T + 2\tau) \tag{7.6}$$

$$\omega_3 = \omega_2 + k_{\text{eff}}a(T + 2\tau) \tag{7.7}$$

the first term of Eq. 7.5 and additionally, by setting the pretrigger delay of the first and the last pulses with respectively:

$$t_{d1} = t_d - \left(1 - \frac{2}{\pi}\right)\tau \tag{7.8}$$

$$t_{d3} = t_d + \left(1 - \frac{2}{\pi}\right)\tau \tag{7.9}$$

we obtain the following discontinuous phase:

$$\phi_{\text{discontinuous}} = 2k_{\text{eff}}a(T + 2\tau)\left[\frac{1}{\Omega_{\text{eff}}^{(3)}}\tan\left(\frac{\Omega_{\text{eff}}^{(3)}\tau}{2}\right) - \frac{2\tau}{\pi}\right] + \omega_1\left[\frac{1}{\Omega_{\text{eff}}^{(3)}}\tan\left(\frac{\Omega_{\text{eff}}^{(3)}\tau}{2}\right) - \frac{1}{\Omega_{\text{eff}}^{(1)}}\tan\left(\frac{\Omega_{\text{eff}}^{(1)}\tau}{2}\right)\right] \tag{7.10}$$

In that case, delays t_{d1} and t_{d3} are relative to the average of the phase sensitivity function $h(t)$ during the pulses, instead of being relative to the timing of the pulses. With the assumption that $\Omega_{\text{eff}}^{(3)}\tau = \Omega_{\text{eff}}^{(1)}\tau = \pi/2$, the phase discontinuous contribution $\phi_{\text{discontinuous}}$ is canceled.

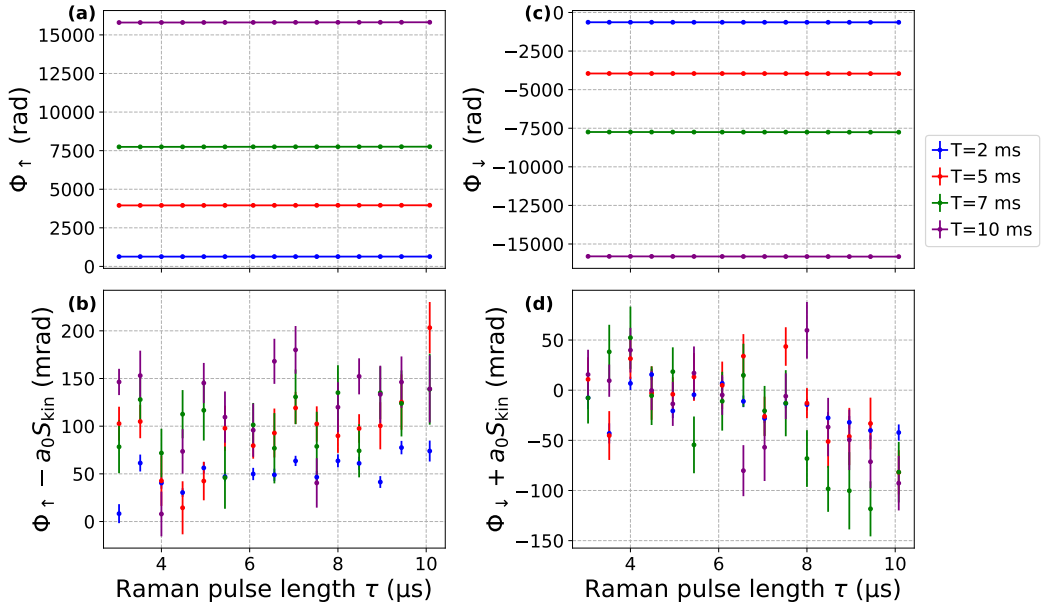

Figure 7.10: Phase difference output of the atom interferometer with phase-discontinuous frequency jumps at different Rabi pulse length τ for different Raman interrogation time T. (a) and (c) raw outputs for respectively $+k_{\text{eff}}$ and $-k_{\text{eff}}$ directions of the effective wavevector. (b) and (d) corresponding outputs where the inertial phase ϕ_{kin} is deduced and the residual discontinuous phase $\phi_{\text{discontinuous}}$ is left.

To determine the impact of the phase discontinuous $\phi_{\text{discontinuous}}$ on the hybrid accelerometer, we decided to filter the classical accelerometer to correlate only the mechanical vibrations. Figure 7.10 shows phase measurements of the atom interferometer with series of phase-discontinuous frequency jumps. Here the measurements are achieved along one axis with the hybrid accelerometer set up vertically. The resulted output of the atom interferometer is $\Phi = -\phi_{a_0} + \phi_{\text{discontinuous}}$. We remove the acceleration phase ϕ_{a_0} with the inertial scale factor calculated in Chapter 2:

$$S_{\text{kin}} = k_{\text{eff}}\,(T+2\tau)\left[T + \frac{1}{\Omega_{\text{eff}}^{(1)}}\tan\left(\frac{\Omega_{\text{eff}}^{(1)}\tau}{2}\right) + \frac{1}{\Omega_{\text{eff}}^{(3)}}\tan\left(\frac{\Omega_{\text{eff}}^{(3)}\tau}{2}\right)\right] \tag{7.11}$$

$$\simeq k_{\text{eff}}\,(T+2\tau)\left(T + \frac{4\tau}{\pi}\right) \tag{7.12}$$

The last expression is valid when the Rabi pulse length is optimized $\Omega_{\text{eff}}^{(1)}\tau \simeq \Omega_{\text{eff}}^{(3)}\tau \simeq \pi/2$. The residual $\phi_{\text{discontinuous}}$ is left with other systematic effects. We do not observe any particular trend with τ or T, meaning that expression Eq. 7.10 is correctly canceled.

Systematic effect (μg)	X-axis bias	Y-axis bias	Z-axis bias	Norm bias
Phase discontinuous	22.19 (0.35)	-18.81 (0.45)	18.11 (0.27)	34.27 (0.63)

Table 7.1: Table of the acceleration bias induced by the phase discontinuous term $\phi_{\text{discontinuous}}$ on the 3-axis hybrid accelerometer with a Raman interrogation time of $T = 10$ ms and the sensor head tilted by $\theta_X = 45$ deg and $\theta_Z = -30$ deg. The estimations are expressed in μg with the uncertainties in parentheses. The norm bias stands for the bias on the norm of the full acceleration vector.

Equation 7.10 is valid when the Rabi frequencies of the atom interferometer are correctly set as $\Omega^{(3)}_{\text{eff}}\tau = \Omega^{(1)}_{\text{eff}}\tau = \pi/2$. However, for the 3-axis hybrid accelerometer, the sensor head is tilted. Therefore the Rabi frequencies are varying during interferometry due to the finite size of the laser beams and their Gaussian profile. The Rabi frequency profile depending on the orientation of the sensor head have been studied in Chapter 6. Table 7.1 shows the acceleration bias induced by the residual phase discontinuous $\phi_{\text{discontinuous}}$ on each axis and on the norm of the full acceleration vector of the 3-axis hybrid accelerometer. It is estimated for an interrogation time T=10 ms and the sensor head tilted with angles $\theta_X = 45$ deg and $\theta_Z = -30$ deg.

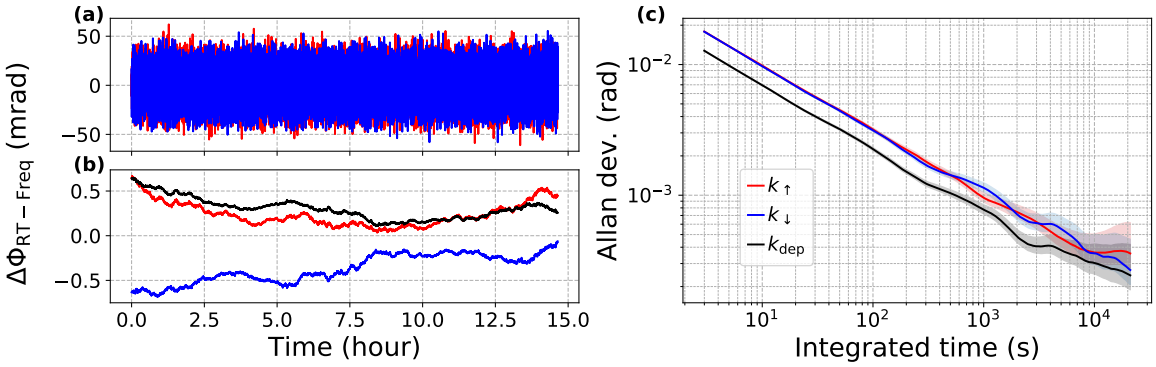

Figure 7.11: Phase shift induced by the frequency compensation of the real-time system $\Delta\Phi_{\text{RT-Freq}} = (\omega_1 - 2\omega_2 + \omega_3)t_d$ where $t_d = 20$ μs over 15 hours. The phase shift is estimated for directions $+k_{\text{eff}}$, $-k_{\text{eff}}$ for the effective wavevector and the rejected case k_{dep} displayed respectively in red, blue and black. (a) Raw measurements of $\Delta\Phi_{\text{RT-Freq}}$. (b) Measurements with a moving average over 10 hours. (c) Allan deviations.

In Equation 7.5, the term $\Delta\Phi_{\text{RT-Freq}} = (\omega_1 - 2\omega_2 + \omega_3)t_d$ is canceled when the expressions from Eq. 7.7 are fulfilled. However the real-time system can exhibit slight shifts over time in the frequencies during the interferometer. Figure 7.11 displays performances on a fixed position during 15 hours. The measurements are achieved on one axis of the hybrid accelerometer set up vertically. It reveals a phase noise contribution of 10 mrad/shot, which is small compared to the phase noise induced by the mechanical vibrations. The noise is integrated over time as white noise and the phase shift reaches a stability of 245 μrad. We observe a mean phase shift contribution

of $\Delta\Phi_{\mathrm{RT-Freq}} = 300$ μrad, corresponding to an acceleration shift of 19 ± 7 ng at $T = 10$ ms.

7.3.4 Systematic effects and calibration of the 3-axis hybrid accelerometer

Accuracy of the 3-axis hybrid accelerometer

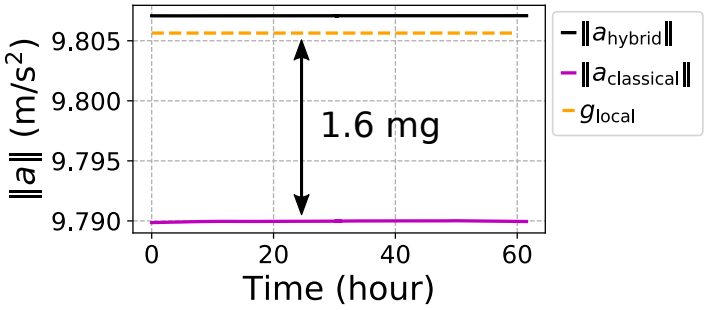

Figure 7.12: Time-series of the norm of the total acceleration vector measured by the 3-axis classical and hybrid accelerometers. The orange dashed line presents the local measurement of the gravitational acceleration.

Figure 7.12 presents the absolute measurements of the 3-axis classical and hybrid accelerometers from Fig. 7.6, and the value of the gravitational acceleration measured locally $g = 9.805642$ m.s^{-2}. The norm of the total acceleration vector measured by the 3-axis classical and hybrid accelerometers are respectively shifted by -1.6 mg and 147 μg. The shift of the 3-axis classical accelerometer derives mainly from the biases of each classical accelerometer. The 3-axis hybrid accelerometer improves the shift by one order of magnitude. The residual 147 μg bias is essentially due to misalignments between the axes and also to systematic effects from the atom interferometers.

Response function

The 3-axis hybrid accelerometer delivers the accelerations of each classical accelerometer where their biases are removed. In addition, the atom interferometers requires the study of the systematic effects. They have been estimated on the 3-axis accelerometer on Chapter 6 with the open-loop operational scheme. The 3-axis accelerometer operates a series of phase-continuous frequency jumps, leading to an error on the scale factor estimation. This error generates a large systematic shift, the scale factor error phase ϕ_{SF} with large uncertainties of several μg. Analogously for the 3-axis hybrid accelerometer operating with phase-discontinuous frequency jumps, the scale factor used to correlate the acceleration of the classical accelerometers is not exact.

The correlation phase $\phi_{\text{cor}} = \phi_{a_0} + \phi_{\text{vib}} + \phi_b$ applied at the last pulse of the interferometer is calculated with the response function $f(t)$ as:

$$\phi_{\text{cor}} = \int_{-\infty}^{+\infty} f(t)(a(t)+b(t))dt \tag{7.13}$$

$$= a_0 \int_{-\infty}^{+\infty} f(t)dt + \int_{-\infty}^{+\infty} f(t)(a_{\text{vib}}(t)+b(t))dt \tag{7.14}$$

where $a(t) = a_0 + a_{\text{vib}}(t)$ is the acceleration measured by the classical accelerometer including a DC acceleration a_0 and mechanical vibrations $a_{\text{vib}}(t)$, $b(t)$ is the bias of the classical accelerometer. The response function is determined from the sensitivity function $g(t)$ as [59]:

$$f(t) = -\int_0^t g(t')dt' \tag{7.15}$$

$$f(t) = \begin{cases} \frac{1}{\Omega_3}\tan\left(\frac{\Omega_3\tau}{2}\right) - \frac{1}{\Omega_1}\tan\left(\frac{\Omega_1\tau}{2}\right), & t \leq 0 \\ \frac{1}{\Omega_1}\frac{\cos(\Omega_1\tau)-\cos(\Omega_1 t)}{\sin(\Omega_1\tau)}, & 0 < t \leq \tau \\ t - \tau + \frac{1}{\Omega_3}\tan\left(\frac{\Omega_3\tau}{2}\right), & \tau < t \leq T+\tau \\ T + \frac{1}{\Omega_3}\tan\left(\frac{\Omega_3\tau}{2}\right) - \frac{1}{\Omega_2}\frac{\cos(\Omega_2\tau)-\cos(\Omega_2(t-T-2\tau))}{\sin(\Omega_2\tau)}, & T+\tau < t \leq T+3\tau \\ -t + 2T + 3\tau + \frac{1}{\Omega_3}\tan\left(\frac{\Omega_3\tau}{2}\right), & T+3\tau < t \leq 2T+3\tau \\ \frac{1}{\Omega_3}\frac{\cos(\Omega_3\tau)-\cos(\Omega_3(t-2T-4\tau))}{\sin(\Omega_3\tau)}, & 2T+3\tau < t \leq 2T+4\tau \\ 0, & t > 2T+4\tau \end{cases} \tag{7.16}$$

where Ω_1, Ω_2 and Ω_3 correspond respectively to the effective Rabi frequencies at first, second and last pulse of the interferometer. Considering that the atom interferometer is experiencing the acceleration $a(t)$, the resulted phase $\Phi = \phi_{\text{kin}} + \phi_{\text{laser}} = -\int_{-\infty}^{+\infty} f(t)a(t)dt + \int_{-\infty}^{+\infty} f(t)(a(t)+b(t))dt$ delivers the phase bias $\phi_b = \int_{-\infty}^{+\infty} f(t)b(t)dt$.

However, to apply in real-time the response function in order to determine correctly the correlation phase ϕ_{cor}, the Rabi frequencies should be known at each pulse. In the real-time FPGA we implemented the approximated response function:

$$f_{\text{RT}}(t) = \begin{cases} 0, & t \leq 0 \text{ and } t > 2T+4\tau \\ \frac{T+4\tau/\pi}{T+2\tau}t, & T+\tau < t \leq T+2\tau \\ \frac{T+4\tau/\pi}{T+2\tau}(-t+2T+4\tau), & T+2\tau < t \leq 2T+4\tau \end{cases} \tag{7.17}$$

The resulted correlation phase depends on a scale factor $S_{\text{RT}} = \int_{-\infty}^{+\infty} f_{\text{RT}}(t)dt$ as $\phi_{\text{cor}} = S_{\text{RT}}a_0$. This scale factor is equal to:

$$\frac{S_{\mathrm{RT}}}{k_{\mathrm{eff}}} = (T + 2\tau)\left(T + \frac{4\tau}{\pi}\right) \tag{7.18}$$

It arises a scale factor error $\delta S_{\mathrm{RT}} = S_{\mathrm{RT}} - S_{\mathrm{kin}}$ on the DC phase ϕ_{a_0} from the phase of the interferometer $\Phi = \phi_{\mathrm{kin}} + \phi_{\mathrm{laser}}$. The resulted bias shift is determined as:

$$\begin{aligned} \phi_{\mathrm{RT,SF}} &= a_0 \delta S_{\mathrm{RT}} && (7.19) \\ &= a_0 k_{\mathrm{eff}} (T + 2\tau) \left[\frac{4\tau}{\pi} - \frac{1}{\Omega_1}\tan\left(\frac{\Omega_1\tau}{2}\right) - \frac{1}{\Omega_3}\tan\left(\frac{\Omega_3\tau}{2}\right)\right] && (7.20) \end{aligned}$$

Systematic effect (μg)	**X-axis bias**	**Y-axis bias**	**Z-axis bias**	**Norm bias**
RT Scale factor error	-26.2 (2.4)	38.4 (1.0)	-39.9 (0.5)	61.3 (2.7)

Table 7.2: Table of the acceleration bias induced by the scale factor error from the real-time system on the 3-axis hybrid accelerometer, with a Raman interrogation time of $T = 10$ ms and the sensor head tilted by $\theta_X = 45$ deg and $\theta_Z = -30$ deg. The estimations are expressed in μg with the uncertainties in parentheses. The norm bias stands for the bias of the norm of the full acceleration vector.

Table 7.2 shows the acceleration bias induced by the scale factor error inside the real-time system and calculated from Eq. 7.20. It is evaluated on each axis and on the norm of the full acceleration vector of the 3-axis hybrid accelerometer. It is estimated for an interrogation time T=10 ms and the sensor head tilted with angles $\theta_X = 45$ deg and $\theta_Z = -30$ deg.

Summary of systematic effects

The systematic effects of the atoms interferometers have been studied in Chapter 6 with the open-loop algorithm. The common effects with the 3-axis hybrid accelerometer operating with the closed-loop algorithm are: the AC Stark shift (rejected at first order with trajectories $\pm k_{\mathrm{eff}}$), the two-photon light shift (TPLS), the asymmetry of the Mach-Zehnder interferometer, the Coriolis effect, the non-linearity from the RF chain, the parasitic lines, the quadratic Zeeman shift, the wavefront aberration and the beam misalignments (alignment of the collimator with the mirror). The scale factor error studied in Chapter 6 is specific to the open-loop algorithm and does not count for the current Chapter. For the 3-axis hybrid accelerometer, we have the residual phase shifts from the phase-discontinuous frequency jumps (Sec. 7.3.3) and the one deriving from the scale factor error in the correlation phase measured by the real-time system (Sec. 7.3.4).

Systematic effect (μg)	X-axis bias	Y-axis bias	Z-axis bias	Norm bias
Total	16.2 (5.0)	-23.3 (2.4)	17.5 (1.7)	33.3 (5.8)

Table 7.3: Table of the acceleration biases including all the contributions from the atom interferometers on the 3-axis hybrid accelerometer, with a Raman interrogation time of $T = 10$ ms and the sensor head tilted by $\theta_X = 54.7$ deg and $\theta_Z = -45$ deg. The estimations are expressed in μg with the uncertainties in parentheses. The norm bias stands for the bias of the norm of the full acceleration vector.

Table 7.3 presents the total acceleration bias from the atom interferometers of the 3-axis hybrid accelerometer on each axis and on the norm of the total acceleration vector. The resulted bias on the norm is 33.3 μg, which is $\simeq 3$ times better than the 3-axis atom interferometer. This due to the opposite sign between the RT scale factor error and the phase discontinuous shift, which tends to reduce the total shift. The confidence on the bias of the norm is 5.8 μg which is the same order as the 3-axis atom interferometer.

Misalignments calibration

The calibration of the triad misalignments conducted on the 3-axis atom accelerometer in Chapter 6 leads to an uncertainty of $\simeq 8$ μg on the estimation of the norm of the total acceleration vector. This correction corresponds to a precision of 8 μrad between the axes.

For the calibration of the 3-axis hybrid accelerometer, the 3-axis accelerometer triad should be considered. Indeed the atom interferometers correct individually each associated classical accelerometer. Residual misalignments between the effective wavevector (defined by the reference mirror and the collimator) and the measurement axis of the classical accelerometer are second order. The corresponding shift has been studied in Chapter 5:

$$1 - \cos(2\alpha + \beta)\cos(\beta/2) \sim 2\alpha^2 + 2\alpha\beta + \frac{5}{8}\beta^2 \tag{7.21}$$

where α is the tilt angle of the collimator and β is the tilt angle of the reference mirror compared to the classical accelerometer measurement axis. α can be corrected mechanically by aligning the retro-reflected beam. β can be optimized if the mirror is on a tip-tilt stage decoupled from the classical accelerometer for instance. This angle can also be "numerically" minimized if the scale factor of the classical accelerometer is calibrated with the atomic one. Correlation measurements between the classical and atom accelerometer allow to compare their scale factors, including the misalignment β. A method is to profit from natural vibrations of the reference mirror to scan the atom interferometer fringes and the classical accelerometer.

We propose the following protocol to calibrate the 3-axis hybrid accelerometer:

- On each axis X,Y and Z:
  - Potentially, if the reference mirror can be tilted with a tip-tilt stage for instance, optimize the reference mirror alignment by minimizing the bias measured with the atom interferometer in closed-loop operation. Eventually, if the reference mirror is fixed, the alignment between the reference mirror and the classical accelerometer can be corrected "numerically" by adjusting the scale factor of the classical accelerometer with correlations.
  - Optimize the collimator alignment by minimizing the bias measured with the atom interferometer in closed-loop operation or maximizing the acceleration measured in open-loop operation.
- Perform measurements with the 3-axis hybrid accelerometer on different orientations for the misalignments calibration (as performed for instance in Chapters 3 and 6 on respectively the 3-axis classical accelerometer triad and the 3-axis atom interferometer).
- Remove systematic biases deriving from the atom interferometers on each axis.
- Apply the 3-axis misalignments calibration method to determine the misalignments matrix.

7.3.5 3-axis hybrid accelerometer outside of the laboratory

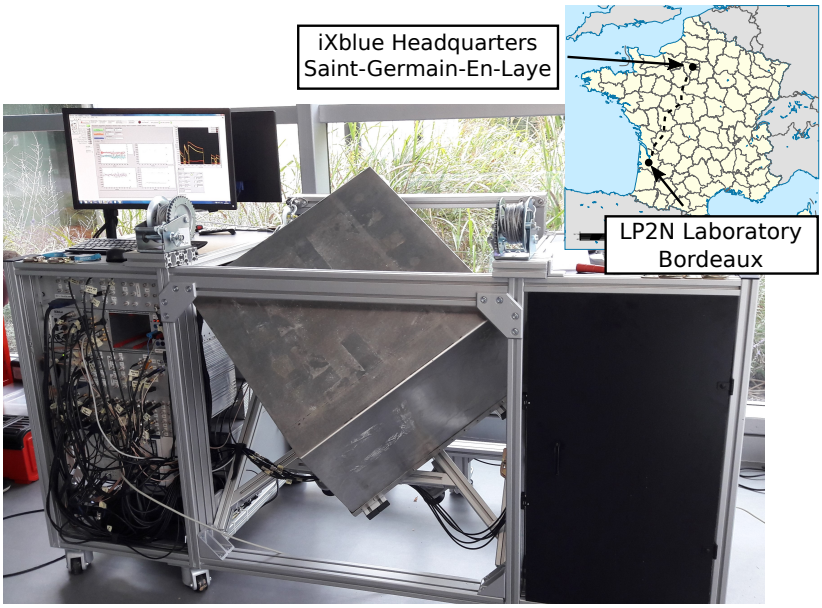

Figure 7.13: Image of the 3-axis hybrid accelerometer on the mobile platform at iXblue facilities. Location of iXblue headquarters at Saint-Germain-En-Laye in inset.

The 3-axis hybrid accelerometer has been evaluated out of our laboratory environment, in iXblue facilities at Saint-Germain-En-Laye. The sensor head is placed on its mobile platform as shown on Figure 7.13. The platform allows to tilt the sensor head to operate the atom interferometers with Doppler frequency shift along the 3 axes simultaneously generated by the projected gravitational force. The sensor is assembled and operational in half of a day. The sensor was placed in a regular room without any control of the environment, in particular the temperature was fluctuating due to the sun exposure. Under those conditions the whole sensor, including the laser system, the sensor head and all the electronics, was able to operate. We validated the 3-axis hybrid accelerometer for transportation and non-laboratory environment. In particular the saturated absorption of the reference laser, the frequency lock of the main laser and the PPLN crystal operated as usual thanks to the temperature controlled boxes where the components are placed. The IQ modulator and the IQ-MBC lock was working properly as well for several days. Further tests should be made to test the sensor under severe environment. For instance the high level of salinity and humidity typically in marine environment can be problematic for the electronic.

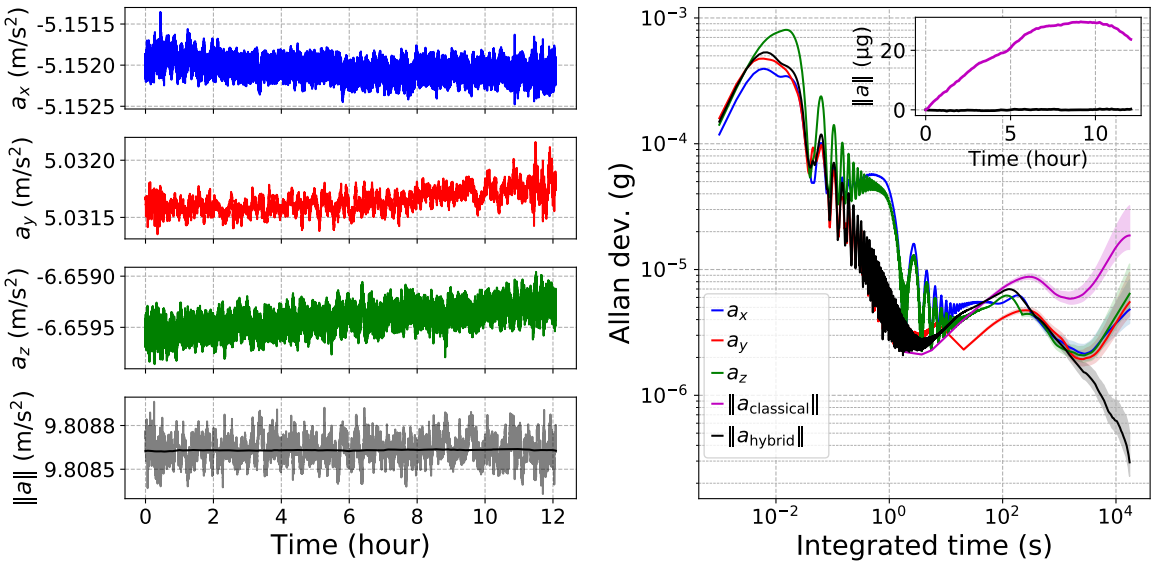

Figure 7.14: Measurements of the 3-axis hybrid accelerometer on the mobile platform over 12h at iXblue facilities. The Raman interrogation time of the atom interferometers is T=5 ms and the sensor head is tilted with an angle of 47 deg. The time-series plots shows measurements at the cycling rate of the atom interferometer and the norm ‖a‖ includes a 5 hours moving average in darker color.

Figure 7.14 presents the measurements of the 3-axis hybrid accelerometer at iXblue facilities. Measurements have been taken over night during 12 hours with a Raman interrogation time of T=5 ms for each atom interferometer. The platform is tilted with an angle of $\simeq$ 47 deg. We retrieve the same behaviors as Fig. 7.6, namely drifts of the

individual axes due to the ground rotation whereas the norm of the full acceleration vector is stable. At that time, the classical accelerometers of the X and Z-axis were not magnetically shielded (Q-Flex QA-750 Honeywell) whereas the one from the Y-axis was (Q-Flex QA-2000 Honeywell). They include a proof mass with a coil measuring its displacement compared to a fixed magnet. In consequence, the acceleration measured is sensitive to external magnetic fields. The high magnetic field generated by the MOT coils during the MOT loading impacts the acceleration measured and explains the larger noise on the time series plots and the oscillations on the Allan deviation plot at $10^{-2} - 10$ s time scale. Moreover no significant efforts were made on the optimization of the atom interferometers, specifically to increase the stability of the biases or increase the Raman interrogation time for better sensitivity. Nevertheless the bias stability of the 3-axis hybrid accelerometer reached 400 ng on the norm after 5 hours of integration.

The gravitational force is locally measured at 9.80861 m/s^2. Based on a trivial mathematical model with the International Gravity Formula (IGF) and the Free Air System (FAC), by knowing the latitude and approximately the height where the measurements where made, we estimate a theoretical local value of the gravitational force of $\simeq$ 9.80939 m/s^2. The measurement is off by -80 μg from the theoretical value. Indeed the misalignments calibration of the 3-axis frame was not performed at that time. This acceleration shift corresponds to an orthogonal misalignment of ~ 80 μrad on the 3-axis triad frame, which is realistic. In addition, no proper estimation of the systematic shifts of individual atom interferometers depending on the orientation of the sensor head have been made at that time either.

Conclusion

In this chapter, we validated the performances of the 3-axis hybrid accelerometer, including the real-time system. It is the first time that such sensor based on data fusion between multi-axis atom interferometry and classical accelerometers is conceived. It generates continuous accelerations on each axis where the biases of the classical accelerometers are tracked and removed. We were able to track the norm of the full vector acceleration at 200 ng level of stability for 60 hours. The 3-axis hybrid accelerometer gains one order of magnitude on the stability of the long term biases compared to the ones from classical accelerometers triad. Furthermore, the 3 acceleration outputs are delivered with a high data rate of 1 kHz. It paves the way of very low biased multi-axis accelerometers compatible for inertial navigation.

For now, the 3-axis hybrid accelerometer have been demonstrated for static operation. Particularly, the mobile platform allowed us to transport and operate the 3-axis hybrid accelerometer easily. We validated the proper operation and reliability of the laser system, the sensor head and all the electronics under temperature varying environment for several days. It represents a successful step before next challenges for mobile operations.

Conclusion and outlook

My thesis represents the first PhD work on the iXatom project. The 3-axis hybrid accelerometer developed over this time paves the way of multi-axis atomic sensors dedicated to inertial navigation. In the scope of GNSS-free navigation, the 3-axis hybrid accelerometer addresses the navigation errors generated by the classical accelerometers and affords a solution to correct the biases. The instrument benefits from the absolute measurement provided by the quantum sensors. The quest of the integration of quantum sensors into inertial navigation systems progresses and needs further efforts.

Improvements of the 3-axis hybrid accelerometer

The performances of the 3-axis hybrid accelerometer can be improved by increasing the cycling rate. Indeed we are facing a technical limitation with long dead-times of $\simeq 1$ s between each shot, with the uploading of the sequence from the CPU to the FPGA sequencer. In consequence the cycling time is extended to $\simeq 1.3$ s. With an adapted control system to optimize the loading sequence, we could reach a cycling rate > 3 Hz and the sensitivity would be better.

The accuracy of our 3-axis hybrid accelerometer declined mainly because of the uncommon operation with frequency jumps to compensate the Doppler frequency shift, whereas usually a chirp is applied for gravimeters. For now, the direct digital synthesizer (DDS) we are using to generate the frequency jumps has a limited resolution to conduct proper chirps. Alternative schemes with a higher resolution on the DDS should be experimented to improve this aspect.

The finite size of the laser beams, as well as the Gaussian profile, reduces the effective exposure of the light onto the atoms when the sensor head is tilted. It impacts the contrast of the signal, but mostly the accuracy of the sensor. Indeed many systematic effects are sensitive to variation of the electric field, and particularly those ones count for almost all the shifts. Implementing top-hat beam collimation would strongly improve those aspects by flatten the intensity profile through the edges of the lasers [97]. An homogeneous Rabi frequency during interferometry will notably correct the accuracy of the quantum sensor. However the phase distribution of the wavefront still needs to be investigate with such collimation.

Another important point, for multi-axis inertial sensing, is the calibration of the misalignments from the triad. For now we are limited by the preliminary study of the systematic effects on each atom interferometer axis, which restrains the proper

calibration of the misalignments. Further study is required to improve the confidence on the accuracy to better calibrate the 3-axis hybrid accelerometer. One may ask the limitations of this calibration method and what is the best precision we could reach on the misalignments correction. Furthermore what is the stability of the alignment between the axes over time, especially with temperature variation during mobile operations.

Challenges of mobile operation

The 3-axis hybrid accelerometer is validated for transportation and static operation. For mobile applications, the instrument requires further developments and qualifications. During mobile operations, large mechanical vibrations occur on the reference mirror and need to be accurately measured by the classical accelerometer to be correlated with the atom interferometer. Otherwise the vibrations evolve as phase noise on the atom interferometer and the sensitivity drops.

Another challenge for dynamic operations is the issue from the rotations. If the apparatus is in rotation during the interferometer, the 3 light pulses of the Mach-Zehnder interferometer are not applied in the same direction. In this case, the wavepackets are not overlapped at the last pulse and the interferometer is not closed correctly. This leads to a strong loss of contrast. A simple solution is to decrease the interrogation time to limit the expansion of the interferometric zone, at the expense of a drop on the sensitivity. A colder atomic cloud would resolve partially the issue, but engages complex technics, like Raman sideband cooling in 3D, or additional lasers, such as dipolar traps. Further developments need to be addressed to compensate the rotations without deteriorating the signal. For instance, the use of a tip-tilt stage to correct the tilt of the reference mirror during the interferometer is an option. It requires gyroscopes to monitor the rotations and feedback in real-time the correction.

For the 3-axis hybrid accelerometer, the quantum accelerometer does not need to be able to operate under large shocks, only the classical aiding sensor does. Whereas the classical accelerometers are already qualified for mobile applications, the resilience of the hybrid system is only limited by the survivability of the quantum one in the presence of large vibrations, shocks or rotations. The resilience to vibrations can be assessed by using a vibrating pot and the resilience to rotations evaluated using motorized three-axis tables.

Toward integrated mobile quantum-classical INS

The development of the 3-axis hybrid accelerometer is the first step in the quest of the integration of the quantum sensor into inertial navigation systems (INS). The 3-axis

hybrid accelerometer alone can not operate inertial navigation, since the measurements of the rotations are missing. In the near future, fiber-optic gyroscopes (FOG) will be added to the instrument to build a fully functional INS.

A technological transfer would lead to further integration of the complicated architecture. Indeed the operation system required for the quantum accelerometer is complex and spacious, including the sensor head, the laser system, the RF chain, the electronic control and the CPU. The compactness targeted is compatible for military applications and can address Space missions with extensive efforts on the compactness and the weight. Civil applications would require more drastic miniaturisation of technological building blocks, such as atom chips for the sensor head, or photonic integrated circuit (PIC) for the laser system.

For now the hybridization of inertial sensors between classical and quantum technologies addresses only the accelerometers. Nevertheless we can imagine a further hybridization between classical and quantum gyroscopes. The approach would be similar as the one between classical and quantum accelerometers. The absolute and very sensitive measurements of the quantum gyroscope would improve the biases of the classical gyroscope. Specially since the main limitation in inertial navigation systems relies on the propagation error generated by the gyroscopes. However, despite the high potential of the atomic gyroscopes to outperform classical gyroscopes, the quantum gyroscopes are not competing today with the high-end classical gyroscope performances, such as FOGs. The ultimate challenge would be to conceive an hybridized INS with 3-axis hybridized accelerometers and gyroscopes where the atomic sensors would correct the classic ones, or to barely replace classical technologies with autonomous quantum sensors.

Bibliography

[1] H.C. Lefevre. *The Fiber-Optic Gyroscope, Second Edition*. Artech House applied photonics series. Artech House Publishers, 2014. ISBN: 9781608076963. URL: https://books.google.fr/books?id=j-PmBgAAQBAJ.

[2] M.S. Grewal, L.R. Weill, and A.P. Andrews. *Global Positioning Systems, Inertial Navigation, and Integration*. Wiley, 2004. ISBN: 9780471463863. URL: https://books.google.fr/books?id=ZM7muB8Y35wC.

[3] R. E. Kalman. "A New Approach to Linear Filtering and Prediction Problems". In: *Journal of Basic Engineering* 82.1 (1960), pp. 35–45. DOI: 10.1115/1.3662552. URL: https://doi.org/10.1115/1.3662552.

[4] P. Groves. 2013. URL: https://ieeexplore.ieee.org/document/9101092.

[5] B. Battelier *et al.* "Development of compact cold-atom sensors for inertial navigation". In: *Proceedings of SPIE Quantum Optics*. Vol. 9900. 2016, p. 990004. DOI: 10.1117/12.2228351. URL: http://proceedings.spiedigitallibrary.org/proceeding.aspx?doi=10.1117/12.2228351.

[6] Mark Kasevich and Steven Chu. "Atomic interferometry using stimulated Raman transitions". In: *Physical Review Letters* 67 (1991), p. 181. DOI: 10.1103/PhysRevLett.67.181. URL: https://doi.org/10.1103/PhysRevLett.67.181.

[7] J. Le Gouët et al. "Limits to the sensitivity of a low noise compact atomic gravimeter". In: *Appl. Phys. B* 92 (2 2008), pp. 133–144. DOI: 10.1007/s00340-008-3088-1. URL: http://link.springer.com/article/10.1007/s00340-008-3088-1.

[8] F. Sorrentino et al. "Sensitivity limits of a Raman atom interferometer as a gravity gradiometer". In: *Phys. Rev. A* 89 (2 2014), p. 023607. DOI: 10.1103/PhysRevA.89.023607. URL: https://link.aps.org/doi/10.1103/PhysRevA.89.023607.

[9] Y. Wang *et al.* "Location-dependent Raman transition in gravity-gradient measurements using dual atom interferometers". In: *Phys. Rev. A* 95.5 (2017), p. 053612. DOI: 10.1103/PhysRevA.95.053612. URL: http://link.aps.org/doi/10.1103/PhysRevA.95.053612.

[10] T. L. Gustavson, P. Bouyer, and M. A. Kasevich. "Precision Rotation Measurements with an Atom Interferometer Gyroscope". In: *Phys. Rev. Lett.* 78 (11 1997), pp. 2046–2049. DOI: 10.1103/PhysRevLett.78.2046. URL: https://link.aps.org/doi/10.1103/PhysRevLett.78.2046.

[11] I. Dutta et al. "Continuous Cold-Atom Inertial Sensor with 1 nrad/sec Rotation Stability". In: *Phys. Rev. Lett.* 116 (18 2016), p. 183003. DOI: 10.1103/PhysRevLett.116.183003. URL: https://link.aps.org/doi/10.1103/PhysRevLett.116.183003.

[12] Canuel, B. and Bertoldi, A. and Amand, L. *et al.* "Exploring gravity with the MIGA large scale atom interferometer". In: *Sci Rep* 8 (2018), p. 14064. DOI: 10.1038/s41598-018-32165-z. URL: https://doi.org/10.1038/s41598-018-32165-z.

[13] Richard H. Parker et al. "Measurement of the fine-structure constant as a test of the Standard Model". In: *Science* 360.6385 (2018), pp. 191–195. DOI: 10.1126/science.aap7706. URL: https://science.sciencemag.org/content/360/6385/191.

[14] Pierrick Cheiney et al. "Navigation-compatible hybrid quantum accelerometer using a Kalman filter". In: *Physical Review Applied* 10.1 (2018), p. 1. DOI: 10.1103/PhysRevApplied.10.034030. URL: https://doi.org/10.1103/PhysRevApplied.10.034030.

[15] J. A. Rushton, M. Aldous, and M. D. Himsworth. "Contributed Review: The feasibility of a fully miniaturized magneto-optical trap for portable ultracold quantum technology". In: *Review of Scientific Instruments* 85.12 (2014), p. 121501. DOI: 10.1063/1.4904066. URL: https://doi.org/10.1063/1.4904066.

[16] Brynle Barrett et al. "Dual matter-wave inertial sensors in weightlessness". In: *Nature Communications* 7 (2016), pp. 1–9. DOI: 10.1038/ncomms13786. URL: https://www.nature.com/articles/ncomms13786.

[17] Y. Bidel et al. "Absolute marine gravimetry with matter-wave interferometry". In: *Nature Communications* 9 (2018), p. 627. DOI: 10.1038/s41467-018-03040-2. URL: https://doi.org/10.1038/s41467-018-03040-2.

[18] Vincent Ménoret et al. "Gravity measurements below 10^{-9} g with a transportable absolute quantum gravimeter". In: *Scientific Reports* 8.1 (2018), pp. 1–11. ISSN: 20452322. DOI: 10.1038/s41598-018-30608-1. URL: https://doi.org/10.1038/s41598-018-30608-1.

[19] AOSense. URL: https://aosense.com/.

[20] μquans. URL: https://www.muquans.com/.

[21] C Freier et al. "Mobile quantum gravity sensor with unprecedented stability". In: *Journal of Physics: Conference Series* 723 (2016), p. 012050. DOI: 10.1088/1742-6596/723/1/012050. URL: https://doi.org/10.1088/1742-6596/723/1/012050.

[22] Xuejian Wu et al. "Gravity surveys using a mobile atom interferometer". In: *Science Advances* 5.9 (2019). DOI: 10.1126/sciadv.aax0800. URL: https://advances.sciencemag.org/content/5/9/eaax0800.

[23] P Gillot et al. "Stability comparison of two absolute gravimeters: optical versus atomic interferometers". In: *Metrologia* 51.5 (2014), pp. L15–L17. DOI: 10.1088/0026-1394/51/5/l15. URL: https://doi.org/10.1088/0026-1394/51/5/l15.

[24] Zhijie Fu et al. "A new type of compact gravimeter for long-term absolute gravity monitoring". In: *Metrologia* 56.2 (2019), p. 025001. DOI: 10.1088/1681-7575/aafcc7. URL: https://doi.org/10.1088/1681-7575/aafcc7.

[25] Chetan Mahadeswaraswamy. "Atom interferometric gravity gradiometer: Disturbance compensation and mobile gradiometry". PhD thesis. Stanford University, 2009.

[26] G. Condon et al. "All-Optical Bose-Einstein Condensates in Microgravity". In: *Phys. Rev. Lett.* 123 (2019), p. 240402. DOI: 10.1103/PhysRevLett.123.240402. URL: https://link.aps.org/doi/10.1103/PhysRevLett.123.240402.

[27] R. Geiger et al. "Detecting inertial effects with airborne matter-wave interferometry". In: *Nature Communications* 2 (2011), pp. 1–7. DOI: 10.1038/ncomms1479. URL: https://www.nature.com/articles/ncomms1479.

[28] Bidel, Y. and Zahzam, N. and Bresson, A. *et al.* "Absolute airborne gravimetry with a cold atom sensor". In: *J Geod* 94 (2020), p. 20. DOI: 10.1007/s00190-020-01350-2. URL: https://doi.org/10.1007/s00190-020-01350-2.

[29] J. Lautier et al. "Hybridizing matter-wave and classical accelerometers". In: *Applied Physics Letters* 105.14 (2014), p. 144102. DOI: 10.1063/1.4897358. URL: https://doi.org/10.1063/1.4897358.

[30] P. Cheiney et al. "Demonstration of a Robust Hybrid Classical/Quantum Accelerometer". In: *2019 IEEE International Symposium on Inertial Sensors and Systems (INERTIAL)*. 2019, pp. 1–4. DOI: 10.1109/ISISS.2019.8739762. URL: https://doi.org/10.1109/ISISS.2019.8739762.

[31] S Merlet et al. “Operating an atom interferometer beyond its linear range”. In: *Metrologia* 46.1 (2009), pp. 87–94. DOI: 10.1088/0026-1394/46/1/011. URL: https://doi.org/10.1088/0026-1394/46/1/011.

[32] Hauth, M. and Freier, C. and Schkolnik, V. *et al.* “First gravity measurements using the mobile atom interferometer GAIN”. In: *Appl. Phys. B* 113 (2013), pp. 49–55. DOI: 10.1007/s00340-013-5413-6. URL: https://doi.org/10.1007/s00340-013-5413-6.

[33] B. Canuel et al. “Six-axis inertial sensor using cold-atom interferometry”. In: *Physical Review Letters* 97 (2006), pp. 1–4. DOI: 10.1103/PhysRevLett.97.010402. URL: https://journals.aps.org/prl/abstract/10.1103/PhysRevLett.97.010402.

[34] Wu Xuejian et al. “Multiaxis atom interferometry with a single-diode laser and a pyramidal magneto-optical trap”. In: *Optica* 4 (2017), pp. 1545–1551. DOI: 10.1364/OPTICA.4.001545. URL: http://www.osapublishing.org/optica/abstract.cfm?URI=optica-4-12-1545.

[35] Olivier Carraz et al. “A Spaceborne Gravity Gradiometer Concept Based on Cold Atom Interferometers for Measuring Earth’s Gravity Field”. In: *Microgravity Science and Technology* 26 (2014), pp. 1875–0494. DOI: 10.1007/s12217-014-9385-x. URL: https://doi.org/10.1007/s12217-014-9385-x.

[36] T. Zanon-Willette et al. “Composite pulses in Hyper-Ramsey spectroscopy for the next generation of atomic clocks”. In: *Journal of Physics: Conference Series* 723 (2016), p. 012057. DOI: 10.1088/1742-6596/723/1/012057. URL: https://doi.org/10.1088{\%}2F1742-6596{\%}2F723{\%}2F1{\%}2F012057.

[37] L. Antoni-Micollier *et al.* “Watt-level narrow-linewidth fibered laser source at 852 nm for FIB application”. In: *Opt. Lett.* 43.16 (2018), pp. 3937–3940. DOI: 10.1364/OL.43.003937. URL: https://www.osapublishing.org/abstract.cfm?URI=ol-43-16-3937.

[38] Becker, D. and Lachmann, M.D. and Seidel, S.T. *et al.* “Space-borne Bose–Einstein condensation for precision interferometry”. In: *Nature* 562 (2018), pp. 391–395. DOI: 10.1038/s41586-018-0605-1. URL: https://doi.org/10.1038/s41586-018-0605-1.

[39] Sabrina Hartmann et al. “Regimes of atomic diffraction: Raman versus Bragg diffraction in retroreflective geometries”. In: *Phys. Rev. A* 101 (5 2020), p. 053610. DOI: 10.1103/PhysRevA.101.053610. URL: https://link.aps.org/doi/10.1103/PhysRevA.101.053610.

[40] P A Altin et al. “Precision atomic gravimeter based on Bragg diffraction”. In: *New Journal of Physics* 15.2 (2013), p. 023009. DOI: 10.1088/1367-2630/15/2/023009. URL: https://doi.org/10.1088/1367-2630/15/2/023009.

[41] J. M. McGuirk, M. J. Snadden, and M. A. Kasevich. “Large Area Light-Pulse Atom Interferometry”. In: *Phys. Rev. Lett.* 85 (21 2000), pp. 4498–4501. DOI: 10.1103/PhysRevLett.85.4498. URL: https://link.aps.org/doi/10.1103/PhysRevLett.85.4498.

[42] Matt Jaffe et al. “Efficient Adiabatic Spin-Dependent Kicks in an Atom Interferometer”. In: *Phys. Rev. Lett.* 121 (4 2018), p. 040402. DOI: 10.1103/PhysRevLett.121.040402. URL: https://link.aps.org/doi/10.1103/PhysRevLett.121.040402.

[43] D. Savoie et al. “Interleaved atom interferometry for high-sensitivity inertial measurements”. In: *Science Advances* 4.12 (2018). DOI: 10.1126/sciadv.aau7948. URL: https://advances.sciencemag.org/content/4/12/eaau7948.

[44] X Alauze et al. “A trapped ultracold atom force sensor with a μm-scale spatial resolution”. In: *New Journal of Physics* 20.8 (2018), p. 083014. DOI: 10.1088/1367-2630/aad716. URL: https://doi.org/10.1088/1367-2630/aad716.

[45] M Dupont-Nivet et al. “Experimental study of the role of trap symmetry in an atom-chip interferometer above the Bose–Einstein condensation threshold”. In: *New Journal of Physics* 20.4 (2018), p. 043051. DOI: 10.1088/1367-2630/aabc72. URL: https://doi.org/10.1088/1367-2630/aabc72.

[46] S. Abend et al. “Atom-Chip Fountain Gravimeter”. In: *Phys. Rev. Lett.* 117 (2016), p. 203003. DOI: 10.1103/PhysRevLett.117.203003. URL: https://link.aps.org/doi/10.1103/PhysRevLett.117.203003.

[47] B. Barrett et al. “Multidimensional Atom Optics and Interferometry”. In: *Phys. Rev. Lett.* 122 (2019), p. 043604. DOI: 10.1103/PhysRevLett.122.043604. URL: https://link.aps.org/doi/10.1103/PhysRevLett.122.043604.

[48] E. L. Raab et al. “Trapping of Neutral Sodium Atoms with Radiation Pressure”. In: *Phys. Rev. Lett.* 59 (23 1987), pp. 2631–2634. DOI: 10.1103/PhysRevLett.59.2631. URL: https://link.aps.org/doi/10.1103/PhysRevLett.59.2631.

[49] D.A. Steck. *Rubidium 87 D Line Data*. (revision 2.2.1,21 November 2019). 2001. URL: http://steck.us/alkalidata.

[50] J. Dalibard and C. Cohen-Tannoudji. “Laser cooling below the Doppler limit by polarization gradients: simple theoretical models”. In: *J. Opt. Soc. Am. B* 6.11 (1989), pp. 2023–2045. DOI: 10.1364/JOSAB.6.002023. URL: http://josab.osa.org/abstract.cfm?URI=josab-6-11-2023.

[51] Sara Rosi et al. “OPEN Λ -enhanced grey molasses on the D 2 transition of Rubidium-87 atoms”. In: *Scientific Reports* 8 (2018), p. 1301. DOI: 10.1038/s41598-018-19814-z. URL: http://dx.doi.org/10.1038/s41598-018-19814-z.

[52] Mark Kasevich and Steven Chu. “Laser cooling below a photon recoil with three-level atoms”. In: *Phys. Rev. Lett.* 69 (12 1992), pp. 1741–1744. DOI: 10.1103/PhysRevLett.69.1741. URL: https://link.aps.org/doi/10.1103/PhysRevLett.69.1741.

[53] J. Reichel et al. “Raman Cooling of Cesium below 3 nK: New Approach Inspired by Lévy Flight Statistics”. In: *Phys. Rev. Lett.* 75 (1995), pp. 4575–4578. DOI: 10.1103/PhysRevLett.75.4575. URL: https://link.aps.org/doi/10.1103/PhysRevLett.75.4575.

[54] Kathryn Moler et al. “Theoretical analysis of velocity-selective Raman transitions”. In: *Physical Review A* 45 (1992), pp. 342–348. DOI: 10.1103/PhysRevA.45.342. URL: http://dx.doi.org/10.1103/PhysRevA.45.342.

[55] D.A. Steck. *Quantum and Atom Optics*. 2007. URL: https://books.google.fr/books?id=bc9TMwEACAAJ.

[56] I. Perrin et al. “Zero-velocity atom interferometry using a retroreflected frequency-chirped laser”. In: *Phys. Rev. A* 100 (5 2019), p. 053618. DOI: 10.1103/PhysRevA.100.053618. URL: https://link.aps.org/doi/10.1103/PhysRevA.100.053618.

[57] Pippa Storey and Claude Cohen-Tannoudji. “The Feynman path integral approach to atomic interferometry. A tutorial”. In: *J. Phys. II France* 4.11 (1994), pp. 1999–2027. DOI: 10.1051/jp2:1994103. URL: https://doi.org/10.1051/jp2:1994103.

[58] Patrick Cheinet et al. “Measurement of the sensitivity function in a time-domain atomic interferometer”. In: *IEEE Transactions on Instrumentation and Measurement* 57 (2008), pp. 1141–1148. DOI: 10.1109/TIM.2007.915148. URL: https://doi.org/10.1109/TIM.2007.915148.

[59] A. Bonnin et al. "Characterization of a simultaneous dual-species atom interferometer for a quantum test of the weak equivalence principle". In: *Phys. Rev. A* 92 (2 2015), p. 023626. DOI: 10.1103/PhysRevA.92.023626. URL: https://link.aps.org/doi/10.1103/PhysRevA.92.023626.

[60] Bess Fang et al. "Improving the phase response of an atom interferometer by means of temporal pulse shaping". In: *New Journal of Physics* 20.2 (2018), p. 023020. DOI: 10.1088/1367-2630/aaa37c. URL: https://doi.org/10.1088/1367-2630/aaa37c.

[61] R. Karcher, F. Pereira Dos Santos, and S. Merlet. "Impact of direct-digital-synthesizer finite resolution on atom gravimeters". In: *Phys. Rev. A* 101 (4 2020), p. 043622. DOI: 10.1103/PhysRevA.101.043622. URL: https://link.aps.org/doi/10.1103/PhysRevA.101.043622.

[62] Florence Yver-Leduc et al. "Reaching the quantum noise limit in a high-sensitivity cold-atom inertial sensor". In: *Journal of Optics B: Quantum and Semiclassical Optics* 5.2 (2003), S136–S142. DOI: 10.1088/1464-4266/5/2/371. URL: https://doi.org/10.1088/1464-4266/5/2/371.

[63] Q. Bodart et al. "A cold atom pyramidal gravimeter with a single laser beam". In: *Applied Physics Letters* 96.13 (2010), p. 134101. DOI: 10.1063/1.3373917. URL: https://doi.org/10.1063/1.3373917.

[64] C. J. Dedman, K. G. H. Baldwin, and M. Colla. "Fast switching of magnetic fields in a magneto-optic trap". In: *Review of Scientific Instruments* 72.11 (2001), pp. 4055–4058. DOI: 10.1063/1.1408935. URL: https://doi.org/10.1063/1.1408935.

[65] *Design Note 399: Low Noise Amplifiers for Small and Large Area Photodiodes*. Linear Technology. URL: https://www.analog.com/media/en/reference-design-documentation/design-notes/dn399f.pdf.

[66] Jie Yang et al. "Improved Iterative Calibration for Triaxial Accelerometers Based on the Optimal Observation". In: *Sensors (Basel)* 12 (2012), pp. 8157–8175. DOI: 10.3390/s120608157. URL: https://dx.doi.org/10.3390{\%}2Fs120608157.

[67] Keil, Mark *et al.* "Fifteen years of cold matter on the atom chip: promise, realizations, and prospects". In: *J Mod Opt* 63.18 (2016). DOI: 10.1080/09500340.2016.1178820. URL: https://pubmed.ncbi.nlm.nih.gov/27499585.

[68] V. Ménoret et al. "Dual-wavelength laser source for onboard atom interferometry". In: *Opt. Lett.* 36.21 (21 2011), pp. 4128–4130. DOI: 10.1364/OL.36.004128. URL: https://www.osapublishing.org/ol/abstract.cfm?uri=ol-36-21-4128.

[69] Schkolnik, V. and Hellmig, O. and Wenzlawski, A. *et al.* "A compact and robust diode laser system for atom interferometry on a sounding rocket." In: *Appl. Phys. B* 122.217 (2016). DOI: 10.1007/s00340-016-6490-0. URL: https://doi.org/10.1007/s00340-016-6490-0.

[70] Zachary L. Newman et al. "Architecture for the photonic integration of an optical atomic clock". In: *Optica* 6.5 (2019), pp. 680–685. DOI: 10.1364/OPTICA.6.000680. URL: http://www.osapublishing.org/optica/abstract.cfm?URI=optica-6-5-680.

[71] ColdQuanta. URL: https://www.coldquanta.com/.

[72] R. Thompson et al. "High power single frequency 780nm laser source generated from frequency doubling of a seeded fiber amplifier in a cascade of PPLN crystals". In: *Optics Express* 11.14 (2003), p. 1709. ISSN: 1094-4087. DOI: 10.1364/OE.11.001709. URL: https://doi.org/10.1364/OE.11.001709.

[73] D.O. Sabulsky, J. Junca, G. Lefèvre, et al. "A fibered laser system for the MIGA large scale atom interferometer". In: *Sci. Rep.* 10 (1 2020), p. 3268. DOI: 10.1038/s41598-020-59971-8. URL: https://doi.org/10.1038/s41598-020-59971-8.

[74] E. Oh, R. A. Horne, and C. A. Sackett. "Fast phase stabilization of a low frequency beat note for atom interferometry". In: *Rev. Sci. Instrum.* 87.6 (2016), p. 063105. DOI: 10.1063/1.4953338. URL: https://aip.scitation.org/doi/10.1063/1.4953338.

[75] W. Li et al. "A phase-locked laser system based on double direct modulation technique for atom interferometry". In: *Appl. Phys. B* 123 (2017), p. 54. DOI: 10.1007/s00340-016-6630-6. URL: http://link.springer.com/10.1007/s00340-016-6630-6.

[76] W. Peng et al. "Locking laser frequency of up to 40 GHz offset to a reference with a 10 GHz electro-optic modulator". In: *Opt. Lett.* 39 (10 2014), pp. 2998–3001. DOI: 10.1364/OL.39.002998. URL: http://ol.osa.org/abstract.cfm?URI=ol-39-10-2998.

[77] F. Theron et al. "Narrow linewidth single laser source system for onboard atom interferometry". In: *Appl. Phys. B* 118 (1 2015), pp. 1–5. DOI: 10.1007/s00340-014-5975-y. URL: https://link.springer.com/article/10.1007/s00340-014-5975-y.

[78] A. Bonnin et al. "Simultaneous dual-species matter-wave accelerometer". In: *Phys. Rev. A* 88.4 (2013), p. 043615. ISSN: 1050-2947. DOI: 10.1103/PhysRevA.88.043615. URL: http://link.aps.org/doi/10.1103/PhysRevA.88.043615.

[79] O. Carraz et al. “Phase shift in an atom interferometer induced by the additional laser lines of a Raman laser generated by modulation”. In: *Phys. Rev. A* 86.3 (2012), p. 033605. DOI: 10.1103/PhysRevA.86.033605. URL: http://link.aps.org/doi/10.1103/PhysRevA.86.033605.

[80] L. Zhu et al. “Application of optical single-sideband laser in Raman atom interferometry”. In: *Opt. Express* 26.6 (2018), pp. 6542–6553. DOI: 10.1364/OE.26.006542. URL: https://www.osapublishing.org/oe/abstract.cfm?uri=oe-26-6-6542.

[81] Bahaa Saleh and Malvin Carl Teich. “Electro-Optics”. In: *Fundamentals of Photonics*. John Wiley & Sons, 1991. Chap. 18, pp. 696–736.

[82] M. Izutsu, S. Shikama, and T. Sueta. “Integrated optical SSB modulator/frequency shifter”. In: *IEEE J. Quantum Electron.* 17.11 (1981), pp. 2225–2227. DOI: 10.1109/JQE.1981.1070678. URL: https://ieeexplore.ieee.org/document/1070678/.

[83] S. Shimotsu et al. “Single side-band modulation performance of a $LiNbO_3$ integrated modulator consisting of four-phase modulator waveguides”. In: *IEEE Photonic Tech. Lett.* 13.4 (2001), pp. 364–366. DOI: 10.1109/68.917854. URL: https://ieeexplore.ieee.org/document/917854/.

[84] J. Lautier, M. Lours, and A. Landragin. “A compact micro-wave synthesizer for transportable cold-atom interferometers”. In: *Rev. of Sci. Instrum.* 85 (2014), p. 063114. DOI: 10.1063/1.4884338. URL: https://aip.scitation.org/doi/abs/10.1063/1.4884338.

[85] Isaiah Morgenstern et al. “A versatile microwave source for cold atom experiments controlled by a field programmable gate array”. In: *Review of Scientific Instruments* 91 (2020), p. 023202. DOI: 10.1063/1.5127880. URL: https://doi.org/10.1063/1.5127880.

[86] Qin Luo et al. “A compact laser system for a portable atom interferometry gravimeter A compact laser system for a portable atom interferometry gravimeter”. In: *Review of Scientific Instruments* 90 (2019). DOI: 10.1063/1.5053132. URL: http://dx.doi.org/10.1063/1.5053132.

[87] J Le Gouët et al. “Influence of lasers propagation delay on the sensitivity of atom interferometers”. In: *European Physical Journal D* 44 (2007), pp. 419–425. DOI: 10.1140/epjd/e2007-00218-2. URL: https://doi.org/10.1140/epjd/e2007-00218-2.

[88] Ch J. Bordeé. *Atomic interferometry with internal state labelling*. 1989. DOI: 10.1016/0375-9601(89)90537-9. URL: https://doi.org/10.1016/0375-9601(89)90537-9.

[89] Anne Louchet-Chauvet et al. "The influence of transverse motion within an atomic gravimeter". In: *New J. Phys.* 13 (2011), p. 065025. DOI: 10.1088/1367-2630/13/6/065025. URL: https://doi.org/10.1088/1367-2630/13/6/065025.

[90] Jake VanderPlas. *Frequentism and Bayesianism: A Python-driven Primer*. 2014. arXiv: 1411.5018 [astro-ph.IM]. URL: https://arxiv.org/abs/1411.5018.

[91] Gauguet, A. and Mehlstäubler, T. E. and Lévèque, T. and Le Gouët, J. and Chaibi, W. and Canuel, B. and Clairon, A. and Dos Santos, F. Pereira and Landragin, A. "Off-resonant Raman transition impact in an atom interferometer". In: *Physical Review A* 78 (2008), p. 043615. DOI: 10.1103/PhysRevA.78.043615. URL: https://doi.org/10.1103/PhysRevA.78.043615.

[92] B. Dubetsky. "Full elimination of the gravity-gradient terms in atom interferometry". In: *Applied Physics B* 125 (2019), p. 187. DOI: 10.1007/s00340-019-7300-2. URL: https://doi.org/10.1007/s00340-019-7300-2.

[93] Shau-Yu Lan et al. "Influence of the Coriolis Force in Atom Interferometry". In: *Phys. Rev. Lett.* 108 (2012), p. 090402. DOI: 10.1103/PhysRevLett.108.090402. URL: https://link.aps.org/doi/10.1103/PhysRevLett.108.090402.

[94] P. Gillot et al. "Limits to the symmetry of a Mach-Zehnder-type atom interferometer". In: *Phys. Rev. A* 93 (2016), p. 013609. DOI: 10.1103/PhysRevA.93.013609. URL: https://link.aps.org/doi/10.1103/PhysRevA.93.013609.

[95] Alexandre Gauguet. "Gyromètre à atomes froids: Etude de la stabilité limite et des effets systématiques liés aux séparatrices lasers." Theses. Université Pierre et Marie Curie - Paris VI, 2008. URL: https://tel.archives-ouvertes.fr/tel-00322150.

[96] V. Schkolnik et al. "The effect of wavefront aberrations in atom interferometry". In: *Applied Physics B: Lasers and Optics* 120 (2015), pp. 311–316. DOI: 10.1007/s00340-015-6138-5. URL: https://doi.org/10.1007/s00340-015-6138-5.

[97] N. Mielec et al. "Atom interferometry with top-hat laser beams". In: *Applied Physics Letters* 113.16 (2018), p. 161108. DOI: 10.1063/1.5051663. URL: https://doi.org/10.1063/1.5051663.